Imaging through obscurants using time-correlated single-photon counting in the short-wave infrared

Rachael Tobin, BSc

Submitted for the degree of Doctor of Philosophy

Heriot-Watt University

School of Engineering and Physical Sciences

Institute of Photonics and Quantum Sciences

Edinburgh, United Kingdom

August 2019

ABSTRACT

Single-photon time-of-flight (ToF) light detection and ranging (LiDAR) systems have emerged in recent years as a candidate technology for high-resolution depth imaging in challenging environments, such as long-range imaging and imaging in scattering media. This Thesis investigates the potential of two ToF single-photon depth imaging systems based on the time-correlated single-photon (TCSPC) technique for imaging targets in highly scattering environments. The high sensitivity and picosecond timing resolution afforded by the TCSPC technique offers high-resolution depth profiling of remote targets while maintaining low optical power levels. Both systems comprised a pulsed picosecond laser source with an operating wavelength of 1550 nm, and employed InGaAs/InP SPAD detectors. The main benefits of operating in the shortwave infrared (SWIR) band include improved atmospheric transmission, reduced solar background, as well as increased laser eye-safety thresholds over visible band sensors.

Firstly, a monostatic scanning transceiver unit was used in conjunction with a single-element Peltier-cooled InGaAs/InP SPAD detector to attain sub-centimetre resolution three-dimensional images of long-range targets obscured by camouflage netting or in high levels of scattering media. Secondly, a bistatic system, which employed a 32×32 pixel format InGaAs/InP SPAD array was used to obtain rapid depth profiles of targets which were flood-illuminated by a higher power pulsed laser source. The performance of this system was assessed in indoor and outdoor scenarios in the presence of obscurants and high ambient background levels.

Bespoke image processing algorithms were developed to reconstruct both the depth and intensity images for data with very low signal returns and short data acquisition times, illustrating the practicality of TCSPC-based LiDAR systems for real-time image acquisition in the SWIR wavelength region - even in the photon-starved regime.

ACKNOWLEDGEMENTS

ACADEMIC REGISTRY
Research Thesis Submission

Name*:*	
School:	

Version: *(i.e. First, Resubmission, Final)*		Degree Sought:	

Declaration

In accordance with the appropriate regulations I hereby submit my thesis and I declare that:

1. The thesis embodies the results of my own work and has been composed by myself
2. Where appropriate, I have made acknowledgement of the work of others
3. Where the thesis contains published outputs under Regulation 6 (9.1.2) these are accompanied by a critical review which accurately describes my contribution to the research and, for multi-author outputs, a signed declaration indicating the contribution of each author (complete Inclusion of Published Works Form – see below)
4. The thesis is the correct version for submission and is the same version as any electronic versions submitted*.
5. My thesis for the award referred to, deposited in the Heriot-Watt University Library, should be made available for loan or photocopying and be available via the Institutional Repository, subject to such conditions as the Librarian may require
6. I understand that as a student of the University I am required to abide by the Regulations of the University and to conform to its discipline.
7. Inclusion of published outputs under Regulation 6 (9.1.2) shall not constitute plagiarism.
8. I confirm that the thesis has been verified against plagiarism via an approved plagiarism detection application e.g. Turnitin.

*   *Please note that it is the responsibility of the candidate to ensure that the correct version of the thesis is submitted.*

Signature of Candidate*:*		Date:	

Submission

Submitted By *(name in capitals):*	
Signature of Individual Submitting:	
Date Submitted:	

For Completion in the Student Service Centre (SSC)

Received in the SSC by *(name in capitals):*		
Method of Submission *(Handed in to SSC; posted through internal/external mail):*		
E-thesis Submitted (mandatory for final theses)		
Signature:		Date:

TABLE OF CONTENTS

LIST OF ABBREVIATIONS

2D	two-dimensional
3D	three-dimensional
ADAS	advanced driver assistance systems
ADC	analogue-to-digital convertor
ADMM	Alternating Direction Method of Multipliers
AM	amplitude modulation
APD	avalanche photodiode
APSS	algebraic point set surfaces
ASE	amplified spontaneous emission
BHL	Battery Hill Laboratory
BIL	burst illumination LiDAR
BP	bandpass
CCD	charged coupled device
CFD	constant fraction discriminator
CMOS	complementary metal-oxide-semiconductor
CW	continuous wave
DAC	digital-to-analogue convertor
DC	direct current
DCR	dark count rate
EFL	effective focal length
FM	frequency modulation
FoR	field-of-regard
FoV	field-of-view
FPA	focal plane array
FPGA	field-programmable gate array
FWHM	full-width at half-maximum
Ge	germanium
Ge-on-Si	germanium on silicon
GM	galvanometer mirror
GPU	graphics processing unit
GUI	graphical user interface
InGaAs	indium gallium arsenide
InP	indium phosphide
InGaAs/InP	indium gallium arsenide / indium phosphide
IRF	instrumental response function
LiDAR	light detection and ranging
LP	longpass
M-NR3D	Multidimensional Nonlocal Reconstruction of 3D images algorithm
MCMC	Markov chain Monte Carlo
NbN	niobium nitride

NbTiN	niobium titanium nitride
ND	neutral density
NDVI	normalised differential vegetation index
NEP	noise equivalent power
NIR	near infrared
OBJ	objective lens
OD	optical density
OSA	optical spectrum analyser
OT	optical thickness
PBS	polarising beam splitter
PLW	Princeton Lightwave
PMT	photomultiplier tube
PPP	photons per pixel
PRI	photochemical reflectance index
RDI-TV	Restoration of Depth and Intensity using the Total Variation algorithm
RGB	red, green, blue
RL	relay lens
RPG	rocket-propelled grenade
Rx	receive channel
SBR	signal-to-background ratio
Si	silicon
SLR	satellite laser ranging
Sn	tin
SNR	signal-to-noise ratio
SNSPDs	superconducting nanowire single-photon detectors
SP	shortpass
SPAD	single-photon avalanche diode
SPDE	single-photon detection efficiency
SRE	signal-to-reconstruction error
SWIR	short-wave infrared
TCSPC	time-correlated single-photon counting
TAC	time-to-amplitude convertor
TDC	time-to-digital convertor
TEC	thermo-electric cooler
ToF	time-of-flight
TTTR	time-tagged-time-resolved
Tx	transmit channel
USB	universal serial bus
VIS	visible
WSi	tungsten silicide

LIST OF PUBLICATIONS

Papers published in peer reviewed Journals

J. Tachella, Y. Altmann, N. Mellado, A. McCarthy, **R. Tobin**, G. S. Buller, J.-Y. Tourneret, and S. McLaughlin, "Real-time 3D reconstruction of complex scenes using single-photon lidar: when image processing meets computer graphics," ArXiv190506700 Phys., *manuscript under review at Nature Communications,* (2019).

A. Halimi, **R. Tobin**, A. McCarthy, J. Bioucas-Dias, S. McLaughlin, and G. S. Buller, "Restoration of multidimensional sparse single-photon 3D-LiDAR images," *manuscript accepted at IEEE, Trans. Comput. Imaging.,* (2019).

R. Tobin, A. Halimi, A. McCarthy, M. Laurenzis, F. Christnacher, and G. S. Buller, "Three-dimensional single-photon imaging through obscurants," Opt. Express 27(4), 4590 (2019).

X. Ren, Y. Altmann, **R. Tobin**, A. Mccarthy, S. Mclaughlin, and G. S. Buller, "Wavelength-time coding for multispectral 3D imaging using single-photon LiDAR," Opt. Express 26(23), 30146–30161 (2018).

R. Tobin, A. Halimi, A. McCarthy, X. Ren, K. J. McEwan, S. McLaughlin, and G. S. Buller, "Long-range depth profiling of camouflaged targets using single-photon detection," Opt. Eng. 57(3), 031303 (2017).

R. Tobin, Y. Altmann, X. Ren, A. McCarthy, R. A. Lamb, S. McLaughlin, and G. S. Buller, "Comparative study of sampling strategies for sparse photon multispectral lidar imaging: towards mosaic filter arrays," J. Opt. 19(9), 094006 (2017).

Conference proceedings

P. Soan, M. Silver, J. Parsons, P. Feneyrou, A. Martin, **R. Tobin**, A. McCarthy, A. Halimi, S. Chan, K. McEwan, J. Miah, B. Stewart, J. Leach, G. S. Buller, "Comparative assessment of different active imaging technologies for imaging through obscurants," Proc. SPIE 10796, *Electro-Optical Remote Sensing XII*, 107960C (2018).

R. Tobin, A. Halimi, A. McCarthy, M. Laurenzis, F. Christnacher, G. S. Buller, "Depth imaging through obscurants using time-correlated single-photon counting," Proc. SPIE 10659, *Advanced Photon Counting Techniques XII*, 106590S (2018).

G. S. Buller, A. Halimi, A. Maccarone, X. Ren, **R. Tobin**, P. W. Connolly, Z. M. Greener, Y. Altmann, and A. McCarthy, "Three-dimensional imaging under extreme conditions using single-photon counting," *in Conference on Lasers and Electro-Optics*, OSA Technical Digest, paper AW3R.4 (2018).

Y. Altmann, **R. Tobin**, A. Maccarone, X. Ren, A.McCarthy, G. S. Buller, S. McLaughlin, "Bayesian restoration of reflectivity and range profiles from subsampled single-photon multispectral Lidar data," *25th European Signal Processing Conference (EUSIPCO)*, 1410-1414 (2017).

A. Maccarone, A. Halimi, A. McCarthy, **R. Tobin**, S. McLaughlin, Y. Petillot, and G. S. Buller, "Underwater Three-Dimensional Imaging using Single-Photon Detection," *in Conference on Lasers and Electro-Optics*, paper SF2M.2. (2017).

A. Halimi, **R. Tobin**, A. McCarthy, S. McLaughlin, and G. S. Buller, "Restoration of multilayered single-photon 3d lidar images," *25th European Signal Processing Conference (EUSIPCO)*, 708-712 (2017).

A. Maccarone, A. McCarthy, A. Halimi, **R. Tobin**, A. M. Wallace, Y. Petillot, S. McLaughlin, G. S. Buller, "Depth imaging in highly scattering underwater environments using time-correlated single-photon counting," Proc. SPIE 9992, *Emerging Imaging and Sensing Technologies*, 99920R (2016).

Conference presentations and contributions

R. Tobin, A. McCarthy, A. Halimi, J. Tachella, Y. Altmann, M. Laurenzis, F. Christnacher, P. Soan, K.J. McEwan, S. McLaughlin and G.S. Buller, "Three dimensional profiling through obscurants using single photon detection in the short wave infrared", SPIE Security + Defence, Strasbourg, France (**invited** September 2019).

G.S. Buller, A. McCarthy, **R. Tobin**, A. Maccarone, A. Halimi, J. Tachella, Y. Altmann, S. McLaughlin, A.M. Wallace, M. Laurenzis, F. Christnacher, P. Soan, K.J. McEwan, "Three-dimensional imaging in extreme conditions using single-photon detection", SPIE Optics + Photonics, San Diego, California, USA (**invited** August 2019).

A. Halimi, **R. Tobin**, A. McCarthy, J. Bioucas-Dias, S. McLaughlin, and G.S. Buller, "Joint Reconstruction of Multitemporal or Multispectral Single-Photon 3D LiDAR Images", IEEE SSPD, Brighton, UK (May 2019).

R. Tobin, A. Halimi, A. McCarthy, M. Laurenzis, F. Christnacher, P.J. Soan, K.J. McEwan, G.S. Buller, "Depth profiling of targets in highly obscuring media using single-photon detection", SPIE Defense + Commercial Sensing, Baltimore, Maryland, USA (**invited** April 2019).

P. Soan, G.S. Buller, M. Silver, K. McEwan, J. Parsons, P. Feneyrou, A. Martin, **R. Tobin**, A. McCarthy, A. Halimi, S. Chan, J. Miah, B. Stewart, and J. Leach, "Comparative assessment of different active imaging technologies for imaging through obscurants", SPIE Security + Defence 2018, Berlin, Germany (**invited** October 2018).

G.S. Buller, A. Halimi, A. Maccarone, X. Ren, **R. Tobin**, P.W.R. Connolly, Z.M Greener, Y. Altmann, A. McCarthy, "Three‑Dimensional Imaging Under Extreme Conditions Using Single‑Photon Counting", CLEO: Applications and Technology 2018, San Jose, USA (**invited** May 2018).

G.S. Buller, A. McCarthy, X. Ren, A. Maccarone, **R. Tobin**, P.W.R. Connolly, A. Halimi, Y. Altmann, Y.R. Petillot, S. McLaughlin, A.M. Wallace, I. Gyongy, R.K. Henderson, A.M. Pawlikowska, R.A. Lamb, "Applications of single‑photon depth imaging", SPIE Commercial + Scientific Sensing and Imaging, Orlando, Florida, USA (**invited** April 2018).

R. Tobin, A. Halimi, A. McCarthy, M. Laurenzis, F. Christnacher, and G.S. Buller, "Depth imaging through obscurants using time‑correlated single‑photon counting", SPIE Defense and Commercial Sensing, Orlando, Florida, USA (April 2018).

G.S. Buller, A. McCarthy, X. Ren, A. Maccarone, **R. Tobin**, Abderrahim Halimi, Y. Altmann, Y.R. Petillot, S. McLaughlin, A.M. Wallace, A.M. Pawlikowska, R.A. Lamb, "Single photon depth imaging", SPIE Security and Defence, Warsaw , Poland (**invited** September 2017)

G. S. Buller, **R. Tobin**, A. McCarthy, A. Halimi, X. Ren, M. Laurenzis, and F. Christnacher, "Single photon imaging through obscurants and camouflage", 6th Workshop on Active Imaging, Institute Saint Louis, France (November 2017).

A. Halimi, **R. Tobin**, A. McCarthy, S. McLaughlin, and G.S. Buller, "Restoration of multilayered single-photon 3D LiDAR images", European Signal Processing Conference (EUSIPCO), Kos Island, Greece, (September 2017).

G.S. Buller, A. McCarthy, X. Ren, A. Maccarone, **R. Tobin**, Abderrahim Halimi, Y. Altmann, Y.R. Petillot, S. McLaughlin, A.M. Wallace, "Depth imaging using single photon detection", SPIE Optics and Photonics, San Diego, USA (**invited** August 2017)

Y. Altmann, **R. Tobin**, X. Ren, A. McCarthy, G.S. Buller, S. McLaughlin, "Comparison of sampling strategies for 3D scene reconstruction from sparse multispectral lidar waveforms", SPIE Optics and Photonics, San Diego (August 2017).

A. Maccarone, A. Halimi, A. McCarthy, **R. Tobin**, S. McLaughlin, Y. Petillot, G.S. Buller, "Underwater Three-Dimensional Imaging using Single Photon Detection", CLEO, San Jose, California, USA (May 2017).

A. Maccarone, A. McCarthy, A. Halimi, **R. Tobin**, A.M.Wallace, Y.R. Petillot and G.S. Buller, "Depth imaging in highly scattering underwater environments using time-correlated single photon counting", SPIE Security + Defence, Edinburgh, UK (September 2016).

X. Ren, Y. Altmann, A. McCarthy, A. Halimi, **R. Tobin**, S. McLaughlin and G.S. Buller, "Depth imaging using sparse single-photon data", Photon16, Leeds, UK (September 2016).

A. Halimi, Y. Altmann, A. McCarthy, X. Ren, **R. Tobin**, G.S. Buller, S. McLaughlin, "Restoration of intensity and depth images constructed using sparse single-photon data", European Signal Processing Conference (EUSIPCO), Budapest, Hungary (August 2016).

Chapter 1: Introduction

1.1 Introduction

In recent years, there has been a rising interest in the use of Light Detection and Ranging (LiDAR) systems for the high-resolution imaging of targets in visually degraded environments. Natural and man-made obscurants, such as smoke, dust, fog, and haze are an impediment to the acquisition of high-resolution images of targets, as a high level of particulate scattering strongly affects image resolution and contrast, eventually degrading the image to a point where target identification is not possible [1.1]. This affects the performance of many applications including defence operations, where high levels of obscurants can prevent effective pilotage, degrade situational awareness, and deny the ability to carry out surveillance and reconnaissance [1.2,1.3]. Additionally, the recent interest in the integration of LiDAR systems in advanced driver assistance systems and fully autonomous vehicles has highlighted the need for real-time depth profiling at distances up to hundreds of metres [1.4–1.8].

Time-of-flight (ToF) LiDAR systems have been around since the 1960s [1.9] and are capable of non-invasive, non-contact measurements of remote targets over a high dynamic range of target distances. These systems measure the ToF of a reflected optical signal to determine the distance to an object relative the system location. Today, LiDAR continues to be the technique of choice in a variety of remote sensing applications, including environmental monitoring [1.10,1.11], surveillance and defence [1.3], and terrain mapping [1.12–1.14]. The time-correlated single-photon counting (TCSPC) technique has more recently emerged as a candidate technology for LiDAR systems, due to its high sensitivity and excellent surface-to-surface resolution [1.15]. The improved depth resolution of this approach allows for identification of closely distributed targets, and has been successfully demonstrated in a number of LiDAR applications, such as long-range imaging [1.16,1.17], multi-spectral imaging [1.18–1.20], and underwater depth imaging [1.21]. The TCSPC technique can be used to obtain both depth and intensity information of an object, and build a three-dimensional image of the target scene by use of single-pixel detectors or multiple detector arrays [1.22]. The use of high-sensitivity single-photon detectors means that low average optical power levels can be used, even at long distances. This results in the potential for low-power, eye-safe imaging.

This Thesis is concerned with the design and evaluation of two reconfigurable single-photon systems based on the TCSPC technique. The high-sensitivity and picosecond timing resolution of the TCSPC technique were exploited to obtain depth and intensity profiles of targets in high levels of scattering media, obscured by camouflage netting, and of complex dynamic scenes. The first system presented is a monostatic scanning transceiver system with a single-element indium gallium arsenide/indium phosphide (InGaAs/InP) SPAD detector designed for free-space depth imaging over long distances. The second system is a bistatic system based on an InGaAs/InP SPAD detector array, which was designed for the rapid acquisition of changing scenes using flood-illumination. Both systems had an operational wavelength of 1550 nm, which was selected for its high atmospheric transmission and because the adverse effect of solar background at this wavelength is significantly lower compared to operating at wavelengths below 1 µm [1.23–1.25]. Moreover, as this wavelength is outside the retinal hazard region [1.26] it permits the use of higher average optical powers in comparison to wavelengths in the visible region of the spectrum.

In addition, several reconstruction algorithms, which exploit spatial correlations in single-photon data, were used for the reconstruction of single-photon data obtained in highly scattering environments [1.27–1.29]. These algorithms were designed to be robust when used in the sparse photon regime under high levels of ambient background light.

1.2 Thesis structure

Chapter 2 introduces the LiDAR technique and presents several types of LiDAR systems designed for imaging targets in challenging environments, such as at long-ranges, in clutter, and in highly scattering media. Although a few examples of LiDAR systems are presented, particular attention is given to TCSPC-based systems. The principal characteristics of scattering effects from small particles and the benefits of free-space imaging using shortwave infrared (SWIR) wavelengths in scattering environments are also discussed.

Chapter 3 provides a brief review of the TCSPC technique, and explains how it can be used in applications that require single-photon sensitivity - particularly for applications in the sparse photon regime where return optical signals are very low. Since appropriate considerations must be made regarding the choice of single-photon detector in order to choose the most suitable detector that meets the requirements of both the optical system and the application, this Chapter also gives an overview of several single-photon detector

technologies, such as PMTs, SNSPDs, and SPAD detectors. Specific attention is given to InGaAs/InP SPAD detectors, which are the detectors used in the experiments reported in this Thesis.

Chapter 4 presents experimental results of camouflaged targets in challenging outdoor environments at a stand-off distance of 230 metres using eye-safe optical power levels [1.30]. These results were acquired using a scanning monostatic ToF single-photon imaging system, which comprised a pulsed illumination source at an operating wavelength of 1550 nm and a single-element InGaAs/InP SPAD detector. A full system description is provided along with a description of an advanced image processing algorithm for the reconstruction of multi-surface single-photon data.

Chapter 5 explores the potential of the scanning monostatic depth imaging system for imaging objects in highly scattering environments at a wavelength of 1550 nm using eye-safe optical power levels [1.31]. Depth profiles of targets obtained in four different types of obscurants in a 26-metre-long indoor obscurant chamber are presented. In additional, optical transmission measurements were performed, and compared to visible band measurements. The experimental results processed using three image processing algorithms of varying sophistication are presented.

Chapter 6 presents the experimental results of targets in highly scattering media acquired with bistatic mode system, using a 32×32 InGaAs/InP SPAD detector array. A full system description, along with a characterisation of the detector, is provided, with discussion of parameters such as the dark count rate (DCR), the single-photon detection efficiency (SPDE), and the timing response of the detector. An adapted LiDAR model for the bistatic active imaging system based on the photon-counting LiDAR equation is also provided. Finally, the performance of the system is evaluated over distances of 50 and 150 metres in the presence of obscurants, and at a longer range of 1463 metres in clear conditions.

Chapter 7 explores the potential of the InGaAs/InP detector array system for the acquisition of full-field, video-rate, three-dimensional data. Experimental results obtained using a state-of-the-art algorithm designed for the 'real-time' image reconstruction of complex scenes at 320 metres are presented [1.29]. Results obtained from a variety of scenes with increasing complexity are investigated and the potential limitations of the algorithm are discussed.

In Chapter 8, a summary of the conclusions drawn from the work contained within this Thesis are presented, as well as a discussion about future work.

1.3 References

1.1. E. J. McCartney, *Optics of the Atmosphere* (Wiley, 1976).

1.2. P. W. Kruse, "Why the military interest in near-millimeter wave imaging?," in *Millimeter Optics* 0259, 94–99 (1981).

1.3. P. Soan, M. Silver, J. Parsons, P. Feneyrou, A. Martin, R. Tobin, A. McCarthy, A. Halimi, S. Chan, K. McEwan, J. Miah, B. Stewart, J. Leach, and G. Buller, "Comparative assessment of different active imaging technologies for imaging through obscurants," in *Electro-Optical Remote Sensing XII* 10796, 107960C (2018).

1.4. J. Hecht, "Lidar for Self-Driving Cars," Opt. Photonics News 29(1), 26–33 (2018).

1.5. A. Azim and O. Aycard, "Detection, classification and tracking of moving objects in a 3D environment," in *2012 IEEE Intelligent Vehicles Symposium*, 802–807 (2012).

1.6. A. Petrovskaya and S. Thrun, "Model based vehicle detection and tracking for autonomous urban driving," Auton. Robots 26(2), 123–139 (2009).

1.7. C. Guo, W. Sato, L. Han, S. Mita, and D. McAllester, "Graph-based 2D road representation of 3D point clouds for intelligent vehicles," in *2011 IEEE Intelligent Vehicles Symposium (IV)*, 715–721 (2011).

1.8. D. Steinhauser, O. Ruepp, and D. Burschka, "Motion segmentation and scene classification from 3D LIDAR data," in *2008 IEEE Intelligent Vehicles Symposium*, 398–403 (2008).

1.9. R. D. Richmond and S. C. Cain, *Direct-Detection LADAR Systems* (SPIE, 2010).

1.10. G. Zhao, M. Lian, Y. Li, Z. Duan, S. Zhu, L. Mei, and S. Svanberg, "Mobile lidar system for environmental monitoring," Appl. Opt. 56(5), 1506–1516 (2017).

1.11. P. Gaudio, M. Gelfusa, A. Malizia, S. Parracino, M. Richetta, L. De Leo, C. Perrimezzi, and C. Bellecci, "Detection and monitoring of pollutant sources with Lidar/Dial techniques," J. Phys. Conf. Ser. 658, 012004 (2015).

1.12. B. Schwarz, "Mapping the world in 3D," Nat. Photonics 4(7), 429–430 (2010).

1.13. D. Cunningham, S.Grebby, K. Tansey, A. Gosar, and V. Kastelic, "Application of airborne LiDAR to mapping seismogenic faults in forested mountain terrain, south-eastern Alps, Slovenia," Geophys. Res. Lett., 33, L20308 (2006).

1.14. W. E. Clifton, B. Steele, G. Nelson, A. Truscott, M. Itzler, M. Entwistle, "Medium altitude airborne Geiger-mode mapping LIDAR system," Proc. SPIE 9465, Laser Radar Technology and Applications XX and Atmospheric Propagation XII, 946506 (2015);

1.15. G. S. Buller and A. Wallace, "Ranging and three-dimensional imaging using time-correlated single-photon counting and point-by-point acquisition," IEEE J. Sel. Top. Quantum Electron 13(4), 1006–1015 (2007).

1.16. A. McCarthy, R. J. Collins, N. J. Krichel, V. Fernández, A. M. Wallace, and G. S. Buller, "Long-range time-of-flight scanning sensor based on high-speed time-correlated single-photon counting," Appl. Opt. 48(32), 6241–6251 (2009).

1.17. A. M. Pawlikowska, A. Halimi, R. A. Lamb, and G. S. Buller, "Single-photon three-dimensional imaging at up to 10 kilometers range," Opt. Express 25(10), 11919–11931 (2017).

1.18. A. M. Wallace, A. McCarthy, C. J. Nichol, X. Ren, S. Morak, D. Martinez-Ramirez, I. H. Woodhouse, and G. S. Buller, "Design and evaluation of multispectral LiDAR for the recovery of arboreal parameters," IEEE Trans. Geosci. Remote Sens. 52(8), 4942–4954 (2014).

1.19. X. Ren, Y. Altmann, R. Tobin, A. McCarthy, S. McLaughlin, and G. S. Buller, "Wavelength-time coding for multispectral 3D imaging using single-photon LiDAR," Opt. Express 26(23), 30146–30161 (2018).

1.20. R. Tobin, Y. Altmann, X. Ren, A. McCarthy, R. A. Lamb, S. McLaughlin, and G. S. Buller, "Comparative study of sampling strategies for sparse photon multispectral lidar imaging: towards mosaic filter arrays," J. Opt. 19(9), 094006 (2017).

1.21. A. Maccarone, A. McCarthy, X. Ren, R. E. Warburton, A. M. Wallace, J. Moffat, Y. Petillot, and G. S. Buller, "Underwater depth imaging using time-correlated single-photon counting," Opt. Express 23(26), 33911–33926 (2015).

1.22. D. Shin, A. Kirmani, V. K. Goyal, and J. H. Shapiro, "Photon-efficient computational 3-D and reflectivity imaging with single-photon detectors," IEEE Trans. Comput. Imaging 1(2), 112–125 (2015).

1.23. D. Killinger, "Free space optics for laser communication through the air," Opt. Photonics News 13(10), 36–42 (2002).

1.24. I. I. Kim, M. Mitchell, and E. J. Korevaar, "Measurement of scintillation for free-space laser communication at 785 nm and 1550 nm," in *Optical Wireless Communications II* 3850, 49–63 (1999).

1.25. F. Nadeem, T. Javornik, E. Leitgeb, V. Kvicera, and G. Kandus, "Continental fog attenuation empirical relationship from measured visibility data," Radioengineering 19(4), 596–600 (2010).

1.26. P. N. Youssef, N. Sheibani, and D. M. Albert, "Retinal light toxicity," Eye 25(1), 1–14 (2011).

1.27. A. Halimi, R. Tobin, A. McCarthy, J. Bioucas-Dias, S. McLaughlin, and G. S. Buller, "Restoration of multidimensional sparse single-photon 3D-LiDAR images," IEEE, Trans. Comput. Imaging, accepted, (2018).

1.28. A. Halimi, Y. Altmann, A. McCarthy, X. Ren, R. Tobin, G. S. Buller, and S. McLaughlin, "Restoration of intensity and depth images constructed using sparse single-photon data," in *2016 24th European Signal Processing Conference (EUSIPCO)*, 86–90 (2016).

1.29. J. Tachella, Y. Altmann, N. Mellado, A. McCarthy, R. Tobin, G. S. Buller, J.-Y. Tourneret, and S. McLaughlin, "Real-time 3D reconstruction of complex scenes using single-photon lidar: when image processing meets computer graphics," ArXiv190506700 Phys. (2019).

1.30. R. Tobin, A. Halimi, A. McCarthy, X. Ren, K. J. McEwan, S. McLaughlin, and G. S. Buller, "Long-range depth profiling of camouflaged targets using single-photon detection," Opt. Eng. 57(3), 031303 (2017).

1.31. R. Tobin, A. Halimi, A. McCarthy, M. Laurenzis, F. Christnacher, and G. S. Buller, "Three-dimensional single-photon imaging through obscurants," Opt. Express 27(4), 4590–4611 (2019).

Chapter 2: Introduction to LiDAR imaging

2.1 Introduction

Imaging in highly scattering environments presents several challenges for the photonics and image processing communities. The high levels of particulate scattering when imaging through an obscuring media, such as fog or smoke, can greatly diminish image contrast, spatial resolution, and optical signal strength [2.1–2.3]. This Chapter aims to give an overview of the current state of the field. A brief introduction to the light detection and ranging (LiDAR) technique (otherwise referred to in some literature as the laser detection and ranging (LADAR) technique) and a review of several types of LiDAR systems is given in Sections 2.2. The principal characteristics of scattering effects from small particles are discussed in Section 2.3. Finally, the benefits of free-space imaging using shortwave infrared (SWIR) wavelengths in scattering environments is given in Section 2.4.

2.2 LiDAR systems for free-space imaging

Over the years, there has been increasing interest in the development of high-resolution remote sensing systems that operate over a wide range of distances. LiDAR systems present a good alternative to conventional detection systems, such as radio detection and ranging (RADAR) systems, as they are capable of accurate detection of very small objects at long-ranges due to the use of much shorter wavelengths [2.4]. In addition, they can attain very high depth resolution that can be at a micrometre level for short-range measurements, as reported by Baumann *et al.* in ref. [2.5] and Massa *et al.* in ref. [2.6]. Moreover, many modern LiDAR system designs are relatively modular and compact, allowing them to be deployed in a variety of ranging and imaging applications, such as in airborne platforms [2.7–2.9], in driverless car navigation systems [2.1,2.9], and for underwater depth imaging [2.10,2.11].

As the name suggests, the LiDAR technique uses the time-of-flight (ToF) of a reflected optical signal to determine the distance to an object relative the system location. A basic active LiDAR system has three main sections: the transmitter, the receiver/detection unit, and the system control and data acquisition unit, as shown in Figure 2.1.

7
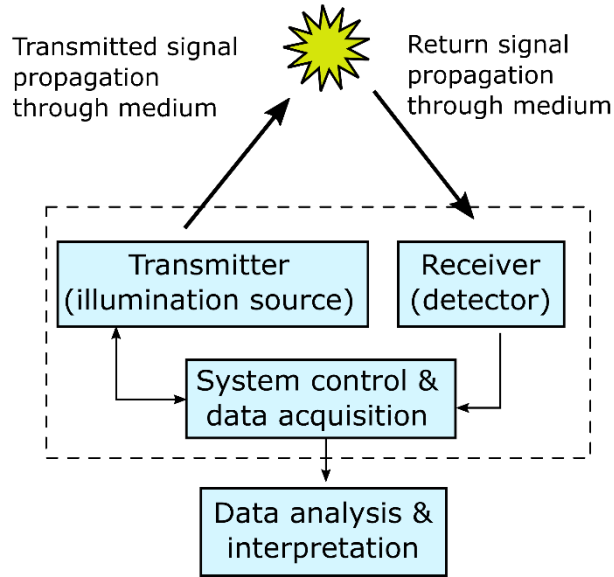
Figure 2.1: A schematic diagram of a typical LiDAR system. A laser in the transmission channel provides the illumination. The receiver collects the backscattered photons and routes them to a detector. The data is then processed, and information relayed to the user.

The transmitter is comprised of an illumination source and an optical system that directs the beam to the target at the appropriate beam size. The receiver collects backscattered light, which is then routed to a detector module. The detector converts the optical signal into an electrical signal, which is then processed by the data acquisition module. This data can then be further analysed to extract the ToF information, and hence, the range information. A variety of illumination sources, such as continuous wave (CW) and periodic pulsed laser sources are employed in LIDAR systems, depending on the configuration used. This will be discussed further in the following Sections of this Chapter.
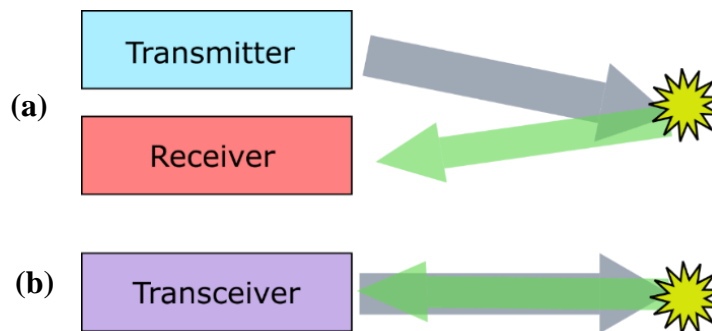
Figure 2.2: Schematic of a LiDAR system with (a) a bistatic configuration and (b) a monostatic configuration.

In general, there are two main optical configurations for LiDAR systems: the bistatic configuration and the monostatic configuration. These two configurations are shown schematically in Figure 2.2. In a bistatic configuration, the transmitter and the receiver are housed in separate locations. This configuration can be useful in applications, such as imaging through high levels of scattering, as the transmitter and receiver can be placed such that the beam does not have to travel through the entire length of the scattering medium. Scattering effects (which will be discussed in detail in Section 2.3) comprise several contributions, which are shown schematically in Figure 2.3 [2.12].
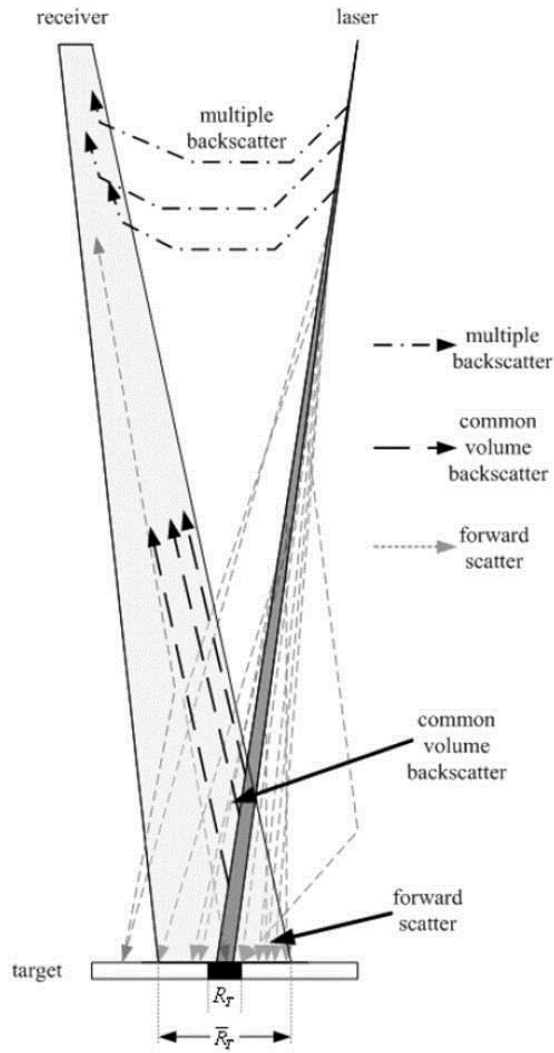
Figure 2.3: Schematic representation of light scattering. From ref. [2.12].

By placing the receiver at a different position than the transmitter, the overlap between the transmitted light and the field-of-view of the receiver is minimised. This technique can improve the performance of the LiDAR system due to a reduction in light

back-scattered through the volume of scattering media. While this technique has been commonly used on small submarines or by underwater robots, as reported in ref. [2.13], it is not always practical to separate the transmitter from the receiver as many applications require compact system designs with limited space for hardware. In addition, due to optical parallax a bistatic configuration LiDAR system will need to be realigned for different target stand-off distances, making it less suitable for applications with multiple target ranges. In this case, a parallax-free monostatic configuration (where the transmission and receive channel share a coaxial optical path) is advantageous, as the optical system does not need to be adjusted for different target stand-off distances. Use of the monostatic configuration can, however, result in back-reflections from optical components due to the shared optical path. This can be a potential issue for single-photon based LiDAR systems, as the signal from back-reflections can result in single-photon detector saturation and even damage the highly sensitive detectors. One potential solution is to use single-photon detectors with electronic gating - where the detector is inactive for a time interval – hence the detector can be de-activated at the return time of the back-reflection signal. Gated-mode detectors will be discussed in detail in Chapter 3 of this Thesis. A monostatic configuration was used in Chapters 4 and 5 of this Thesis for a scanning LiDAR system, and a bistatic configuration was used in Chapters 6 and 7 for an arrayed detector LiDAR system.

Today, LiDAR continues to be the technique of choice in a variety of remote sensing applications, including environmental monitoring [2.14–2.16], surveillance and defence [2.17], and terrain mapping [2.7,2.8,2.18,2.19]. Many different types of active LiDAR systems (i.e., systems which incorporate laser sources as a means of illumination) have been developed since the 1960s [2.20]. Some examples of LiDAR systems will be given in the following Section.

2.2.1 ToF LiDAR using amplitude and frequency modulation

In indirect ToF LIDAR, a continuous wave (CW) laser source is used to measure target distance by measuring the phase shift between a modulated outbound signal and the return signal from the object of interest. These systems are generally known as amplitude modulation (AM) or frequency modulation (FM) systems. In an AM LiDAR, the illumination source intensity is modulated in time and the return signal undergoes a phase

shift, $\Delta\Phi$, relative to the modulated source, which relates to the round-trip ToF (τ_{ToF}). If the signal is periodic, the phase shift is given by:

$$\Delta\phi = 2\pi f \tau_{ToF}, \tag{2.1}$$

where f is the frequency of the illumination source. The phase shift can be measured by introducing known electronic delays to either the modulation or the detection signal. Thus, the distance, d, to the target is given by:

$$d = \frac{\tau_{ToF}c}{2} = \frac{\Delta\phi}{2\pi}\frac{c}{2}. \tag{2.2}$$

where c is the speed of light in vacuum. If $\Delta\Phi$ exceeds 2π, the target distance cannot be unambiguously identified.

FM LiDAR ranging systems employ a tunable illumination source that allows for a variable frequency, where the frequency of the light beats periodically with a total frequency shift of Δf. This variable frequency signal is then mixed with the transmitted optical signal, and the round-trip ToF is determined via observation of the beating signal, as shown in Figure 2.4 [2.21].
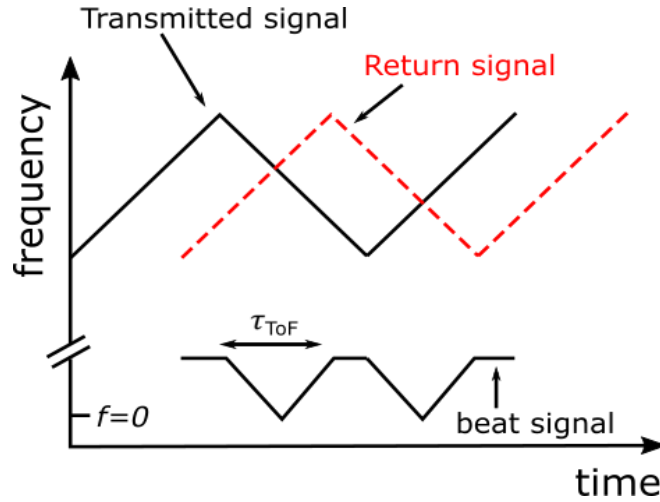
Figure 2.4: ToF measurement in a FM LiDAR system, which uses a CW illumination source. The frequency of the transmitted signal is modulated and mixed with the return signal. Beating can be observed that corresponds to the phase shift between the transmitted signal and the return signal, and hence, relates directly to the round-trip ToF.

The first CW FM LiDAR system was first demonstrated by Honeycutt *et al.* in 1972 [2.22]. Later that same year, the technique was shown to be capable of operating at target distances of up to several kilometres by Hughes *et al.* [2.23].

2.2.2 ToF LiDAR using pulsed illumination sources

The work presented in this Thesis was performed using direct-detection LiDAR systems, which necessarily require pulsed laser sources to provide ToF measurements by measuring the time difference, τ_{ToF}, between an outbound optical pulse and the return signal corresponding to that pulse (i.e., the round-trip ToF). Thus, the photon ToF can be calculated simply as:

$$\tau_{ToF} = \frac{2R}{c},$$

(2.3)

where R is the target range [2.20]. However, this method gives rise to the inherent problem of range ambiguity in high-repetition rate ToF systems [2.24]. In a fixed repetition rate LiDAR system, range ambiguity occurs when there is more than one possible position for a reflecting surface, which occurs when, instantaneously, there is more than one optical pulse in transit. This maximum unambiguous distance, d_{rep}, is dependent on the fixed repetition rate, f_{rep}, of the laser as in Equation 2.4:

$$d_{rep} = \frac{c}{2f_{rep}}.$$

(2.4)

For example, for a laser source operated at a repetition rate of 19.5 MHz (as was the case in the imaging system described in Chapter 4 of this Thesis), the unambiguous range is limited to 7.7 metres. Range ambiguity can be removed by a reduction in repetition rate - which can significantly increase measurement time - or by using techniques such as laser pulse trains composed of pseudo-random patterns or by use of multiple sequential repetition rates [2.25,2.26]. However, the work performed in this Thesis was concentrated on the depth profiling of long-range targets rather than ascertaining their absolute range without ambiguity. Consequently, a periodic repetition rate was used for all measurements presented in this Thesis. Some examples of LiDAR designs that employ pulsed illumination sources are presented in the following Section.

2.2.2.1 Full-waveform LiDAR
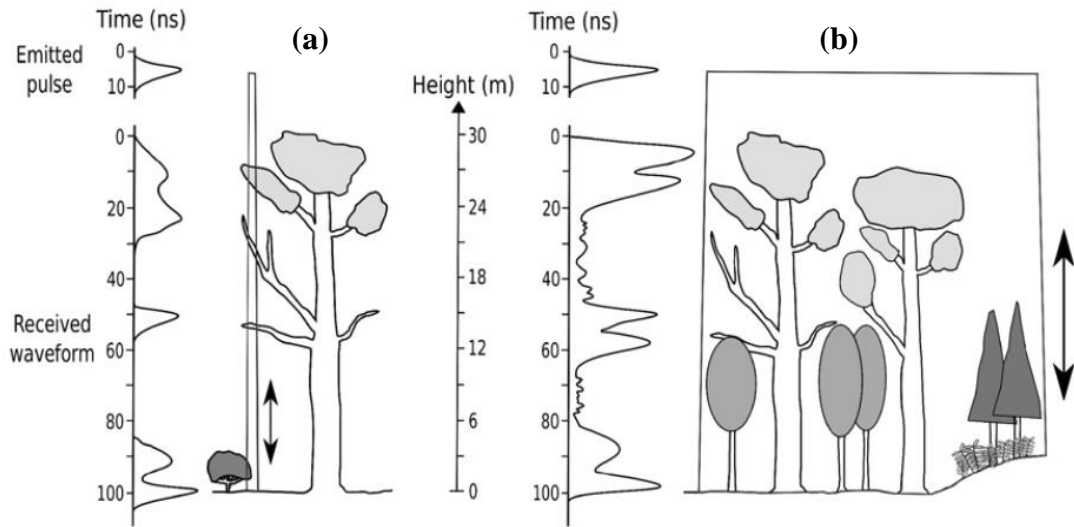
Figure 2.5: Full-waveform LiDAR return in an airborne measurement of a forest for a system with (a) a small footprint and (b) a large footprint. From ref. [2.27].

The first full-waveform LiDAR systems were designed in the 1980s for bathymetry (i.e., the study of the underwater depth of lake or ocean floors [2.28]). More recently, commercially available topographic full-waveform LiDAR systems have become available, such as the Mapper II from YellowScan [2.29]. Full-waveform LiDAR systems record the full temporal shape of a target response to pulsed illumination, and the amount of information received is dependent on both the footprint and the pulse energy of the system. The return waveform of topographic systems provide a measurement of the vertical distribution of the scene. Most commercial systems have a small footprint (e.g., $0.2 - 3$ m diameter, depending on flying height and beam divergence), providing an accurate altimetric description, as shown in Figure 2.5 [2.27]. However, these systems often miss treetops, and are unable to determine whether the ground has been reached under dense vegetation, making it is difficult to estimate ground and tree heights. Large footprint systems (e.g., $10 - 70$ m diameter) increase the probability of reaching both the ground and the canopy top. Over the years, these systems have been widely employed in a range of remote sensing applications, such as recording the full-waveform return from tree canopies to analyse the structure of forests [2.30,2.31].

2.2.2.2 Lunar and satellite laser range-finding

One of the early motivations for increasing the precision of LiDAR ranging systems was the study of extra-terrestrial objects, such as the Moon. For example, in 1973, Bender *et al.* listed a number of incentives to increase laser-ranging distance measurements to the Moon, such as the study of lunar orbit and determination of range finder locations by means of triangulation [2.32].

In 1962, Smullin *et al.* used a high power laser source and a nitrogen-cooled photomultiplier tube (PMT) detector to receive optical echoes from the moon [2.33]. However, these systems used illuminations sources with a pulse energies of 50 J, which is well above eye-safety thresholds. A few years later in 1965, Alley *et al.* proposed that the expected optical return signal could be increased by two orders of magnitude if corner-cube retro-reflectors were deployed on the lunar surface [2.34]. Therefore, in 1969, a fused silica corner-reflector array was deployed by the American endeavour Apollo 11 [2.35]. In 1971, Apollo 14 and Apollo 15 installed a second array of the same type and an improved array on the lunar surface. A fourth retro-reflector cube was also installed by the Soviet moon lander in 1970 [2.36], and subsequently updated in 1973. With current improvements in range-accuracy and resolution of state-of-the-art LiDAR systems, these four reference points are still used today for the study of the effects of gravitation [2.37,2.38].

LiDAR systems can also be used in satellite laser ranging (SLR), for low Earth orbit satellites. This was first successfully demonstrated by NASA Goddard Space Flight Center in 1964, when the round-trip time of an optical pulse transmitted from Earth to a passive retro-reflector mounted on an orbiting satellite was measured [2.39]. This system used a pulsed illumination source at an operating wavelength of 1064 nm. The repetition rate of the laser source was 20 Hz with picosecond duration pulses with a pulse energy of 100 mJ. The optical signal reflected from the retro-reflector was collected by a ground-based telescope and then detected by a single-photon counting PMT. The ToF of the optical signal was measured using a time interval analyser with 70 ps resolution [2.40]. It was reported that 2 – 3 m resolution could be achieved using SLR compared to the 50 m or more provided by radar systems at that time [2.39].

The most precise SLR systems achieve sub-cm accuracy [2.38,2.39], with exact figures depending on numerous factors such as target reflectivity and weather conditions during

the time of measurement. There are currently approximately 23 available SLR systems with satellite-mounted retro-reflectors orbiting the Earth at ranges between 960 – 20,000 km. They are mainly used for facilitating orbit calibration and for measurements of the Earth's gravity and rotation characteristics [2.40].

2.2.2.3 Range-gated LiDAR systems

Ranged-gated LiDAR systems, also known as Burst illumination (BIL) LiDAR systems, acquire ToF measurements based on the incidence time of photon events. A pulsed laser source provides a dispersed burst of light to flood-illuminate the scene, and a camera detects the reflected light. Instead of measuring the arrival time of back-scattered photons, the detector takes a two-dimensional image with an extremely short exposure time after a pre-defined time interval following the illumination pulse. In this image, only back-scattered photons at a particular range (or 'time-slice') within this exposure time are collected, as shown in Figure 2.6 [2.41]. Thus, the image contains only reflections of objects within that range. A three-dimensional intensity image of the scene can be constructed by repeating this process for different the delay times.
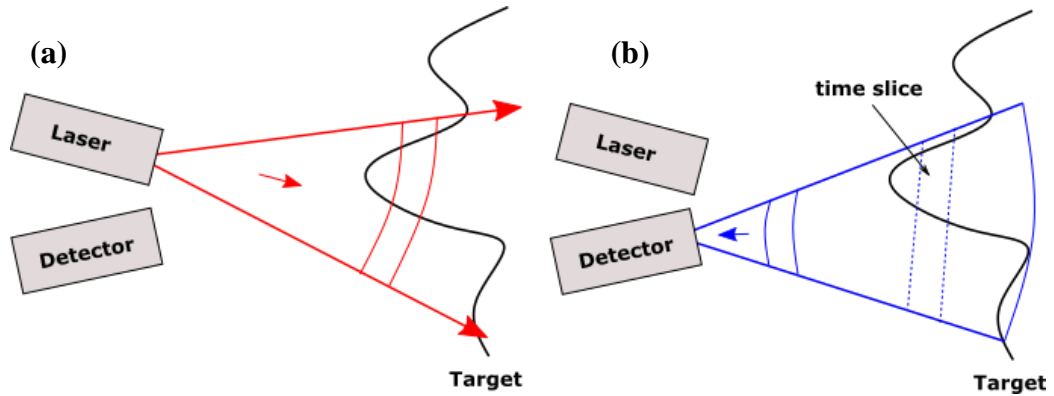
Figure 2.6: Schematic of range-gated LiDAR depth imaging. (a) A laser illuminates the target scene with a dispersed burst of light. (b) A highly sensitive detector with a short exposure time collects light after a controlled time delay relative to the illumination pulse. Only target returns corresponding to this 'time slice' are collected, and a range can be assigned to the returns. From ref. [2.41].

The principle of range-gated LiDAR was first described and demonstrated by Busck *et al.* in 2004 [2.41]. The authors used a CCD camera alongside a microchannel plate, which was used to amplify the return signal. Gate times as low as 200 ps with controlled time delay steps down to 100 ps were used at frame-rates of 32 kHz. This system was used to

obtain 582×752 pixel images at stand-off distances of 14 m for acquisition times of less than 1 second. For these measurements, the authors reported a range accuracy of 1 mm. However, due to the short exposure times, a non-eye safe average optical power of 140 mW at the operating wavelength of 532 nm was required to obtain satisfactory images.

In 2006, a range-gated LiDAR system design to work outdoors at long-ranges was described and demonstrated by *Andersson* in ref. [2.42]. Depth images of a T72 battle tank were obtained at stand-off distances between $0.8 - 2.7$ km using the more eye-safe illumination wavelength of 1550 nm, as shown in Figure 2.7. The authors did not report the typical illumination powers used in these measurements; however, they were described as extremely high compared to those used in other depth profiling methods.
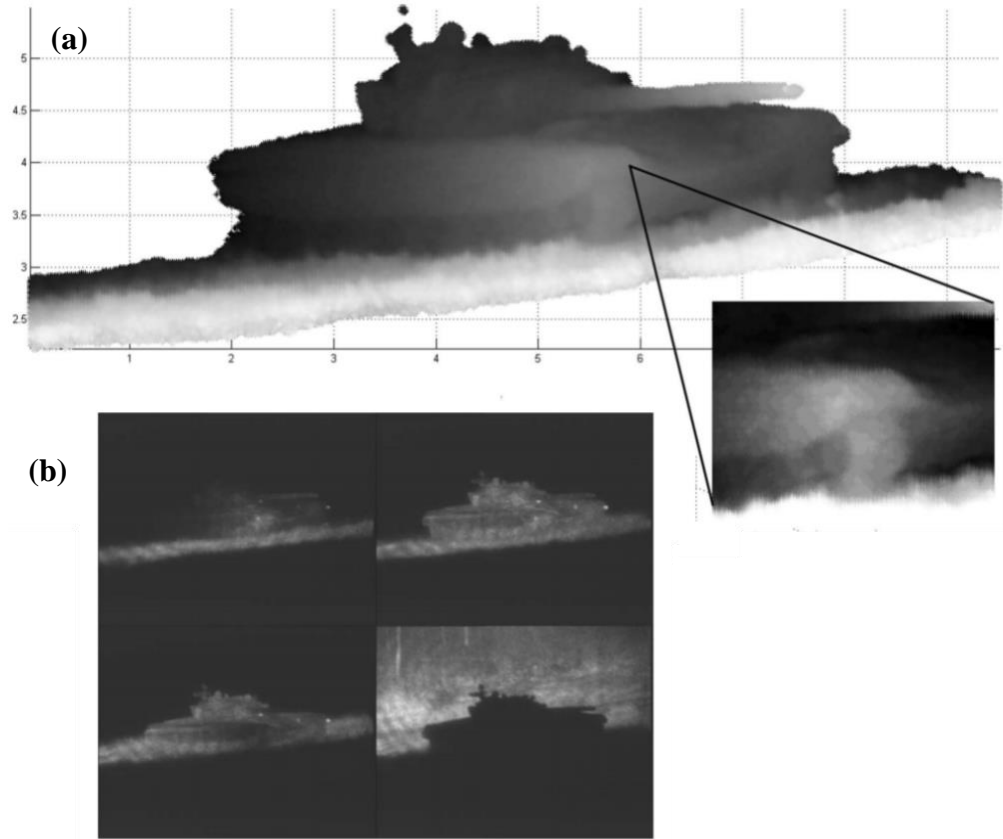
Figure 2.7: Range-gated LiDAR depth profile of a T72 battle tank at a stand-off distance of 830 m. (a) shows a point cloud representation of the target. The enlarged area shows a contrast-optimised section of the scene. (b) Two-dimensional intensity images of the scene taken at four different time delays of width 40 ns (i.e., a ~ 6 m range-slice). From ref. [2.42].

16

More recently, in 2018, Ren *et al.* demonstrated a ranged-gated depth imaging system that employed a CMOS SPAD detector with a single-photon detection efficiency (SPDE) of 18% [2.43]. The system used an illumination wavelength of 685 nm with an average optical power of 420 µW to obtain 256×256 pixel depth images of a mannequin head at a stand-off distance of 2 m. The gate duration was set to 10 ns and the delay applied to the sensor gate was iteratively increased in 10 ps increments for frame-rates of 100 kHz. The authors reported depth images with millimetre scale depth uncertainty for sparse photon data with total exposure times of 75 ms or less.

2.2.3 TCSPC-based LiDAR systems for depth profiling in challenging environments

In recent years, the TCSPC technique has emerged as a candidate technology for LiDAR, due to its high sensitivity and excellent surface-to-surface resolution [2.44]. The TCSPC approach has been successfully demonstrated in a number of LiDAR applications such as long-range depth imaging [2.45–2.48], underwater depth imaging [2.10,2.49] and multi-spectral depth imaging [2.50–2.53]. The use of high-sensitivity single-photon detectors, such as InGaAs/InP and Si single-photon avalanche diode (SPAD) detectors [2.48,2.54,2.55] and superconducting nanowire single-photon detectors (SNSPDs) [2.56,2.57], means that low average optical power levels can be used even at long distances, resulting in the potential for low-power eye-safe imaging. The operating principles of these detectors will be discussed in detail later in Chapter 3.

2.2.3.1 TCSPC-based LiDAR systems for long-range depth profiling

In 1997, a TCSPC-based imaging LiDAR system was demonstrated by Massa *et al.* from the Single-Photon Group at Heriot-Watt University [2.58]. This system used a short-pulse laser diode and a Si-based single-photon detector to obtain distance measurements up to a range of 1.5 metres in laboratory conditions. The authors reported a timing accuracy in the range of $0.2 - 10$ ps for up to 10^6 photon counts, with a measurement precision down to approximately 30 µm. Later in 2009, the same group demonstrated a single-pixel scanning system based on the TCSPC approach for the depth profiling of long-range targets in outdoor environments [2.46]. This system used a 90 ps full-width at half-maximum (FWHM) pulse-width laser diode with an illumination wavelength of 842 nm and a thick-junction Si-SPAD detector to obtain depth profiles of targets at stand-off distances up to 330 metres, as shown in Figure 2.8. The authors reported a 20 mm depth uncertainty for these measurements.
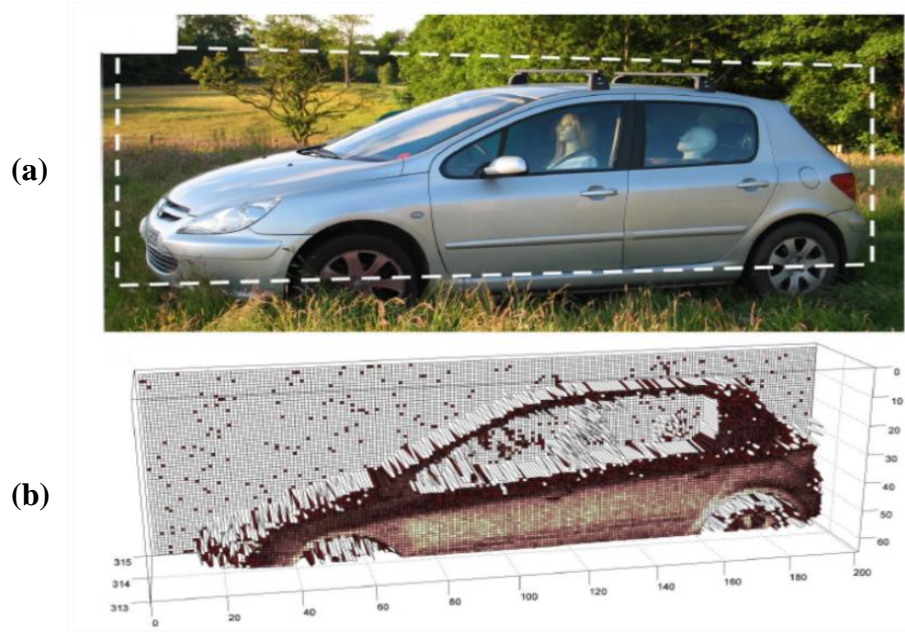
Figure 2.8: (a) Close-up photograph of the target (in this case a car). (b) The reconstructed 200 × 60 pixel depth profile of the car at 330 m obtained using the TCSPC-based scanning system from ref. [2.46].

In 2007, Warburton *et al.* reported depth-ranging studies carried out using a 100 nm wide niobium nitride (NbN) SNSPD at an operating wavelength of 1550 nm [2.59]. The SNSPD detector had a low SPDE of 1% and a timing jitter of approximately 70 ps, at an operating temperature of 3 K. This system was used to obtain depth profiles with a depth resolution of 1 cm at stand-off distances of 330 m in outdoor conditions. Moreover, the SPDE of the detector was relatively low compared that of many commercially available SPAD detectors. In 2013, McCarthy *et al.* reported a ToF scanning depth imager that incorporated a niobium titanium nitride (NbTiN) SNSPD with an improved SPDE of 18% and a dark count rate of 1 kHz at the operating temperature of 3 K and an illumination wavelength of 1560 nm [2.60]. Using a pulsed illumination source with an average optical power level of 250 μW, the authors reported millimetre-scale depth resolution of targets at ranges up to 910 m – far beyond the capabilities of other single-photon approaches at such ranges. Despite the high temporal resolution provided by SNSPDs, the cryogenic systems required for cooling can be bulky and expensive, limiting the practicality of this system for some applications that require compact, portable solutions. However, miniaturised closed cycle cryogenic systems have been recently demonstrated by Gemmell *et al.*[2.61].

In 2013, McCarthy *et al.* demonstrated an updated ToF scanning depth imager capable of measuring depth profiles at long distances at SWIR wavelengths that using a gated-mode InGaAs/InP SPAD detector [2.55]. This detector had a timing jitter of 140 ps FWHM, a SPDE of approximately 26% at an operating temperature of 230 K. A 50 ps pulse-width laser source was used to provide a pulsed illumination at a wavelength of 1550 nm. The average optical power was reported to be 600 µW. This system was used to obtain depth profiles of targets with sub-centimetre resolution at ranges of up to 4.5 km. More recently, the distance range of ToF single-photon depth imagers using single-pixel InGaAs/InP SPAD detectors has been extended up to 10s of kilometres. Depth profiles at ranges up to 10 km obtained by a ToF imaging system using a InGaAs/InP SPAD detector with a 210 mm aperture telescope receiver were reported in 2017 by Pawlikowska *et al.* [2.47]. This study used a fibre laser with an operating wavelength of 1550 nm with an average optical power level of 10 mW to obtain 32 × 32 pixel scans of a hillside terrain (shown in Figure 2.9) with a per pixel acquisition time of 0.3 s (i.e., a total measurement time of approximately 5 minutes).
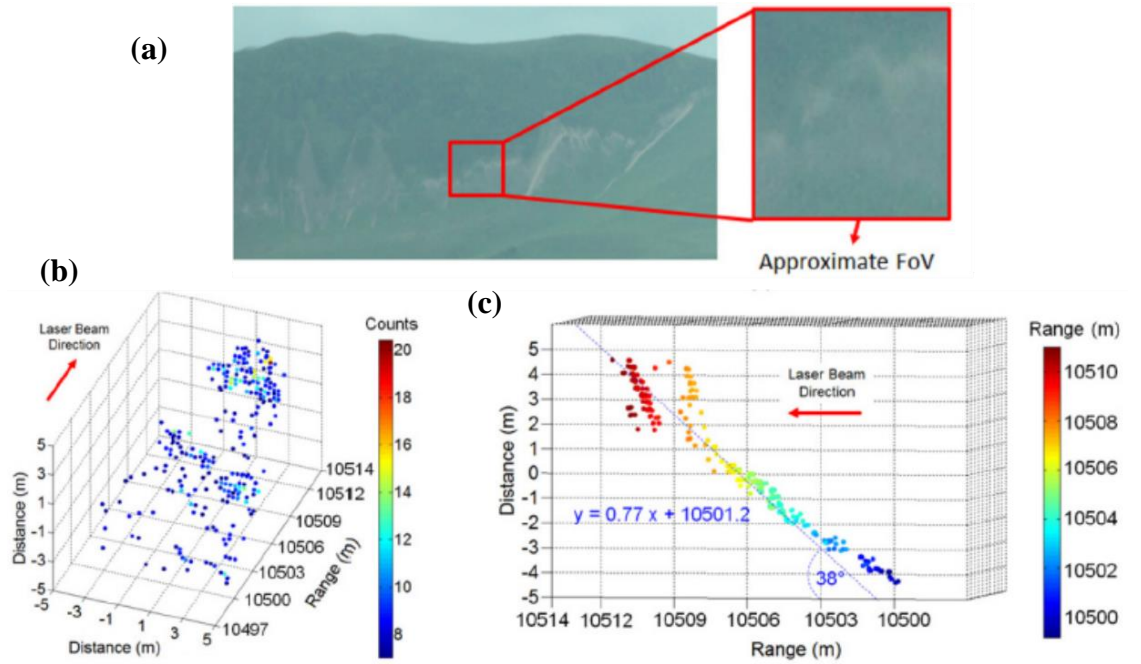
Figure 2.9: (a) Reference images of the scene acquired with a visible band camera. The stand-off distance was 10.5 km and the depth and intensity profiles were recorded with 32 × 32 scan points with an acquisition time of 0.3 ms per scan point. (b) presents a front-side view of the reconstructed depth and intensity point cloud and (c) shows a side view. From ref. [2.47].

In 2019, Li *et al.* reported a depth imager based on the TCSPC approach capable of acquiring depth profiles of objects at stand-off distances up to 21.6 km [2.62]. The group presented 256×256 pixel scans of a building using a per-pixel acquisition time of 22 ms and with a laser power of 100 mW.

More recently, ToF single-photon depth imagers using InGaAs/InP SPAD detector arrays have been developed, which allow for much shorter acquisition times. In 2017, Hiskett *et al.* reported a ToF depth imaging system that employed a Princeton Lightwave InGaAs/InP arrayed detector with a pixel format of 32×32 [2.63] for distributed targets at stand-off distances up to 9 km [2.64]. The system used a fibre laser source operating at an average pulse repetition rate of 125 kHz with a pulse energy of 2.4 μJ. A point cloud reconstruction for a representative result is shown in Figure 2.10. The authors reported a depth resolution of below 4 cm.
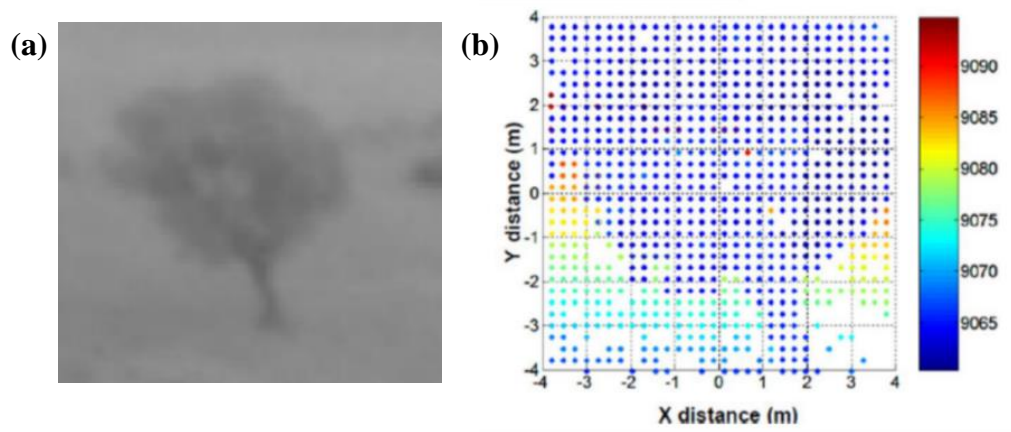
Figure 2.10: Depth profiling of a distributed target (in this case a tree) at a stand-off distance of 9 km obtained using a 32×32 InGaAs/InP SPAD array. (a) An RGB photograph of the target at 9 km. (b) The reconstructed depth profile of the target. From ref. [2.64].

2.2.3.2 Multi-spectral imaging using TCSPC-based LiDAR systems

Most LiDAR system use a single illumination wavelength, which is typically chosen based on the application of the system. This choice is generally a trade-off between factors such as eye-safety, detector responsivity, and atmospheric attenuation. Multi-spectral LiDAR systems use multiple illumination wavelengths to ensure satisfactory performance for a wider range of applications or to obtain the spectral response information of a target object. An example of several photon-counting histograms for different illumination wavelengths acquired by a multi-spectral LiDAR system is shown

in Figure 2.11 [2.65]. The spectral response, also known as a spectral 'fingerprint', of an object is dependent mainly on the relative scatter and specular reflection of the target object.
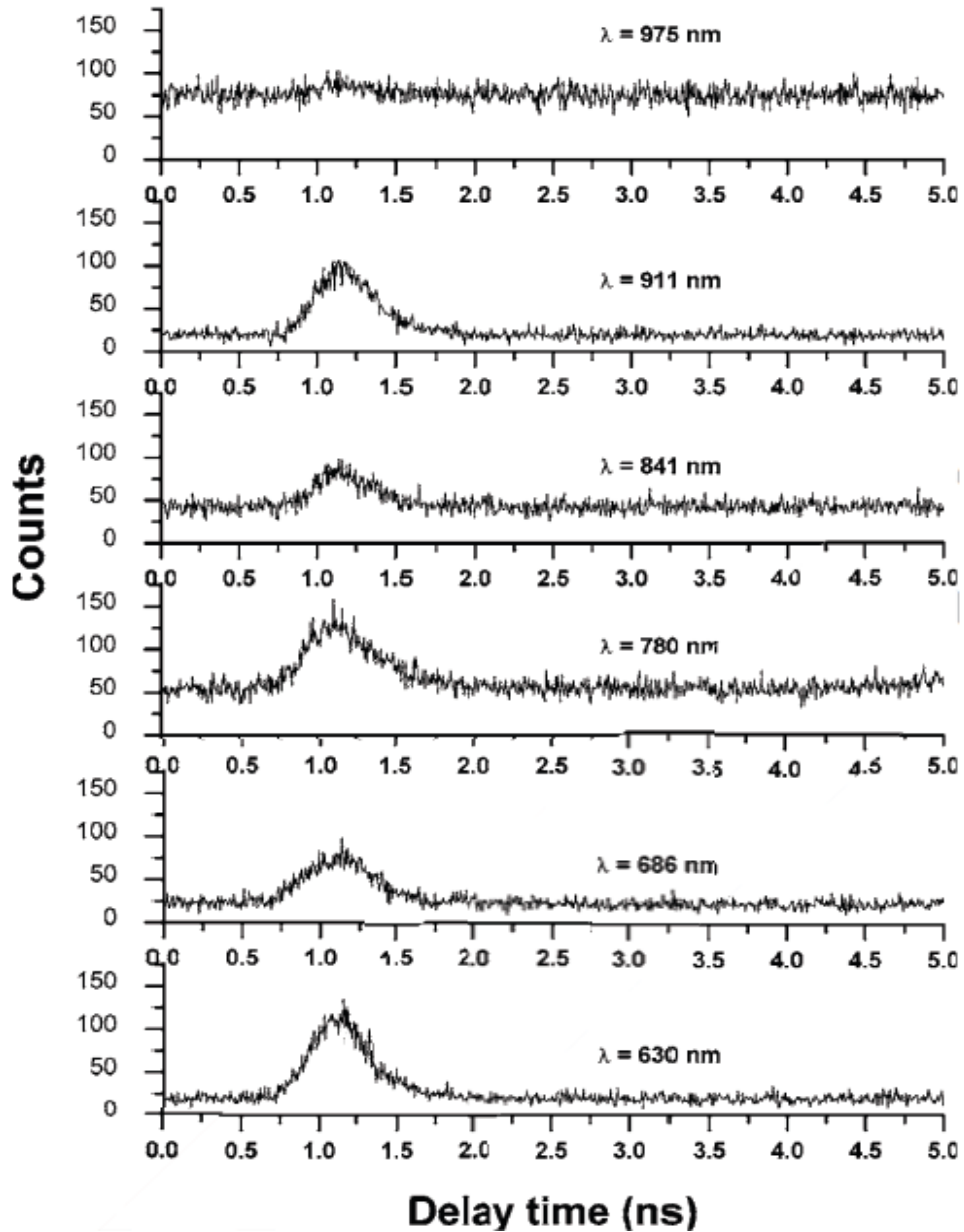
Figure 2.11: Example of a sensor response for a multi-spectral LiDAR system with six discrete wavelength channels. From ref. [2.65].

In 2005, Buller *et al.* presented a multi-spectral ToF LiDAR system based on the TCSPC approach with six wavelength channels ranging from $630 - 975$ nm [2.65]. This system simultaneously used six pulsed laser diodes to provide an average optical power level of $100 \, \mu W$ to ensure eye-safety. A commercially available $200 \, mm$ diameter aperture

telescope was used to collect photon returns from the six wavelengths. An optical grating was used to spectrally de-multiplex the return signal and relay each corresponding wavelength to its own SPAD detector. In ref. [2.65], these different spectral signatures were used to identify a variety of different targets.

Multi-spectral LiDAR systems can be used for several applications, such as the recovery of arboreal parameters [2.51,2.66]. There are two typical vegetation indices: (i) the normalised differential vegetation index (NDVI) which is related to canopy biomass and light absorption [2.67]; and (ii) the photochemical reflectance index (PRI), which is indicative of photosynthetic light use efficiency [2.68]. The chlorophyll reflectance in plants changes sharply on the spectral edge from red wavelengths (e.g., 670 nm) to NIR wavelengths (e.g., 780 nm) and also have a strong peak in the reflectance at green wavelengths [2.66]. Thus, the physiological state of a plant can be determined via the NDVI, which is given as:

$$NDVI = \frac{R_{NIR} - R_{VIS}}{R_{NIR} + R_{VIS}}, \tag{2.5}$$

where R_{NIR} is the reflectance in the near-infrared (NIR) wavelength band and R_{VIS} is the reflectance within the visible wavelength band [2.67]. Since healthy vegetation reflects more in the NIR, a high NDVI indicates a healthy plant. The PRI can be obtained by examining the reflectance peak at a wavelength of 531 nm at green wavebands, and comparing that with a nearby reference wavelength (e.g., $\lambda = 570$ nm), and is given as:

$$PRI = \frac{R_{\lambda=570nm} - R_{\lambda=531nm}}{R_{\lambda=570nm} + R_{\lambda=531nm}}, \tag{2.6}$$

where $R_{\lambda=570nm}$ and $R_{\lambda=531nm}$ are the reflectance at λ=531 nm and 570 nm, respectively.

Multispectral LiDAR systems can exploit this to perform analysis of vegetation and foliage. For example, in 2014 Wallace *et al.* reported the design and evaluation of a multi-spectral TCSPC LiDAR system that was used to recover structure and physiological parameters of arboreal samples (i.e., plants) [2.51]. Four pulsed illumination wavelengths of 531, 570, 670, and 780 nm with $< 200\ \mu$W average optical power were used alongside four appropriate Si-SPAD detectors to scan a small Nordmann fir sample. From this data, the NDVI and PRI were examined, and the health of the vegetation determined. A full-waveform multi-spectral LiDAR measurement for a single

pixel from this system, which shows the responses through the canopy and differences in spectral ratios, is shown in Figure 2.12.
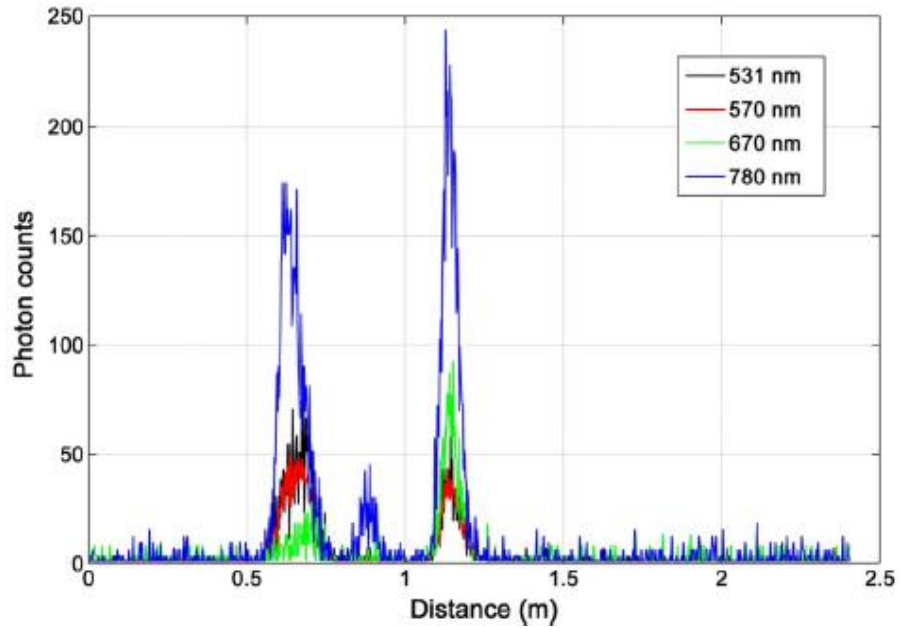
Figure 2.12: The full-waveform LiDAR data for a single pixel using a multi-spectral TCSPC LiDAR system, which shows the responses through the canopy and differences in spectral ratios. From ref. [2.51].

2.2.3.3 TCSPC-based LiDAR systems for imaging complex scenes

The identification of targets that have been obscured by clutter is a subject of significant relevance for long-range field applications. Several experiments involving 'seeing' behind or through various obscuring media have been performed previously using LiDAR systems [2.69–2.73].

For example, in 2010, Wallace *et al.* reported depth profiling of distributed targets at stand-off distances up to 325 m using a ToF LiDAR system based on the TCSPC technique [2.74]. The system comprised a single pixel Si-SPAD detector and a pulsed illumination source, which was operated at an illumination wavelength of 842 nm and a pulse energy of < 30 pJ. An example of a timing histogram representing a scene with distributed targets in the field-of-view of a single pixel acquired using this system is shown in Figure 2.13 [2.74], where each peak corresponds to a specific target depth.
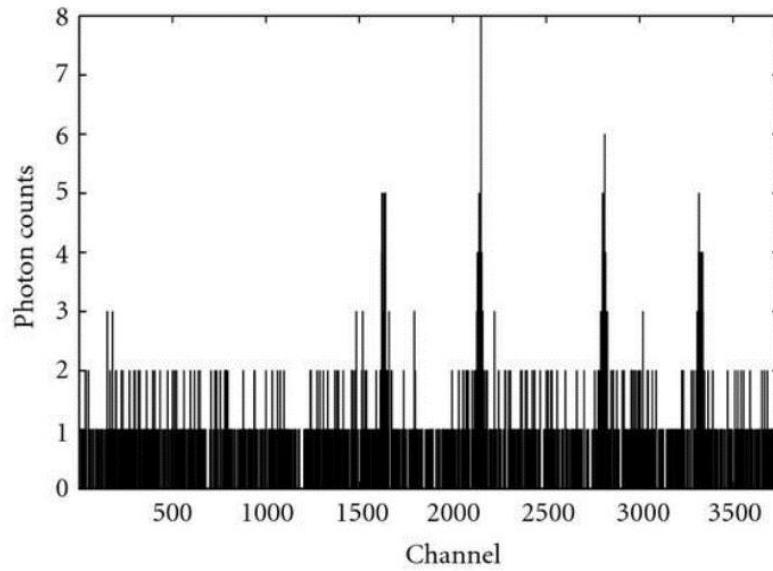
Figure 2.13: An example of a timing histogram of distributed targets in the field of view of a single pixel. The horizontal axis is equivalent to the round-trip distance. From ref. [2.74].

In 2016, Henriksson *et al.* presented a scanning TCSPC system that was successful in imaging targets through foliage at a distance of approximately 300 metres using an illumination wavelength of 1550 nm with average optical power levels of 19 mW [2.71]. This system incorporated a single pixel InGaAs/InP SPAD detector with a 25 µm diameter active area. An example result taken from ref. [2.71] is shown in Figure 2.14. However, the slow scan speed of the system meant that the acquisition time was 30 minutes for a 5 × 1 degree scene with many of the pixels providing no depth information due to a lack of returned photons.
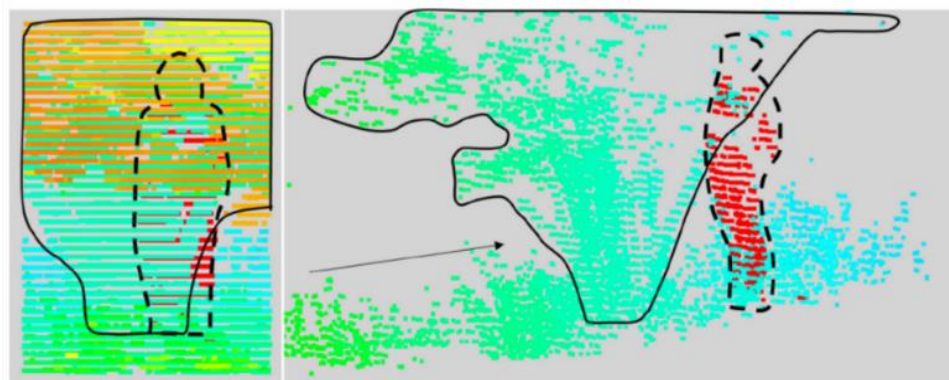
Figure 2.14: The reconstructed 3D point cloud representation of a human standing behind foliage. The dashed lines show the outline of the person and the solid line shows the outline of the foliage. From ref. [2.71].

24

Later, Henriksson *et al.* reported similar measurements of cluttered scenes that cut down data acquisition time to approximately 4 seconds. This was achieved by using a ToF depth imager that employed a Princeton Lightwave 32×128 pixel format InGaAs/InP SPAD array [2.75] and an illumination wavelength of 1550 nm. This system was able to obtain panoramic 3D depth profiles of scenes at stand-off distances of up to 340 metres [2.76]. A representative result from ref. [2.76] is shown in Figure 2.15.
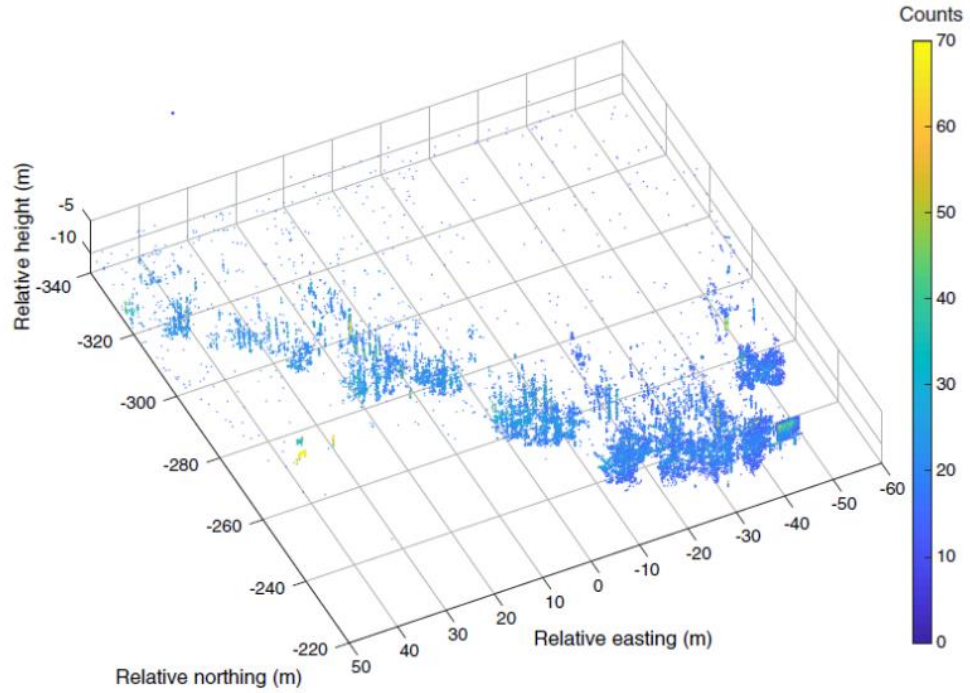
Figure 2.15: A point cloud representation of a cluttered scene with dense foliage at 340 m obtained using a 128×32 pixel format InGaAs/InP SPAD array. From ref. [2.76].

High-resolution measurements of targets obscured by camouflage obtained using a scanning TCSPC based LiDAR system at an operating wavelength of 1550 nm are presented in Chapter 4 of this Thesis [2.48]. Real-time measurements of dynamic targets obscured by camouflage obtained using a 32×32 pixel format InGaAs/InP SPAD array are presented in Chapter 7 [2.77].

2.2.3.4 TCSPC-based LiDAR systems for imaging in highly scattering environments

Another challenge for free-space LiDAR imaging is the depth profiling of targets in highly scattering environments. The presence of a scattering media between a LiDAR system and a target of interest reduces the number of return photons received by the system, limiting the system performance. The optical signal is attenuated over the full

round-trip distance of propagation through the scattering medium, resulting in a low target return signal and an increased background level, and hence, a poor image reconstruction.

The use of the TCSPC approach in LiDAR systems for free-space imaging through obscuring media is a relatively new field. In 2018, Satat *et al.* reported an investigation of the effects of water-based fog on the reconstructed depth profile of a target placed inside a $0.5 \times 0.5 \times 1$ m³ indoor enclosure using an illumination wavelength of 850 nm [2.3]. The detector used was a PhotonForce PF32 SPAD camera with a pixel format of 32×32 pixels with a timing bin size of 56 ps and an exposure time of 100 µs. The laser source had a pulse width of 5 ps and an average power level of 0.15 W at a repetition rate of 80 MHz, which is well under the eye-safety threshold for 850 nm light. The reconstructed depth profiles for the ground truth and for increasing fog densities are shown in Figure 2.16 [2.3]. The authors report the fog density in terms of optical thickness (OT), which is defined as the natural logarithm of the ratio of incident to transmitted spectral radiant power through a material. Here, a high OT (i.e., $OT > 2.0$ or an optical transmission of approximately 14%) corresponds to very dense fog. For low densities of fog, the depth profile was successfully reconstructed, while in high densities of fog, reconstruction falls apart.
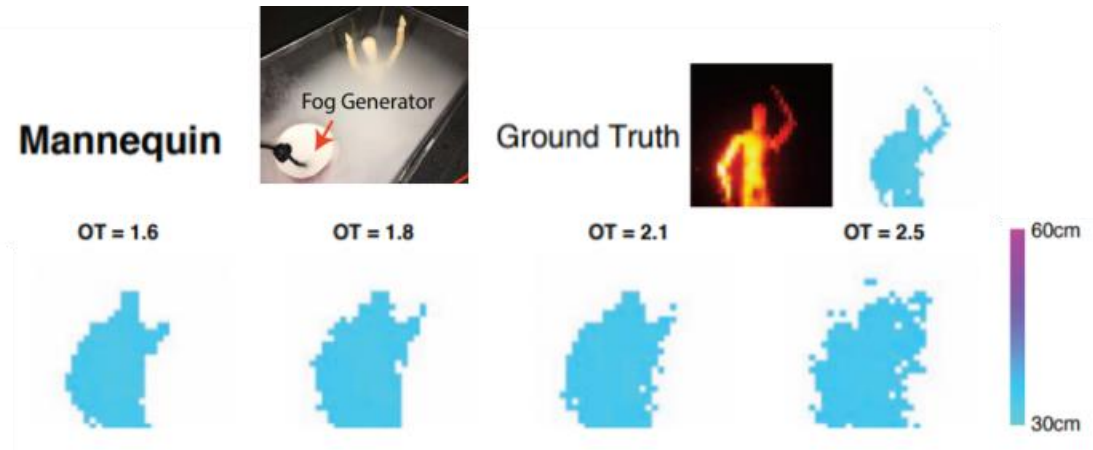
Figure 2.16: Results for imaging through fog with a TCSPC SPAD array as reported in ref. [2.3]. As the OT increases (i.e., for higher densities of fog), the quality of the reconstructed depth profiles decreases.

These results were obtained using a silicon-based SPAD detector, which is sensitive in the wavelength range of $400 - 1100$ nm. Several studies have suggested that scattering effects from small particles have a wavelength dependence, with SWIR wavelengths

suffering less attenuation than visible wavelengths [2.78–2.82]. Thus, extending the operating wavelength of TCSPC based LiDAR systems into the SWIR spectral band through use of InGaAs/InP SPAD detectors, may be advantageous for imaging through large volumes of scattering media. Scattering effects will be discussed in detail in the following Section of this Chapter. The depth profiling of long-range targets through high levels of scattering media using InGaAs/InP SPAD detectors is presented in Chapter 5 and Chapter 6 of this Thesis.

2.3 Principal characteristics of scattering effects from small particles

Light scattering is the process by which small particles deviate the path of propagating light, due to a difference in the refractive index of the particles from that of the surrounding medium. The level of scattering is dependent on both the particle size and the concentration of particles, where a larger particle size and a higher concentration correspond to an increase in scattering. In the atmosphere, the size distribution of particles responsible for scattering ranges from small air molecules with particle radii of 10^{-4} µm to raindrops with particle radii of up to 10^{4} µm. The typical concentrations of these particles can be as high as 10^{19} cm^{-3} for small air molecules and as low as $10^{-5} – 10^{-2}$ cm^{-3} for raindrops [2.83]. Table 2.1 shows typical radii and concentrations for several types of particles found in the atmosphere that contribute to light scattering.

Table 2.1: Several types of particles responsible for atmospheric scattering. From ref. [2.83].

Type	Radius (µm)	Concentration (cm^{-3})
Air molecules	10^{-4}	10^{19}
Haze particle	$10^{-2} – 1$	$10^{3} – 10$
Fog droplet	1-10	$10 – 100$
Cloud droplet	1-10	$10 – 300$
Raindrop	$10^{2} - 10^{4}$	$10^{-5} – 10^{-2}$

Upon interaction with a particle, a characteristic three-dimensional (3D) pattern in the scattered light is formed in space. If the particle is isotropic, this pattern is typically symmetric about the direction of the incident light. The shape of this pattern is strongly dependent on the ratio of the particle radii to the wavelength of the incident light, as illustrated in Figure 2.17 [2.84]. The relative size of a scattering particle with respect to the incident light is defined using the size parameter, χ, and is given as:

$$\chi = \frac{2\pi r_{particle}}{\lambda}, \qquad\qquad (2.7)$$

where $r_{particle}$ is the radius of the scattering particle and λ is the wavelength of the incident light [2.85].

(a)
Particles sizes **smaller than 1/10** of the wavelength of the light

incident beam

pattern description: symmetric

(b)
Particle sizes **comparable to** the wavelength of the light

incident beam

pattern description: scattering concentrated in forward direction

(c) Particle sizes **larger** than the wavelength of the light

incident beam

pattern description: extreme concentration of scattering in forward direction; development of maxima and minima of scattering at wider angles

Figure 2.17: Angular patterns of scattered intensity from (a) particles with a size of less than one-tenth of the wavelength of incident light, (b) particles with a size comparable to that of wavelength of the incident light, and (c) particles with a size larger than the wavelength of the incident light. Adapted from ref. [2.84].

2.3.1 Rayleigh and Mie scattering

Measurements by optical imaging systems in adverse weather conditions, such as those presented in this Thesis, are affected by two main scattering processes: Rayleigh and Mie scattering [2.86]. J. W. S. Rayleigh first proposed Rayleigh scattering in 1871 as an explanation for sky phenomena, such as rainbows and sky colours [2.87]. Rayleigh scattering occurs when the scattering particle size is smaller than one-tenth of the wavelength of the incident light, as shown in Figure 2.17 (a) [2.87]. When light interacts with a dielectric scattering particle, it creates an oscillating electric dipole moment, which results in the reemission of the light with the same wavelength and frequency, but with a scattering angle, Θ, as shown in Figure 2.18.
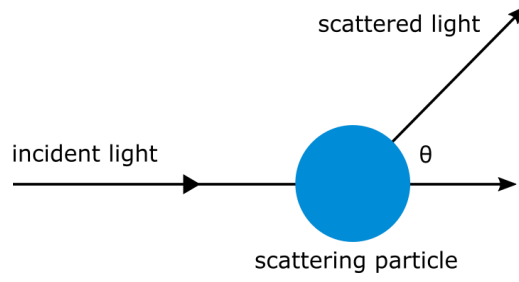
Figure 2.18: Incident light interacts with the dielectric particle causing the light to scatter with the same wavelength and frequency, but at a different scattering angle, Θ.

For this type of scattering, the pattern of the scattered light is typically symmetric, as the particle tends to scatter the light equally in both the forward and backwards direction (as shown in Figure 2.19 [2.84].
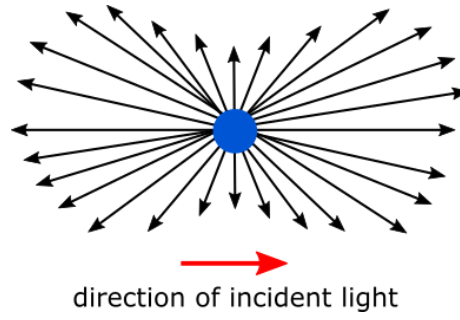
Figure 2.19: Schematic of symmetric Rayleigh scattering, which is strongly wavelength dependent.

For Rayleigh scattering, the intensity, *I*, of light scattered by a particle of diameter, *d*, and refractive index, *n*, is given by:

$$I = I_0 \frac{1 + \cos^2 \theta}{2R^2} \left(\frac{2\pi}{\lambda} \right)^4 \left(\frac{n^2 - 1}{n^2 + 2} \right)^2 \left(\frac{d}{2} \right)^6 , \tag{2.8}$$

where *R* is the distance to the particle, λ is the wavelength of the incident light, I_0 is the initial intensity of the light, and Θ is the angle of scattering [2.88]. The term $1 + cos^2\theta$ in Equation 2.8 contains the angular dependence of scattering and suggests that Rayleigh scattering is one-half in the forward and backwards direction at $\theta = 90°$, which explains the symmetrical scatter pattern. The most important point to note here is that the scattered intensity, *I*, is inversely proportional to the fourth power of wavelength of the incident light, λ, as given in Equation 2.9:

$$I \propto \frac{1}{\lambda^4}. \tag{2.9}$$

This indicates that Rayleigh scattering has a strong dependence on the wavelength of the incident light, where scattering at shorter wavelengths is greater than at longer wavelengths. For example, using Equation 2.9, the scattering at 700 nm is approximately 24 times greater than at 1550 nm for an equal incident intensity. This wavelength dependence is the explanation as to why the sky appears to be blue in colour, as the blue wavelengths of broadband solar radiation experience greater scattering by atmospheric molecules than the longer wavelengths [2.87]. However, as previously stated, this type of scattering only applies when the particle size is much smaller than the wavelength of the incident light, and so typically applies only to air molecules and very light haze with small water particles.

For particles that are comparable to the wavelength of the incident light, scattering increases and tends to be concentrated in a forward direction, as shown in Figure 2.20. This type of scattering, first proposed by G. Mie in 1908, is now known as Mie scattering [2.89].

direction of incident light
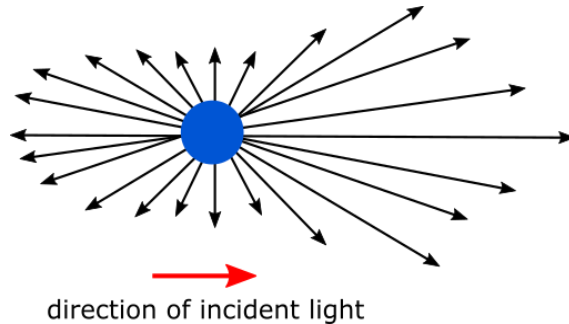
Figure 2.20: Schematic of Mie scattering. A forward lobe forms due to the increased particle size.

When the particle size is larger than the wavelength of the incident light, the overall scattering is increased and is mostly concentrated in the forward direction, with secondary minima and maxima emerging at various angles. This pattern will further increase in complexity for increasing particle sizes [2.84]. The complexity of this scattering pattern is dependent on the relative refractive index of the particle to that of the surrounding media due to contributions from both surface and diffuse scattering. Surface scattering takes place at the interface between the medium and the particle surface, and is responsible for creating the directional forward lobe. Diffuse scattering occurs when light

penetrates the surface-medium interface, undergoes subsurface scattering inside the particle, and subsequently re-emerges into the medium in a specific scatter pattern, creating the secondary maxima and minima [2.90].

Most imaging applications are concerned with large volumes of scattering media with large concentrations of particles, such as in fog or smoke [2.3,2.91–2.93]. When particles in a given volume of space are separated by a distance that is several times the particle radius, each particle is considered to scatter light independently. This means that each scatter pattern is unaffected by scattering from neighbouring particles. This is known as independent scattering. Independent scattering is the primary source of scattering in the atmosphere, as this separation criterion is met by most meteorological conditions arising from the presence of the particles listed in Table 2.1. If this separation criterion is not met, multiple scattering may occur. For example, in a closely packed atomic structure, such as a crystal lattice, the scattered light may interact with multiple particles. This can result in the production of maxima and minima in the scatter pattern, as was shown in Figure 2.17 (c) [2.83,2.94].

2.3.2 Attenuation of light in scattering media

The total attenuation of light in a scattering media, α_{tot}, is dependent on both the attenuation due to scattering and the attenuation due to absorption [2.83]. As mentioned in the previous Section, the level of scattering is dependent on both the wavelength of the incident light and the size of the scattering particles. Absorption includes all thermodynamically irreversible processes within the material that result in the transformation of photon energy into thermal kinetic energy or chemical energy [2.95]. The level of absorption is strongly dependent on both the wavelength of the incident light and particle properties such as material and size [2.96]. In free-space imaging, scattering tends to dominate, and absorption effects are typically very low [2.97]. However, contributions from absorption cannot be entirely ignored. In order to attain the total attenuation coefficient in a scattering media, both the absorption coefficient, α_{ab}, and scattering coefficient, α_{sc}, must both be considered. The total attenuation coefficient is given as:

$$\alpha_{tot} = \alpha_{sc} + \alpha_{ab}. \tag{2.10}$$

Although the attenuation is a combination of both scattering and absorption effects, for simplicity, this will simply be referred to as 'scattering' or 'particulate scattering' in this Thesis as the operational wavelengths used in these studies is at a wavelength of 1550 nm, which is a low-loss atmospheric window. The relationship between total scattering and the attenuation of the spectral irradiance of a propagating beam is relatively straightforward. The amount of flux removed from a propagating beam in a scattering media over a differential distance, dx, is given as:

$$\frac{dE_\lambda}{E_\lambda} = -\alpha_{tot}dx, \qquad (2.11)$$

where E_λ is the spectral irradiance of the beam at dx and α_{tot} is the attenuation coefficient per unit length that includes both scattering and absorption effects. The attenuation coefficient is assumed to be negative to represent the loss of optical signal. A unit cross-section of an incident beam travelling over a distance of x through a scattering medium is shown schematically in Figure 2.21.
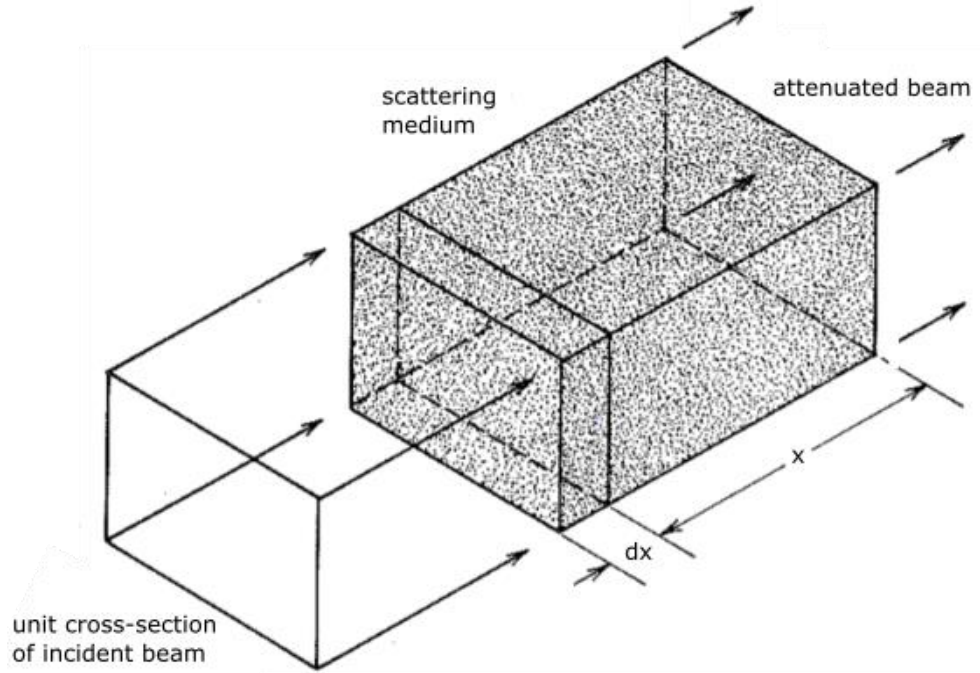
Figure 2.21: Schematic of the attenuation of light due to a scattering medium.
The particles scatter a fraction of the light in all directions, resulting in a loss
in optical signal. Adapted from ref. [2.83].

The spectral irradiance of the propagating light at a distance of x into the scattering media can be found by integrating Equation 2.11 between the limits of zero and x and is given as [2.98]:

$$E_x = E_0 \, e^{-(\alpha_{tot})x},$$

(2.12)

where E_0 is the beam irradiance at $x = 0$. It can be useful to apply a quantitative metric to the level of scattering in an environment to allow for comparisons of measurements taken in different obscurants. When the distance $x = 1/\alpha_{tot}$, Equation 2.12 becomes:

$$E_x = E_0 \, e^{-1},$$

(2.13)

and the beam irradiance is reduced to 36.8% (i.e., $1/e$) of its original value. The value of x that causes this is known as the 'mean free path' of the light. For distances under this value, the beam will travel without being scattered. From this principle, a dimensionless value corresponding to the number of attenuation lengths, N_{AL}, between the target and the imaging system can be obtained, where x is the stand-off distance to the target. This value is given by:

$$N_{AL} = \alpha_{tot} x.$$

(2.14)

This metric will be used in Chapters 5 and 6 of this Thesis to evaluate the level of attenuation in measurements performed in a variety of scattering media. In some cases it can be useful to express the optical attenuation in terms of decibels per kilometre, where a decibel is defined as:

$$dB = 10 \log_{10} \frac{E}{E_0},$$

(2.15)

where E is the attenuated power of the optical signal and E_0 is the original power. From Equation 2.12, the ratio of emergent to incident optical signal for a 1 km path is simply:

$$E_x = E_0 \, e^{-(\alpha_{tot})}.$$

(2.16)

Combining these two expressions gives:

$$dBkm^{-1} = -4.343 \alpha km^{-1}.$$

(2.17)

Atmospheric scattering can often be characterised in terms of visibility, V, and is given by:

$$V = \frac{1}{\alpha_{tot}} \ln\left[\frac{C_0}{C_{th}}\right], \tag{2.18}$$

where C_0 is the contrast of the target against the background and C_{th} is the minimum threshold contrast of the observer [2.99,2.100]. The minimal threshold contrast for the human eye is typically given as 0.05, as defined by the CIE (International Commission on Illumination) [2.101]. Example visibility ranges for a variety of weather conditions, as defined by Hulbert *et. al*, are listed in Table 2.2.

Table 2.2: Examples of visible ranges for a variety of weather conditions. From ref. [2.102]

Weather condition	Visible range
Dense fog	< 50 m
Thick fog	50 – 200 m
Moderate fog	200 – 500 m
Light fog	500 – 1000 m
Thin fog	1 – 2 km
Haze	2 – 4 km
Light haze	4 – 10 km
Clear	10 – 20 km
Very clear	20 – 50 km
Exceptionally clear	> 50 km
Pure air	277 km

2.4 The advantages of shortwave infrared wavelengths for imaging in highly scattering environments

This Section presents an overview of the main advantages of using SWIR wavelengths in free-space imaging in highly scattering environments when compared to the visible band. The SWIR band is immediately adjacent to the near infrared (NIR) band in the electromagnetic spectrum and refers to non-visible light in the wavelength range of 1400 – 3000 nm. The measurements reported in this Thesis were all performed using an illumination wavelength of 1550 nm. These advantages of this wavelength band include: high atmospheric transmission [2.103,2.104], low solar background [2.105], increased eye-safety [2.106], and compatibility with the optical fibre low-loss telecommunications window [2.107].

Section 2.3 introduced the two main types of scattering for small particles, and presented the idea that, depending on the size of the particle, scattering may have a strong dependence on the wavelength of the propagating light.

Several studies have investigated the propagation of light through the atmosphere and various types of atmospheric obscurants [2.78–2.81,2.93,2.99,2.108]. These studies, which included both theoretical modelling and experimental measurements, clearly illustrate the detrimental effects of obscurants on laser beam propagation and image quality. Most studies suggest that SWIR wavelengths have lower levels of attenuation through fog than shorter wavelengths, such as those in the visible region of the spectrum [2.78–2.82]. However, there is ongoing debate regarding the wavelength dependence of optical propagation through high densities of water-based fog. Some studies suggest that, at very high densities of fog, there are no clear benefits to using longer wavelengths [2.109,2.110].

For example, in 2010, Nadeem *et al.* conducted an investigation of the influences of continental fog on free-space optical systems [2.79]. In this work, the authors proposed a new model to predict optical attenuation for different measurement ranges, and compared it to three well-established models, which predict fog specific attenuation using target visibility [2.81,2.109,2.111]. In order to validate this model, the authors used measurements in fog performed at wavelengths of 830 nm and 1550 nm. These measurements were obtained concurrently for a parallel path over a range of 100 m. The authors reported that the attenuation of the 1550 nm wavelength light was relatively low in comparison with that of the 830 nm light [2.79]. For example, for fog with visibilities of between 200 – 400 m, the 1550 nm wavelength experienced an attenuation of up to approximately 110 dB/km while the 830 nm wavelength experienced increased attenuations of up to approximately 150 dB/km. These results were supported by investigations performed by Ijaz *et al.* in 2012 [2.80]. In these measurements, an enclosed 5.5 m long chamber was filled with a controlled volume of fog, which was allowed to disperse from the chamber over a period of approximately 12 minutes. Two laser diodes were used to provide illumination wavelengths of 830 nm and 1550 nm. Two appropriate power meters were placed at the far end of the chamber to measure the transmission of the beams, as shown in Figure 2.22 (a). These measurements were performed concurrently so that a valid comparison between both wavelengths could be made. A plot of the optical attenuation in dB as a function of measurement time for an unspecified density of fog is shown in Figure 2.22 (b) for both illumination wavelengths.
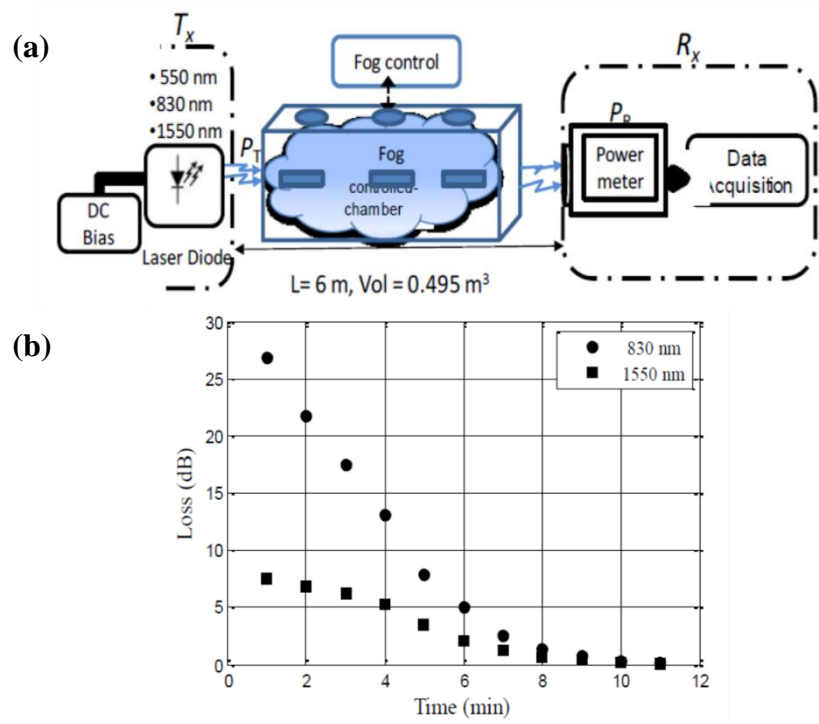
Figure 2.22: (a) A schematic of the experimental set-up to measure optical attenuation due to the fog. (b) A comparison of the measured signal loss in dB at wavelengths of 830 nm and 1550 nm. From ref. [2.80].

The authors reported that, at the start of the measurements when the fog was most dense, the light was attenuated by approximately 27 dB and 7 dB for wavelengths of 830 nm and 1550 nm, respectively. As the fog dispersed, the loss was reduced for both wavelengths. It is important to note that the authors did not state the type of fog used in the measurements, only that they used a 'fog machine' to generate the obscurant. Thus, the assumption must be made that the obscurant in this study was an artificial fog that is more comparable in terms of particle size to smoke than to water-based fog. This difference in the optical attenuation in visible and SWIR wavelengths is consistent with results reported earlier by Grabner *et al.* in 2010 [2.112] and also with measurements presented in Chapter 5 of this Thesis, which were performed in an artificial fog (i.e., glycol vapour) [2.100].

While is it generally accepted that light propagation for SWIR wavelengths may suffer from less attenuation than shorter wavelengths in haze and light fog, Kim *et al.* have suggested that this may not be the case for dense fog [2.109]. This conclusion was based on further modelling of the effects of particulate scattering after conducting a meta-analysis of available literature. They report that for moderate to very dense water-based fog (i.e., visibilities of less than 500 m), there is no advantage to the use of

1550 nm illumination over 785 nm illumination when considering the effects of atmospheric attenuation. Table 2.3 presents the optical losses due to scattering calculated by Kim *et al.* using this new model for 785 nm and 1550 nm light propagation. The results indicate no benefit to the use of longer wavelengths in moderate to dense fog.

Table 2.3: A table of optical loss in dB/km as a function of visibility for wavelengths of 785 nm and 1550 nm. The results were obtained using an updated model of atmospheric scattering and indicate there is no benefit to the use of SWIR wavelengths in moderate to dense fog. From ref. [2.109]

Visibility (km)	dB/km 785 nm	dB/km 1550 nm	Weather
0.05	340	340	Fog
0.2	85	85	Fog
0.5	34	34	Fog
1	14	10	
2	7	4	Haze
4	3	2	Haze
10	1	0.4	Clear
23	0.5	0.2	Clear

While these results were obtained from theoretical modelling, they are supported by the results presented in Chapter 5 of this Thesis, where the use of 1550 nm illumination indicated only a small benefit over visible band sensors in high densities of water-based fog [2.100]. Despite this caveat, there are a number of other advantages to the use of SWIR wavelengths for imaging in highly scattering environments.

In many free-space applications, such as LiDAR imaging, the eye-safety threshold of the laser source places limits on the maximum optical power of the system [2.113]. However, the use of SWIR wavelengths can increase this threshold significantly when compared to visible band wavelengths. The retinal hazard region is defined as the wave band between 400 – 1400 nm, which can cause clinical damage to the retina [2.114]. For example, this eye-safety threshold increases by a factor of approximately 20 or more when the illumination wavelength is increased from 850 nm to 1550 nm [2.106]. This maintains eye-safety requirements in active imaging systems while permitting the use of increased optical power levels. An increase in the maximum optical power level results in an increase in the maximum attainable range and/or improvements in achievable depth resolution of the system.

One of the main limitations in single-photon based LiDAR systems is the level of background relative to the target signal. Background can be defined as the level of signal collected by the detector that does not originate from the laser transmitter. In single-photon systems, the background level is dependent on two main factors: dark counts from the detector and solar radiation, with solar radiation being the main contributor [2.55]. An increased background level lowers the signal-to-background ratio (SBR), which results in reduced system performance [2.115]. This will be discussed in more detail in Chapter 3 of this Thesis. Typically, single-photon LiDAR systems use high-performance spectral filters to decrease the level of ambient background detected by the receiver [2.47,2.48,2.55]. However, due to the very high sensitivity of single-photon detectors, this does not solve the problem entirely. One way to minimise this is through the use of SWIR illumination, as solar radiation decreases considerably in this spectral band compared to the visible band, as shown in Figure 2.23 [2.103,2.105,2.116,2.117].
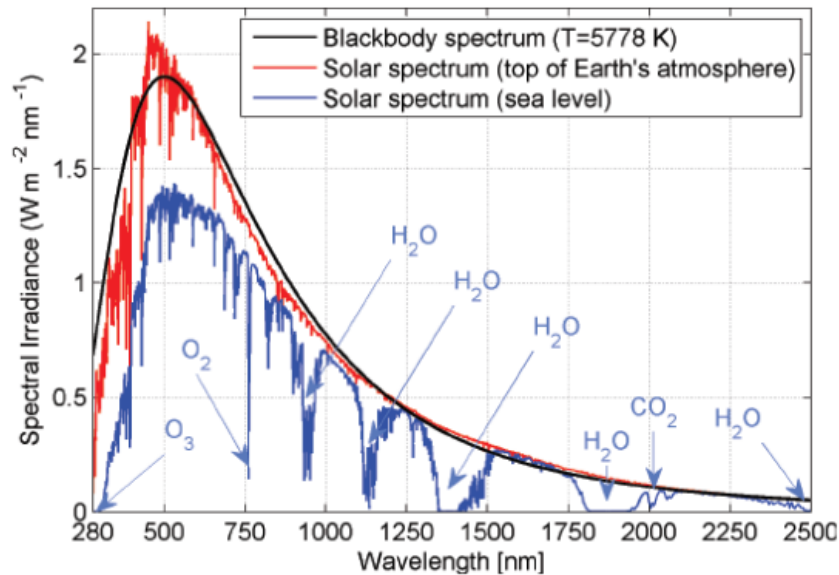
Figure 2.23: Solar spectrum of irradiation from the Sun after passing through the atmosphere. The emission curve for a blackbody radiator (i.e., the sun) and prominent absorption bands and their causes are also shown. The spectral data is from ref. [2.116] and the absorption data from ref. [2.117].

Finally, it is a fundamental advantage in most fibre-based applications to have compatibility with the optical fibre low-loss telecommunications window. Fibre-optic based communication is mainly conducted in the wavelength range of 1260 nm to 1625 nm where optical fibres have small transmission loss [2.118,2.119]. An example of the attenuation of a typical commercially available G.652 optical fibre as a function of

wavelength is shown in Figure 2.24. Thus, fibre-based LiDAR systems operating at SWIR wavelengths benefit from both the low-loss of optical fibres and the high level of commercial availability of components.
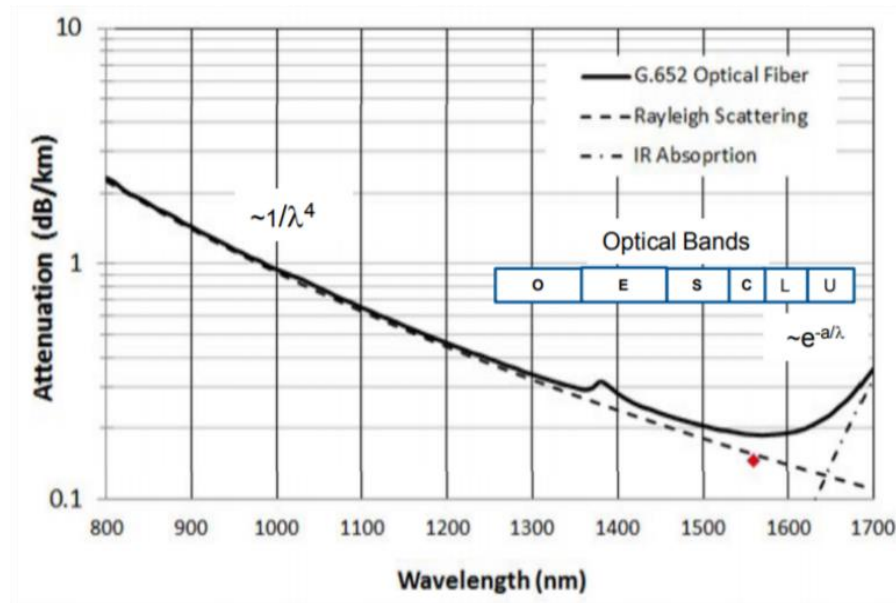
Figure 2.24: The attenuation of a typical commercially available G.652 optical fibre as a function of wavelength. The optical bands of the telecommunications window are also shown. From ref. [2.119].

2.5 Conclusions

This Chapter has given a brief review of LiDAR imaging, and explained how it can be used to obtain high-resolution depth profiles of remote targets. An overview of several types of LiDAR systems was presented, with particular attention given to LiDAR systems based on the TCSPC approach were presented for imaging in extreme scenarios, such as for long-range targets [2.47,2.55], targets in cluttered environments [2.48,2.71,2.76], and targets in high levels of scattering media [2.3,2.100]. The excellent surface-to-surface resolution and picosecond temporal resolution provided by the TCSPC technique make it the ideal candidate technology for ToF measurements of long-range targets. A full description of the TCSPC technique will be provided in Chapter 3.

This Chapter has also provided an introduction to the principal characteristics of scattering effects from small particles, such as Rayleigh scattering and Mie scattering [2.86], and their effects on optical propagation through scattering media. Particular attention was given to the wavelength dependency of particulate scattering and the indication that SWIR wavelengths are less affected than visible band wavelengths.

Finally, the advantages of SWIR wavelengths for imaging in highly scattering environments were discussed in Section 2.4. These advantages include higher atmospheric transmission, low background from solar radiation, an increased eye-safety threshold for equivalent optical power levels, and compatibility with the optical fibre low-loss telecommunications window.

2.6 References

2.1.   J. Hecht, "Lidar for self-driving cars," Opt. Photonics News 29(1), 26–33 (2018).

2.2.   S. Hasirlioglu and A. Riener, "Introduction to rain and fog attenuation on automotive surround sensors," in 2017 IEEE 20th International Conference on Intelligent Transportation Systems (ITSC), 1–7 (2017).

2.3.   G. Satat, M. Tancik, and R. Raskar, "Towards photography through realistic fog," in 2018 IEEE International Conference on Computational Photography (ICCP), 1–10 (2018).

2.4.   V. Molebny, P. F. McManamon, O. Steinvall, T. Kobayashi, and W. Chen, "Laser radar: historical prospective—from the east to the west," Opt. Eng. 56(3), 031220 (2016).

2.5.   E. Baumann, F. R. Giorgetta, J. -. Deschênes, I. Coddington, L. C. Sinclair, W. C. Swann, and N. R. Newbury, "Micrometer-precision 3D imaging at 4-meter standoff distance," in Advanced Solid-State Lasers Congress, OSA Technical Digest, LW3A.5 (2013).

2.6.   J. S. Massa, G. S. Buller, A. B. D. Walker, G. V. S. Smith, S. Cova, M. Umasuthan, and A. Wallace, "Optical design and evaluation of a three-dimensional imaging and ranging system based on time-correlated single-photon counting.," Appl. Opt. 41(6), 1063–1070 (2002).

2.7.   D. Cunningham, S.Grebby, K. Tansey, A. Gosar, and V. Kastelic, "Application of airborne LiDAR to mapping seismogenic faults in forested mountain terrain, south eastern Alps, Slovenia," Geophys. Res. Lett., 33, L20308 (2006).

2.8.   W. E. Clifton, B. Steele, G. Nelson, A. Truscott, M. Itzler, M. Entwistle, "Medium altitude airborne Geiger-mode mapping LIDAR system," Proc. SPIE 9465, Laser Radar Technology and Applications XX and Atmospheric Propagation XII, 946506 (2015);

2.9.   M. A. Itzler, M. Entwistle, S. Wilton, I. Kudryashov, J. Kotelnikov, X. Jiang, B. Piccione, M. Owens, and S. Rangwala, "Geiger-mode LiDAR: from airborne platforms to driverless cars," in Imaging and Applied Optics, ATu3A.3 (2017).

2.10. A. Maccarone, A. McCarthy, X. Ren, R. E. Warburton, A. M. Wallace, J. Moffat, Y. Petillot, and G. S. Buller, "Underwater depth imaging using time-correlated single-photon counting," Opt. Express 23(26), 33911–33926 (2015).

2.11. J. S. Jaffe, "Underwater optical imaging: the past, the present, and the prospects," IEEE J. Ocean. Eng. 40(3), 683–700 (2015).

2.12. F. M. Caimi and F. R. Dalgleish, "Performance considerations for continuous-wave and pulsed laser line scan (LLS) imaging systems," J. Eur. Opt. Soc. - Rapid Publ. 5(0), (2010).

2.13. J. S. Jaffe, "Computer modeling and the design of optimal underwater imaging systems," IEEE J. Ocean. Eng. 15(2), 101–111 (1990).

2.14. G. Zhao, M. Lian, Y. Li, Z. Duan, S. Zhu, L. Mei, and S. Svanberg, "Mobile lidar system for environmental monitoring," Appl. Opt. 56(5), 1506–1516 (2017).

2.15. N. U. Singh, Lidar Remote Sensing for Environmental Monitoring, (SPIE, 2017).

2.16. P. Gaudio, M. Gelfusa, A. Malizia, S. Parracino, M. Richetta, L. De Leo, C. Perrimezzi, and C. Bellecci, "Detection and monitoring of pollutant sources with Lidar/Dial techniques," J. Phys. Conf. Ser. 658, 012004 (2015).

2.17. P. Soan, M. Silver, J. Parsons, P. Feneyrou, A. Martin, R. Tobin, A. McCarthy, A. Halimi, S. Chan, K. McEwan, J. Miah, B. Stewart, J. Leach, and G. Buller, "Comparative assessment of different active imaging technologies for imaging through obscurants," in Electro-Optical Remote Sensing XII 10796, 107960C, (2018).

2.18. B. Schwarz, "Mapping the world in 3D," Nat. Photonics 4(7), 429–430 (2010).

2.19. Y. Lin, J. Hyyppa, and A. Jaakkola, "Mini-UAV-borne LIDAR for fine-scale mapping," IEEE Geosci. Remote Sens. Lett. 8(3), 426–430 (2011).

2.20. R. D. Richmond and S. C. Cain, Direct-Detection LADAR Systems (SPIE, 2010).

2.21. P. A. Forrester and K. F. Hulme, "Laser rangefinders," Opt. Quantum Electron. 13(4), 259–293 (1981).

2.22. T. E. Honeycutt and W. F. Otto, "FM-CW radar range measurement with a CO2 laser," IEEE J. Quantum Electron. QE-8(2), 91–92 (1972).

2.23. A. Hughes, J. O'Shaughnessy, and E. Pike, "FM-CW radar range measurement at 10-μm wavelength," IEEE J. Quantum Electron. 8(12), 909–910 (1972).

2.24. P. A. Hiskett, C. S. Parry, A. McCarthy, and G. S. Buller, "A photon-counting time-of-flight ranging technique developed for the avoidance of range ambiguity at gigahertz clock rates," Opt. Express 16(18), 13685–13698 (2008).

2.25. N. J. Krichel, A. McCarthy, and G. S. Buller, "Resolving range ambiguity in a photon counting depth imager operating at kilometer distances," Opt. Express 18(9), 9192–9206 (2010).

2.26. Y. Liang, J. Huang, M. Ren, B. Feng, X. Chen, E. Wu, G. Wu, and H. Zeng, "1550-nm time-of-flight ranging system employing laser with multiple repetition rates for reducing the range ambiguity," Opt. Express 22(4), 4662–4670 (2014).

2.27. C. Mallet and F. Bretar, "Full-waveform topographic lidar: State-of-the-art," ISPRS J. Photogramm. Remote Sens. 64(1), 1–16 (2009).

2.28. G. C. Guenther and H. C. Mesick, "Analysis of airborne laser hydrography waveforms," in Ocean Optics IX 0925, pp. 232–241 (1988).

2.29. "YellowScan Mapper II datasheet," (YellowScan, accessed June 2019).

2.30. M. A. Lefsky, W. B. Cohen, G. G. Parker, D. J. Harding, "Lidar remote sensing for ecosystem studies", BioScience, 52 (1), 19–30 (2002).

2.31. K. Lim, P. Treitz, M. Wulder, B. St-Onge, and M. Flood, "LiDAR remote sensing of forest structure," Prog. Phys. Geogr. Earth Environ. 27(1), 88–106 (2003).

2.32. P. L. Bender, D. G. Currie, S. K. Poultney, C. O. Alley, R. H. Dicke, D. T. Wilkinson, D. H. Eckhardt, J. E. Faller, W. M. Kaula, J. D. Mulholland, H. H. Plotkin, E. C. Silverberg, J. G.Williams, "The Lunar Laser Ranging Experiment", Science, 182 (4109), 229–238 (1973).

2.33. L. D. Smullin and G. Fiocco, "Optical echoes from the moon," Nature 194(4835), 1267 (1962).

2.34. C. O. Alley, P. L. Bender, R. H. Dicke, J. E. Faller, P. A. Franken, H. H. Plotkin, and D. T. Wilkinson, "Optical radar using a corner reflector on the Moon," J. Geophys. Res. 1896-1977 70(9), 2267–2269 (1965).

2.35. W. F. Hoffmann, R. Krotkov, and R. H. Dicke, "Precision optical tracking of artificial satellites," IRE Trans. Mil. Electron. MIL–4(1), 28–37 (1960).

2.36. Y. L. Kokurin, V. V. Kurbasov, V. F. Lobanov, A. N. Sukhanovskii, N. S. Chernykh, "Laser Location of the Reflector on Board Lunokhod-1", Soviet Journal of Quantum Electronics, 1 (5), 555–557 (1972).

2.37. J. G. Williams and J. O. Dickey, "Lunar geophysics, geodesy, and dynamics," (2002).

2.38. J. G. Williams, S. G. Turyshev, and D. H. Boggs, "Progress in lunar laser ranging tests of relativistic gravity," Phys. Rev. Lett. 93(26 Pt 1), 261101 (2004).

2.39. J.J. Degnan, "Thirty years of satellite laser ranging", Keynote Speech, Proc. Of the 9th Intern. Workshop on Laser Ranging Instrumentation, Australia (1994).

2.40. E. Vermaat, J. J. Degnan, P. J. Dunn, R. Noomen, and A. T. Sinclair, "Satellite laser ranging, status and impact for WEGENER," J. Geodyn. 25(3), 195–212 (1998).

2.41. J. Busck and H. Heiselberg, "Gated viewing and high-accuracy three-dimensional laser radar," Appl. Opt. 43(24), 4705–4710 (2004).

2.42. P. Andersson, "Long-range three-dimensional imaging using range-gated laser radar images," Opt. Eng. 45(3), 034301 (2006).

2.43. X. Ren, P. W. R. Connolly, A. Halimi, Y. Altmann, S. McLaughlin, I. Gyongy, R. K. Henderson, and G. S. Buller, "High-resolution depth profiling using a range-gated CMOS SPAD quanta image sensor," Opt. Express 26(5), 5541–5557 (2018).

2.44. G. S. Buller and A. Wallace, "Ranging and three-dimensional imaging using time-correlated single-photon counting and point-by-point acquisition," IEEE J. Sel. Top. Quantum Electron 13(4), 1006–1015 (2007).

2.45. S. Chan, A. Halimi, F. Zhu, I. Gyongy, R. K. Henderson, R. Bowman, S. McLaughlin, G. S. Buller, and J. Leach, "Long-range depth imaging using a single-photon detector array and non-local data fusion," Sci. Rep. 9(1), 8075 (2019).

2.46. A. McCarthy, R. J. Collins, N. J. Krichel, V. Fernández, A. M. Wallace, and G. S. Buller, "Long-range time-of-flight scanning sensor based on high-speed time-correlated single-photon counting," Appl. Opt. 48(32), 6241–6251 (2009).

2.47. A. M. Pawlikowska, A. Halimi, R. A. Lamb, and G. S. Buller, "Single-photon three-dimensional imaging at up to 10 kilometers range," Opt. Express 25(10), 11919–11931 (2017).

2.48. R. Tobin, A. Halimi, A. McCarthy, X. Ren, K. J. McEwan, S. McLaughlin, and G. S. Buller, "Long-range depth profiling of camouflaged targets using single-photon detection," Opt. Eng. 57(3), 031303 (2017).

2.49. A. Maccarone, A. McCarthy, A. Halimi, R. Tobin, A. M. Wallace, Y. Petillot, S. McLaughlin, and G. S. Buller, "Depth imaging in highly scattering underwater environments using time-correlated single-photon counting," in Emerging Imaging and Sensing Technologies 9992, 99920R (2016).

2.50. Y. Altmann, A. Maccarone, A. McCarthy, G. Newstadt, G. S. Buller, S. McLaughlin, and A. Hero, "Robust Spectral Unmixing of Sparse Multispectral Lidar Waveforms Using Gamma Markov Random Fields," IEEE Trans. Comput. Imaging 3(4), 658–670 (2017).

2.51. A. M. Wallace, A. McCarthy, C. J. Nichol, X. Ren, S. Morak, D. Martinez-Ramirez, I. H. Woodhouse, and G. S. Buller, "Design and evaluation of multispectral LiDAR for the recovery of arboreal parameters," IEEE Trans. Geosci. Remote Sens. 52(8), 4942–4954 (2014).

2.52. X. Ren, Y. Altmann, R. Tobin, A. Mccarthy, S. Mclaughlin, and G. S. Buller, "Wavelength-time coding for multispectral 3D imaging using single-photon LiDAR," Opt. Express 26(23), 30146–30161 (2018).

2.53. R. Tobin, Y. Altmann, X. Ren, A. McCarthy, R. A. Lamb, S. McLaughlin, and G. S. Buller, "Comparative study of sampling strategies for sparse photon multispectral lidar imaging: towards mosaic filter arrays," J. Opt. 19(9), 094006 (2017).

2.54. G. S. Buller and R. J. Collins, "Single-photon generation and detection," Meas. Sci. Technol. 21(1), 012002 (2009).

2.55. A. McCarthy, X. Ren, A. D. Frera, N. R. Gemmell, N. J. Krichel, C. Scarcella, A. Ruggeri, A. Tosi, and G. S. Buller, "Kilometer-range depth imaging at 1550 nm wavelength using an InGaAs/InP single-photon avalanche diode detector," Opt. Express 21(19), 22098–22113 (2013).

2.56. R. H. Hadfield, "Single-photon detectors for optical quantum information applications," Nat. Photonics 3(12), 696–705 (2009).

2.57. M. J. Stevens, R. H. Hadfield, R. E. Schwall, S. W. Nam, and R. P. Mirin, "Time-correlated single-photon counting with superconducting single-photon detectors," in Advanced Photon Counting Techniques, Proc. of SPIE 6372, 63720U (2006).

2.58. J. S. Massa, A. M. Wallace, G. S. Buller, S. J. Fancey, and A. C. Walker, "Laser depth measurement based on time-correlated single-photon counting," Opt. Lett. 22(8), 543–545 (1997).

2.59. R. E. Warburton, A. McCarthy, A. M. Wallace, S. Hernandez-Marin, R. H. Hadfield, S. W. Nam, and G. S. Buller, "Subcentimeter depth resolution using a single-photon counting time-of-flight laser ranging system at 1550 nm wavelength.," Opt. Lett. 32(15), 2266–2268 (2007).

2.60. A. McCarthy, N. J. Krichel, N. R. Gemmell, X. Ren, M. G. Tanner, S. N. Dorenbos, V. Zwiller, R. H. Hadfield, and G. S. Buller, "Kilometer-range, high resolution depth imaging via 1560 nm wavelength single-photon detection," Opt. Express 21(7), 8904–8915 (2013).

2.61. N. R. Gemmell, M. Hills, T. Bradshaw, T. Rawlings, B. Green, R. M. Heath, K. Tsimvrakidis, S. Dobrovolskiy, V. Zwiller, S. N. Dorenbos, M. Crook, and R. H. Hadfield, "A miniaturized 4 K platform for superconducting infrared photon counting detectors," Superconductor Science and Technnology 30(11), 11LT01 (2017).

2.62. Z.-P. Li, Z.-P. Li, X. Huang, X. Huang, Y. Cao, Y. Cao, B. Wang, B. Wang, Y.-H. Li, Y.-H. Li, J. Zhang, J. Zhang, Q. Zhang, Q. Zhang, C.-Z. Peng, C.-Z. Peng, F. Xu, F. Xu, J.-W. Pan, and J.-W. Pan, "All-Time Single-Photon 3D Imaging Over 21 km," in Conference on Lasers and Electro-Optics, Paper SM1N.1 (2019).

2.63. M. Entwistle, M.A. Itzler, J. Chen, M. Owens, K. Patel, X. Jiang, K. Slomkowski, and S. Rangwala, "Geiger-mode APD camera system for single-photon 3D LADAR imaging," Proc. SPIE 8375, Advanced Photon Counting Techniques VI, 83750D (2012).

2.64. P. A. Hiskett, K. J. Gordon, J. W. Copley, and R. A. Lamb, "Long range 3D imaging with a 32x32 Geiger mode InGaAs/InP camera," in Advanced Photon Counting Techniques VIII 9114, 91140I (2014).

2.65. G. S. Buller, R. D. Harkins, A. McCarthy, P. A. Hiskett, G. R. MacKinnon, G. R. Smith, R. Sung, A. M. Wallace, R. A. Lamb, K. D. Ridley, and J. G. Rarity, "Multiple wavelength time-of-flight sensor based on time-correlated single-photon counting," Rev. Sci. Instrum. 76(8), 083112 (2005).

2.66. O. Nevalainen, T. Hakala, J. Suomalainen, R. Mäkipää, M. Peltoniemi, A. Krooks, and S. Kaasalainen, "Fast and nondestructive method for leaf level chlorophyll estimation using hyperspectral LiDAR," Agric. For. Meteorol. 198–199, 250–258 (2014).

2.67. A.K. Bhandari, A. Kumar, G.K. Singh, "Feature extraction using normalized difference vegetation index (NDVI): A case study of Jabalpur city," Procedia Technology 6, 612-621 (2012).

2.68. J. A. Gamon, L. Serrano, and J. S. Surfus, "The photochemical reflectance index: an optical indicator of photosynthetic radiation use efficiency across species, functional types, and nutrient levels," Oecologia 112(4), 492–501 (1997).

2.69. B. W. Schilling, D. N. Barr, G. C. Templeton, L. J. Mizerka, and C. W. Trussell, "Multiple-return laser radar for three-dimensional imaging through obscurations," Appl. Opt. 41(15), 2791–2799 (2002).

2.70. O. Steinvall, H. Larsson, F. Gustafsson, D. Letalick, T. Chevalier, A. Persson, and P. Andersson, "Performance of 3D laser radar through vegetation and camouflage," in Laser Source and System Technology for Defense and Security 5792, 129–143 (2005).

2.71. M. Henriksson, H. Larsson, C. Grönwall, and G. Tolt, "Continuously scanning time-correlated single-photon-counting single-pixel 3-D lidar," Opt. Eng. 56(3), 031204 (2016).

2.72. A. M. Wallace, J. Ye, N. J. Krichel, A. McCarthy, R. J. Collins, and G. S. Buller, "Full Wave Form Analysis for Long-range 3D Imaging Laser Radar," EURASIP J Adv Signal Process 33, 1–12 (2010).

2.73. D. Shin, F. Xu, F. N. C. Wong, J. H. Shapiro, and V. K. Goyal, "Computational multi-depth single-photon imaging," Opt. Express 24(3), 1873–1888 (2016).

2.74. A. M. W. E. Member, J. Y. E. Member, N. J. Krichel, A. McCarthy, R. J. Collins, and G. S. Buller, "Full Waveform Analysis for Long-Range 3D Imaging Laser Radar," EURASIP J. Adv. Signal Process. 2010(1), 896708 (2010).

2.75. M.A. Itzler, M. Entwistle, M. Owens, K. Patel, X. Jiang, K. Slomkowski, S. Rangwala, P.F. Zalud, T. Senko, J. Tower, and J. Ferraro, "Comparison of 32 x 128 and 32 x 32 Geiger-mode APD FPAs for single photon 3D LADAR imaging," Proc. SPIE 8033, Advanced Photon Counting Techniques V, 80330G (2011).

2.76. M. Henriksson and P. Jonsson, "Photon-counting panoramic three-dimensional imaging using a Geiger-mode avalanche photodiode array," Opt. Eng. 57(9), 093104 (2018).

2.77. J. Tachella, Y. Altmann, N. Mellado, A. McCarthy, R. Tobin, G. S. Buller, J.-Y. Tourneret, and S. McLaughlin, "Real-time 3D reconstruction of complex scenes using single-photon lidar: when image processing meets computer graphics," ArXiv190506700 Phys. (2019).

2.78. F. Christnacher, J.-M. Poyet, E. Bacher, N. Metzger, S. Schertzer, and J.-R. Simard, "Influence of the obscurants and the illumination wavelengths on a range-gated active imaging system performance," in Electro-Optical Remote Sensing XII 10796, 1079603 (2018).

2.79. F. Nadeem, T. Javornik, E. Leitgeb, V. Kvicera, and G. Kandus, "Continental fog attenuation empirical relationship from measured visibility data," Radioeng.19(4), 596-600 (2010).

2.80. M. Ijaz, Z. Ghassemlooy, S. Rajbhandari, H. L. Minh, J. Perez, and A. Gholami, "Comparison of 830 nm and 1550 nm based free space optical communications link under controlled fog conditions," in 8th International Symposium on Communication Systems, Networks Digital Signal Processing (CSNDSP), 1–5 (2012).

2.81. M. C. A. Naboulsi, H. Sizun, and F. de Fornel, "Fog attenuation prediction for optical and infrared waves," Opt. Eng. 43(2), 319–330 (2004).

2.82. M. S. Khan, E. Leitgeb, S. S. Muhammad, M. S. Awan, V. Kvicera, and M. Grabner, "Further results on fog modeling for terrestrial free-space optical links," Opt. Eng. 51(3), 031207 (2012).

2.83. E. J. McCartney, Optics of the Atmosphere (Wiley, 1976).

2.84. R. S. Stein, R. L. Rowell, and H. Brumberger, "Light scattering," Intern. Sci. Tech. 83, 34–42 (1968).

2.85. R. Vaillon, "Radiative properties of particles," in Handbook of Thermal Science and Engineering, 1143–1172 (2018).

2.86. D. J. Lockwood, "Rayleigh and Mie Scattering," in Encyclopedia of Color Science and Technology, 1097–1107 (2016).

2.87. J. W. S. Rayleigh, "On the light from the sky, its polarization and color," Phil Mag 41, 107–120 (1899).

2.88. J. H. Seinfeld and S. N. Pandis, Atmospheric chemistry and physics: from air pollution to climate change (Wiley, 2006).

2.89. H. Horvath, "Gustav Mie and the scattering and absorption of light by particles: Historic developments and basics," J. Quant. Spectrosc. Radiat. Transf. 110(11), 787–799 (2009).

2.90. H. Zhan, D. G. Voelz, S.-Y. Cho, and X. Xiao, "Complex index of refraction estimation from degree of polarization with diffuse scattering consideration," Appl. Opt. 54(33), 9889–9895 (2015).

2.91. L. R. Bissonnette, "Imaging through fog and rain," Opt. Eng. 31(5), 1045–1053 (1992).

2.92. M. Gebhart, E. Leitgeb, S. Sheikh Muhammad, B. Flecker, C. Chlestil, M. Al Naboulsi, F. de Fornel, H. Sizun, "Measurement of light attenuation in dense fog conditions for FSO applications," Proc. SPIE 5891, Atmospheric Optical Modeling, Measurement, and Simulation, 58910K (2005).

2.93. G. Méjean, J. Kasparian, J. Yu, E. Salmon, S. Frey, J.-P. Wolf, S. Skupin, A. Vinçotte, R. Nuter, S. Champeaux, and L. Bergé, "Multifilamentation transmission through fog," Phys. Rev. E Stat. Nonlin. Soft Matter Phys. 72(2.2), 026611 (2005).

2.94. K.-N. Liou and P. Yang, Light scattering by ice crystals: fundamentals and applications (Cambridge University Press, 2016).

2.95. S. Q. Duntley, "Light in the Sea," JOSA 53(2), 214–233 (1963).

2.96. C. Bohren and D. Huffman, Absorption and Scattering of Light by Small Particles (Wiley, 1983).

2.97. A. A. G. Abushagur, F. M. Abbou, M. Abdullah, N. Misran, "Performance analysis of a free-space terrestrial optical system in the presence of absorption, scattering, and pointing error," Opt. Eng. 50(7) 075007 (1 July 2011)

2.98. D. F. Swinehart, "The Beer-Lambert Law," J. Chem. Educ. 39(7), 333 (1962).

2.99. F. Christnacher, S. Schertzer, N. Metzger, E. Bacher, M. Laurenzis, and R. Habermacher, "Influence of gating and of the gate shape on the penetration capacity of range-gated active imaging in scattering environments," Opt. Express 23(26), 32897–32908 (2015).

2.100. R. Tobin, A. Halimi, A. McCarthy, M. Laurenzis, F. Christnacher, and G. S. Buller, "Three-dimensional single-photon imaging through obscurants," Opt. Express 27(4), 4590–4611 (2019).

2.101. International Commission on Illumination 17 1407, www.cie.co.at/eilv/1407

2.102. E. O. Hulburt, "Optics of atmospheric haze," JOSA 31(7), 467–476 (1941).

2.103. D. Killinger, "Free space optics for laser communication through the air," Opt. Photonics News 13(10), 36–42 (2002).

2.104. A. Arnulf, J. Bricard, E. Curé, and C. Véret, "Transmission by haze and fog in the spectral region 0.35 to 10 microns," JOSA 47(6), 491–498 (1957).

2.105. R. E. Bird, R. L. Hulstrom, and L. J. Lewis, "Terrestrial solar spectral data sets," Sol. Energy 30(6), 563–573 (1983).

2.106. "Safety of laser products − Part 1: Equipment classification, requirements and user's guide" (IEC 60825-1, 1993).

2.107. "Low-Loss Optical Fiber - an overview | ScienceDirect Topics," https://www.sciencedirect.com/topics/engineering/low-loss-optical-fiber.

2.108. M. Grabner and V. Kvicera, "Multiple scattering in rain and fog on free-space optical links," J. Light. Technol. 32(3), 513–520 (2014).

2.109. I. I. Kim, B. McArthur, and E. J. Korevaar, "Comparison of laser beam propagation at 785 nm and 1550 nm in fog and haze for optical wireless communications," in Optical Wireless Communications III 4214, 26–38 (2001).

2.110. R. M. Pierce, J. Ramaprasad, and E. C. Eisenberg, "Optical attenuation in fog and clouds," in Optical Wireless Communications IV 4530, 58–72 (2001).

2.111. P. W. Kruse, L. D. McGlauchlin, and R. B. McQuistan, Elements of Infrared Technology: Generation, Transmission and Detection (Wiley, 1962).

2.112. M. Grabner and V. Kvicera, "Fog attenuation dependence on atmospheric visibility at two wavelengths for FSO link planning," Loughborough Antennas & Propagation Conference, 193-196 (2010).

2.113. T. Beuth, D. Thiel, and M. G. Erfurth, "The hazard of accommodation and scanning LIDARs," in Optical Instrument Science, Technology, and Applications 10695, 1069506 (2018).

2.114. P. N. Youssef, N. Sheibani, and D. M. Albert, "Retinal light toxicity," Eye 25(1), 1–14 (2011).

2.115. S. Pellegrini, G. S. Buller, J. M. Smith, A. M. Wallace, and S. Cova, "Laser-based distance measurement using picosecond resolution time-correlated single-photon counting," Meas. Sci. Technol. 11(6), 712–716 (2000).

2.116. "Standard Tables for Reference Solar Spectral Irradiances: Direct Normal and Hemispherical on 37° Tilted Surface", Technical report ASTM G173-03, American Society for Testing and Materials, ASTM International, USA (2003).

2.117. L. S. Rothman, D. Jacquemart, A. Barbe, D. Chris Benner, M. Birk, L. R. Brown, M. R. Carleer, C. Chackerian, K. Chance, L. H. Coudert, V. Dana, V. M. Devi, J.-M. Flaud, R. R. Gamache, A. Goldman, J.-M. Hartmann, K. W. Jucks, A. G. Maki, J.-Y. Mandin, S. T. Massie, J. Orphal, A. Perrin, C. P. Rinsland, M. A. H. Smith, J. Tennyson, R. N. Tolchenov, R. A. Toth, J. Vander Auwera, P. Varanasi, and G. Wagner, "The HITRAN 2004 molecular spectroscopic database," J. Quant. Spectrosc. Radiat. Transf. 96(2), 139–204 (2005).

2.118. F. P. Kapron, D. B. Keck, and R. D. Maurer, "Radiation losses in glass optical waveguides," Appl. Phys. Lett. 17(10), 423–425 (1970).

2.119. S. Ten, "Ultra low-loss optical fiber technology," in Optical Fiber Communication Conference, Th4E.5 (2016).

Chapter 3: Time-correlated single-photon counting and single-photon detection in the short-wave infrared

3.1 Introduction

At the most fundamental level, a photon can be described as the elementary particle of light that carries a small, quantised amount of electromagnetic radiation known as the photon energy (E_{photon}) [3.1]. This energy is dependent on the frequency (ν), and hence the wavelength (λ), of the photon as follows:

$$E_{photon} = h\nu = \frac{hc}{\lambda},\qquad(3.1)$$

where c is the speed of light in a vacuum and h is Planck's constant ($6.63 \times 10^{-34}\,\mathrm{m^2kgs^{-1}}$). In recent years, the development of highly sensitive detectors capable of single-photon detection and rapid data acquisition hardware has allowed for the implementation of the time-correlated single-photon counting (TCSPC) technique in a wide range of applications.

This Chapter presents a review of the main principles of the TCSPC technique. In addition, a brief introduction to the operation and key characteristics of modern single-photon detectors designed to operate in the shortwave infrared (SWIR) wavelength range is given. Specific attention is given to indium gallium arsenide/indium-phosphide (InGaAs/InP) single-photon avalanche diode (SPAD) detectors, as they were the detectors chosen for the single-photon measurements performed in this Thesis.

3.2 Time-correlated single-photon counting

The TCSPC technique is now a well-established candidate technology used in a wide range of applications, such as fluorescence lifetime imaging [3.2–3.4], quantum communications [3.5,3.6], and laser-based distance measurements [3.7–3.10]. Due to the high temporal resolution offered by modern TCSPC detectors and data acquisition modules, the technique achieves excellent surface-to-surface resolution for three-dimensional imaging, even at kilometre ranges [3.11–3.13]. This Section gives an overview of TCSPC principles and hardware.

3.2.1 TCSPC principles

The TCSPC technique relies on a basic start-stop principle where the photon time-of-flight (ToF) is measured as the time difference between an optical input and a

photon detection event recorded by a single-photon detector [3.14]. In a forward start-stop configuration, the start trigger signal is typically provided to the TCSPC data acquisition module by a pulsed laser source operated at high repetition rates. For example, kHz – MHz repetition rate sources were used for the measurements presented in this Thesis. This signal acts as a master clock for the system. When a detection event occurs, the single-photon detector provides an electrical stop trigger signal to the TCSPC module, which is configured to output time-tagged data, as shown in Figure 3.1. Thus, the time difference, and hence, ToF information can be extracted from this data. These detection events can originate from either a photon arrival or a dark event from the SPAD detector itself. In a reverse start-stop configuration, the start trigger signal is provided by the detector, while the stop trigger signal is given by the next master clock signal [3.14]. A schematic of a basic TCSPC set-up in a forward start-stop configuration is shown in Figure 3.2.
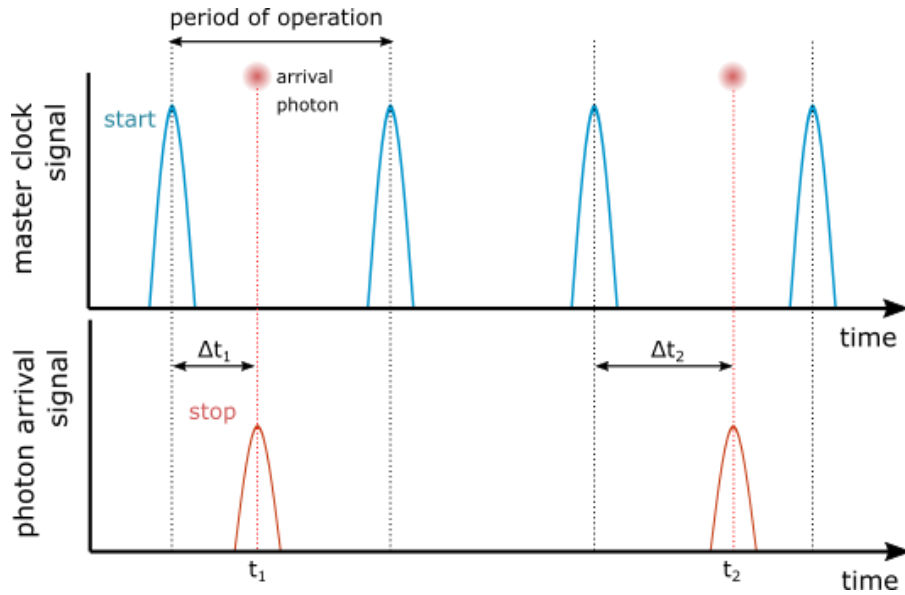
Figure 3.1: Timing diagram illustrating the basic principles of operation of a TCSPC measurement in a forward start-stop configuration. In this case, a forward mode configuration is used where a master clock provides the start signal and the detector provides the stop signal. The start-stop time differences (Δt_x) are measured for each independent photon event.

The TCSPC approach can also be used with non-repetitive illumination sources. As discussed in Chapter 2, direct ToF measurements have the inherent problem of range ambiguity and aliasing. Pseudorandom illumination sources can be used to avoid this issue and provide an absolute target range [3.15,3.16].
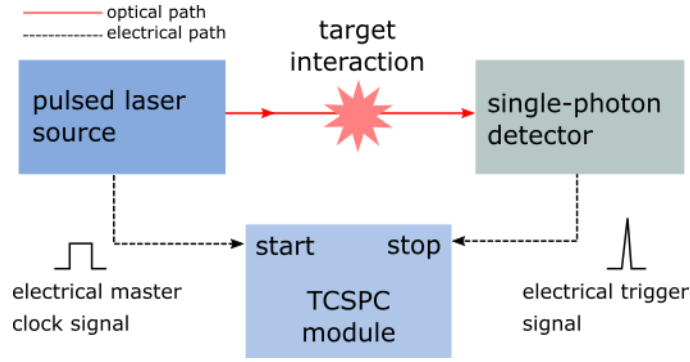
Figure 3.2: Schematic of a typical TCSPC configuration. The start trigger signal is provided by the pulsed laser source while the detector provides the stop trigger signal.

Measurements are typically recorded over many laser pulses to acquire highly accurate ToF information, and hence a high-resolution depth estimate of the target. Although contributions from detector dark counts, ambient light background, and other stray light contributions place a lower limit on the dynamic range of the system. The data are compiled into a timing histogram, which represents the number of detection events recorded for each timing bin over the duration of the measurement. Histogram timing bins have a discrete width, which are pre-determined before ToF measurements commence. Modern TCSPC data acquisition modules, such as the HydraHarp 400 (PicoQuant, Germany), offer timing resolution as low as 1 ps for up to 65536 histogram bins per input channel [3.17]. An example of a TCSPC timing histogram is shown in Figure 3.3.
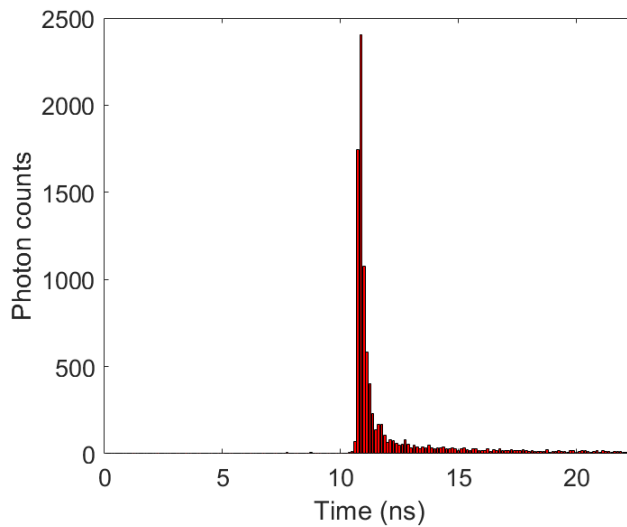
Figure 3.3: Example of a timing histogram acquired from a TCSPC measurement. The value for each timing bin represents the number of detection events within that time range.

50

It should be noted that TCSPC timing histograms are typically asymmetric with narrow peaks followed by long exponential tails, as shown in Figure 3.3. The narrow peak corresponds to charge carriers generated in the junction depletion layer of the detector, which are accelerated immediately by the electric field. The exponential tail is due to charge carriers generated outside the depletion region, which slowly diffuse towards the junction, where they are finally accelerated by the electric field, potentially leading to the initiation of a self-sustaining avalanche [3.18]. This will be discussed in more detail in Section 3.3 of this Chapter.

Single-photon counting follows Poissonian statistics, where each individual detection can be considered as an independent event. For single-photon counting, laser pulses are typically attenuated so that the mean number of photons per pulse, μ, is smaller than one. The probability, $P(N, \mu)$, of a pulse attenuated to a particular value of μ containing N photons is given by [3.19]:

$$P(N,\mu) = \frac{\mu^N e^{-\mu}}{N!}. \qquad (3.2)$$

Figure 3.4 illustrates the probability distribution of a Poissonian process for different values of μ.
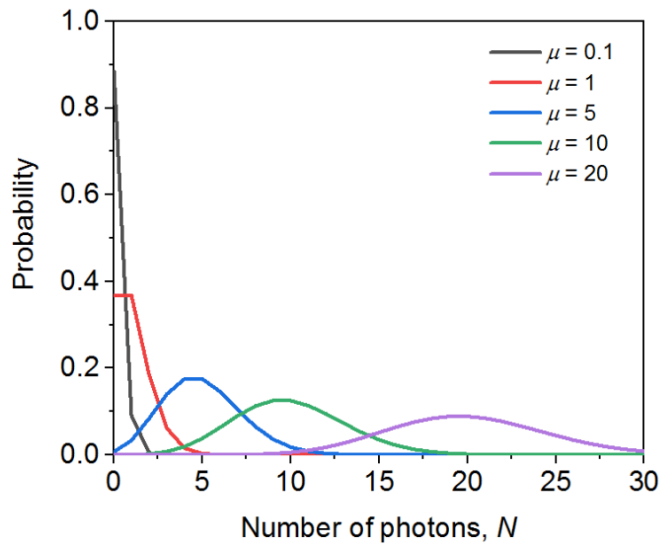
Figure 3.4: The Poisson probability distribution for different values of the expected number of photon detections.

Figure 3.4 indicates that, for higher values of μ, both the shape of the distribution is altered, and the centroid position is shifted. A shift in the centroid position of a TCSPC timing histogram will result in an inaccurate depth estimation. Thus, to obtain statistical integrity in ToF measurements, it is imperative to maintain a low probability of multiple

photon detection events in each laser pulse cycle. This is required in order to maintain a sufficiently uniform probability of detection across the timing range. Too high a count rate will increase the probability of detection towards the beginning of the timing window, distorting the expected timing profile. A high count rate can lead to this effect, which is known as 'pulse pile-up', where waveform becomes distorted due to a shift in centroid position. In order to satisfy this condition, the overall count rate typically must not exceed 5% of the pulse repetition rate of the laser source [3.19].

Usually, the first photon arrival in a signal cycle is registered, skewing the measurement towards shorter arrival times, and hence, causing this waveform distortion. This occurs because after a detection event is registered, the system enters a period of detector insensitivity – or 'dead-time' - where no more photon arrivals can be recorded in that laser pulse cycle, as shown schematically in Figure 3.5.
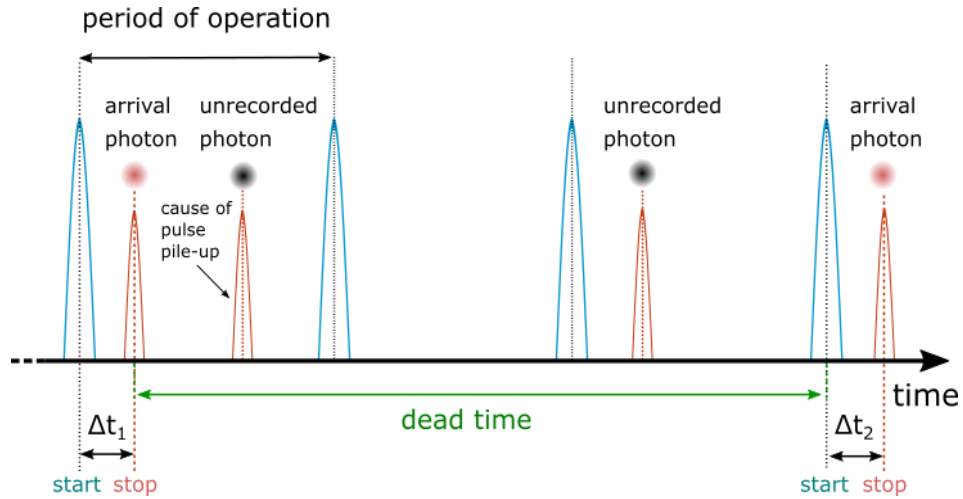
Figure 3.5: Photon arrivals go unrecorded if they arrive during the system dead time. The dead time starts when the first photon arrival is detected. A high probability of multiple photon arrivals in one period of operation can result in pulse pile-up.

The uncertainty associated with the Poisson distribution of single-photon measurements can be estimated as the standard deviation in the number of recorded counts, given by:

$$\sigma = \sqrt{N}.$$ (3.3)

This places a lower limit on the overall achievable depth resolution of the TCSPC system that is entirely dependent on the number of photons detected [3.10], where a higher number of counts provides a better resolution. This means that in order to improve system performance, the number of counts associated with target returns must be recorded at the

highest count rate possible, while still considering the aforementioned limitations to the overall count rate. In addition, the return signal must be much higher than the recorded background level. Background counts in single-photon measurements generally arise from two main sources: uncorrelated counts arising from ambient background illumination and dark counts originating from within the single-photon detector. This is discussed in more detail in Section 3 of this Chapter. The signal-to-background ratio (SBR) can be defined as:

$$SBR = \frac{n_p}{n_b},$$ (3.4)

where n_p is the number of photon returns in the bin containing the highest peak in the timing histogram, and n_b is the average number of background photons per bin. A good SBR can generally be achieved with the use of high optical power levels, outside the expected limits of pulse pile-up. It is also important to consider the signal-to-noise ratio (SNR). The SNR is given as:

$$SNR = \frac{n_p}{\sqrt{n_p + n_b}} = \sqrt{n_p}\sqrt{\frac{SBR}{SBR+1}}.$$ (3.5)

This indicates that the value of the actual SNR is close to ideal only as long as the SBR is very high. An example of two TCSPC timing histograms acquired using the same acquisition time, but with vastly different levels of return signal is shown in Figure 3.6. In Figure 3.6 (a), the SBR was 1.64 and the SNR was approximately 10.9. In Figure 3.6 (b), the SBR was much higher at 10.5, which resulted in a SNR of approximately 35.2.
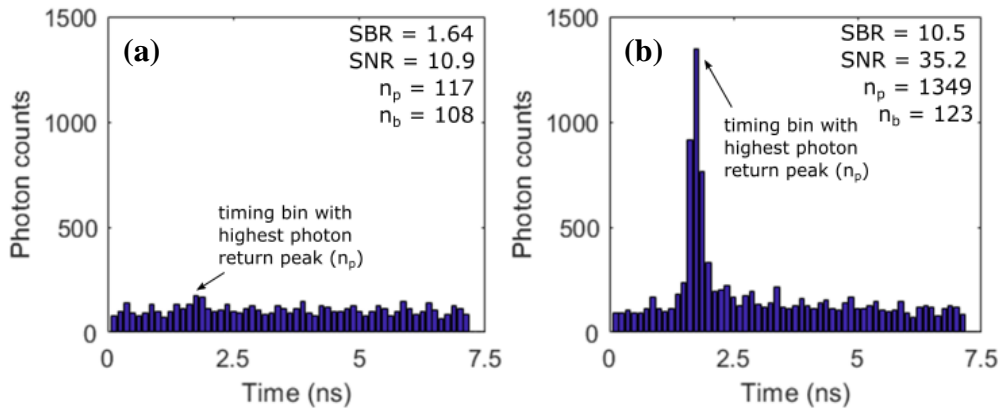
Figure 3.6: Example TCSPC timing histograms acquired using the same acquisition time, but (a) a relatively low SBR and (b) a relatively high SBR. In both cases the SNR is also shown.

3.2.2 TCSPC hardware

A block diagram depicting a conventional TCSPC data acquisition module is shown in Figure 3.7.
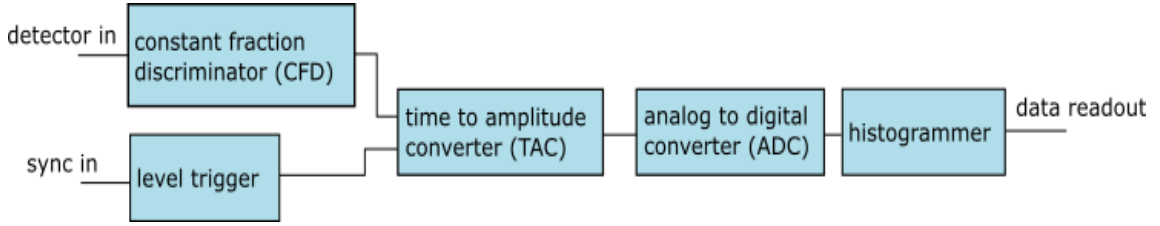
Figure 3.7: Block diagram of a conventional TCSPC system.

In a conventional TCSPC design, the start signal must meet a certain trigger level in order to be accepted by the data acquisition module. A level trigger within the module adapts the signal until the triggering criteria is met. The stop signal from the SPAD may vary in width and shape due to the stochastic nature of avalanche multiplication in the semiconducting material of the detector. Thus, if the TCSPC module set a constant voltage threshold, the arrival time would differ for each detector pulse, introducing additional jitter to the timing histogram. Therefore, to counteract this, a constant fraction discriminator (CFD) [3.20] is implemented, which effectively 'cleans up' the stop signal by creating a constant timing point for all detector pulses. The operating principle of a CFD is shown in Figure 3.8. Firstly, the detector signal is split into two identical signals. One signal is inverted and delayed by a timing factor, δ, as shown in Figure 3.8 (a), and the discriminator set at a constant factor, f, of the pulse amplitude V_a. The second signal is attenuated to a maximum level of fV_a (shown in Figure 3.8(b)). Finally, these two signals are multiplied, and the sum provides the zero-crossing signal, as shown in Figure 3.8 (c).
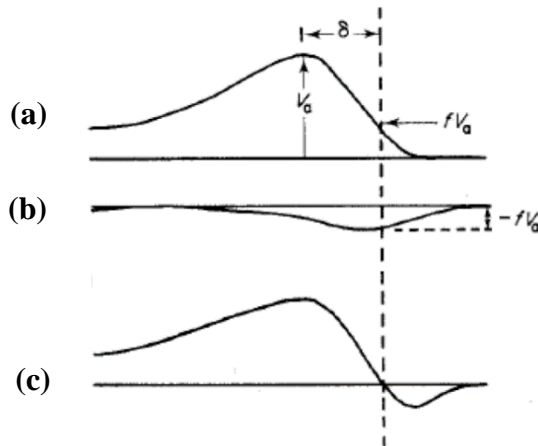
Figure 3.8: Operating principle of a CFD. From ref. *[3.20].*

The signals from the level trigger and the CFD are then passed to a time-to-amplitude convertor (TAC), which generates a voltage ramp. The operating principle of a TAC is shown in Figure 3.9. The recorded voltage is proportional to the elapsed start-stop time of the measurement, and hence, provides the photon ToF. This voltage is then passed to an analogue-to-digital convertor (ADC), which converts the signal amplitude to a digital value that assigns the detection event to a corresponding bin in the timing histogram.
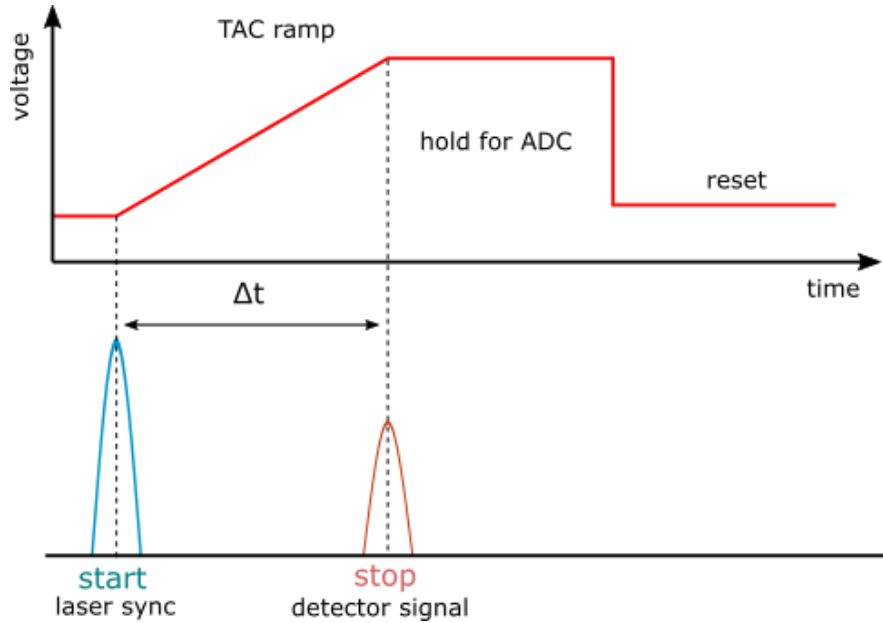
Figure 3.9: Operating principle of a time-to-amplitude convertor (TAC).

Although the combination of the TAC and the ADC provides high-resolution ToF measurements, there is a significant limitation to this design. When high repetition rate laser sources are used (as is typical in many TCSPC applications), the dead time caused by the TAC must be considered. The operating cycle of the TAC is initialised for each start signal, even if no detection event is then recorded. In addition, this operating cycle must be completed for each detection event before it can be reset. Moreover, if the dead time of the TAC is longer than the repetition rate of the source, the next start signal would be missed, resulting in many wasted laser pulses. This problem can be solved by operating in a reverse stop-start configuration, where the detector provides the start trigger signal and the next master clock pulse provides the stop trigger signal. This means that only registered detection events will initiate the TAC, reducing system dead time.

Many modern TCSPC data acquisition modules have moved away from the use of the TAC/ADC combination [3.17]. Instead, the implementation of a time-to-digital convertor (TDC) in both the start and the stop channel of the module can perform the same function. A block diagram of a modern TCSPC design is shown in Figure 3.10.
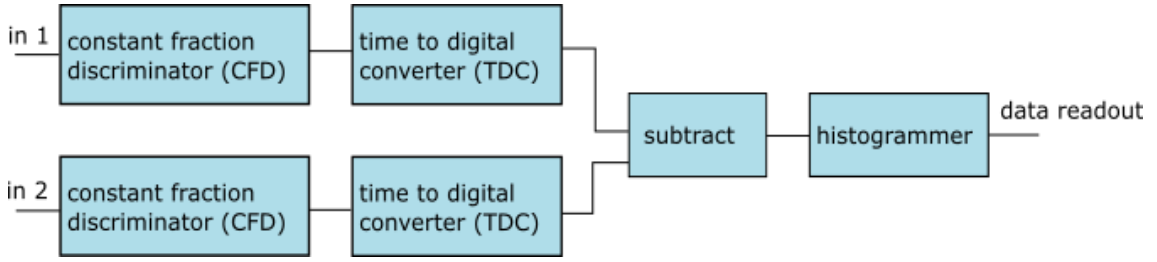
Figure 3.10: Block diagram of a modern TCSPC system.

A TDC measures the time difference between signals using logic gates, offering high-speed, timing resolution on the order of picoseconds. The most commonly used TDC is based on crystal clock digital counter technology. More details on this technology can be found in ref. [3.21] and ref. [3.22]. This configuration is used in many modern TCSPC modules as it permits the acquisition of Time-Tagged Time-Resolved (TTTR) data, which provides temporal information about detection events with respect to the master clock signal [3.14,3.17]. This will be discussed in more detail in Chapter 4 of this Thesis.

3.3 Single-photon detection in the short-wave infrared

In the most basic of terms, a single-photon detector produces one electrical output signal for each individual input photon. The ideal single-photon detector would do this with 100% efficiency, with negligible timing jitter and a very low dead time. However, in reality, the choice of detector typically involves a number of trade-offs between performance characteristics, which will depend on application requirements. Several characteristics will be briefly defined in this Section, and then discussed later in more detail for several types of single-photon detectors.

The most important characteristic of single-photon detectors is the single-photon detection efficiency (SPDE). The SPDE is a measure of the probability that a photon incident on the active area of the detector will generate an electrical pulse [3.19,3.23]. The overall SPDE is dependent on a number of factors including the coupling efficiency, the absorption efficiency and triggering probability (the probability of a carrier in the multiplication region triggering an avalanche) and other factors dependent on the detector geometry and microstructure.

The timing jitter is defined as the measure of the pulse-to-pulse variation between the input and output pulses of the detector [3.23]. For TCSPC applications, the timing jitter is typically determined by characterising the instrumental response function (IRF) of the detector by performing a highly accurate measurement under controlled conditions, using

a long integration time [3.24]. The IRF will contain timing jitter contributions from several sources including the illumination source and the TCSPC timing electronics, however, the main contribution typically comes from the detector itself. The timing jitter is typically defined using the full-width at half-maximum (FWHM) of the IRF.

Another useful metric for characterising and comparing single-photon detectors is the dark count rate (DCR). These so called 'dark counts' occur when the detector registers a count in the absence of illumination. Sources of dark counts include thermally generated carriers, carrier tunnelling, and afterpulsing effects caused by defects within the semiconducting material of the detector [3.25–3.28]. DCR is strongly dependent on the operating temperature of the device, and therefore, many detector technologies require additional cooling mechanisms - such as inbuilt thermo-electric cooling (TEC) systems.

Since single-photon detectors operate over a variety of wavelength ranges, it is useful to develop figures of merit for comparison. One such metric is the noise equivalent power (NEP), which is defined as the signal power required to attain a unity SNR within a one second integration time [3.19,3.29]. The NEP is given as:

$$NEP = \frac{hc}{\lambda} \frac{\sqrt{2DCR}}{SPDE}, \tag{3.6}$$

where h is Planck's constant, c is the speed of light in vacuum, and λ is the wavelength of the incident photon. A lower NEP corresponds to a higher detector sensitivity. Note that NEP contains no information about the detector jitter performance.

3.3.1 Photomultiplier tubes

One of the first widely available single-photon detectors was the photomultiplier tube (PMT), which has been used in a wide range of photon counting applications [3.30–3.32]. A schematic diagram of the operating principle of a PMT is shown in Figure 3.11.
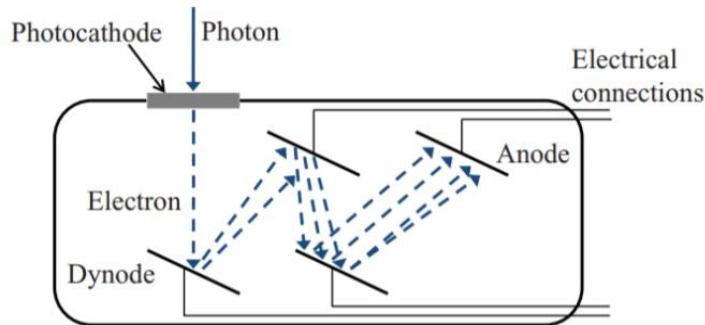
Figure 3.11: Schematic of a photomultiplier tube. From ref. [3.33].

In a PMT, a series of positively charged dynodes are arranged inside a vacuum tube between a photocathode and an anode. The photocathode absorbs incoming photons and then emits one electron per incident photon due to the photoelectric effect. These electrons are then accelerated towards the first dynode where, upon collision, further electrons are emitted. Each successive dynode in the PMT is charged with a higher positive potential than the last, resulting in a multiplication of the number of electron emissions. The multiplication factor, M, for $N_{dynodes}$ number of dynodes is given as:

$$M = \alpha^{N_{dynodes}}, \tag{3.7}$$

where α is the secondary electron coefficient. Finally, the electron cascade collides with an anode, which creates an easily detectable current pulse typically comprised of $> 10^6$ electrons [3.19]. While most PMTs operate in the visible region of the spectrum, Hamamatsu has manufactured devices containing indium gallium arsenide (InGaAs) photocathodes, which extend this range in to the SWIR band (i.e., up to 1700 nm) [3.34]. While these detectors offer high gain and a large active area, they typically have low SPDEs of up to 2% and DCRs of up to 10^5 counts per second when cooled to 200 K. Moreover, the timing jitter of PMTs is typically in the region of 1 ns [3.35], making these detectors unsuitable for some ToF ranging applications where high temporal resolution and high detection efficiency are required [3.10].

3.3.2 Superconducting nanowire single-photon detectors

Superconducting nanowire single-photon detectors (SNSPDs) are a relatively new class of single-photon detectors that offer very low timing jitter, low dark counts, and very wide spectral range. These detectors take advantage of the phenomenon of superconductivity where, at low temperatures, the resistance of some metals is zero below a temperature known as the critical temperature, T_c. The operating principle of SNSPDs [3.36–3.39] is shown in Figure 3.12.
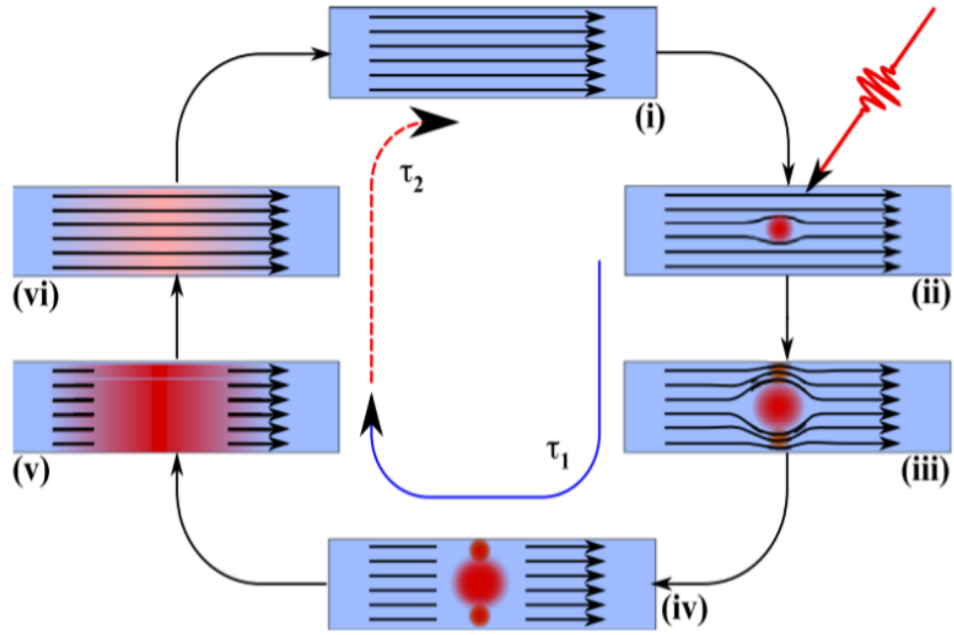
Figure 3.12: The operating principle of a SNSPD. The diagram is described in detail in the main text. The time constants τ_1 and τ_2 represent the rise time and the decay time of the voltage pulse. From ref. [3.36].

(i) First, the nanowire (kept at a temperature that is below the critical temperature of the metal) is biased just below the critical current. (ii) When the nanowire absorbs a photon with an energy much greater than the superconducting energy gap, a small resistive hotspot is created. (iii) The hotspot forces the current to flow around the resistive region. (iv) Due to the narrowness of the nanowires, the local current density around the hotspot increases until the superconducting critical current density is exceeded. This results in the formation of a resistive region across the width of the nanowire. (v) The resistive barrier expands along the nanowire until the current flow stops. Here the voltage pulse can be recorded. (vi) Finally, an external circuit is used to shunt the bias to allow the resistive region to subside. Once the nanowire is fully superconductive, the detector is once again biased to just below the critical current and is ready to absorb the next photon (i).

The nanowires must be very narrow so that the resistive region can form across the width of the wire and prevent the current from flowing. However, this narrowness represents a very small area for photon absorption. Therefore, to maximise the detection efficiency, many SNSPDS are designed so that the nanowires are arranged in a meander pattern. A scanning electron microscope (SEM) image of an SNSPD and a schematic of this meander design is shown in Figure 3.13 (a) and Figure 3.13 (b), respectively.

(a) (b)
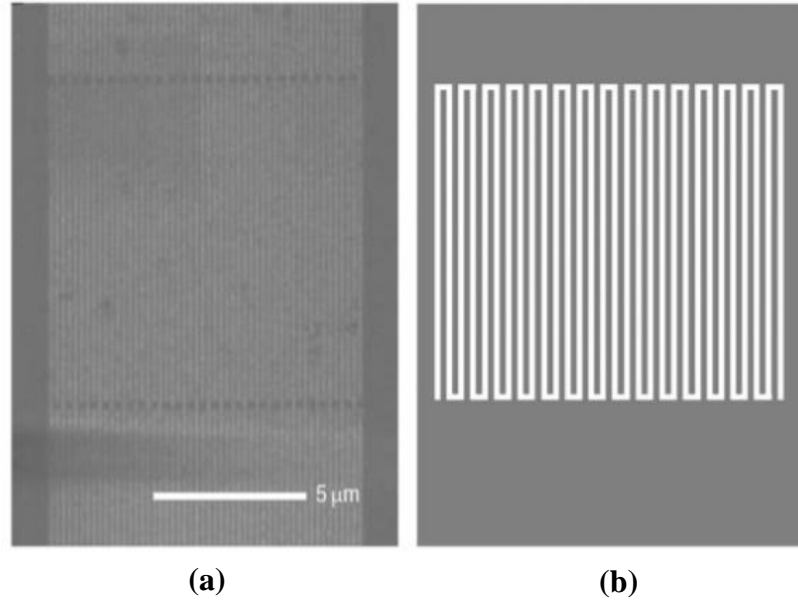
Figure 3.13: (a) An SEM image of an SNSPD with 100 nm wires at a 100 nm pitch arranged in a 10 × 10 µm meander line design. Taken from ref. [3.40]. (b) A schematic representation of a meander design. From ref. [3.19].

The first niobium nitride (NbN) SNSPD was demonstrated in 2001 by Gol'tsman *et al.* [3.41]. This detector was sensitive in both the visible and SWIR wavelength regions. However, this device was not a meander line design, and therefore suffered from a low detection efficiency due to a poor fill factor. Although many early SNSPDs demonstrated low SPDEs of less than 3% at a wavelength of 1550 nm [3.42–3.44], they provided very low timing jitters. For example, in 2002, Verevkin *et al.* reported a 10 × 10 µm meander SNSPD with a timing jitter of 68 ps [3.43]. Later in 2005, Pearlman *et al.* reported a timing jitter of 18 ps using a similar structure [3.44].

More recently, Korzh *et al.* reported a device with a timing jitter as low as 4.6 ps at a wavelength of 1550 nm and 2.7 ps at a wavelength of 400 nm [3.45]. This detector is a short nanowire device optimised to achieve record low jitter. Unfortunately, the authors did not report the SPDE for these detectors, however, the active area is low and so efficiency is expected to be poor. In recent years, SNSPDS with very high SPDEs have also been reported. For example, in 2013 Marsili *et al.* reported a tungsten silicide (WSi) meander SNSPD in an optical cavity that demonstrated an SPDE greater than 90% and a timing jitter of 150 ps at a wavelength of 1550 nm [3.46]. In 2019, Taylor *et al.* reported a niobium titanium nitride (NbTiN) SNSPD that extended detection sensitivity to 2.3 µm [3.47]. These devices were reported to have relatively large timing jitter of 280 ps and a low SPDE of 0.1% at a wavelength of 2.3 µm. However, the development of SNSPDs

that operate in this longer wavelength region is of great interest due to advantages over shorter wavelength bands, such as lower solar background and less atmospheric absorption [3.48].

While SNSPD detectors typically demonstrate better performance than alternative semiconductor-based single-photon detectors in terms of both timing jitter and SPDE, they have a distinct disadvantage in that they require bulky cryogenic systems to achieve operating temperatures below 3 K [3.49]. This can make them expensive and impractical for applications that require compact and low-power configurations, such as deployment on mobile platforms.

3.3.3 Single-photon avalanche diode detectors

The past few decades have seen a rise in the use of semiconductor-based detectors, such as avalanche photodiodes (APDs). These devices exploit the impact ionisation properties of semiconductor materials to convert incident photons into a measurable electrical signal. This Section will briefly introduce the principles of operation of these detectors and discuss how they can be used in applications that require single-photon sensitivity.

3.3.3.1 P-N and P-I-N junctions

In a semiconducting material, an electron is excited from the valence band to the conduction band when a photon with an energy equal to or higher than the band-gap is absorbed, meaning that each material has specific wavelength detection range. Examples of various semiconducting materials along with their band-gap energies and equivalent cut-off wavelengths at a temperature of 300 K are listed in Table 3.1 [3.50]. This results in a 'hole' in the valence band that acts as a positive charge [3.51]. In an intrinsic semiconductor, there is an equal ratio of electrons to holes, and so its Fermi level lies in the middle of the band-gap. An intrinsic semiconductor material becomes an 'n-type' or 'p-type' extrinsic semiconductor when it is doped with donor or acceptor impurities, respectively. In an n-type semiconductor, there is a greater concentration of electrons, and so the Fermi level is shifted closer to the valence band of the material; in a p-type semiconductor, there is a greater concentration of holes, shifting the Fermi level towards the conduction band.

Table 3.1: Examples of semiconducting materials, along with their respective band-gap energy and equivalent cut-off wavelengths at a temperature of 300 K [3.50].

Symbol	Material name	Band-gap energy at 300 K	Equivalent cut-off wavelength
Si	Silicon	1.12 eV	~1107 nm
Ge	Germanium	0.66 eV	~1879 nm
GeAs	Gallium Arsenide	1.42 eV	~873 nm
InAs	Indium Arsenide	0.35 eV	~3.5 μm
InP	Indium Phosphide	1.34 eV	~925 nm
InSb	Indium Antimonide	0.17 eV	~7.3 μm
HgCdTe	Mercury cadmium telluride	0 – 1.5 eV	~827 nm
InGaAs	Indium Gallium Arsenide	0.74 eV	~1675 nm

The most basic detectors use a p-n junction, which is an interface between an 'n-type' and 'p-type' semiconductor. Under equilibrium conditions (i.e., when with no external voltage is applied), the charge carriers from each side of the p-n junction begin to diffuse across the interface. As a result, the dispersion of the negative carriers creates positive ion donors in the n-type material and the dispersion of the positive carriers creates negative ion acceptors in the p-type material. Thus, the interface loses its neutrality and gives rise to an electric field as shown in Figure 3.14 [3.52].
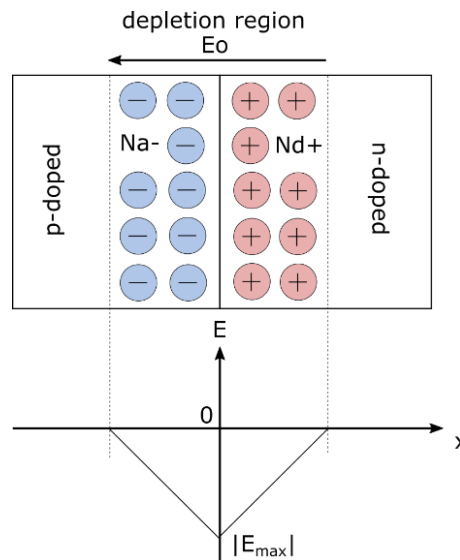
Figure 3.14: P-n junction in equilibrium conditions. In equilibrium, the charge carriers diffuse across the depletion region creating a charged region, which gives rise to an electric field.

The region where the electric field is formed is known as the depletion region. It has an in-built potential (V_{bi}), which is given as:

$$V_{bi} = \frac{k_b T}{q} \ln(\frac{N_a N_d}{n_i^2}),$$

(3.8)

where k_b is Boltzmann's constant, T is temperature, q is the electron charge, n_i is the intrinsic carrier concentration, and N_a and N_d are donor and acceptor concentrations, respectively. In equilibrium, the drift current created by the electric field will be negated due to the components of the positive and negative carriers cancelling each other out. However, if an external voltage is applied to the junction, the built in potential can be lowered (forward bias) or increased (reverse bias), as shown in Figure 3.15 [3.53]. In forward bias, a positive voltage is applied to the device, resulting in a narrowing of the depletion region. This allows carriers to flow into the junction region, where free charge carriers can recombine, resulting in a current flow. In reverse bias, a negative voltage is applied to the p-type side of the diode, attracting the positive carriers and pulling them away from the depletion region, and likewise the positive carriers in the n-type material move towards the negative terminal. This results in a widening of the depletion region, increasing the voltage barrier and restricting the flow of charge carriers, prohibiting the current flow across the p-n junction. An I-V characteristic curve for a p-n photodiode is shown in Figure 3.15 (c). When forward biased, the current will increase as a larger external voltage is applied. When reversed biased only leakage current flows until a high enough voltage, known as the breakdown voltage, V_b, is applied. This will be discussed in more detail later in this Section.
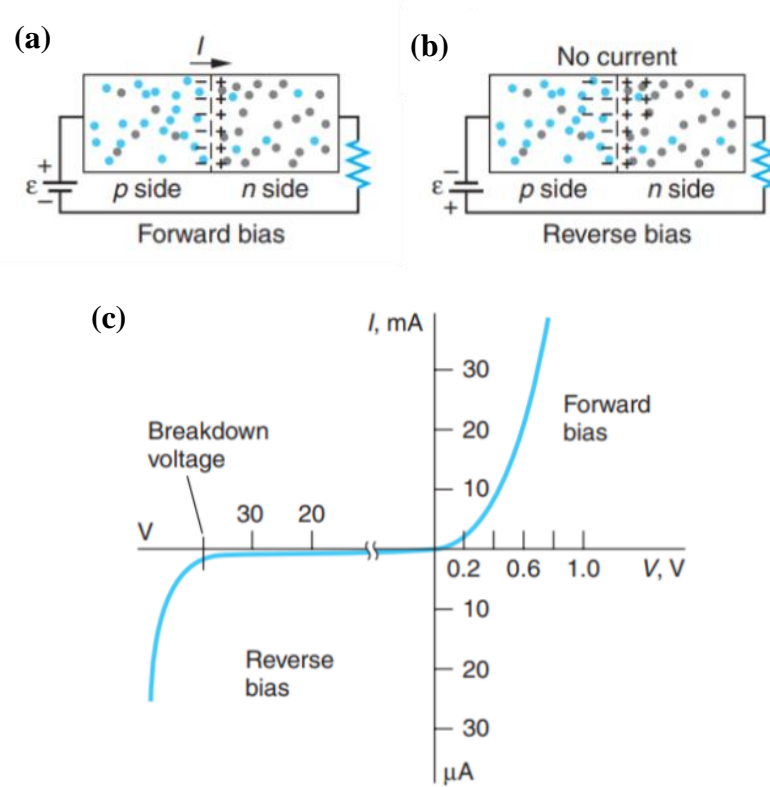
Figure 3.15: A p-n junction diode operated in forward bias (a) and in reverse bias (b). In forward bias, charge carriers diffuse across the depletion region, resulting in a current. In reverse bias, no current flows as charge carriers are prohibited from moving. (c) An I-V characteristic curve for a photodiode. From ref. [3.53].

While p-n junction technology is quite effective in forming a basic photodiode that is capable of converting light into current, they are not without their disadvantages. The current flow (known as the photocurrent) in a p-n junction is dependent on the creation of electron-hole pairs caused by the absorption of a photon in the depletion region, which is relatively narrow. If a photon is absorbed outside the depletion region of the p-n junction, this diffusion process can take a relatively long time, slowing the operation of the device. Another drawback of p-n junctions is that the responsivity of the junction can be dependent on carrier diffusion lengths. In order for a p-n junction to function effectively, carriers must reach the high field region of the junction. However, if the carrier diffusion length is large, electron-hole pairs may recombine outside this region, reducing the detection efficiency. Therefore, it is desirable to have a wide depletion region so that the probability of photon absorption in this region is increased.

This can be achieved through use of a p-i-n photodiode configuration. In this configuration, an intrinsic layer of semiconducting material is grown between the n-type

and p-type interface of the p-n junction. When operated in reverse bias mode, the intrinsic region of a p-i-n photodiode is depleted due to its low dopant level and high resistivity [3.54]. This creates a wide depletion region with a high electric field, resulting in significantly more electron-hole pairs contributing to the photocurrent. A reverse bias p-n photodiode configuration and a p-i-n photodiode configuration are shown in Figure 3.16.
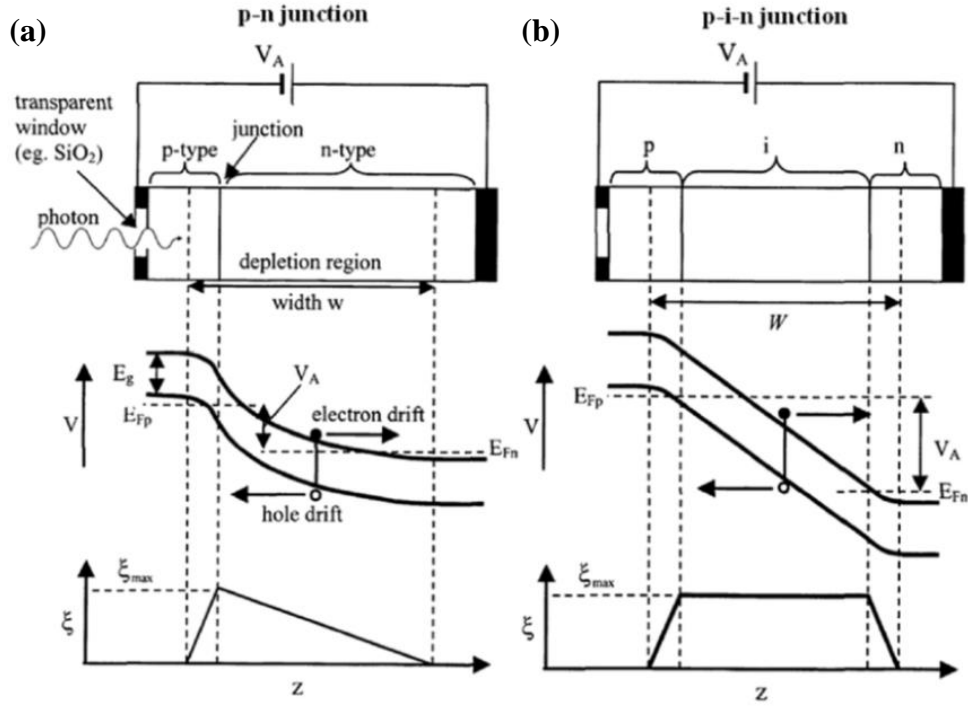
Figure 3.16: Diagrams and electric field plots of (a) a reversed biased p-n junction and (b) a reversed biased p-i-n junction. From ref. [3.55].

Therefore, p-i-n photodiodes provide increased detection efficiency and a higher carrier mobility, which allows for faster carrier transport.

3.3.3.2 Avalanche photodiodes

Avalanche photodiode (APD) detectors exploit impact ionisation effects in semiconducting materials to achieve a high internal gain, which can be in the region of 1000s [3.56,3.57]. The phenomenon of impact ionisation occurs when the electric field in the depletion region becomes so high that free electrons can gain sufficient kinetic energy to knock an electron out of its bound state in the lattice and promote it to the conduction band. This may also happen for the positively charge holes. These secondary charge carriers are then accelerated by the electric field and may result in further impact ionisations. Therefore, this process is strongly dependent on the strength of the electric field, with a higher field strength resulting in an increase in the average number of

electron-hole pairs. The process of impact ionisation is shown schematically in Figure 3.17.
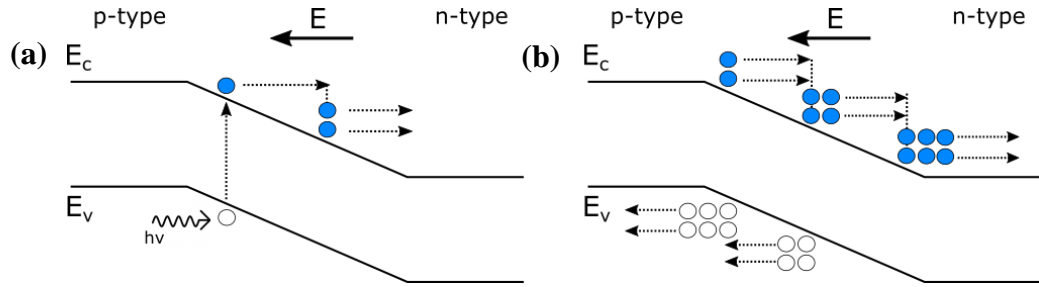
Figure 3.17: (a) When a photon with energy equal to or greater than the bandgap of the material is absorbed in the depletion region, an electron is promoted from the valence band to the conduction band, leaving a positively charged hole in the valence band. (b) If the electric field in the junction is very high, the charge carriers can gain sufficient kinetic energy to initiate the impact ionisation process. The initial electron (in this case) and resulting secondary electrons and holes can then undergo further impact ionisation events, resulting in an avalanche effect. Electrons are shown in blue and holes in white.

APDs are typically operated just below their breakdown voltage, V_{bi}, where the current flow of a reverse biased junction increases dramatically (see Figure 3.15 (c)) as the number of charge carriers rapidly grows due to the multiplication process. The multiplication factor of an APD, M, can be expressed as [3.58]:

$$M = \frac{I_{photo} - I_{dark}}{I_{primary,photo} - I_{primary,dark}}, \tag{3.9}$$

where I_{dark} and I_{photo} are the dark current and the multiplied photocurrent respectively, when impact ionisation is observed. $I_{primary,\,dark}$ and $I_{primary,\,photo}$ are the dark current and the photocurrent before the multiplication process has started.

This mode of operation is called 'linear-mode', where the photocurrent is linearly proportional to the incident light level. Whilst the internal amplification of signal can mean that APDs have an advantage over p-i-n photodiodes for detecting weak optical signals, they do not have single-photon sensitivity when operated in this mode.

3.3.3.3 Single-photon avalanche diode detectors

APDs that are biased above their breakdown voltage, V_b, (as shown in Figure 3.18) are known as Geiger-mode APDs or single-photon avalanche diode (SPAD) detectors [3.59]. While APDs operated in Geiger-mode were first observed at the Shockley laboratory in the 1960s [3.60], the first custom-made device was demonstrated by Cova *et al.* in 1981 [3.61].
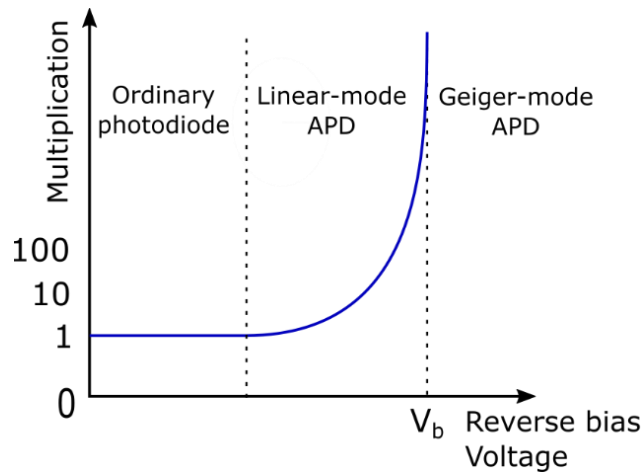
Figure 3.18: Operating modes of photodiodes. Ordinary photodiodes do not exhibit impact ionisation and so have a gain of unity. Linear-mode APDs do exhibit impact ionisation and therefore have an internal amplification proportional to the detected optical signal. In a Geiger-mode APD, a single charge carrier is capable of initiating a self-sustaining avalanche current, resulting in infinite gain.

When an APD is biased above the breakdown voltage, a single charge carrier can initiate a self-sustaining avalanche process that is readily detectable, resulting in a device with single-photon sensitivity. As the avalanche current is self-sustaining, current will flow through the junction until an external stimulus quenches it. The process of quenching reduces the bias voltage back down to below breakdown level until the original operating voltage is restored [3.59,3.62,3.63]. One quenching method is the use of a resistor in series with the SPAD – this is known as passive quenching. After the onset of the avalanche current, a higher proportion of the detector bias will be dropped across the quenching resistor as the SPAD moves to a conducting mode. This will mean that the SPAD bias will reduce below breakdown, quenching the avalanche current. During the quenching process, the detector is insensitive and unable to register further detection events for a period of time known as detector dead time. For detectors that use passive quenching circuits, dead times are typically of the order of 1 µs [3.59]. These times can

be reduced to the order of a few nanoseconds through the use of active quenching circuits [3.61]. Long dead times result in significant loss of detection events and therefore are a significant disadvantage [3.24].

In a SPAD detector, the SPDE increases with increasing bias voltage above the breakdown voltage level, primarily due to an increase in avalanche triggering probability. However, an increase in the bias voltage also results in an increase in the DCR of the detector. As mentioned previously in Section 3, the DCR gives a measure of the internal noise of a detector and can place limitations on the performance of the device. In a SPAD, three mechanisms contribute the overall DCR: thermal noise, charge carriers generated by tunnelling, and afterpulsing effects [3.25,3.26]. Charge carriers that are thermally generated in the active volume of the detector can cause a self-sustaining avalanche, even in the absence of an incident photon. However, the occurrence of these carriers can be significantly reduced by lowering the operating temperature of the device by using an in-built cooling device such as a TEC [3.64]. The probability of charge carriers generated by tunnelling processes is dependent on the strength of the electric field across the junction, with an increase in electric field strength resulting in an increase in charge carriers. Therefore, this places a lower limit on the DCR as a high field strength is imperative to the initiation of a self-sustaining avalanche, and hence, to the operation of the SPAD itself. Afterpulsing effects can greatly contribute to the overall DCR of a SPAD detector. Afterpulsing is caused by local defects with deep energy levels between the mid-gap and band-edge in the depletion layer of the semiconducting material [3.65–3.67]. Charge carriers can be trapped by these states, and then subsequently released, triggering spurious avalanches. In order to counteract afterpulsing effects, an electronic gating circuit can be implemented in the SPAD detector. In this operating mode, a hold-off time can be used to deactivate the detector for a predetermined duration after a recorded event, in order to allow the traps to empty without triggering further avalanches. While a long hold-off time can allow traps to depopulate, it places a limit on the achievable maximum count rate of the system, as the detector is active only for a short time interval known as the gate width. Hold-off times in InGaAs/InP SPADs are typically in the region of microseconds while gate widths are typically in the region of nanoseconds. More details on gated-mode SPADs are given in ref. [3.68].

3.3.3.4 InGaAs/InP SPAD detectors

While silicon (Si) based SPADs offer very high multiplication at room temperatures, they are only sensitive in the wavelength range of $400 - 1100$ nm [3.69]. Currently,

InGaAs/InP based SPADs are the most promising candidate for single-photon counting at SWIR wavelengths [3.27,3.70]. These detectors operate at near room temperatures over a wavelength range of approximately 1000 – 1700 nm, making them an ideal candidate for many applications where thermo-electric cooling is required. Figure 3.19 shows a cross-section through a planar geometry InGaAs/InP SPAD for $\lambda = 1550$ nm photon detection [3.71].
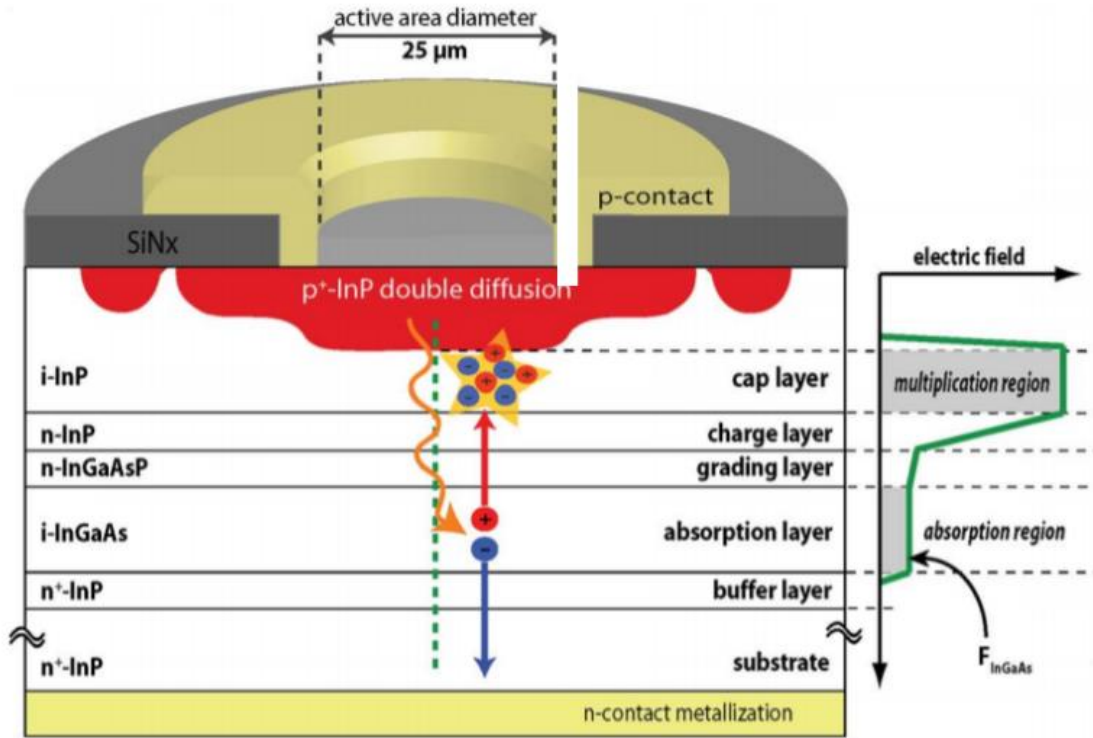
Figure 3.19: Schematic of a typical InGaAs/InP SPAD structure. The electric field along the centre of the active area is also shown. From ref. [3.71].

In this structure, photons are absorbed in a narrow band-gap InGaAs layer causing holes to drift into the higher field indium phosphide (InP) multiplication layer. InGaAs and InP have band-gap energies of 0.75 eV and 1.35 eV at a temperature of 300 K, respectively [3.51]. This mismatch in band-gap energies results in a valence band discontinuity, that creates a barrier for holes to drift into the multiplication region. This can lead to a reduced detection efficiency as hole recombination can then occur at the interface instead of the multiplication region. This mismatch can be addressed by the growth of an indium gallium arsenide phosphide (InGaAsP) layer between the two materials as it has an intermediate band-gap energy that smooths the gradient in the valence band energies [3.72]. This allows the charge carriers to reach the multiplication region. Figure 3.20 shows a diagram of the energy band structure of an InGaAs/InP SPAD detector.
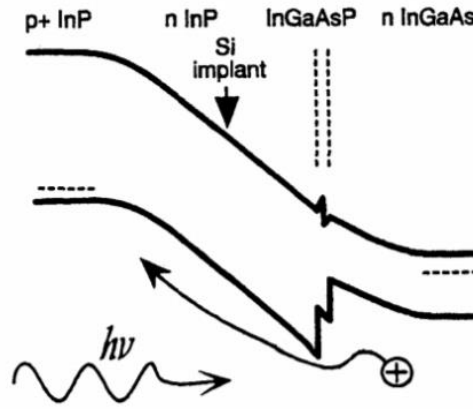
Figure 3.20: Energy band structure of an InGaAs/InP SPAD detector From ref. [3.73].

Commercial InGaAs/InP APDs used as SPADs were first demonstrated by Zappa *et al.* in 1994 [3.73]. These detectors had a diameter of 50 µm and were operated at an excess bias of 6 V and a temperature of 150 K. A minimum NEP of 1×10^{-14} WHz$^{-1/2}$, a maximum SPDE of 1%, and a timing jitter of approximately 1 ns using an illumination wavelength of 1310 nm was reported. In addition, during this investigation, an exponential dependence of the DCR with the operating temperature of the detector was found. In 2000, Hiskett *et al.* reported a NEP of 4×10^{-17} WHz$^{-1/2}$ using an 80 µm diameter commercially available Fujitsu InGaAs/InP SPAD that was cryogenically cooled to 77 K and biased at 3 V. The maximum SPDE for this device was found to be approximately 16% at a temperature of 140 K. The first custom-design SPADs were demonstrated by Pellegrini *et al.* in 2006 [3.74]. These devices had a SPDE of 10%, a DCR of 2×10^5 Hz, and a NEP of 6×10^{-16} WHz$^{-1/2}$ at 200 K. Shortly after this, InGaAs/InP SPADs very quickly became a popular candidate technology with many groups developing high performance detectors [3.75–3.77]. For example, in 2007 Itzler *et al.* demonstrated a detector with a maximum SPDE of 45% at a wavelength of 1550 nm, a minimum timing jitter of 30 ps, and a minimum DCR of 3×10^3 counts per second [3.77].

Although these InGaAs/InP SPAD detectors demonstrated low timing jitter, high SPDE, and near room temperature operation, the deleterious effects of afterpulsing (as discussed previously in Section 3.3.3) was still a major drawback. Therefore, a significant amount of research was conducted to find a way to limit these effects. One proposed solution is an electrically gated-mode configuration, as discussed in Section 3.3.3. In 2012, Tosi *et al.* presented a gated-mode InGaAs/InP SPAD detector, which operated at a temperature of 225 K at high count rates of up to 1 MHz [3.77]. This detector had a low DCR below

100×10^3 counts per second, a timing jitter of 90 ps, and a SPDE of 25% at the illumination wavelength of 1550 nm and a 5 V excess bias. Later in 2014, Tosi *et al.* reported improved devices, which exhibited a reduced DCR of 1×10^3 counts per second, a timing jitter of 90 ps, and a higher SPDE of 30% at the same illumination wavelength and excess bias [3.78]. This improvement was made by operating the device at a lower count rate of 10 kHz.

Many applications, such as ToF measurements, can benefit greatly from arrayed SPAD detectors, as they allow for rapid data acquisition using high average optical power level sources [3.80,3.81]. In an arrayed system, every pixel has an individual SPAD detector, each with their own timing electronics (typically a TAC is used in these systems) that provide the start trigger signal for timing measurements. A global master clock provides the stop trigger signal for the whole array. In recent years, Geiger-mode camera systems incorporating InGaAs/InP SPAD arrays flip-chip bonded to Si complementary metal-oxide-semiconductor (CMOS) integrated readout circuits (as shown in Figure 3.21) have been developed.

(a) 32 x 32 focal plane array

(b) sensor chip assembly

(c) SWIR LiDAR camera
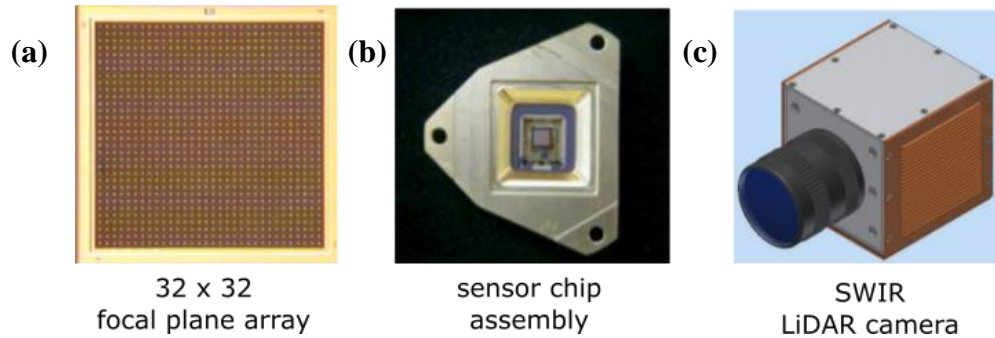
Figure 3.21: A 32 × 32 SPAD detector array camera. (a) A photograph of the 32 × 32 focal plane array. (b) This array is then bonded on to a Si CMOS readout circuit for the sensor chip assembly. (c) The sensor chip assembly is then integrated into a camera package. Adapted from ref. [3.81].

The camera assembly demonstrated in 2010 by Yuan *et al.* (shown in Figure 3.21) was optimised for applications requiring a wavelength of 1060 nm, and incorporates a 32 × 32 format SPAD array [3.81]. This camera is capable of operating at frame rates of up to 30 kHz. At the illumination wavelength of 1060 nm, the camera was reported to have an SPDE of 40%, a timing jitter of 0.5 ns, and a DCR of 20 kHz, and an NEP of 6.6×10^{-17} WHz$^{-1/2}$ when operated at a temperature of 240 K and an excess bias of 4 V. In 2012, Entwistle *et al.* demonstrated a 32 × 32 format SPAD array designed to operate in the wavelength range of $920 - 1620$ nm (optimised for $\lambda = 1550$ nm) [3.80]. This

detector provides a minimum timing jitter of 250 ps and is capable of operating at frame rates up to 186 kHz. A mean SPDE of approximately 18%, typical DCR of 20 kHz, and a NEP of 1.16×10^{-16} WHz$^{-1/2}$ using a wavelength of 1550 nm were reported for this detector. A 128×32 format version of this camera is also available.

One of the main drawbacks of SPAD arrays is optical coupling, otherwise known as optical crosstalk. When biased above the breakdown voltage, 'hot' carriers in one SPAD may lead to intense emission of secondary photons, which may escape from the chip [3.82]. While some of these photons are reabsorbed back into the pixel of origin, others are absorbed by a neighbouring pixel. If this reabsorption occurs in the active area of the neighbouring pixel, it can trigger a spurious avalanche process, resulting in an increase in the DCR of that pixel. The crosstalk probability in SPADs increases with increasing excess voltage (see Figure 3.22), due to a higher average number of free charge carriers.
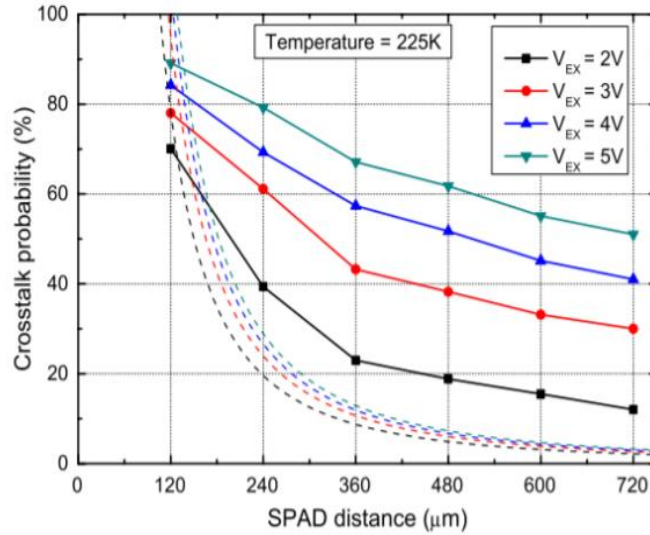
Figure 3.22: Optical crosstalk between SPAD detectors occurs when the avalanche current in one pixel triggers an avalanche in surrounding pixels, due to escaped photon emissions. Example of the crosstalk probability for different excess biases in an InGaAs/InP SPAD detector as a function of the spacing between pixels [3.83].

Crosstalk probability can be reduced by increasing the spacing between pixels, at the expense of reduced array fill-factor, where the fill-factor is the ratio of the active area of the detector to the pixel area [3.65,3.83]. As the pixel spacing is increased, fewer escaped photons reach the active area of the neighbouring pixels. Figure 3.22 shows a plot of crosstalk probability as a function of the spacing between two InGaAs/InP SPAD detectors [3.83]. Another method of reducing crosstalk probability is to mill trenches in

the spacing between pixels. Figure 3.23 (a) shows an SEM image of a trench, which was milled between two SPAD detectors in an array using a focused ion beam [3.83]. The active area of the SPAD was 25 µm and the trench was milled to be 40 µm in length and 5 µm in width. The milled depth was 6 µm so that it travelled through to the InGaAs layer of the device structure, creating a barrier between the pixels. This process can be further enhanced by coating the trench in a thin layer of metal, which acts as a mirror that shields neighbouring pixels from photons travelling along a direct path between the two pixels. In 2016, Tosi *et al.* reported that crosstalk probability decreased from 88% to 47% for empty trenches and to 37% for trenches filled with platinum for an InGaAs/InP device operated at a 3 V excess bias, as shown in Figure 3.23 (b) [3.79]. The initial crosstalk event in a pixel is known as first order crosstalk. Each instance of first order crosstalk has a probability of initiating further events known as second order (or higher) crosstalk. The crosstalk probability that includes all secondary crosstalk events is known as the cumulative crosstalk. As an example, the total cumulative crosstalk probability of the Princeton Lightwave 32×32 camera used in Chapters 6 and 7 is typically 35% (calculated from a 9×9 pixel neighbourhood) at an SPDE of 18%, using an illumination wavelength of 1550 nm, as stated by the manufacturer.
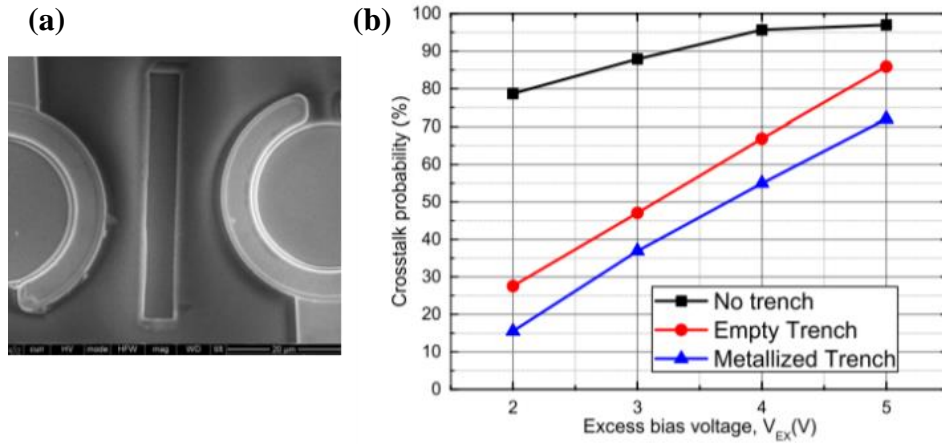
Figure 3.23: (a) An SEM image of a trench, which has been milled between two SPADs. (b) A plot of the crosstalk probability as a function of the excess voltage for: no trench, an empty trench, and a trench that has been metallised with platinum. Both figures were taken from ref. [3.83].

Currently, InGaAs/InP SPAD detectors represent the state-of-the-art for single-photon detection in the SWIR wavelength region, due to their low timing jitter and compatibility with compact Peltier cooling systems. The work presented in Chapters 4-7 of this Thesis was performed using both single-pixel and arrayed InGaAs/InP detectors. However, even

when operated in an electronically gated configuration, the SPDE of commercial InGaAs/InP devices is limited to approximately 45% due to their relatively high afterpulsing when compared with other SPAD technologies, such as Si-based SPADs. These detectors are typically operated at near-room temperatures, which greatly reduces afterpulsing, allowing for an increased SPDE.

3.3.3.5 Ge-on-Si SPAD detectors

Due to the good absorption properties exhibited by germanium (Ge) at room temperatures for wavelengths up to 1600 nm and the excellent multiplication properties of Si [3.85], Ge-on-Si SPAD detectors have become potential candidates for SWIR single-photon detection. These devices have the potential for reduced afterpulsing and increased single-photon sensitivity over InGaAs/InP SPADs as they use silicon as a multiplication layer and have potential to be operated at near-room temperatures. An example cross-section of a Ge-on-Si SPAD is shown in Figure 3.24 (a) [3.86]. In this structure, photons are absorbed in the Ge layer, creating an electron-hole pair. The negative charge carriers are then accelerated towards the Ge/Si interface, before entering the high charge Si multiplication layer. Here, the process of impact ionisation takes place and, if the electric field is above the avalanche breakdown level, a self-sustaining avalanche is triggered, resulting in a measurable photocurrent.

(a) **(b)**
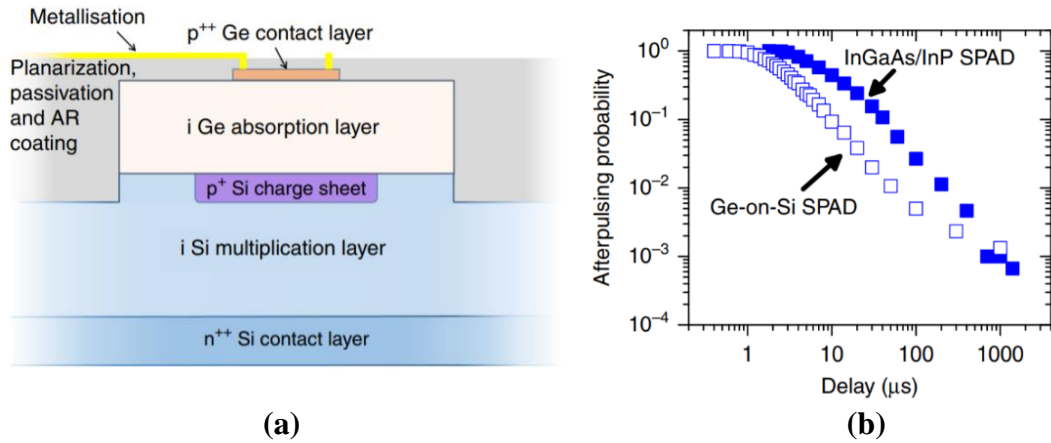
Figure 3.24: (a) A cross-section of a Ge-on-Si SPAD. (b) Plot of the afterpulsing probability as a function of gate delay time for both a Ge-on-Si SPAD and an InGaAs/InP SPAD. Both figures were taken from ref. [3.86].

In 2002, Loudon *et al.* demonstrated early versions of Ge-on-Si SPADs [3.87]. At an illumination wavelength of 1210 nm these devices were reported to have a maximum SPDE of approximately 0.002%, a timing jitter of 300 ps, and a NEP of 5×10^{-12} WHz$^{-1/2}$

using an operating temperature of 200 K and an excess bias of 1 V [3.87]. Later, in 2013, Warburton *et al.* demonstrated devices that incorporated a thicker layer of Ge to allow for a higher probability of photon absorption [3.88]. These detectors were reported to have an improved SPDE of 4%, a timing jitter of 300 ps, and a NEP of 1×10^{-14} WHz$^{-1/2}$ using an operating temperature of 100 K and an illumination wavelength of 1310 nm. This study also reported measurements made at an illumination wavelength of 1550 nm. However, when cooled to 125 K, the band-gap of Ge increases to 0.84 eV, meaning that $\lambda = 1550$ nm photons ($E_{photon} \approx 0.80$ eV) lie just outside the absorption edge [3.85]. Thus, the authors reported a reduced SPDE of approximately 0.15%, a NEP of 5×10^{-12} WHz$^{-1/2}$, and an increased timing jitter of 420 ps. More recently, in 2019, Vines *et al.* demonstrated a new generation of planar Ge-on-Si SPAD detectors with much improved SPDE and NEP, when compared to previous devices [3.86]. The authors reported an SPDE of 38% at an operating temperature of 125 K at an illumination wavelength of 1310 nm. The timing jitter and NEP were measured at 78 K and reported as 310 ps and 1.9×10^{-16} WHz$^{-1/2}$, respectively. This represented a 50-fold improvement in NEP compared to previously reported Ge-on-Si SPADs. The authors also investigated the afterpulsing probability of these detectors when compared to state-of-the-art InGaAs/InP detectors. A plot of the afterpulsing probability as a function of gate delay time for both a Ge-on-Si SPAD and an InGaAs/InP SPAD is shown in Figure 3.24 (b) [3.86]. The afterpulsing probability was found to be much lower in the Ge-on-Si detector than in the InGaAs/InP detector. Moreover, a 50 to 75% reduction in detector dead time was reported compared to commercial InGaAs/InP SPADs under the same operating conditions. These results point to Ge-on-Si detectors being capable of SWIR operation at, or near, room temperature, with low DCR, low afterpulsing, and high count rate operation. An increased operating temperature will also allow these detectors to operate with high efficiency at a wavelength of 1550 nm, making them good candidates for ToF ranging applications, such as those presented in this Thesis.

3.3.3.6 Frequency up-conversion

An emerging technology in infrared detection is the use of frequency up-conversion. This technique aims to convert SWIR wavelength photons to shorter wavelength photons that can be detected by commercially available visible region single-photon detectors, which typically have improved performance over infrared detectors in terms of DCR and timing jitter [3.49,3.89]. This is typically achieved through sum-frequency generation in nonlinear optical crystals, where a weak signal with frequency ω_{in} is combined with a

strong pump signal with frequency ω_{pump} to give an output signal with a summation frequency, ω_{out}, given as:

$$\omega_{out} = \omega_{in} + \omega_{pump}. \tag{3.10}$$

Filters can then be used to allow transmission of the appropriate wavelength to the detector. This conversion can be performed with a very high efficiency. For example, Albota *et al.* demonstrate that 1550 nm photons can be converted to 630 nm photons with approximately 90% efficiency using a 1064 nm pump signal [3.90]. Frequency up-conversion has been demonstrated in quantum key distribution experiments using both thick-junction and shallow-junction Si SPAD detectors [3.91, 3.92]. In 2005, Takesue *et al.* demonstrated an up-conversion scheme using a thick-junction Si SPAD with a SPDE of 46%, a timing jitter of 400 ps, and a DCR of 800 kHz for 1550 nm wavelength photons [3.91]. Later in 2006, Thew *et al.* demonstrated a set-up with implemented a shallow-junction Si SPAD with an improved timing jitter of 40 ps and a DCR of 20 kHz but a reduced SPDE of 2% for 1550 nm photons [3.92]. However, there are drawbacks of this technique which include difficulty in stabilizing the nonlinear crystal required for up-conversion and potential output coupling losses from the optical waveguides that are used to concentrate the pump signal [3.49].

3.4 Conclusions

This Chapter has given a brief review of the TCSPC technique, and explained how it can be used in applications that require single-photon sensitivity, such as fluorescence lifetime imaging [3.2–3.4], quantum communications [3.5,3.6], and laser-based distance measurements [3.7–3.10]. The high sensitivity and picosecond temporal resolution provided by the TCSPC technique make it the ideal candidate technology for ToF measurements of long-range targets - particularly in the sparse photon regime where return optical signals are very low. The use of this technique for the three-dimensional profiling of targets in degraded visual environments will be presented in Chapters 4 – 7 of this Thesis.

Appropriate considerations must be made regarding the choice of single-photon detector in order to choose the most suitable detector that meets the requirements of both the optical system and the application. Hence, this Chapter has also presented a brief review of several types of single-photon detectors (such as PMTs, SNSPDs, and SPAD detectors), which are sensitive in the SWIR region of the spectrum, with particular attention given to both their advantages and their limitations.

Currently, InGaAs/InP SPAD detectors are the best candidate technology for single-photon counting applications in the SWIR due to their compatibility with compact Peltier cooling systems. These detectors are commercially available in both single-pixel formats [3.67] and as SPAD arrays [3.79,3.80], and offer relatively low DCRs, low timing jitters and SPDEs of up to a maximum of 45% at a detection wavelength of 1550 nm. Therefore, InGaAs/InP SPADs were selected in this work as the most appropriate choice of detector for imaging in highly scattering environments where optical signals are greatly attenuated.

3.5 References

3.1. A. Einstein, "Über einen die Erzeugung und Verwandlung des Lichtes betreffenden heuristischen Gesichtspunkt," Ann. Phys. 322(6), 132–148 (1905).

3.2. L. M. Hirvonen and K. Suhling, "Wide-field TCSPC: methods and applications," Meas. Sci. Technol. 28(1), 012003 (2017).

3.3. W. Becker, A. Bergmann, M. A. Hink, K. König, K. Benndorf, and C. Biskup, "Fluorescence lifetime imaging by time-correlated single-photon counting," Microsc. Res. Tech. 63(1), 58–66 (2004).

3.4. D. J. S. Birch and R. E. Imhof, "Time-domain fluorescence spectroscopy using time-correlated single-photon sounting," in *Topics in Fluorescence Spectroscopy: Techniques* 1, 1–95 (1999).

3.5. R. J. Collins, R. H. Hadfield, V. Fernandez, S. W. Nam, and G. S. Buller, "Low timing jitter detector for gigahertz quantum key distribution," Electron. Lett. 43(3), 180–181 (2007).

3.6. F. Zhu, W. Zhang, Y. Sheng, and Y. Huang, "Experimental long-distance quantum secure direct communication," Sci. Bull. 62(22), 1519–1524 (2017).

3.7. J. S. Massa, A. M. Wallace, G. S. Buller, S. J. Fancey, and A. C. Walker, "Laser depth measurement based on time-correlated single-photon counting," Opt. Lett. 22(8), 543–545 (1997).

3.8. J. S. Massa, G. S. Buller, A. C. Walker, S. Cova, M. Umasuthan, and A. M. Wallace, "Time-of-flight optical ranging system based on time-correlated single-photon counting," Appl. Opt. 37(31), 7298–7304 (1998).

3.9. M. Umasuthan, A. M. Wallace, J. S. Massa, G. S. Buller, and A. C. Walker, "Processing time-correlated single photon counting data to acquire range images," IEE Proc. Vis. Image Signal Process. 145(4), 237–243 (1998).

3.10. S. Pellegrini, G. S. Buller, J. M. Smith, A. M. Wallace, and S. Cova, "Laser-based distance measurement using picosecond resolution time-correlated single-photon counting," Meas. Sci. Technol. 11(6), 712–716 (2000).

3.11. A. McCarthy, X. Ren, A. D. Frera, N. R. Gemmell, N. J. Krichel, C. Scarcella, A. Ruggeri, A. Tosi, and G. S. Buller, "Kilometer-range depth imaging at 1550 nm wavelength using an InGaAs/InP single-photon avalanche diode detector," Opt. Express 21(19), 22098–22113 (2013).

3.12. A. M. Pawlikowska, A. Halimi, R. A. Lamb, and G. S. Buller, "Single-photon three-dimensional imaging at up to 10 kilometers range," Opt. Express 25(10), 11919–11931 (2017).

3.13. Z.-P. Li, X. Huang, Y. Cao, B. Wang, Y.-H. Li, W. Jin, C. Yu, J. Zhang, Q. Zhang, C.-Z. Peng, F. Xu, and J.-W. Pan, "Single-photon computational 3D imaging at 45 km," ArXiv190410341 Phys. (2019).

3.14. "The bh TCSPC handbook" (Becker and Hickl Gmbh, accessed 2019).

3.15 N. J. Krichel, A. McCarthy, and G. S. Buller, "Resolving range ambiguity in a photon counting depth imager operating at kilometer distances," Opt. Express 18(9), 9192–9206 (2010).

3.16. P. A. Hiskett, C. S. Parry, A. McCarthy, and G. S. Buller, "A photon-counting time-of-flight ranging technique developed for the avoidance of range ambiguity at gigahertz clock rates," Opt. Express 16(18), 13685–13698 (2008).

3.17. "HydraHarp 400 datasheet," (PicoQuant, accessed 2019).

3.18. S. Cova, M. Ghioni, A. Lotito, I. Rech, and F. Zappa, "Evolution and prospects for single-photon avalanche diodes and quenching circuits," J. Mod. Opt. 51(9–10), 1267–1288 (2004).

3.19. G. S. Buller and R. J. Collins, "Single-photon generation and detection," Meas. Sci. Technol. 21(1), 012002 (2009).

3.20. D. V. O'Connor, and D. Phillips, Time-Correlated Single Photon Counting (Academic, London, 1984).

3.21. J. Kalisz, "Review of methods for time interval measurements with picosecond resolution", Metrologis 41, 17-32 (2004).

3.22. G. W. Roberts and M. Ali-Bakhshian, "A brief introduction to time-to-digital and digital-to-time converters," IEEE Trans. Circuits Syst. II Express Briefs 57(3), 153–157 (2010).

3.23. A. Migdall, S. Polyakov, J. Fan, J. Bienfang, *Single-Photon Generation and Detection: Physics and Applications* (Academic Press, 2013).

3.24. W. Becker, *Advanced Time-Correlated Single Photon Counting Techniques*, (Springer, 2005).

3.25. E. A. G. Webster and R. K. Henderson, "A TCAD and spectroscopy study of dark count mechanisms in single-photon avalanche diodes," in *IEEE Transactions on Electron Devices* 60(12), 4014-4019 (2013).

3.26. D. P. Palubiak and M. J. Deen, "CMOS SPADs: design issues and research challenges for detectors, circuits, and arrays," IEEE J. Sel. Top. Quantum Electron. 20(6), 409–426 (2014).

3.27. P. A. Hiskett, G. S. Buller, A. Y. Loudon, J. M. Smith, I. Gontijo, A. C. Walker, P. D. Townsend, and M. J. Robertson, "Performance and design of InGaAs/InP photodiodes for single-photon counting at 1.55 µm," Appl. Opt. 39(36), 6818–6829 (2000).

3.28. A. Lacaita, P. A. Francese, F. Zappa, and S. Cova, "Single-photon detection beyond 1 µm: performance of commercially available germanium photodiodes," Appl. Opt. 33(30), 6902–6918 (1994).

3.29. F. Zappa, A. L. Lacaita, S. D. Cova, P. G. Lovati, "Solid-state single-photon detectors," Opt. Eng. 35(4), (1996).

3.30. R. Foord, R. Jones, C. J. Oliver, and E. R. Pike, "The use of photomultiplier tubes for photon counting," Appl. Opt. 8(10), 1975–1989 (1969).

3.31. G. A. Morton, "Photon counting," Appl. Opt. 7(1), 1–10 (1968).

3.32. J. P. Rodman and H. J. Smith, "Tests of photomultipliers for astronomical pulse-counting applications," Appl. Opt. 2(2), 181–186 (1963).

3.33. M. D. Eisaman, J. Fan, A. Migdall, and S. V. Polyakov, "Invited review article: single-photon sources and detectors," Rev. Sci. Instrum. 82(7), 071101 (2011).

3.34. "Photomultiplier tubes: basics and applications," (Hamamatsu, accessed 2019).

3.35. "NIR photomultiplier tubes: R5509-43/R5509-73," (Hamamatsu, accessed 2019).

3.36. C. M. Natarajan, M. G. Tanner, and R. H. Hadfield, "Superconducting nanowire single-photon detectors: physics and applications," Supercond. Sci. Technol. 25(6), 063001 (2012).

3.37. W. J. Skocpol, M. R. Beasley, and M. Tinkham, "Self-heating hotspots in superconducting thin-film microbridges," J. Appl. Phys. 45(9), 4054–4066 (1974).

3.38. A. D. Semenov, G. N. Gol'tsman, and A. A. Korneev, "Quantum detection by current carrying superconducting film," Phys. C Supercond. 351(4), 349–356 (2001).

3.39. J. K. W. Yang, A. J. Kerman, E. A. Dauler, V. Anant, K. M. Rosfjord, and K. K. Berggren, "Modeling the electrical and thermal response of superconducting nanowire single-photon detectors," IEEE Trans. Appl. Supercond. 17(2), 581–585 (2007).

3.40. H. Takesue, S. W. Nam, Q. Zhang, R. H. Hadfield, T. Honjo, K. Tamaki, and Y. Yamamoto, "Quantum key distribution over a 40-dB channel loss using superconducting single-photon detectors," Nat. Photonics 1(6), 343–348 (2007).

3.41. G. N. Gol'tsman, O. Okunev, G. Chulkova, A. Lipatov, A. Senenov, K. Smirnov, B. Voronov, and A. Dzardanov, "Picosecond superconducting single-photon optical detector," Appl. Phys. Lett. 79, 705–707 (2001).

3.42. S. Miki, M. Fujiwara, M. Sasaki, B. Baek, A. J. Miller, R. H. Hadfield, S. W. Nam, and Z. Wang, "Large sensitive-area NbN nanowire superconducting single-photon detectors fabricated on single-crystal MgO substrates," Appl. Phys. Lett. 92, 061116 (2008).

3.43. A. Verevkin, J. Zhang, R. Sobolewski, A. Lipatov, O. Okunev, G. Chulkova, A. Korneev, K. Smirnov, G. N. Gol'tsman, and A. Semenov, "Detection efficiency of large-active-area NbN single-photon superconducting detectors in the ultraviolet to near-infrared range," Appl. Phys. Lett. 80(25), 4687–4689 (2002).

3.44. A. Pearlman, A. Cross, W. Slysz, J. Zhang, A. Verevkin, M. Currie, A.Korneev, P. Kouminov, K. Smirnov, B. Voronov, G. Gol'tsman, R. Sobolewski, "Gigahertz counting rates of NbN single-photon detectors for quantum communications," in *IEEE Transactions on Applied Superconductivity* 5(2), 579-582 (2005).

3.45. B. A. Korzh, Q.-Y. Zhao, S. Frasca, J. P. Allmaras, T. M. Autry, E. A. Bersin, M. Colangelo, G. M. Crouch, A. E. Dane, T. Gerrits, F. Marsili, G. Moody, E. Ramirez, J. D. Rezac, M. J. Stevens, E. E. Wollman, D. Zhu, P. D. Hale, K. L. Silverman, R.

P. Mirin, S. W. Nam, M. D. Shaw, and K. K. Berggren, "Demonstrating sub-3 ps temporal resolution in a superconducting nanowire single-photon detector," arXiv:1804.06839 (2018).

3.46. F. Marsili, V. B. Verma, J. A. Stern, S. Harrington, A. E. Lita, T. Gerrits, I. Vayshenker, B. Baek, M. D. Shaw, R. P. Mirin, and S. W. Nam, "Detecting single infrared photons with 93% system efficiency," Nat. Photonics 7(3), 210–214 (2013).

3.47. G. G. Taylor, D. Morozov, N. R. Gemmell, K. Erotokritou, and R. H. Hadfield, "2.3μm wavelength single photon LIDAR with superconducting nanowire detectors," in *Conference on Lasers and Electro-Optics,* JTh2A.93, (2019).

3.48. E. V. P. Smith and D. M. Gottlieb, "Solar flux and its variations," Space Sci. Rev. 16(5), 771–802 (1974).

3.49. R. H. Hadfield, "Single-photon detectors for optical quantum information applications," Nat. Photonics 3(12), 696–705 (2009).

3.50. "NSM archive - physical properties of semiconductors" (http://www.ioffe.ru/SVA/NSM/Semicond/, accessed August 2019).

3.51. C. Kittel, *Introduction to solid state physics* (John Wiley & Sons, Inc., 2005).

3.52. G. W. Neudeck, *The PN Junction Diode* (Addison-Wesley Longman, Inc., 1983).

3.53. P. A. Tipler, and R. A. Llewellyn*, Modern Physics (*Clancy Marshall*, 2008).*

3.54. G. P. Agrawal, *Fiber-Optic Communication Systems* (Wiley-Interscience, 2002).

3.55. C. E. Webb, and J. D. Jones, *Handbook of Laser Technology and applications: Laser design and laser systems* (CRC Press, 2004).

3.56. K. Nishida, K. Taguchi, and Y. Matsumoto, "InGaAsP heterostructure avalanche photodiodes with high avalanche gain," Appl. Phys. Lett. 35(3), 251–253 (1979).

3.57. O. K. Kim, S. R. Forrest, W. A. Bonner, and R. G. Smith, "A high gain $In_{0.53}Ga_{0.47}As/InP$ avalanche photodiode with no tunneling leakage current," Appl. Phys. Lett. 39(5), 402–404 (1981).

3.58. "Avalanche Multiplication," (Science Direct, accessed 2019).

3.59. S. Cova, M. Ghioni, A. Lacaita, C. Samori, and F. Zappa, "Avalanche photodiodes and quenching circuits for single-photon detection," Appl. Opt. 35(12), 1956–1976 (1996).

3.60. A. Goetzberger, B. McDonald, R. H. Haitz, and R. M. Scarlett, "Avalanche effects in silicon p—n junctions. II. structurally perfect junctions," J. Appl. Phys. 34(6), 1591–1600 (1963).

3.61. S. Cova, A. Longoni, and A. Andreoni, "Towards picoseconds resolution with single-photon avalanche diodes," Rev. Sci. Instrum. 52(3), 408–412 (1981).

3.62. R. G. W. Brown, K. D. Ridley, and J. G. Rarity, "Characterization of silicon avalanche photodiodes for photon correlation measurements. 1: Passive quenching," Appl. Opt. 25(22), 4122–4126 (1986).

3.63. P. Antognetti, S. Cova, and A. Longoni, "A study of the operation and performances of an avalanche diode as a single-photon detector," Commission of the European Communities (CEC), EUR-5370 (1975).

3.64. N. I. Samsuddin, N. F. Hasbullah, and S. Ahmad, "Fuzzy logic based temperature control of thermoelectric cooler (TEC) for single photon avalanche diode (SPAD) application," in *4th International Conference on Mechatronics (ICOM)*, 1-7 (2011).

3.65. F. Zappa, S. Tisa, A. Tosi, and S. Cova, "Principles and features of single-photon avalanche diode arrays," Sens. Actuators Phys. 140(1), 103–112 (2007).

3.66. R. Ben-Michael, M. A. Itzler, B. Nyman, and M. Entwistle, "Afterpulsing in InGaAs/InP single photon avalanche photodetectors," in *2006 Digest of the LEOS Summer Topical Meetings*, 15-16 (2006).

3.67. M. Hofbauer, B. Steindl, and H. Zimmermann, "Temperature dependence of dark count rate and afterpulsing of a single-photon avalanche diode with an integrated active quenching circuit in 0.35 μm CMOS," J. Sens., 9585931 (2018).

3.68. A. Tosi, A. Della Frera, A. Bahgat Shehata, and C. Scarcella, "Fully programmable single-photon detection module for InGaAs/InP single-photon avalanche diodes with clean and sub-nanosecond gating transitions," Rev. Sci. Instrum. 83(1), 013104 (2012).

3.69. H. Dautet, P. Deschamps, B. Dion, A. D. MacGregor, D. MacSween, R. J. McIntyre, C. Trottier, and P. P. Webb, "Photon counting techniques with silicon avalanche photodiodes," Appl. Opt. 32, 3894-3900 (1993).

3.70. A. Lacaita, F. Zappa, S. Cova, and P. Lovati, "Single-photon detection beyond 1 μm: performance of commercially available InGaAs/InP detectors," Appl. Opt. 35(16), 2986–2996 (1996).

3.71. F. Acerbi, M. Anti, A. Tosi, and F. Zappa, "Design criteria for InGaAs/InP single-photon avalanche diode," IEEE Photonics J. 5(2), 6800209–6800209 (2013).

3.72. J. S. Escher, G. A. Antypas, and J. Edgecumbe, "High-quantum-efficiency photoemission from an InGaAsP photocathode," Appl. Phys. Lett. 29(3), 153–155 (1976).

3.73. F. Zappa, A. Lacaita, S. Cova, and P. Webb, "Nanosecond single-photon timing with InGaAs/InP photodiodes," Opt. Lett. 19(11), 846–848 (1994).

3.74. S. Pellegrini, R. E. Warburton, L. J. J. Tan, Jo Shien Ng, A. B. Krysa, K. Groom, J. P. R. David, S. Cova, M. J. Robertson, and G. S. Buller, "Design and performance of an InGaAs-InP single-photon avalanche diode detector," IEEE J. Quantum Electron. 42(4), 397–403 (2006).

3.75. A. Tosi, S. Cova, F. Zappa, M. A. Itzler, and R. Ben-Michael, "InGaAs/InP Single Photon Avalanche Diode Design and Characterization," in *2006 European Solid-State Device Research Conference*, 335-338 (2006).

3.76. M. Liu, C. Hu, X. Bai, X. Guo, J. C. Campbell, Z. Pan, and M. M. Tashima, "High-performance InGaAs/InP single-photon avalanche photodiode," IEEE J. Sel. Top. Quantum Electron. 13(4), 887–894 (2007).

3.77. M. A. Itzler, r. Ben-Michael, C.-F. Hsu, K. Slomkowski, A. Tosi, S. Cova, F. Zappa, and R. Ispasoiu, "Single photon avalanche diodes (SPADs) for 1.5 μm photon counting applications," J. Mod. Opt. 54(2–3), 283–304 (2007).

3.78. A. Tosi, F. Acerbi, M. Anti, and F. Zappa, "InGaAs/InP single-photon avalanche diode with reduced afterpulsing and sharp timing response with 30 ps tail," IEEE J. Quantum Electron. 48(9), 1227–1232 (2012).

3.79. A. Tosi, N. Calandri, M. Sanzaro, and F. Acerbi, "Low-noise, low-jitter, high detection efficiency InGaAs/InP single-photon avalanche diode," IEEE J. Sel. Top. Quantum Electron. 20(6), 192–197 (2014).

3.80. M. Entwistle, M.A. Itzler, J. Chen, M. Owens, K. Patel, X. Jiang, K. Slomkowski, and S. Rangwala, "Geiger-mode APD camera system for single-photon 3D LADAR imaging," Proc. SPIE 8375, Advanced Photon Counting Techniques VI, 83750D (2012).

3.81. P. Yuan, R. Sudharsanan, X. Bai, J. Boisvert, P. McDonald, E. Labios, M. S. Salisbury, G. M. Stuart, H. Danny, A. A. Portillo, A. B. Roybal, S. Van Duyne, G. Pauls, S. Gaalema, "32 x 32 Geiger-mode ladar camera," Proc. SPIE 7684, Laser Radar Technology and Applications XV, 76840C (2010).

3.82. A. L. Lacaita, F. Zappa, S. Bigliardi, and M. Manfredi, "On the bremsstrahlung origin of hot-carrier-induced photons in silicon devices," IEEE Trans. Electron Devices 40(3), 577–582 (1993).

3.83. N. Calandri, M. Sanzaro, L. Motta, C. Savoia, and A. Tosi, "Optical crosstalk in InGaAs/InP SPAD array: analysis and reduction with FIB-etched trenches," IEEE Photonics Technol. Lett. 28(16), 1767–1770 (2016).

3.84. "Kestrel 32 x 32 Geiger-Mode Flash 3-D LiDAR Camera data sheet," (Princeton Lightwave, accessed 2017).

3.85. W. C. Dash and R. Newman, "Intrinsic Optical Absorption in Single-Crystal Germanium and Silicon at 77°K and 300°K," Phys. Rev. 99(4), 1151–1155 (1955).

3.86. P. Vines, K. Kuzmenko, J. Kirdoda, D. C. S. Dumas, M. M. Mirza, R. W. Millar, D. J. Paul, and G. S. Buller, "High performance planar germanium-on-silicon single-photon avalanche diode detectors," Nat. Commun. 10(1), (2019).

3.87. A. Y. Loudon, P. A. Hiskett, G. S. Buller, R. T. Carline, D. C. Herbert, W. Y. Leong, and J. G. Rarity, "Enhancement of the infrared detection efficiency of silicon photon-countinavalanche photodiodes by use of silicon germanium absorbing layers," Opt. Lett. 27(4), 219–221 (2002).

3.88. R. E. Warburton, G. Intermite, M. Myronov, P. Allred, D. R. Leadley, K. Gallacher, D. J. Paul, N. J. Pilgrim, L. J. M. Lever, Z. Ikonic, R. W. Kelsall, E. Huante-Cerón, A. P. Knights, and G. S. Buller, "Ge-on-Si single-photon avalanche diode detectors: design, modeling, fabrication, and characterization at wavelengths 1310 and 1550 nm," IEEE Trans. Electron Devices 60(11), 3807–3813 (2013).

3.89 J. S. Dam, P. Tidemand-Lichtenberg, C. Pedersen, "Room temperature mid-IR single photon spectral imaging," Nat. Photonics 6, 788 (2012).

3.90 M. A. Albota & F. N. C. Wong, "Efficient single-photon counting at 1.55 μm by means of frequency upconversion," Opt. Lett. 29, 1449–1451 (2004).

3.91 H. Takesue, E. Diamanti, T. Honjo, C. Langrock, M. M. Fejer, K. Inoue, and Y. Yamamoto, "Differential phase shift quantum key distribution experiment over 105 km fibre," New J. Phys. 7, 232–243 (2005).

3.92 R. T. Thew, S. Tanzilli, L. Krainer, S. C. Zeller, A. Rochas, I. Rech, S. Cova, H. Zbinden, and N. Gisin, "Low jitter up-conversion detectors for telecom wavelength GHz QKD," New J. Phys. 8, 32–43 (2006).

Chapter 4: Long-range imaging of camouflaged objects using single-photon counting

4.1 Introduction

A time-of-flight (ToF) single-photon imaging system based on the time-correlated single-photon counting (TCSPC) technique was used to obtain images of camouflaged targets in challenging outdoor environments [4.1]. The detection system comprised of a single-pixel InGaAs/InP single-photon avalanche diode (SPAD), and an operating wavelength of 1550 nm with an average optical power level of less than 1 mW was used for all measurements. This was the maximum available output power available using this system configuration. This optical power level provided eye-safe imaging at the target range of 230 metres. The identification of targets, which have been obscured by clutter, is a subject of significant relevance for long-range field applications for both military and scientific applications. Several investigations involving 'seeing' behind or through various obscuring media (such as foliage or camouflage) have been performed previously using light detection and ranging (LiDAR) systems based on a range-gated approach [4.2,4.3]. While this approach achieves high-resolution gated imaging using very few laser pulses, it typically requires high-energy laser pulses (typically μJ). The use of the single-photon approach alongside high-sensitivity single-photon detectors allows relatively covert and eye-safe depth and intensity profiling. Other studies of obstructed targets have been performed using single-photon depth imaging [4.4]. While the results of this study were successful at acquiring depth and intensity profiles from single-photon data, the acquisition times of these measurements were prohibitively slow.

Firstly, this Chapter will present an overview of the $\lambda = 1550$ nm system components, alignment, and configuration. Then, two algorithms designed to reconstruct depth and intensity profiles from single photon data will be described in Section 4.3. The experimental set-up and key system parameters used during NATO SET 205 field trials will be described in Section 4.4. Finally, the results of these field trials and a discussion of the system performance will be presented in Section 4.5. Conclusions and future work are presented in Section 4.6.

4.2 Overview of the system configuration and key experimental parameters

The depth imaging system used to obtain the results presented in both this Chapter and Chapter 5 of this Thesis was comprised of a monostatic scanning transceiver unit, a

single-pixel InGaAs/InP SPAD detector, a pulsed supercontinuum laser source, and a TCSPC module. A schematic of the depth imaging system used for the measurements presented in this Chapter is shown in Figure 4.1. This Section will give details about the system components, alignment, and key experimental parameters.
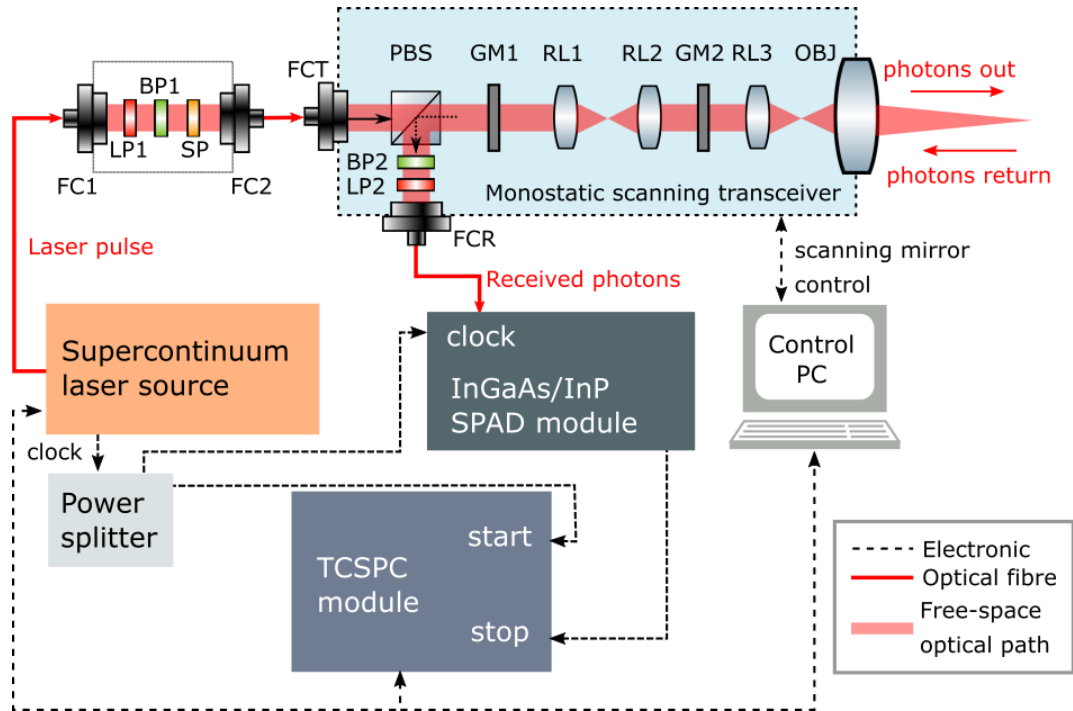
Figure 4.1: Schematic of the single-pixel depth imaging system that was operated at a wavelength of 1550 nm. This system was used for all measurements in Chapter 4 and Chapter 5 of this Thesis. It comprised a custom-built transceiver unit, a supercontinuum laser source, a TCSPC module, and an InGaAs/InP SPAD detector. Optical components include: polarising beam splitter (PBS); fibre collimation packages (FC1, FC2, FCR, FCT); scanning galvanometer mirrors (GM1, GM2); relay lenses (R1, R2, R3); objective lens (OBJ); longpass filters (LP1, LP2); shortpass filter (SP); bandpass filters (BP1, BP2).

A summary of the key system components, parameters, and optical components used for all measurements is given in Table 4.1. All optical components used were optimised for the $\lambda = 1550$ nm operating wavelength of the system.

Table 4.1: Summary of key system parameters and optical components.

Parameter	Value/comment
Illumination source	NKT Photonics supercontinuum (SuperK EXTREME EXW-12)
Illumination wavelength	1550 nm (10 nm) FWHM
Laser repetition rate	19.5 MHz
Laser pulse duration	< 100 ps
Average optical power	< 1 mW
Detector	Fibre-coupled, electrically gated-mode InGaAs/InP SPAD (www.micro-photon-devices.com)
Detector single-photon detection efficiency	~35% at λ = 1550 nm
Detector excess bias	5 V
Detector gate width	14 ns
Detector hold-off time	40 μs
Data acquisition hardware	HydraHarp 400, PicoQuant (www.picoquant.com)
Histogram timing bin size	2 ps timing bin width
System timing jitter	~ 220 ps
Objective Lens	500 mm focal length; 80 mm aperture diameter
Spectral filters in transmit channel	Longpass: Cut-on 1500 nm, transmission >98% (ThorLabs, FELH1500) Shortpass: Cut-off 1845 nm, transmission >90% (Spectrogon, SP-1845) Bandpass: 10 nm wide, 1550 nm central wavelength, transmission >95% (Edmund Optics, #86-091)
Spectral filters in receive channel	Longpass: Cut-on 1500 nm, transmission >98% (ThorLabs, FELH1500) Bandpass: 10 nm wide, 1550 nm central wavelength, transmission >95% (Edmund Optics, #86-091)

4.2.1 Monostatic scanning transceiver unit

The scanning transceiver unit was designed for long-range, free-space depth imaging and was custom-built by the Single-Photon group at Heriot-Watt University. Due to the modular design of the system, it has been reconfigured for use at a variety of operating wavelengths (475 – 1550 nm), and used in a range of LiDAR applications such as long-range depth imaging [4.1,4.5,4.6], underwater depth imaging [4.7,4.8], and multispectral imaging [4.9–4.12].

The transceiver unit has dimensions of $275 \times 275 \times 170$ mm and is made of black anodised aluminium to minimise ambient background light and reduce stray light inside the transceiver. The optical components were installed within the unit using a semi-kinetic mounting system comprised of a slotted baseplate and magnetic fasteners. This set-up reduces the degrees of freedom of the optical components allowing for straightforward optical alignment and helping to maintain long-term stability. This high

level of modularity and stability allows the system to be aligned and reconfigured in the field, outside of controlled laboratory conditions. A schematic of the monostatic transceiver unit depicting the key optical components is shown in Figure 4.2 and a schematic of the optical path inside the transceiver unit is shown in Figure 4.3.
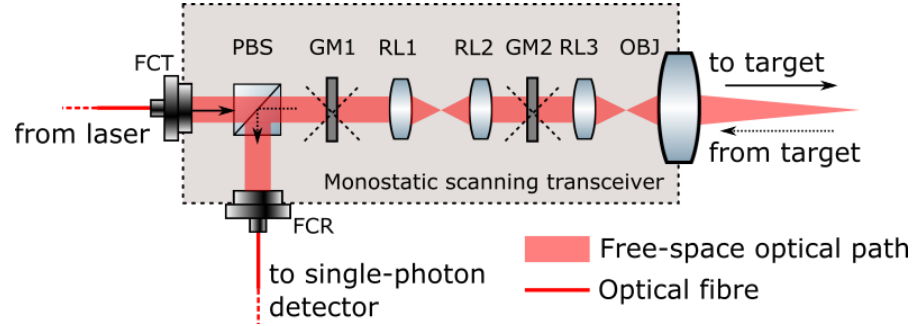
Figure 4.2: Schematic of the monostatic scanning transceiver unit. Optical components include: a polarising beam splitter (PBS); fibre collimation packages (FCR, FCT); scanning galvanometer mirrors (GM1, GM2); relay lenses (RL1, RL2, RL3); and an objective lens (OBJ).
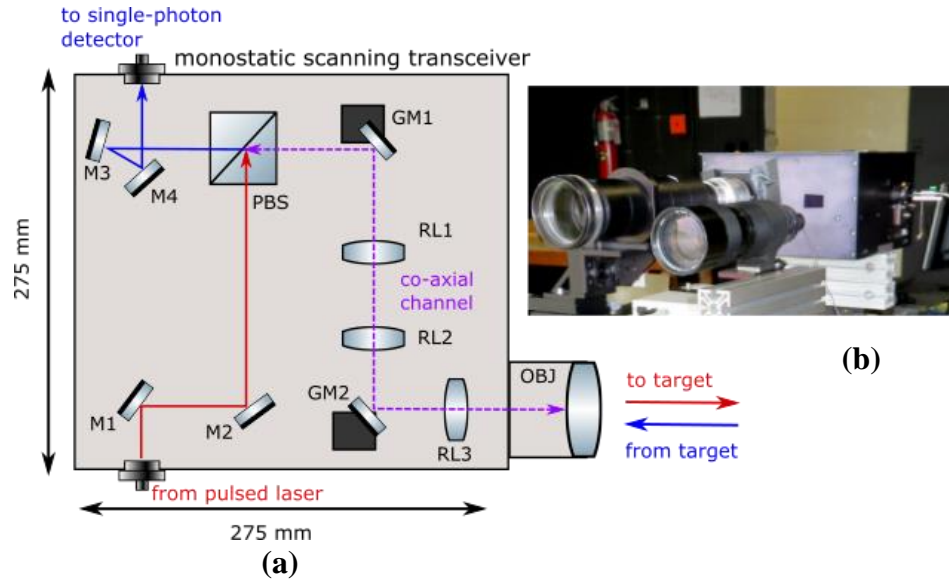
Figure 4.3: (a) Schematic of the optical path inside the transceiver unit. The red path shows the transmit channel, which was fibre-coupled to the illumination source. The blue path shows the receive channel, which was fibre-coupled to an InGaAs/InP SPAD detector. The coaxial channel (common to both the transmit and receive channels) is shown in purple. (b) A photograph of the monostatic scanning transceiver unit.

Within the transceiver unit, a fibre collimation package (FCT in Figure 4.2) was used in the transmit channel (Tx) to de-couple the laser pulses into a collimated optical beam with

a beam diameter of approximately 2.7 mm. The light was then routed to a polarising beam splitter (PBS) via alignment mirrors M1 and M2 where the Tx channel and the receive channel (Rx) were subsequently overlapped to create a coaxial common channel. The PBS was aligned through tilt adjustment and rotation in the transverse plane. The light transmitted by the PBS was maximised by adjusting the Tx channel fibre collimation package (FCT). A pair of galvanometer mirrors were placed at conjugate planes within the transceiver in order to scan the beam in the x- and y- directions (GM1 controls y- and GM2 for x-). The two scanning galvanometer mirrors were controlled by an electrical driver system. A schematic diagram of this system is shown in Figure 4.4. A digital-to-analogue convertor (DAC) was used to deliver control voltages to drive the x-axis and y-axis motors in a raster scan pattern. The amplitude of the voltages (set by custom software) determined the magnitude of the motor movement and thus, the size of the area scanned by the system. The number of pixels within the scan area (i.e., the instantaneous field-of-view (FoV) of the system) is also set via this custom software, and the DAC provides a trigger signal to the TCSPC data acquisition module, which in turn generates a marker for each position change (i.e., marks each new pixel).
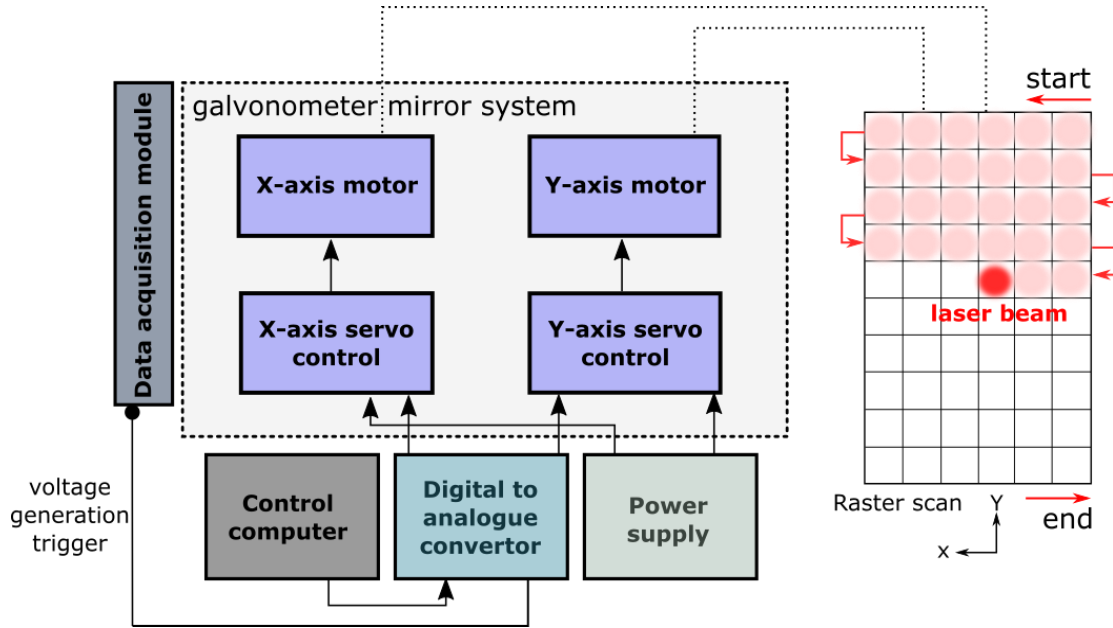
Figure 4.4: Schematic of the scanning galvanometer mirror system. A DAC is used to generate a voltage, which controls the x-axis and y-axis galvanometer mirrors. This voltage is set such that a raster scan, with a pixel size that is dependent on the magnitude of the voltage, is performed. The DAC also provides a corresponding electrical signal to the data acquisition module that subsequently marks the movement of the beam to each subsequent pixel.

Two relay lenses (RL1 and RL2) were placed between GM1 and GM2 at one focal length away from each respective scanning mirror. These lenses were used in a telecentric configuration as shown in Figure 4.5.
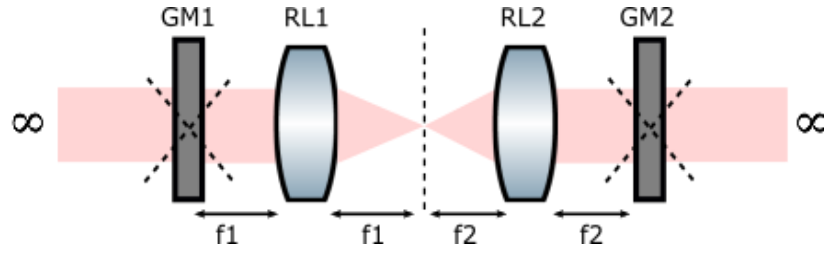
Figure 4.5: Telecentric configuration of relay lenses RL1 and RL2. The focal length of each lens is denoted as f1 and f2, respectively.

Achromatic lenses were chosen to minimise the effects of chromatic and spherical aberrations. This is particularly useful if the operating wavelength of the system has to be changed during measurements (e.g., for multispectral measurements). The use of a telecentric configuration allows the highest possible accuracy in the optical alignment to be obtained and guarantees that the return signal is always on axis. After passing through the telecentric pair, the light was then reflected off of GM2 and through a third relay lens (RL3), which then formed an image at the image plane of the objective lens (OBJ). The field-of-view (FoV) of the image at the image plane of the objective lens was the primary limiting factor on the maximum field-of-regard (FoR) of the system (i.e., the maximum achievable scanned area). The light was subsequently passed through the objective lens, which was used to both focus the transmitted light on the target scene and collect back-scattered photon returns from the target. The received photons were then routed back through the relay lens system via the same optical path, and de-coupled from the common channel by the polarising beam splitter. This signal was then coupled to a 10 µm optical fibre using alignment mirrors M3, M4, and a second collimation package (FCR in Figure 4.2). This signal was subsequently sent on to an InGaAs/InP SPAD detector.

In order to achieve the maximum performance of the imaging system, the proper alignment of the coaxial channel and corresponding optical components is imperative. Thus, a series of alignment checks were performed using a concave mirror to focus the illumination beam on to an infrared CCD camera, allowing the beam spot to be monitored (as shown in Figure 4.6). The first alignment check was performed on RL3 by inserting a temporary alignment lens after GM1 to focus the light on to GM2 (see Figure 4.6 (a)). GM2 was set to perform a sinusoidal oscillation in x-, which was then minimised by adjusting the position of RL3. Then, the temporary lens was removed and the telecentric

pair RL1 and RL2 were placed between GM1 and GM2. A temporary lens was then inserted after the PBS in order to focus the light on GM1. GM1 was set to perform a sinusoidal oscillation in y-, which was then minimised by the appropriate adjustment of RL1 and RL2. Finally, the temporary lens was then removed from the optical path.
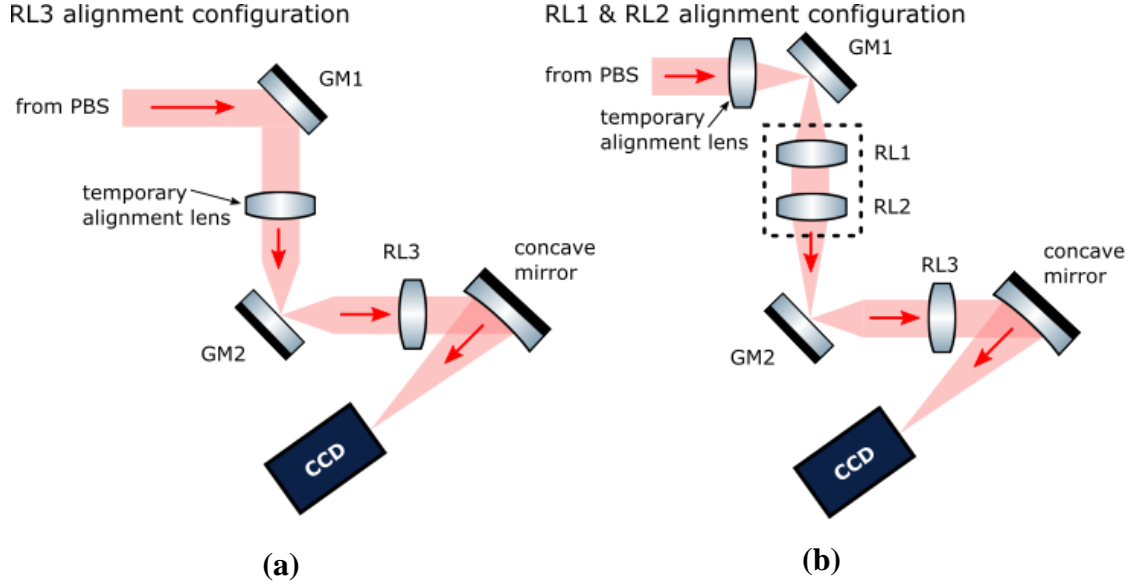
Figure 4.6: Optical set-up for the alignment of relay lenses RL1, RL2, and RL3 with galvanometer mirrors GM1 and GM2. A concave mirror focused the optical path on to a CCD camera, which was used to check the alignment. Temporary lenses were used in each set-up to adjust the focus. (a) shows the configuration for RL3 alignment and (b) for the achromatic pair (RL1 and RL2) alignment.

Finally, alignment of the coaxial channel was performed using the concave mirror and CCD camera. A fibre splitter was used to deliver $\lambda = 1550$ nm light from a pulsed laser source through both the Tx and Rx channels simultaneously, and the two beams were imaged at the focus position on the CCD camera as shown in Figure 4.7.

In order to achieve a precise alignment of the two channels, a microscope objective lens was mounted to the CCD camera interface in order to magnify the image - allowing for very fine adjustments. The proper alignment of these two channels is imperative for the use of the system in long-range imaging applications. Thus, the overlap of the Tx and Rx channels was checked in both the near and far fields by moving the camera back and forth between the focus position and de-focus position denoted in Figure 4.7 while small adjustments to the optics within the transceiver were performed.

Figure 4.7: Schematic of the coaxial channel alignment. A CCD camera was used to image the beam spots, and the two channels (Tx and Rx) were aligned such that the imaged spots overlapped in both the near and far-field (focus and de-focus) positions.

4.2.2 Illumination source

The illumination source used for all measurements in this Chapter and Chapter 5 of this Thesis was a pulsed supercontinuum laser source. Supercontinuum laser sources have the capability of providing broadband illumination over a wide wavelength range, making them ideal for applications that require the use of different operating wavelengths. Supercontinuum generation is the result of a severe spectral broadening of a master seed pumped laser beam, and is achieved in many commercial supercontinuum sources by means of nonlinear processes in photonic crystal fibres [4.13,4.14]. Two supercontinuum laser sources were available for these measures: the SuperK EXTREME EXW-6 and EXW-12 by NKT Photonics, Germany [4.15]. Both of these sources had a diode-pumped Nd:YAG master seed laser source at $\lambda = 1064$ nm, resulting in an operating wavelength range of approximately $460 - 2400$ nm, as shown in Figure 4.8. However, the EXW-12 was selected for all measurements as it provided a higher optical output power at $\lambda = 1550$ nm.
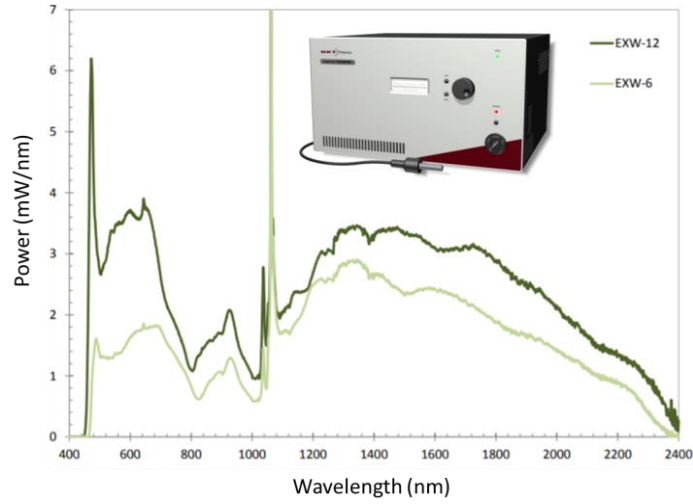
Figure 4.8: Spectra of the NKT Photonics EXW-12 and EXW-6 supercontinuum laser sources available for the measurements presented in Chapter 4 and Chapter 5 of this Thesis. The EXW-12 (pictured) was chosen for all measurements in this Thesis due to a higher available power output at $\lambda = 1550$ nm. Taken from ref. [4.15].

This laser has a pulse duration of < 100 ps and a variable repetition rate in the MHz regime. In order to select an operating wavelength of 1550 nm, a filter rig containing a series of high-performance optical filters was used. A fibre collimation package (FC1 in Figure 4.9) was used to de-couple the light from the supercontinuum laser source, which was then passed through three optical filters. These filters included a longpass filter with a cut-on wavelength of 1500 nm (LP1), a bandpass filter centred on 1550 nm with a full-width half-max (FWHM) of 10 nm (BP1), and a shortpass filter with a cut-off wavelength of 1800 nm (SP). A second fibre collimation package (FC2) was then used to couple the transmitted light back into the Tx channel via a 10 µm optical fibre.
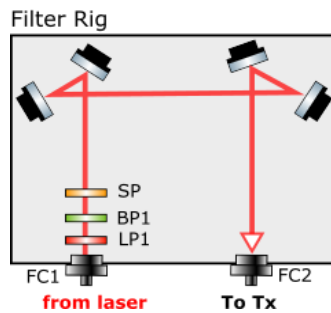
Figure 4.9: A schematic diagram of the filter rig set-up that was used to select an operating wavelength of $\lambda = 1550$ nm. Optical components include two fibre-collimation packages (FC1 and FC2), and a set of high-performance filters comprising a longpass filter (LP1), a bandpass filter (BP1), and a shortpass filter (SP).

4.2.3 Single-photon detector and TCSPC data acquisition module

An electrically gated InGaAs/InP SPAD detector (Micro Photon Devices, Italy [4.16]) was used for all measurements in this Chapter and Chapter 5 of this Thesis. This single-pixel detector (shown in Figure 4.10 (a)) has an operating wavelength range of 900 – 1700 nm and an active-area of 25 µm. This detector was thermoelectrically cooled meaning that the initiation process is relatively fast, allowing the detector to be used in the field quickly and efficiently. A plot of the single-photon detection efficiency (SPDE) as a function of wavelength is shown in Figure 4.10 (b). An excess bias of 5 V was selected during measurements to provide a SPDE of approximately 35% at the operating wavelength of 1550 nm. The jitter of the detector at a 5 V excess bias was < 200 ps, as stated by the manufacturer.
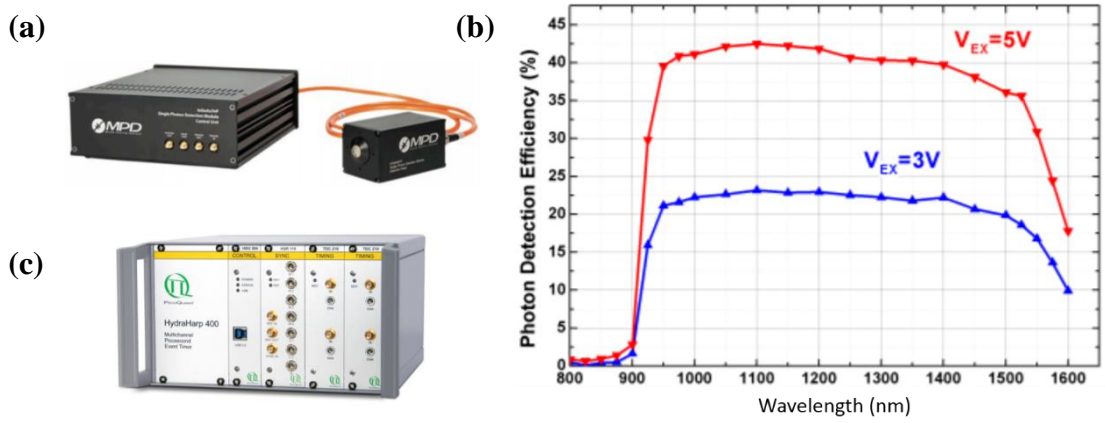
Figure 4.10: (a) A photograph of the single-pixel InGaAs/InP SPAD detector (Micro Photon Devices, Italy). (b) A plot of the SPDE over the operational wavelength range of the detector for excess biases of 3 V and 5 V. Both taken from ref. [4.16]. (c) A photograph of the TCSPC data acquisition module used in these measurements. Taken from ref. [4.17].

Due to the monostatic configuration of the system, the presence of back-reflections from optical components within the transceiver unit could result in the saturation of the sensitive detector, and potentially create false peaks in the resultant histograms during measurements. To avoid this, the detector was operated in an electrically gated-mode, with the detector gate positioned to avoid potential spurious back-reflections. A detailed description of the electronic gating approach for this detector is provided in ref. [4.18]. For the measurements presented in this Chapter, a relatively short gate duration of 14 ns was used to limit increased background levels resulting from detector afterpulsing effects. As discussed in detail in Chapter 3, afterpulsing is caused by charge carriers being trapped

in defects, which are subsequently released causing spurious avalanches [4.19–4.21]. In order to further reduce the deleterious effects of detector afterpulsing, a hold-off time of 40 µs was used to deactivate the detector after a recorded event, in order to allow the traps to empty without triggering further avalanches. The dark count rate of the detector was measured to be approximately 33 kcs^{-1} for a 40 µs hold-off time. This hold-off time was selected as a compromise between reducing the effects of afterpulsing and restricting the maximum count rate possible.

When a detection event occurred, the detector module provided an electrical stop signal to a TCSPC data acquisition module, which was configured to output time-tagged detection events. The TCSPC technique was described in detail in Chapter 3 of this Thesis. A HydraHarp 400 (PicoQuant, Germany [4.17]), as shown in Figure 4.10 (c), was used for all measurements presented in this Chapter and in Chapter 5 of this Thesis. The HydraHarp 400 boasts four independent input channels with a photon count rate up to 12.5 million counts/sec per channel. This module offered two time-tagged-time-resolved (TTTR) modes denoted T2 and T3 mode. The main difference between these two modes is the format in which the timing information is recorded. In T2 mode, there is no channel dedicated to the synchronisation of an input signal from a laser source, hence all detection events are recorded relative to the start time of the measurement (i.e., the macro-time of the measurement). In T3 mode, a channel is dedicated to this laser input signal so the detection events are recorded relative to the last synchronisation signal from the pulsed laser source (i.e., the micro-time of the measurement) [4.17]. In all measurements using the HydraHarp 400, T3 mode was selected as it is specifically designed to be used with high-repetition rate pulsed laser sources (up to 150 MHz), and can precisely determine which synchronised laser pulse a photon event belongs to - resulting in highly precise timing measurements with up to 1 ps timing resolution. A trade-off when using T3 mode is that it can increase the overall system jitter due to a contribution from the synchronisation signal, and the dead time of the module is slightly longer (up to 80 ns) in T3 mode.

The HydraHarp 400 identified each pixel in the scan through an electrical signal provided by the galvanometer mirror system to the 'Marker' input of the module and stored this information alongside the time-tagged data in a single data file. This data file was transferred to the control computer via a USB 3.0 connection. This information was then used to construct timing histograms via a custom software, designed to deal with the T3 mode data structure.

4.3 Computational methods

In recent years, there has been much interest in the implementation of algorithms designed to reconstruct sparse photon data obtained from outdoor, long-range targets [4.22–4.24]. This Chapter presents results obtained using two algorithms, (i) a simple cross-correlation algorithm and (ii) the Restoration of Depth and Intensity using the Total Variation (RDI-TV) algorithm, which exploits spatial correlations in single-photon data.

4.3.1 Pixel-wise cross-correlation

Pixel-wise cross-correlation is a simple and computationally inexpensive method commonly used in single-photon three-dimensional image reconstruction [4.5–4.7,4.22,4.25]. This algorithm provides an estimate of depth and intensity for each pixel by calculating the cross-correlation, C, between an acquired timing histogram, y, and the known instrumental response of the system, R, such that:

$$C_t = \sum_{i=1}^{T} y_{t+i} R_i,\tag{4.1}$$

where y_t is the timing histogram value at the tth bin and T is the total number of timing bins. Using this method, a time position corresponding to the highest cross-correlation can be found for each pixel, which represents the target's position and is related to the depth measurement Z. Once the relevant time positions (or bin location) are picked up for each pixel, through combining the spatial (i.e. X and Y) information and time-correlated depth measurement (i.e. Z), a depth profile of the scanned scene can be reconstructed. For these measurements, the instrumental response function, R, was obtained by performing a single-point measurement of a uniform, flat surface (i.e., a wooden board painted white) placed in the same nominal plane as the target position at a range of 230 metres. An example of the instrumental response function, obtained using a 100 second integration time and a 14 ns gate duration, is shown in Figure 4.11.
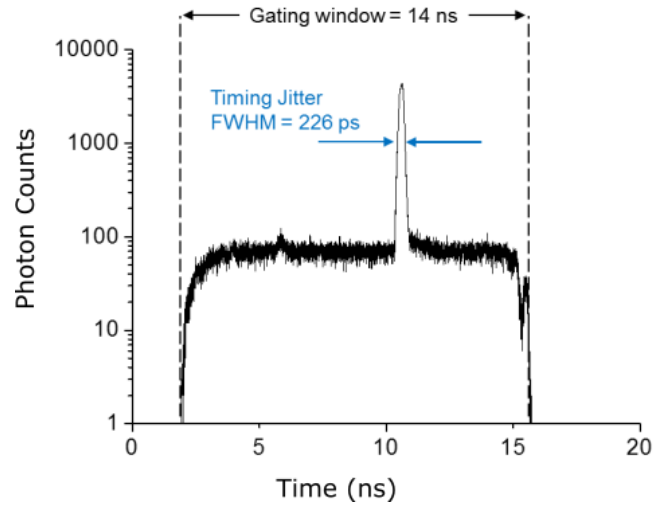
Figure 4.11: The timing histogram of the instrumental response taken from a uniform surface located in the same nominal plane as the target. The system had an overall timing jitter of 226 ps at FWHM. The detector was operated in electrically gated-mode with a 14 ns gate duration. An arbitrary zero was chosen for the displayed time-scale.

The overall timing jitter of the system was found to be approximately 226 ps at FWHM with contributions from the detector response, laser pulse duration and other electronic components such as the TCSPC module, with the largest contribution being the detector jitter. Typically, targets with a single reflecting surface will result in one peak per histogram, corresponding to the target position (not including any peaks arising from back-reflections as previously discussed in Section 4.2.3). This means that pixel-wise cross-correlation can give satisfactory results when there is only one distinct target return. However, for targets behind camouflage netting, such as those examined in this Chapter, the timing histograms may include multiple peaks with the largest peak not necessarily corresponding to the target position. In this case, the cross-correlation will assign a single depth estimate based only on the largest return peak. This can result in an inaccurate depth estimation if this peak corresponds to the camouflage netting instead of the target.

4.3.2 RDI-TV algorithm

Imaging scenes in cluttered environments with very low acquisition times can lead to a large proportion of pixels where either no data were obtained due to low photon returns or containing information on only irrelevant surfaces. The image processing community has already studied this problem in detail, and several algorithms have been developed based on the Poissonian statistics of single-photon data [4.4,4.25–4.27]. Therefore, a more sophisticated reconstruction algorithm of this variety, developed by Dr Abderrahim

Halimi, was applied to the results presented in this Chapter. A brief explanation of this algorithm will be given here, however, a detailed description of this algorithm can be found in ref. [4.28]. The Restoration of Depth and Intensity using the Total Variation (RDI-TV) algorithm was selected because it has been previously shown to be a good candidate algorithm for the reconstruction of single-photon data that contains a single depth plane but multiple surfaces [4.22,4.29]. The algorithm aims to reduce the effects of Poisson noise found in single-photon data, and reconstruct depth (D_{init}) and intensity (I_{init}) profiles in pixels containing target information. The RDI-TV algorithm achieves this by using several approximations based on prior knowledge of the target scene. The main approximations are: (i) a single depth layer per pixel is present, (ii) there is an absence of background counts, (iii) the system has an approximately Gaussian instrumental response, (iv) the positions of corrupted pixels are known, and (v) the target position is sufficiently far from the edges of the timing histogram. To start, a cross-correlation is performed using a known instrumental response (as described in the previous Section), and then a total variation denoising approach is performed [4.30]. This approach is a common denoising algorithm used in image processing and is implemented by optimising the cost function (C_f) associated with the restored depth (D) and intensity (I) estimates through means of a convex algorithm. In this case the convex algorithm used is the alternating direction method of multipliers (ADMM) algorithm described in ref. [4.31]. The cost function in this case is given by:

$$C_f(D,I) = L(D_{INIT}, I_{INIT}) + TV(D) + TV(I), \qquad (4.2)$$

where $L(D_{init}, I_{init})$ is the log-likelihood of the Poisson distributed data and $TV(D)$ and $TV(I)$ are the total variation regularisation terms. This process makes RDI-TV algorithm a computationally fast and robust way to analyse single-photon data that contains only a single-depth surface. However, the data of the target obstructed by camouflage netting presented in this Chapter contained two distinct depth surfaces (i.e., the camouflage netting and the target). Therefore, an additional data-gating step was performed where only data from the 1900 timing bins centred on the target was selected. This corresponds to a 0.6 m depth range around the target, eliminating the histogram bins containing photon returns originating from the camouflage netting.

4.4 Experimental layout

An evaluation of the long-range performance of the single-pixel depth imaging system was performed as part of the NATO SET-205 "Active Electro-optic Sensing for Target

Identification and Tactical Applications" field trials in Virginia, USA. These field trials comprised a series of outdoor measurements in daylight conditions at a target range of 230 metres from the system position. The aim of these measurements was the successful imaging and identification of targets in challenging outdoor scenarios with a high level of ambient background. The system was housed in an enclosed building to shield the sensitive components from adverse weather, such as rain and wind. Large retractable doors, which faced out on to a 5 km long laser range, were opened to allow for measurements. Photographs of the system position, the target location, and the depth imaging system in-situ at the field trials are shown in Figure 4.12.
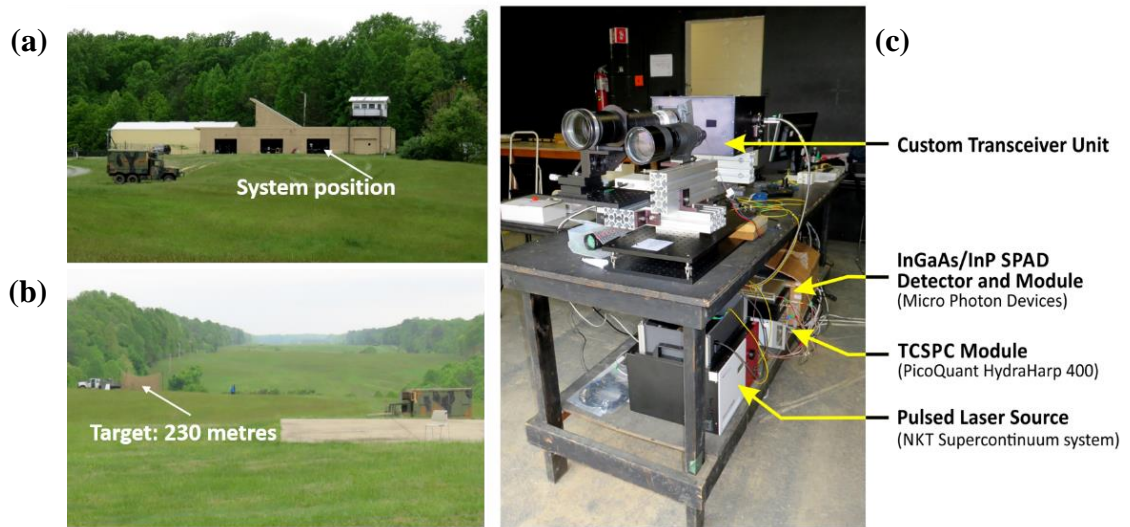
Figure 4.12: (a) A photograph of the system position taken from the target location. (b) The target location at 230 m as seen from the system position. (c) A photograph of the single-pixel depth imaging system in-situ in Virginia, USA.

The stand-off distance of the target was approximately 230 metres from the system position. The illumination beam exiting the system had an average optical power level of less than 1 mW at a repetition rate of 19.5 MHz for all measurements, and an operating wavelength of 1550 nm. This wavelength and power level selection resulted in eye-safe imaging. However, it should be noted that actors wore laser safety googles as a further precaution. This wavelength was also selected for its high atmospheric transmission, and because the adverse effect of solar background at this wavelength is significantly lower compared to operating at wavelengths below 1 µm [4.32–4.34]. In order to further reduce the effects of solar background during outdoor measurements, the Rx channel of the transceiver unit was spectrally filtered using a longpass filter with a cut-on wavelength of 1500 nm (LP2 in Figure 4.1), and a bandpass filter centred on 1550 nm with a FWHM of

10 nm (BP2). An objective lens with a 500 mm focal length and an aperture size of 80 mm provided a scanned FoR (i.e., the area scanned at the target position) of approximately 1 × 2 metres. The scanned FoR was mapped by 80 × 160 pixels (X × Y), equivalent to an instantaneous FoV (i.e., a pixel-to-pixel pitch) of approximately 12.5 mm in both X and Y at the target location. The focused beam diameter at the target was approximately 1 cm, meaning that there was little or no overlap between adjacent pixels for each scan position. A per-pixel acquisition time of 3.2 ms was used for all measurements, resulting in a total scan time of approximately 41 seconds. This long acquisition time was chosen to provide a large amount of photon returns in all pixels containing target information.

The target scene comprised of several actors holding a variety of target items in different poses. Target items included both non-hazardous objects such as umbrellas, wooden boards, and backpacks, and hazardous items such as several types of weapons and other lethal objects (e.g., a suicide vest and belt). A selection of these targets along with images of the actors posing during measurements is shown in Figure 4.13.

Figure 4.13: Photographs of the actors holding hazardous and non-hazardous target items (left) and a selection of the target items imaged during these field trials (right). The faces of the two actors have been blurred for anonymity.

Two different target scenarios were investigated during the field trials. The first set of measurements comprised of an unobstructed actor holding a target item as shown in Figure 4.13. In the second set of measurements, the target scene comprised of the actor holding the target items behind a double layer of commercially available camouflage netting. The camouflage netting was placed approximately 1 metre in front of the target

position perpendicular to the laser beam propagation, and a second single layer was erected approximately 2 metres behind the target position. A photograph of the camouflaged target set-up is shown in Figure 4.14.
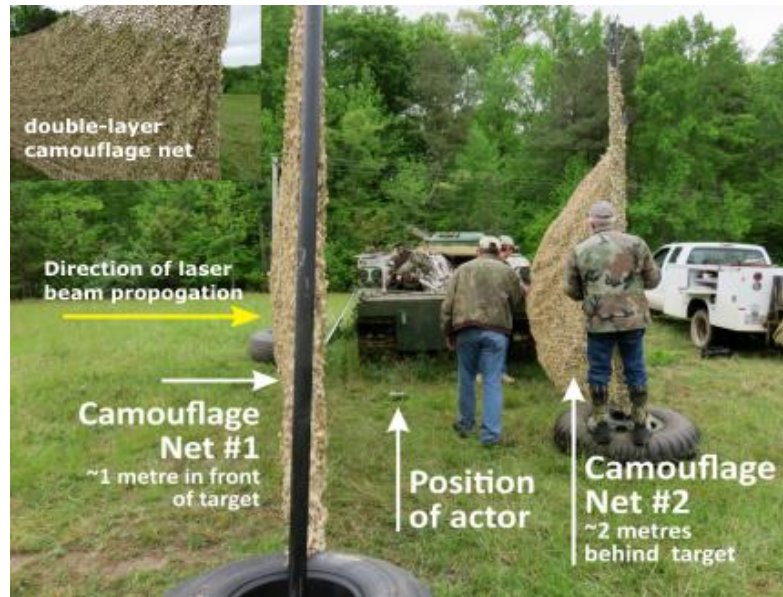
Figure 4.14: Photograph of the camouflaged target set-up at 230 metres from the system position. A double layer camouflage net was placed approximately 1 metre in front of the target position, and a single layer of camouflage net approximately 2 metres behind.

A summary of the experimental set-up, key parameters, and a list of the target items is given in Table 4.2.

Table 4.2: Summary of the experimental set-up used in these field trials.

Parameter	Value/comment
Environment	Outdoors. Dry and bright (but overcast), with atmospheric conditions remaining relatively constant for the duration of the measurement set.
Target stand-off distance	~ 230 metres
Target items	AK-47, AT-4, backpack, Dragunov, M-4, RPG, suicide belt, suicide vest, tripod, wooden plank, umbrella, sledgehammer
Illumination beam diameter at target	~ 1 cm
Pixel format	80×160
Scan Area	1000×2000 mm (X $\times$ Y)
Pixel pitch	~12.5 mm in X and Y
Acquisition time	~3.2 ms per-pixel (~41 seconds total scan time)

4.5 Experimental results and discussion

A full set of measurements were taken in order to image and identify each of the target items. This Section presents results from a select number of these measurements for both

the unobstructed and camouflaged scenarios. Results obtained via pixel-wise cross-correlation for unobstructed measurements and also using the RDI-TV algorithm for camouflaged measurements are presented.

4.5.1 Non-camouflaged targets

The first series of images of the target items were taken at a distance of 230 metres, unobstructed by camouflage netting. An example of an aggregated timing histogram from one such scenario is shown in Figure 4.15.
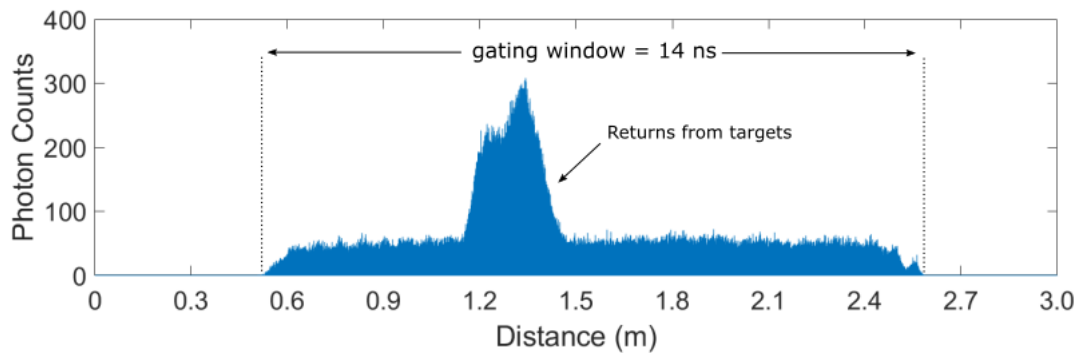
Figure 4.15: Example of an aggregated timing histogram obtained from a measurement of an unobstructed target at 230 metres from the system position. The zero point in the depth axis was chosen arbitrarily.

In this aggregated histogram, data from all 12,800 pixels in the image is summed and displayed in this single histogram. A detector gate duration of 14 ns was used, equivalent to a one-way distance of approximately 2.1 metres. Two separate bumps in the peak were observed. The first bump in the peak corresponded to the location of the target object held across the chest by the actor and the second larger peak corresponded to the actor. The target depth was found to be approximately 30 cm (corresponding to 1000 timing bins at a 2 ps resolution) from the front surface of the target object to the rear surface of the actor. The total number of photon counts in this peak was found to be approximately 179,000, giving an average number of photons per timing bin of approximately 179 − with 308 photon returns the highest bin in the peak. Depth profiles depicting three target objects (i.e., an AT-4, a sledgehammer, and a suicide vest) reconstructed using the pixel-wise cross-correlation algorithm are shown in Figure 4.16.
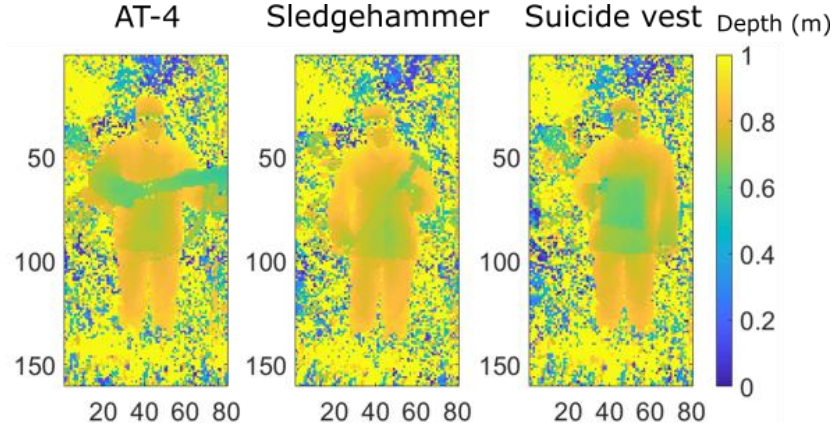
Figure 4.16: Depth profiles of actors holding (or wearing) various target items (AT-4, sledgehammer, and a suicide vest) at a range of 230 metres with no camouflage netting present. These profiles were all obtained using pixel-wise cross-correlation.

The results show that the profile of each item was easily identifiable, and hence the items could be distinguished from one another. For example, the strap of the AT-4 and the head of the sledgehammer were readily discernible in the depth profiles. However, many return photons were also collected from foliage located far behind the target location due to the inherent problem of range ambiguity in high repetition rate ToF systems. In a fixed repetition rate LiDAR system, range ambiguity occurs when there is more than one possible position for a reflecting surface. This occurs when, instantaneously, there is more than one optical pulse in transit. This means that surfaces far behind the target position can appear as though they are in the same plane as the target due to earlier laser pulses. This can result in noisy images as seen in the results presented in Figure 4.16. This maximum unambiguous distance (d_{rep}) is dependent on the fixed repetition rate (f_{rep}) of the laser and is given by:

$$d_{rep} = \frac{c}{2 f_{rep}}, \tag{4.3}$$

where c is the speed of light in a vacuum. Given that a laser repetition rate of 19.5 MHz was used in these measurements, the maximum range for unambiguous determination of target distance was approximately 7.7 metres. Range ambiguity can be removed by a reduction in repetition rate (which can significantly increase measurement time), by use of multiple sequential repetition rates, or by using techniques such as laser pulse trains composed of pseudo-random patterns [4.35,4.36]. Photon returns from the foliage behind the target did not contain data of any interest for these measurements. Therefore, a gating threshold of approximately 0.6 metres centred on the target location was applied during

processing to the timing histogram in order to remove some of this data and improve the image of the target. Figure 4.17 shows RGB photographs, intensity profiles, and depth profiles obtained using the pixel-wise cross-correlation algorithm from two measurement scenarios. The first scenario comprised of an actor holding a rocket-propelled grenade (RPG) across his chest, while the second scenario comprised of a different actor holding a wooden plank in the same position. Both the aforementioned gating threshold and intensity threshold were applied to the data. The intensity threshold excluded pixels with very low levels of photon returns, since they were unlikely to originate from target returns. The corresponding pixels in the depth profile were subsequently excluded.
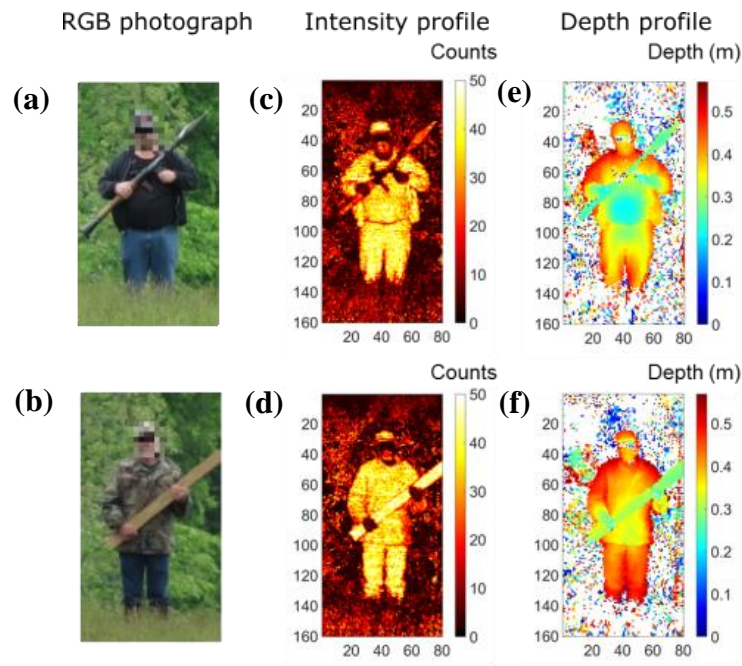
Figure 4.17: Depth and intensity profiles of two unobstructed targets: an actor holding an RPG across his chest and an actor with a wooden plank in the same position. Images (a) and (b) show photographs of the two actors holding the RPG and a wooden plank, respectively. In the photographs, the faces of the two actors were blurred for anonymity. Images (c) and (d) show the intensity maps of both target scenes. Images (e) and (f) show the depth profiles of both target scenes. These results were obtained using the pixel-wise cross-correlation algorithm.

The depth resolution of both of the depth profiles appeared to be sub-centimetre for most features of the target, and differences in the material reflectivity and dimensions of both the RPG and the wooden plank are evident in the intensity and depth profiles, making the two objects easily discernible in this example. The number of photon returns is dependent on a variety of factors such as the optical power level used, the acquisition time of the

scan, and the reflectivity of the target material at the illumination wavelength [4.5,4.35,4.37]. It is evident from these images that the clothes of the actors yielded a significant quantity of photon returns, whereas the gun handle and the actors' dark eye-wear yielded few photon returns at the operating wavelength of 1550 nm. In addition, the low reflectivity of human skin at $\lambda = 1550$ nm [4.38] is evident due to a low number of photon returns from the face and hands in the intensity profiles. However, most target pixels yielded more photon returns than required to construct a satisfactory depth profile due to the long acquisition time (41 seconds) of the scan. Due to the time-tagged nature of the data as discussed in Section 4.2.3, per-pixel acquisition times that were shorter than the full measurement time were investigated by using shorter duration sections of each pixel's entire measurement data for the scenario with the wooden plank (seen in Figure 4.17). The resulting depth profiles, for the scenario with the wooden plank shown in Figure 4.17, for per-pixel acquisition times of $\tau_{acq} = 3.2$, 1, 0.5, and 0.1 ms, which correspond to image acquisition times of 41.0, 12.8, 6.4, and 1.3 seconds, respectively are shown in Figure 4.18. The average photons per pixel (PPP) in the target and the number of pixels with relevant target data (denoted 'sampled pixels') are given for each acquisition time.
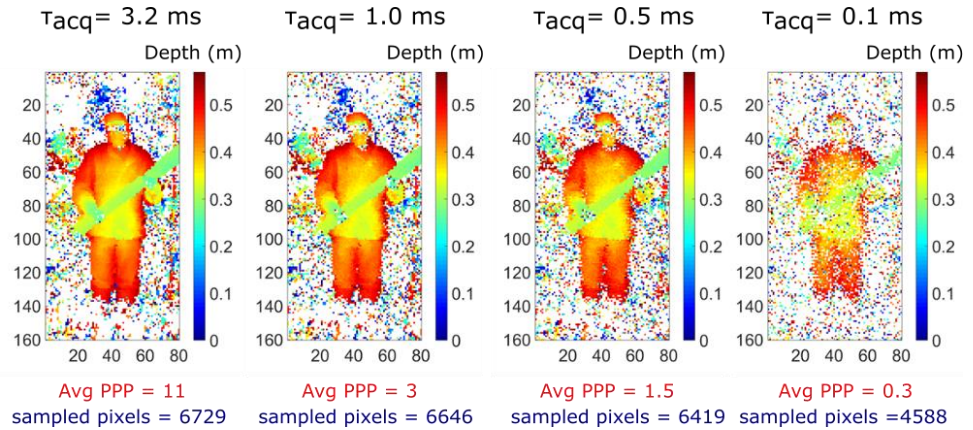
Figure 4.18: Depth profiles of an unobstructed target (an actor with a wooden plank held across the chest) at a range of 230 metres obtained using pixel-wise cross-correlation. The depth profiles were reconstructed from the full data with an acquisition time of $\tau_{acq} = 3.2$ ms per-pixel, and reduced acquisition times of $\tau_{acq} = 1.0$, 0.5, and 0.1 ms per-pixel.

Figure 4.18 shows that the number of photons collected by the system is approximately linear to the acquisition time of the scan with 11 average PPP for the 41 second scan and 0.3 average PPP for the 1.3 second scan. In addition, as the number of photons arriving back from the target decreased, the quality of the depth profile degraded, as fewer pixels

with relevant target data were successfully reconstructed. However, this degradation was not significant until the acquisition time was very low (i.e., 0.1 ms per pixel), meaning that much shorter measurement times are viable in these conditions. In addition, these results were obtained using only the pixel-wise cross-correlation algorithm and the use of the RDI-TV algorithm could result in a much better reconstruction. This demonstrates the potential of the single-pixel system for the rapid imaging and identification of hazardous objects in military scenarios.

4.5.2 Camouflaged targets

Using the same experimental parameters as used for the unobstructed scenarios, a series of measurements were performed with the target object and actor obscured by camouflage netting at 230 metres, as described in Section 4.4. The target scene consisted of an actor holding the object of interest (in this case a wooden plank held across the chest) approximately 1 metre behind two layers of commercially available camouflage netting. An example aggregated timing histogram from all 12,800 pixels from this measurement is shown in Figure 4.19.
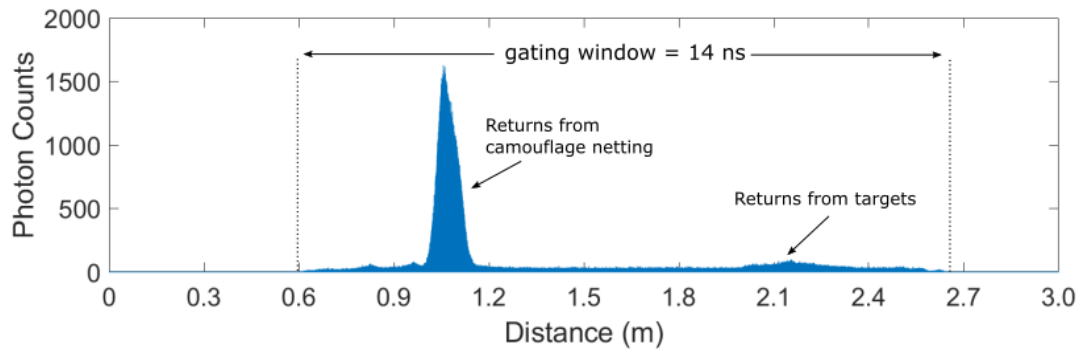
Figure 4.19: The aggregated timing histogram of a measurement of a target placed approximately one metre behind camouflage netting at a range of 230 metres from the system position. The larger peak represents the returns from the camouflage netting and the smaller peak represents the returns from the target. The zero point in the depth axis was chosen arbitrarily.

In comparison to the unobstructed measurements, two peaks were obtained in the aggregated timing histogram, one from the camouflage netting, and the other from the target behind the camouflage. The number of photon returns in the peaks arising from the camouflage netting and the target was found to be 401,612 and 52,348, respectively. This means that approximately 87% of the return photons were reflected by the

camouflage netting, and only 13% was reflected by the target. Figure 4.20 shows the resultant depth and intensity profiles obtained using pixel-wise cross-correlation.
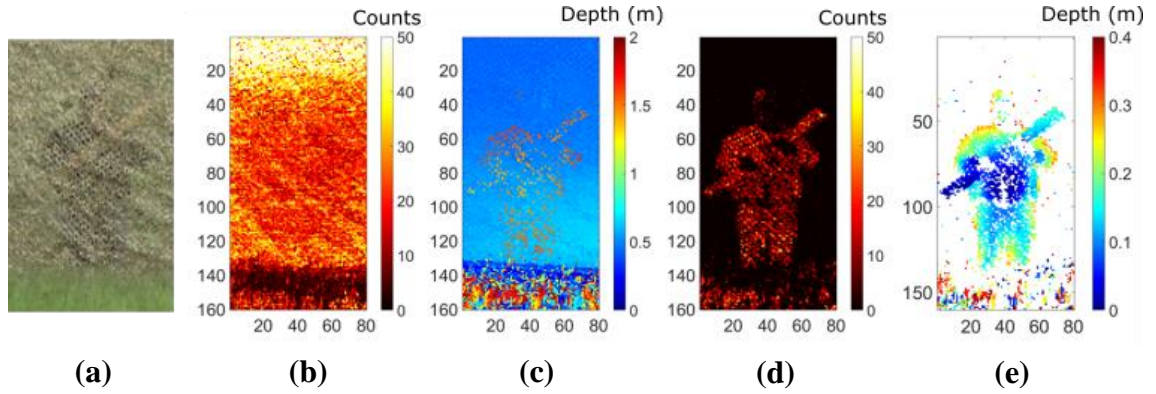
Figure 4.20: Analysis of a scene with an actor holding a wooden plank across his chest and standing one metre behind camouflage netting at an overall range of approximately 230 metres from the system position. Image (a) shows a photograph of the actor holding the wooden plank behind the camouflage net. (b) and (c) show the intensity and depth profiles of the target scene using the entire collected single-photon data. (d) and (e) show the intensity and depth profiles after time gating to exclude all data except those within a 0.6 metre range around the target location. These results were obtained using pixel-wise cross-correlation.

Figure 4.20 (b) and (c) show the intensity and depth profiles reconstructed using data from the full timing histogram. The depth profile in (c) shows a limited amount of detail from the obscured target where the photons propagated through gaps in the camouflage net. The camouflage netting is shown to be at a distance of 0.5 metres from the zero-depth reference point, whilst small regions of the target can be seen at a depth of approximately 1.5 m - a distance of 1 metre behind. Therefore, in order to more fully profile the target behind the camouflage, data gating was performed where only data selected from the 1900 timing bins (corresponding to a 0.6 m depth range centred around the target) were used in the depth and intensity reconstruction shown in Figure 4.20 (d) and (e). Using this gating approach, a good representation of the target profile was reconstructed, and both the actor and the wooden plank were easily identified. However, there were still many 'missing' pixels in the image where there was insufficient photon returns to provide a depth estimate. Therefore, in order to improve the quality of the depth and intensity profiles, the data was processed using the RDI-TV algorithm described in Section 4.3.2. Figure 4.21 and Figure 4.22 show the resultant depth and intensity profiles obtained using the cross-correlation and RDI-TV algorithms, for acquisition times of $\tau_{acq} = 3.2, 1.0, 0.5,$

and 0.1 ms per pixel. The results present down-sampled images of 40 × 80 pixels from the full 80 × 160 pixel scan.

Figure 4.21: Depth profiles of the target (actor holding a wooden plank) standing one metre behind camouflage netting for acquisition times of τ_{acq} = 3.2, 1.0, 0.5, and 0.1 ms pier-pixel reconstructed using (a) the pixel-wise cross-correlation algorithm and (b) the RDI-TV algorithm. This figure shows down-sampled images of 40 × 80 pixels.

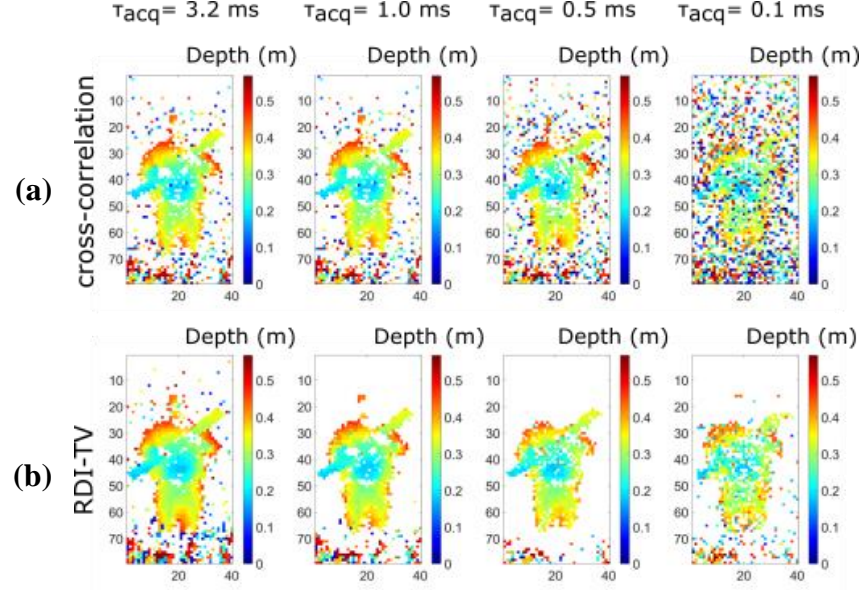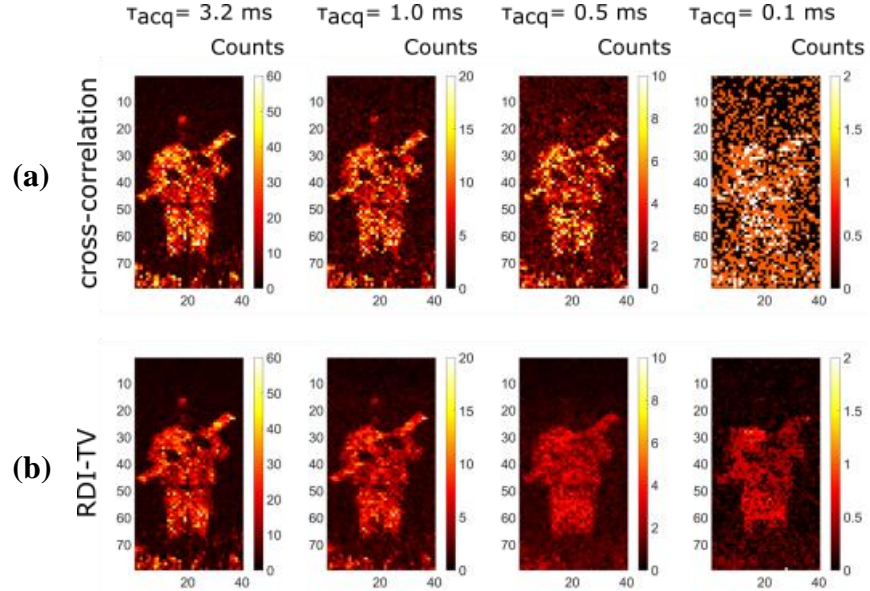*Figure 4.22: Intensity profiles of the target (actor holding a wooden plank) standing one metre behind camouflage netting for acquisition times of τ_{acq} = 3.2, 1.0, 0.5, and 0.1 ms pier-pixel reconstructed using (a) the pixel-wise cross-correlation algorithm and (b) the RDI-TV algorithm. This figure shows down-sampled images of 40 × 80 pixels.*

An analysis of the average PPP and number of sampled pixels for both algorithms is shown in Table 4.3.

Table 4.3: Analysis of the average PPP and number of sampled pixels for both cross-correlation and the RDI-TV algorithms.

Acquisition time per pixel (ms)	Average photons per pixel (PPP)		Sampled pixels	
	Cross-correlation	RDI-TV	Cross-correlation	RDI-TV
$\tau_{acq} = 3.2$	9.0	10.0	2594	2649
$\tau_{acq} = 1.0$	2.3	2.3	2918	2609
$\tau_{acq} = 0.5$	0.6	1.5	7250	2258
$\tau_{acq} = 0.1$	0.2	0.5	9567	1421

As expected, a decrease in the quality of the reconstructed images in Figure 4.21 and Figure 4.22 was observed in the depth and intensity profiles for both algorithms as the acquisition time was reduced. This was due to the photon returns being correspondingly lower (shown in Table 4.3). However, the depth estimates obtained using cross-correlation exhibit a much higher level of noise than the RDI-TV estimates at low acquisition times. In fact, the number of sampled pixels (indicated in Table 4.3) increases for the results obtained using cross-correlation due to the presence of noise. This can be linked to the limitation in the cross-correlation algorithm discussed previously in Section 4.3.1, where only the highest peak in the timing histogram is considered. Overall, the RDI-TV algorithm offers better restoration results where both the noise surrounding the target is reduced, and many of the 'missing' pixels of the target of interest are restored. This performance was achieved as a result of considering the spatial correlation between pixels, and the use of collaborative sparsity to limit the number of active depths. Moreover, the intensity profiles obtained using the RDI-TV algorithm were smoother and less noisy, especially at $\tau_{acq} = 0.1$ ms per pixel, where the average photon return from the human target is well below one photon per pixel. These results demonstrate that even behind a double layer of camouflage netting, the TCSPC approach alongside the appropriate reconstruction algorithm can provide fast depth and intensity imaging with approximately centimetre resolution – even in the sparse photon regime.

4.6 Conclusions and future work

A monostatic depth imaging system based on the TCSPC approach was used to obtain three-dimensional depth profiles of targets at a stand-off distance of 230 metres. The system was based on a single-pixel InGaAs/InP SPAD detector with a wavelength range

of $900 - 1700$ nm and a single-photon detection efficiency of approximately 35% at the operating wavelength of 1550 nm. A pulsed supercontinuum laser source alongside a series of high-performance filters was used to deliver a fibre-coupled illumination of $\lambda = 1550$ nm with an average optical power level of < 1 mW at a repetition rate of 19.5 MHz.

Two different target scenarios were investigated: (i) unobstructed targets and (ii) targets hidden behind a double-layer of commercially available camouflage netting. Field trials were performed as part of NATO SET 205 to evaluate the long-range imaging performance of the $\lambda = 1550$ nm depth imaging system. This investigation was successful in both the imaging and identification of a range of hazardous and non-hazardous targets in challenging outdoor scenarios with a high level of ambient background.

The first set of measurements were performed on unobstructed targets. The results showed that depth and intensity profiles of the targets could be reconstructed using a simple cross-correlation algorithm from data with acquisition times as low as 1 second. The target objects of interest were easily identifiable in the depth profiles with sub-centimetre depth resolution. The second set of measurements were performed using the same target set behind camouflage netting. The results showed that, by gating the timing histogram, the target profile could be successfully reconstructed with the target items easily identifiable. However, in this case, many missing pixels where no data was acquired were present in both the depth and intensity estimates. Therefore, the results obtained of targets behind camouflage netting were processed using the more sophisticated RDI-TV algorithm, which was designed to exploit spatial correlations in single-photon data. The RDI-TV algorithm provided good reconstruction results, with accurate depth and intensity estimates obtained with well below one photon per pixel.

This Chapter has demonstrated the use of TCSPC for obtaining high-resolution images for the identification of hidden objects at long-ranges in challenging outdoor conditions. The results presented in this Chapter demonstrate the excellent surface-to-surface resolution afforded by the TCSPC approach. Such high surface-to-surface resolution allows for much better reconstructions of targets in clutter than can be achieved by conventional depth imaging approaches such as non-single-photon depth imaging or range-gated LiDAR systems. This shows that the TCSPC approach is ideal for applications where the target scene is complex with multiple surfaces, such as imaging through foliage and vegetation. Improved background filtering, a larger aperture objective lens, and a higher optical power level would further enhance system

performance. Thus, future work will investigate the performance of the system at even longer stand-off distances, at kilometre ranges. The use of bespoke image processing algorithms such as the one presented in this Chapter will contribute to a more complete depth imaging model to inform next generation single-photon transceiver design and test the performance limits in terms of maximum stand-off distance, optical power requirements, and system frame rate. The use of this system for imaging targets in high levels of attenuating media will be discussed in the next Chapter of this Thesis.

4.7 Acknowledgements

4.8 References

4.1. R. Tobin, A. Halimi, A. McCarthy, X. Ren, K. J. McEwan, S. McLaughlin, and G. S. Buller, "Long-range depth profiling of camouflaged targets using single-photon detection," Opt. Eng. 57(3), 031303 (2017).

4.2. B. W. Schilling, D. N. Barr, G. C. Templeton, L. J. Mizerka, and C. W. Trussell, "Multiple-return laser radar for three-dimensional imaging through obscurations," Appl. Opt. 41(15), 2791–2799 (2002).

4.3. O. Steinvall, H. Larsson, F. Gustafsson, D. Letalick, T. Chevalier, A. Persson, and P. Andersson, "Performance of 3D laser radar through vegetation and camouflage," in *Laser Source and System Technology for Defense and Security*, 5792, 129–143 (2005).

4.4. M. Henriksson, H. Larsson, C. Grönwall, and G. Tolt, "Continuously scanning time-correlated single-photon-counting single-pixel 3-D lidar," Opt. Eng. 56(3), 031204 (2016).

4.5. A. McCarthy, X. Ren, A. D. Frera, N. R. Gemmell, N. J. Krichel, C. Scarcella, A. Ruggeri, A. Tosi, and G. S. Buller, "Kilometer-range depth imaging at 1550 nm wavelength using an InGaAs/InP single-photon avalanche diode detector," Opt. Express 21(19), 22098–22113 (2013).

4.6. A. McCarthy, R. J. Collins, N. J. Krichel, V. Fernández, A. M. Wallace, and G. S. Buller, "Long-range time-of-flight scanning sensor based on high-speed time-correlated single-photon counting," Appl. Opt. 48(32), 6241–6251 (2009).

4.7. A. Maccarone, A. McCarthy, X. Ren, R. E. Warburton, A. M. Wallace, J. Moffat, Y. Petillot, and G. S. Buller, "Underwater depth imaging using time-correlated single-photon counting," Opt. Express 23(26), 33911–33926 (2015).

4.8. A. Maccarone, A. McCarthy, A. Halimi, R. Tobin, A. M. Wallace, Y. Petillot, S. McLaughlin, and G. S. Buller, "Depth imaging in highly scattering underwater environments using time-correlated single-photon counting," in *Emerging Imaging and Sensing Technologies*, 9992, 99920R (2016).

4.9. Y. Altmann, A. Maccarone, A. McCarthy, G. Newstadt, G. S. Buller, S. McLaughlin, and A. Hero, "Robust Spectral Unmixing of Sparse Multispectral Lidar Waveforms Using Gamma Markov Random Fields," IEEE Trans. Comput. Imaging 3(4), 658–670 (2017).

4.10. R. Tobin, Y. Altmann, X. Ren, A. McCarthy, R. A. Lamb, S. McLaughlin, and G. S. Buller, "Comparative study of sampling strategies for sparse photon multispectral lidar imaging: towards mosaic filter arrays," J. Opt. 19(9), 094006 (2017).

4.11. X. Ren, Y. Altmann, R. Tobin, A. Mccarthy, S. Mclaughlin, and G. S. Buller, "Wavelength-time coding for multispectral 3D imaging using single-photon LiDAR," Opt. Express 26(23), 30146–30161 (2018).

4.12. A. M. Wallace, A. McCarthy, C. J. Nichol, X. Ren, S. Morak, D. Martinez-Ramirez, I. H. Woodhouse, and G. S. Buller, "Design and evaluation of multispectral LiDAR for the recovery of arboreal parameters," IEEE Trans. Geosci. Remote Sens. 52(8), 4942–4954 (2014).

4.13. J. M. Dudley, G. Genty, and S. Coen, "Supercontinuum generation in photonic crystal fiber," Rev. Mod. Phys. 78(4), 1135–1184 (2006).

4.14. J. M. Dudley and J. R. Taylor, *Supercontinuum Generation in Optical Fibers* (Cambridge University Press, 2010).

4.15. "SUPERK EXTREME/FIANIUM High Power Supercontinuum fibre laser series datasheet," (NKT Photonics, accessed 2019).

4.16. "MPD - InGaAs SPAD - gated datasheet," (Micro Photon Devices, accessed 2019).

4.17. "HydraHarp 400 datasheet," (PicoQuant, accessed 2019).

4.18. A. Tosi, A. Della Frera, A. Bahgat Shehata, and C. Scarcella, "Fully programmable single-photon detection module for InGaAs/InP single-photon avalanche diodes with clean and sub-nanosecond gating transitions," Rev. Sci. Instrum. 83(1), 013104 (2012).

4.19. Y. Kang, H. X. Lu, Y.-H. Lo, D. S. Bethune, and W. P. Risk, "Dark count probability and quantum efficiency of avalanche photodiodes for single-photon detection," Appl. Phys. Lett. 83(14), 2955–2957 (2003).

4.20. P. A. Hiskett, G. S. Buller, A. Y. Loudon, J. M. Smith, I. Gontijo, A. C. Walker, P. D. Townsend, and M. J. Robertson, "Performance and design of InGaAs/InP photodiodes for single-photon counting at 1.55 µm," Appl. Opt. 39(36), 6818–6829 (2000).

4.21. G. Ribordy, J.-D. Gautier, H. Zbinden, and N. Gisin, "Performance of InGaAs/InP avalanche photodiodes as gated-mode photon counters," Appl. Opt. 37(12), 2272–2277 (1998).

4.22. A. M. Pawlikowska, A. Halimi, R. A. Lamb, and G. S. Buller, "Single-photon three-dimensional imaging at up to 10 kilometers range," Opt. Express 25(10), 11919–11931 (2017).

4.23. Z.-P. Li, X. Huang, Y. Cao, B. Wang, Y.-H. Li, W. Jin, C. Yu, J. Zhang, Q. Zhang, C.-Z. Peng, F. Xu, and J.-W. Pan, "Single-photon computational 3D imaging at 45 km," in ArXiv190410341 Phys. (2019).

4.24. S. Chan, A. Halimi, F. Zhu, I. Gyongy, R. K. Henderson, R. Bowman, S. McLaughlin, G. S. Buller, and J. Leach, "Long-range depth imaging using a single-photon detector array and non-local data fusion," in ArXiv181204943 Phys. (2018).

4.25. Y. Altmann, X. Ren, A. McCarthy, G. S. Buller, and S. McLaughlin, "Lidar waveform-based analysis of depth images constructed using sparse single-photon data," IEEE Trans. Image Process. 25(5), 1935–1946 (2016).

4.26. D. Shin, F. Xu, F. N. C. Wong, J. H. Shapiro, and V. K. Goyal, "Computational multi-depth single-photon imaging," Opt. Express 24(3), 1873–1888 (2016).

4.27. A. Kirmani, D. Venkatraman, D. Shin, A. Colaço, F. N. C. Wong, J. H. Shapiro, and V. K. Goyal, "First-photon imaging," Science 343(6166), 58–61 (2014).

4.28. A. Halimi, R. Tobin, A. McCarthy, S. McLaughlin, and G. S. Buller, "Restoration of multilayered single-photon 3d lidar images," 2017 25th European Signal Processing Conference (EUSIPCO), Kos, 708-712 (2017).

4.29. A. Halimi, R. Tobin, A. McCarthy, J. Bioucas-Dias, S. McLaughlin, and G. S. Buller, "Restoration of multidimensional sparse single-photon 3D-LiDAR images," IEEE, Trans. Comput. Imaging, accepted (2018).

4.30. L. I. Rudin, S. Osher, and E. Fatemi, "Nonlinear total variation based noise removal algorithms," Phys. Nonlinear Phenom. 60(1), 259–268 (1992).

4.31. S. Boyd, N. Parikh, E. Chu, B. Peleato, and J. Eckstein, "Distributed optimization and statistical learning via the alternating direction method of multipliers," Found Trends Mach Learn 3(1), 1–122 (2011).

4.32. D. Killinger, "Free space optics for laser communication through the air," Opt. Photonics News 13(10), 36–42 (2002).

4.33. I. I. Kim, M. Mitchell, and E. J. Korevaar, "Measurement of scintillation for free-space laser communication at 785 nm and 1550 nm," in *Optical Wireless Communications II*, 3850, 49–63 (1999).

4.34. F. Nadeem, T. Javornik, E. Leitgeb, V. Kvicera, and G. Kandus, "Continental fog attenuation empirical relationship from measured visibility data," Radioeng., 19(4), 596-600 (2010).

4.35. N. J. Krichel, A. McCarthy, and G. S. Buller, "Resolving range ambiguity in a photon counting depth imager operating at kilometer distances," Opt. Express 18(9), 9192–9206 (2010).

4.36. Y. Liang, J. Huang, M. Ren, B. Feng, X. Chen, E. Wu, G. Wu, and H. Zeng, "1550-nm time-of-flight ranging system employing laser with multiple repetition rates for reducing the range ambiguity," Opt. Express 22(4), 4662–4670 (2014).

4.37. J. S. Massa, G. S. Buller, A. C. Walker, S. Cova, M. Umasuthan, and A. M. Wallace, "Time-of-flight optical ranging system based on time-correlated single-photon counting," Appl. Opt. 37(31), 7298–7304 (1998).

4.38. C. C. Cooksey, B. K. Tsai, and D. W. Allen, "A collection and statistical analysis of skin reflectance signatures for inherent variability over the 250 nm to 2500 nm spectral range", Proc. SPIE, 9082, 908206 (2014).

Chapter 5: Imaging through obscurants at λ = 1550 nm with a single-pixel depth imaging system

5.1 Introduction

In this Chapter, a scanning single-photon depth imager in the presence of atmospheric obscurants was investigated [5.1]. The time-of-flight (ToF) imager was based on the time-correlated single-photon counting (TCSPC) technique and used an individual InGaAs/InP single-photon avalanche diode (SPAD) detector operating at a wavelength of 1550 nm. The system was used to obtain high-resolution depth and intensity profiles of targets through a variety of obscurants in a 26-metre-long obscurant chamber using low optical power levels. This system has previously been successful in acquiring depth images for long ranges [5.2,5.3], in turbid water [5.4], and for multi-spectral imaging [5.5–5.8].

Several studies have shown that short-wave infrared (SWIR) wavelengths have lower levels of attenuation through water-based fog than wavelengths in the visible band because of the wavelength dependence of optical propagation due to the effects of particulate scattering [5.9,5.10]. However, others studies suggest that depending on the nature of the fog (for example, if the fog is extremely dense), there are no clear benefits to using longer wavelengths [5.11,5.12]. Studies have also shown that λ = 1550 nm light also has extremely high propagation (up to 10 times better than visible light) through different types of smoke with particle size distributions up to 1 µm [5.13].

Firstly, this Chapter will present an overview of the system configuration and key experimental parameters used in these field trials. Then, the computational methods used to obtain the depth and intensity profiles from single-photon data are described in Section 5.4. Finally, the performance of the system was evaluated in Section 5.5 for four types of obscuring media over a range of target stand-off distances. In addition, attenuation coefficient measurements comparing visible band and SWIR (λ = 1550 nm) light propagation in highly scattering media are also provided. Conclusions and future work are presented in Section 5.6.

5.2 System configuration and key parameters

This Section describes the system configuration and key experimental parameters used for all measurements presented in this Chapter. The monostatic depth imaging system used in these field trials was broadly similar to that used in the Chapter 4 of this

Thesis - with optical components and detector settings optimised for each measurement scenario as required. A detailed description of the system alignment, hardware, and optical components was provided in Chapter 4. A schematic of the imaging system used in these measurements is shown in Figure 5.1.
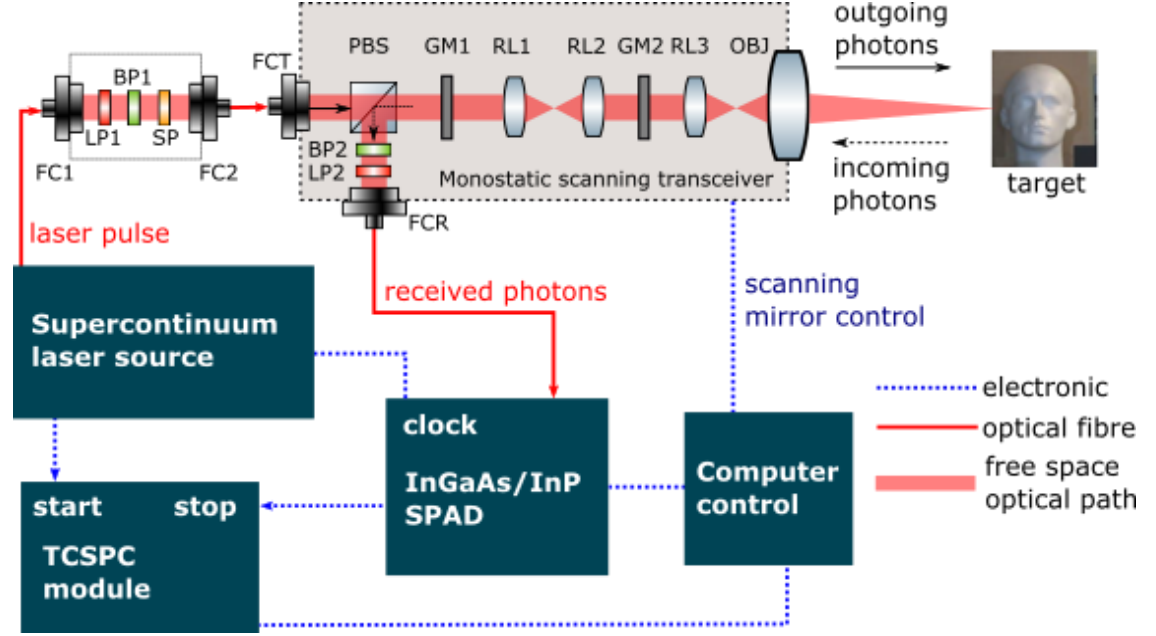
Figure 5.1: Schematic of the single-photon depth imaging system operated at a wavelength of 1550 nm. The system comprised of a pulsed supercontinuum laser source, a single-pixel InGaAs/InP SPAD detector, a monostatic scanning transceiver unit, and a TCSPC timing module. Optical components include: polarising beam splitter (PBS); fibre collimation packages (FC1, FC2, FCR, FCT); scanning galvanometer mirrors (GM1, GM2); relay lenses (RL1, RL2, RL3); objective lens (OBJ); longpass filters (LP1, LP2); shortpass filter (SP); bandpass filters (BP1, BP2).

The illumination source used for these measurements was a broadband supercontinuum pulsed laser (SuperK EXTREME EXW-12, NKT photonics) [5.14] operated at a repetition rate of 15.6 MHz. This laser was selected as it provided a high level of wavelength tunability with a selectable wavelength range of 450 − 2400 nm. This provided the option to investigate alternative operating wavelengths during field trials. A filter rig containing a series of high-performance optical filters was used to select a fibre-coupled illumination wavelength centred on λ =1550 nm. This set of filters was comprised of a longpass filter (LP1) with a cut-on wavelength of 1500 nm, a shortpass filter (SP) with a cut-off wavelength of 1845 nm, and a 10 nm full-width half-maximum (FWHM) bandpass filter (BP1) centred on 1550 nm. The average optical power used for all measurements presented in this Chapter was approximately 1.5 mW. This optical

power level was the maximum available power level from the laser source with these filters and provided eye-safe imaging at the illumination wavelength of 1550 nm.

Several target stand-off distances were used during these field trials depending on the type and density of obscurant used. Thus, due to the frequent change in target range, the parallax-free system configuration provided by the monostatic transceiver unit was highly beneficial during these field trials. The transmit and receive paths inside the transceiver unit were configured to be coaxial using a polarising beam splitter (PBS in Figure 5.1). This PBS was also used to de-multiplex the return signal from the common channel before the signal was routed to the detector. The two galvanometer mirrors (GM1 and GM2 in Figure 5.1) were used to raster scan the beam on the target scene.

An objective lens (OBJ in Figure 5.1) was used to both focus the outgoing illumination beam on the target and collect return photons, which had been scattered back from the target and from particles suspended in the air. The collected photons were subsequently routed to the receive channel and fibre-coupled to the single-photon detector via a 10 μm diameter core armoured optical fibre. A single-pixel InGaAs/InP SPAD detector (Micro Photon Devices, Italy [5.15]) with an operating wavelength range of 900 – 1700 nm and a single-photon detection efficiency of 35% at λ = 1550 nm (for a 5 V excess bias) was used in these measurements.

As discussed in Chapter 4, light scattered from optical components within the transceiver unit can cause significant levels of back-reflections due to the monostatic configuration of the system. This can result in 'false' target peaks in the timing histogram and could result in saturation of the highly sensitive SPAD detector. Thus, the detector was operated in electronically gated mode to avoid these spurious back-reflections. This means that the detector was activated approximately in synchronisation with the expected pulsed laser return and de-activated at other times. For the measurements presented in this Chapter a detector gate width of 30 ns was selected, equivalent to a distance of 9 metres. As previously discussed in Chapter 3, relatively high levels of afterpulsing effects are typically found in InGaAs/InP SPAD detectors. This occurs when charge carriers are trapped in defects that are subsequently released much later causing spurious avalanches, directly leading to an increased background count level and to a reduction in the signal-to-noise ratio. Thus, in order to reduce the effects of afterpulsing, the SPAD detector was de-activated for a hold-off time of 40 μs after each photon detection event to allow trapped charge carriers to be released without resulting in further avalanche events.

To reduce the effects of ambient light on the background level, the receive channel was spectrally filtered using a 10 nm FWHM bandpass filter and a longpass filter (LP2) with a cut-on wavelength of 1500 nm. These filters have a high transmission at the operating wavelength while providing sufficient out-of-band rejection. The overall timing jitter of the system was measured to be approximately 220 ps (FWHM) on a uniform, cooperative surface. The detector was a significant source of the overall system jitter; however, the laser source and data acquisition hardware also contribute.

To measure photon ToF, the pulsed laser source provided an electrical start trigger to the TCSPC module (HydraHarp 400, PicoQuant, Germany [5.16]). The stop trigger was provided by an electrical output from the SPAD module for each detection event. The TCSPC module was configured to record time-tags for the detection events with a 2 ps timing bin resolution and this data was then transferred via USB to the control computer. A summary of these key system parameters is given in Table 5.1.

Table 5.1: Summary of key system parameters

Parameter	Value/comment
Illumination source	NKT Photonics supercontinuum (SuperK EXTREME EXW-12)
Illumination wavelength	1550 nm (10 nm) FWHM
Laser repetition rate	15.6 MHz
Average optical power	~ 1.5 mW
Obscurants	glycol-based smoke; white canister smoke; black canister smoke; water fog
Detector	Fibre-coupled, electrically gated-mode InGaAs/InP SPAD, MPD (www.micro-photon-devices.com)
Detector single-photon detection efficiency	~35% at λ = 1550 nm
Detector excess bias	5 V
Detector gate width	30 ns
Detector hold-off time	40 μs
Data acquisition hardware	HydraHarp 400, PicoQuant (www.picoquant.com)
Histogram timing bin size	2 ps timing bin width
System timing jitter	~ 220 ps
Spectral filters in transmit channel	Longpass: Cut-on 1500 nm, transmission >98% (ThorLabs, FELH1500) Shortpass: Cut-off 1845 nm, transmission >90% (Spectrogon, SP-1845) Bandpass: 10 nm wide, 1550 nm central wavelength, transmission >95% (Edmund Optics, #86-091)
Spectral filters in receive channel	Longpass: Cut-on 1500 nm, transmission >98% (ThorLabs, FELH1500) Bandpass: 10 nm wide, 1550 nm central wavelength, transmission >95% (Edmund Optics, #86-091)

5.3 Experimental layout

This Section provides details of the target configurations, obscurant types, and attenuation measurements performed for the experiments detailed in this Chapter.

5.3.1 Target configuration

The measurements presented in this Chapter were performed within an obscurant chamber housed in an indoor facility at The French-German Research Institute of Saint-Louis (ISL), France. The obscurant chamber (as shown in Figure 5.2) had approximate dimensions of 26 × 2.3 × 2.5 metres (L × W × H). During measurements, the obscurant was contained in the chamber by plastic sheeting that ran the entire length of the chamber. A black fabric curtain was used for further containment during obscurant generation, and then subsequently drawn back to allow for measurements of the target within the chamber. This obscurant chamber has been previously used to examine range-gated active imaging at SWIR wavelengths using non single-photon detection based approaches [5.13,5.17]. The use of this facility allowed for stable atmospheric conditions, experimental repeatability, and slow obscurant dispersion.

(a)   (b)
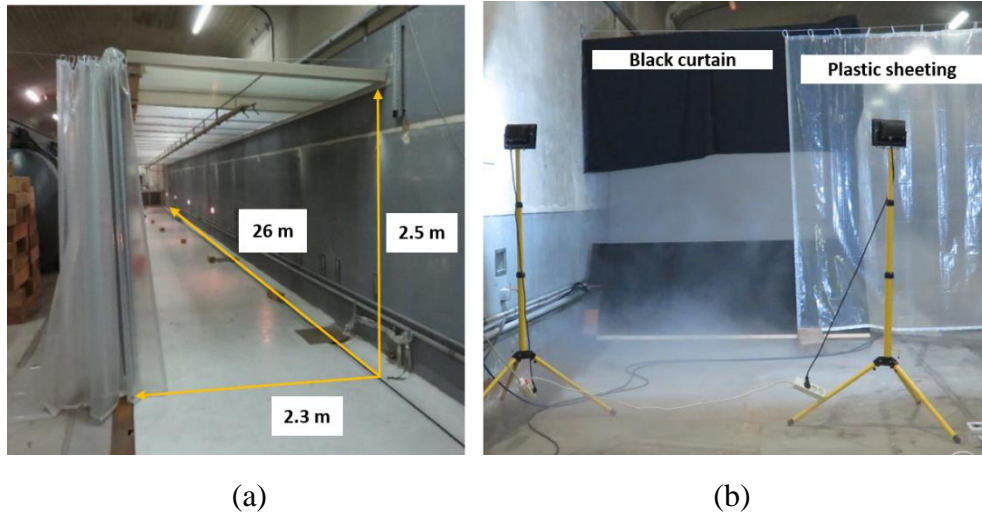
Figure 5.2: (a) Photograph from the rear of the chamber with no obscurant
present. (b) Photograph from the front of the chamber with obscurant present.
The chamber was lined with plastic sheeting to help contain the obscurant for
the duration of the measurement set. A black curtain was used to limit the
dispersion of the obscurant before measurements.

The target scene for all measurements presented in this Chapter comprised of a life-size polystyrene head mounted directly in front of a smooth wooden backboard, as shown in Figure 5.3.
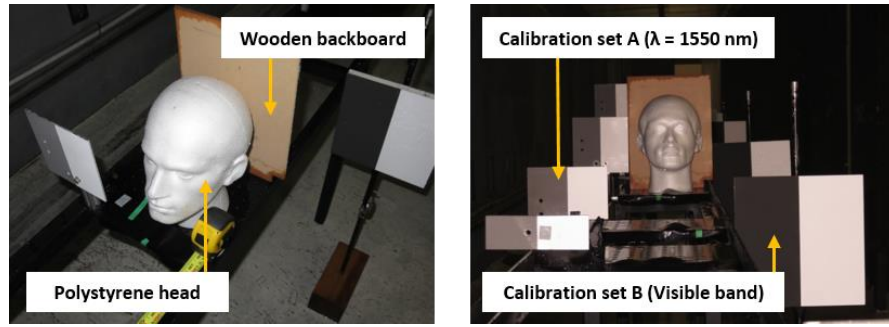
Figure 5.3: Photographs of the life-size polystyrene head target and wooden backboard in the obscurant chamber mounted alongside calibration panel sets A and B.

Two sets of calibration panels were positioned at several points throughout the chamber to calculate the level of attenuation in the chamber for both λ = 1550 nm and the visible band (400 – 800 nm wavelength range) in each measurement. The polystyrene head, wooden backboard, and both sets of calibration panels were mounted on a metal rail so that the target scene could be easily positioned in the chamber. This set-up also allowed for quick yet calibrated changes to the target range. Calibration set A(1,2,3,4) was used for the λ = 1550 nm measurements as indicated in Figure 5.3, and set B(1,2,…,8) for the visible band. Set A comprised four panels which were mounted to the left of the polystyrene head at one metre equidistant increments. These panels had dimensions of 150 × 150 mm and were made from a thin sheet of aluminium. Half of the panel had a 94% reflectance Permaflect coating [5.18] and the other half had a 18% reflectance Permaflect coating. These coatings act as near Lambertian reflectors to provide a good contrast measurement. In order to attain an accurate measurement of the level of scattering at the target position for λ = 1550 nm, calibration panel A3 was placed nominally in the same plane as the front of the polystyrene head.

A Si-based camera (Prosilica GT1380) with a 100 mm EFL objective lens (NIKON 18-300 zoom lens) was used to measure the visibility in the visible band using a passive imaging approach. These measurements were achieved using contrast measurements from calibration set B. This measurement approach used a combination of broadband illumination and detection in the wavelength band 400 – 800 nm. This wavelength band can be approximated to the responsivity of the human eye. The eight panels of calibration set B extended from the front to the rear of the chamber at a pre-determined spacing. Each panel had dimensions of 250 × 250 mm and was coated with 5% and 94% Permaflect. This visible camera system was placed at approximately 27 metres from the entrance of the obscurant chamber, 10 metres behind the λ = 1550 nm depth imaging

system. A schematic diagram and photograph of the target set-up at 5 metres from the front of the chamber is shown below in Figure 5.4.
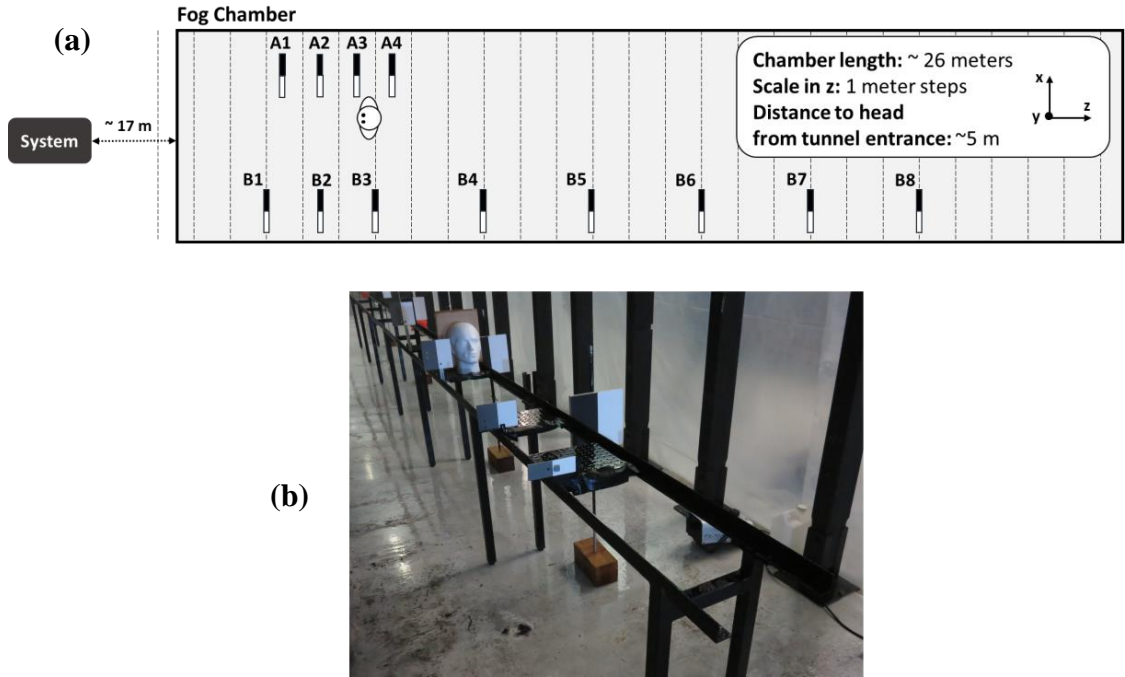
Figure 5.4: (a) A schematic diagram of the experimental layout inside the 26-metre-long fog chamber with the polystyrene head placed at approximately 5 metres. Calibration set A(1-4) was used to calculate the attenuation coefficient for λ = 1550 nm and set B(1,2...,8) was used to measure the attenuation coefficient for the visible band. (b) Photograph of the target configuration for set-up #2 prior to measurements.

Three different target configurations were used for the measurements presented in this Chapter. The configuration was dependent on the type of obscurant used in each measurement. In the first configuration (set-up #1), the target was mounted on the rail at a distance of ~ 9.5 metres from the front of the chamber alongside calibration set A. The effects of black canister smoke were investigated at this range. In the second target configuration (set-up #2), the target and calibration set A were placed at a distance of 5 metres from the front of the chamber. The effects of water vapour were also investigated at this range. Finally, for the third target configuration (set-up #3), the target and calibration set A were moved to the end of the obscurant chamber at a distance of 24 metres from the front of the chamber (41 metres from the system position). The effects of white canister smoke, glycol vapour, and water fog were investigated at this range. For scenes at 5 and 9.5 metres into the obscurant, an objective lens with an effective focal length (EFL) of 200 mm and an aperture of 50 mm was used, providing a field-of-view

(FoV) of approximately 350 × 275 mm and 335 × 270 mm, respectively. For targets at 24 metres into the obscurant, a 500 mm EFL objective lens with an aperture size of 80 mm was used providing a FoV of approximately 335 × 270 mm. The illumination beam diameter at the target was approximately 2 mm. The per-pixel acquisition time for measurements using white canister smoke, glycol vapour, and water fog was 3 ms, and a 6 ms per pixel acquisition time was used for black canister smoke, corresponding to total acquisition times of approximately 30 seconds and 60 seconds, respectively. A summary of the experimental set-ups and key parameters used for each configuration is given in Table 5.2.

Table 5.2: Summary of the three experimental set-ups used in this Chapter and key parameters used in these field trials.

Parameter	Value/comment		
Set-up #N	**Set-up #1**	**Set-up #2**	**Set-up #3**
Stand-off distance to chamber	17 metres		
Stand-off distance within obscurant	5 metres	9.5 metres	24 metres
Obscurants	water fog	black canister smoke	white canister smoke glycol vapour water fog
Objective lens focal length	200 mm	200 mm	500 mm
Objective lens aperture	Ø50 mm	Ø50 mm	Ø80 mm
Illumination beam diameter at target	~ 2 mm	~2 mm	~ 1.5 mm
Scan area (X×Y)	~350 × 275 mm	~350 × 275 mm	~335 × 270 mm
Pixels (X×Y)	117 × 92	113 × 97	115 × 93
Acquisition time per pixel	3 ms per pixel (6 ms per pixel for black canister smoke)		
Spacing of Calibration Set(A#)	1 metre equidistant spacing		
Spacing of Calibration Set(B#)	B1-3: 1.5 metre equidistant spacing B4-8: 3 metre equidistant spacing		

5.3.2 Obscurants used in this study

Four different types of obscurants were used in this study: black canister smoke, white canister smoke, glycol vapour, and water fog. Both the black and white smoke were generated by igniting Björnax AB Ventilax smoke canisters. These canisters were based on the combustion of potassium chlorate and ammonium chloride and produced particles with a particle diameter distribution of approximately 400 nm - typical of the type of smoke found in most pyrotechnic smoke grenades. A transmission spectrum for this particular smoke can be found in ref. [5.19]. The glycol vapour was generated by a JB Systems FX-700 smoke machine vaporising Universal Effects ST-Smoke Fluid Light. The glycol vapour had a particle size distribution of approximately 1 µm, meaning the

particles were larger than those from the canister smoke. A system of high-pressure nozzles mounted along the ceiling of the full length of the obscurant chamber generated the water fog. These nozzles were capable of creating a very fine mist, with an average particle size distribution of $18 \pm 8 \, \mu m$ (measured using a LISST-100X granulometer (Sequoia Scientific Inc.)) which is a realistic particle size for atmospheric water particles [5.20]. Further details on these obscurants is provided in ref. [5.13]. Photographs showing each of these obscurants in the obscurant chamber are shown in Figure 5.5.

(a)   **(b)**   **(c)**   **(d)**
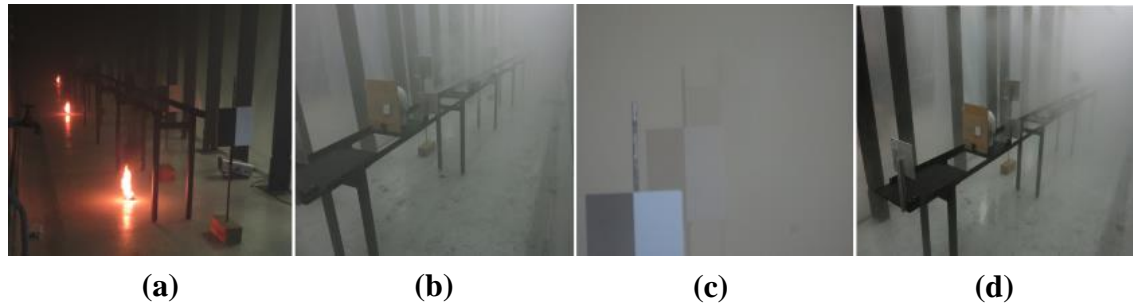
Figure 5.5: Photographs of (a) the black canister smoke ignited in the chamber; (b) the target set up with a low density of white canister smoke; (c) view of the target scene at the start of a measurement with glycol vapour; and (d) view of the target set-up within the chamber with a low density of water fog.

The obscurant was pumped into the chamber (or, in the case of the canister smoke, ignited in the chamber at equidistant intervals) until a sufficient density was achieved. Fans were used to help homogenise the obscurant throughout the length of the chamber. Over the duration of the measurement set, the obscurant would slowly disperse out of the open ends of the chamber until the scene was fully visible as shown in Figure 5.6.

Figure 5.6: Photographs taken during a measurement set showing the dispersion of glycol vapour from the obscurant chamber over the duration of the measurement set.

5.3.3 Attenuation measurements for $\lambda = 1550$ nm and the visible band

As discussed previously in Chapter 2 of this Thesis, scattering and absorption effects from particles suspended in the atmosphere can result in a significant reduction in the signal received by the light detection and ranging (LiDAR) system. Therefore, it was necessary to obtain the attenuation coefficient, α, for each measurement made in obscurants for both $\lambda = 1550$ nm and the visible band due to variations in the obscurant density over the duration of the measurement set. These attenuation measurements were made using calibration panels from set A and set B as discussed previously in Section 5.3.1. The methods used to calculate the attenuation coefficient for both SWIR and visible wavelengths are described in this Section. It is important to note that the methods used to calculate the attenuation coefficients for both the visible and SWIR wavelengths may have been affected differently by obscurant inhomogeneity since very different spatial averaging is used in the two measurement approaches.

5.3.3.1 Calculating the attenuation coefficient for the visible band

In order to make a measurement of the attenuation coefficient for the visible part of the spectrum, the contrast over a central region of the 5% and the 94% Permaflect in calibration set B was made. Each measurement was performed in the presence of an obscurant, and then compared with the same region of the calibration panel in a reference set of images with good visibility (i.e. no obscurant present). At the beginning of each measurement set, when the obscurant is thickest, the visible band images show very poor contrast. However, the contrast improves as time passes and the obscurant disperses from the chamber. In order to calculate the visible band attenuation coefficient, $N_{AL(visible)}$, the atmospheric visibility was calculated using the contrast measurements from the images acquired with the passive imaging system. As defined by Koschmieder [5.21], atmospheric visibility, V, is related to the attenuation coefficient, α, by the law:

$$V = \frac{1}{\alpha_{visible}} \ln\left[\frac{C_0}{C_{th}}\right],$$
(5.1)

where C_0 corresponds to the target contrast ($C_0 = 1$) and C_{th} is set equal to 0.05, as discussed in Chapter 2. This is the human eye's minimal perceptible contrast as defined by the CIE (International Commission on Illumination) [5.22]. This corresponds to a visibility limit of approximately three attenuation lengths for the human eye. This limit was calculated for each measurement performed in obscurant to find the point at which

the contrast is 5% through use of polynomial fitting. Given these values, the relation between visibility and attenuation can be expressed as:

$$\alpha_{visible} = \frac{3}{V}. \tag{5.2}$$

For the measurements presented in this Chapter, the visibility calculations had good agreement with estimations made with the naked eye.

5.3.3.2 Calculating the attenuation coefficient for λ = 1550 nm

Due to the wavelength dependence on the level of particulate scattering in the atmosphere [5.23–5.26] (discussed previously in Chapter 2 of this Thesis), a separate measurement of the attenuation coefficient by the λ = 1550 nm imaging system was made for each single-photon measurement. This was calculated by examining the single-photon return from a known region of calibration panel A3 (as indicated in Figure 5.7) when compared to a free-space reference measurement of exactly the same part of the panel, when no obscurant was present.

(a)   **(b)**
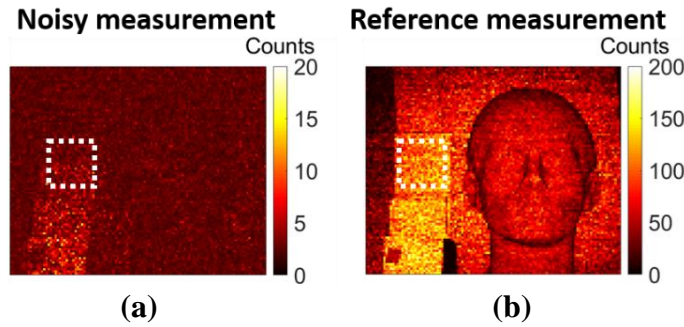
Figure 5.7: Intensity profiles obtained using pixel-wise cross-correlation of (a) a noisy measurement taken of the target in a high level of scattering and (b) a reference measurement taken of the same scene with no obscurant present. The region of calibration panel A3 used to calculate the attenuation coefficient is indicated in each intensity profile.

The number of attenuation lengths ($N_{AL(1550\ nm)}$) between the transceiver and target was then calculated from the Beer-Lambert law as follows:

$$N_{AL(1550nm)} = \alpha_{1550nm}d = \frac{1}{2}\ln\left[\frac{n_0}{n}\right], \tag{5.3}$$

where d is the one-way distance of propagation in the obscurant, α_{1550nm} is the attenuation coefficient for the level of obscurant present in the chamber, n is the number of returned photons in the presence of obscurant, and n_0 is the number of returned photons in the

reference measurement (i.e., in the absence of obscurant), as discussed in Chapter 2 [5.27]. These measurements were performed for each obscurant type from the highest attenuation level to the lowest as the obscurant dispersed out of the chamber.

5.4 Computational Methods

In recent years, there has been great interest in the development of reconstruction algorithms for single-photon data processing, with several algorithms demonstrating good reconstruction results of single-photon data in scenarios where the background level is relatively high and the return signal is very low [5.28–5.31]. These algorithms were all designed to improve the quality of the reconstructed depth and intensity profiles in the sparse-photon regime. This Chapter presents results obtained using three algorithms of varying complexity; (i) pixel-wise cross-correlation, (ii) the Restoration of Depth and Intensity using the Total Variation (RDI-TV) algorithm, and (iii) the Multidimensional Nonlocal Reconstruction of 3D (M-NR3D) images algorithm.

5.4.1 Pixel-wise cross-correlation algorithm

The pixel-wise cross-correlation algorithm is a computationally simple algorithm that can be used to provide estimates of depth and intensity in single-photon data by comparing the data to a known instrumental response of the system. This algorithm was described in detail in Chapter 4 of this Thesis. The instrumental response function used for this analysis was acquired using a 100 second integration time single-pixel measurement, on the 94 % reflectivity region of panel A3 providing a uniform response.

Since the cross-correlation algorithm approximates the depth position of the target assuming the absence of background noise, it performs poorly in the presence of high levels of obscurants due to low levels of photon returns from the target. Figure 5.8 shows timing histograms taken from a single pixel in measurements of the target scene under the same illumination conditions taken in glycol vapour at $\alpha_{1550nm} = 0.08$ m^{-1} (i.e., low level of obscurant) and $\alpha_{1550nm} = 0.18$ m^{-1} (i.e., high level of obscurant). Figure 5.8 (a) indicates that in clear conditions, the timing bins containing the target return peak are easily discernible. However, in the presence of an obscuring media as indicated in Figure 5.8 (b) the corresponding target bins may contain a similar number of photon counts to the background level and no discernible target return peak due to high levels of scattering. This high level of background can potentially lead to an incorrect depth estimate, as cross-correlation is only effective at finding the highest peak in the histogram. This highlights the need to apply advanced processing algorithms capable of dealing with

scenarios involving high levels of scatter or low target returns such as the RDI-TV or M-NR3D algorithms. Figure 5.8 (c) and (d) also show aggregated timing histograms (containing data acquired from all 10,695 pixels) of the target scene through 24 metres of glycol vapour obtained with the cross-correlation algorithm. The return peaks from the target are shown in Figure 5.8 (c) with an attenuation coefficient of α_{1550nm} = 0.08m^{-1}. The average background level per timing bin at this level of attenuation was approximately 5 counts. When the glycol vapour is much denser (i.e., α_{1550nm} = 0.18m^{-1}), the level of scattering increases resulting in a higher background level of 25 counts per timing bin and a reduced signal-to-noise ratio.
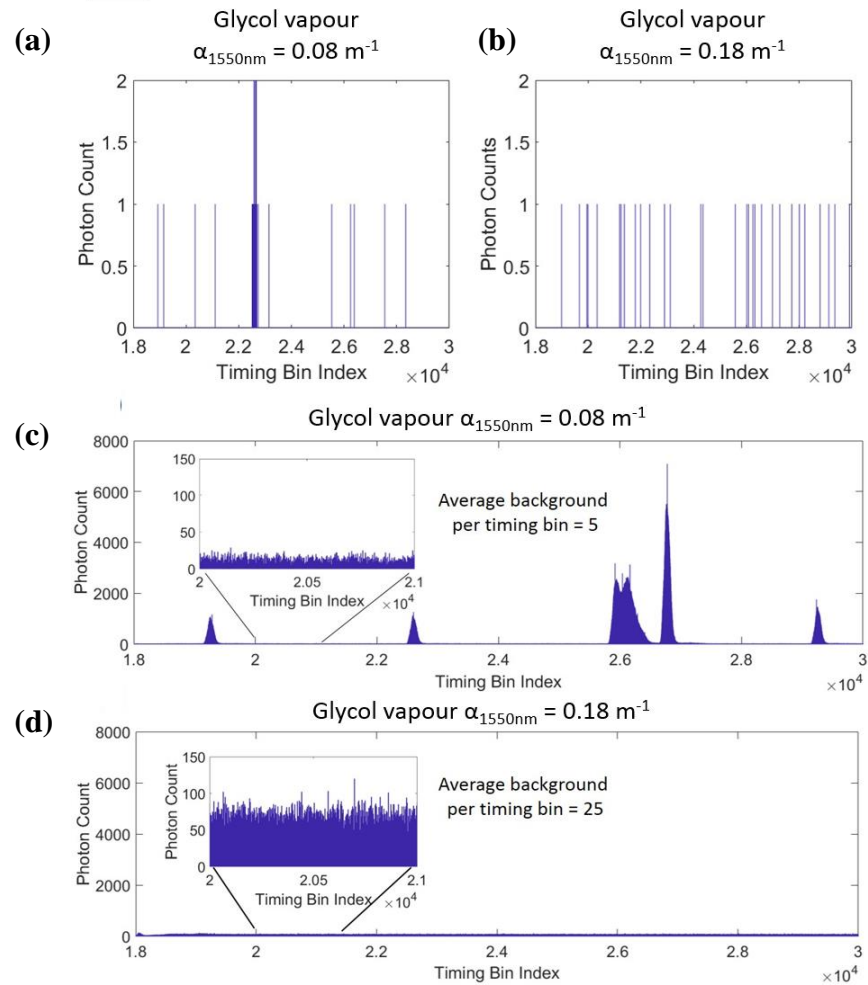
Figure 5.8: (a) and (b) show single pixel timing histograms extracted from a measurement of the target through 24 metres of glycol vapour. Each histogram shows the number of photon returns obtained in a single pixel over an acquisition time of ~ 3 ms for (a) α_{1550nm} = 0.08 m^{-1} (i.e., low level of obscurant) and (b) α_{1550nm} = 0.18 m^{-1} (i.e., high level of obscurant). (c) and (d) show aggregated timing histograms of the target and calibration set A# for attenuation coefficients of 0.08 m^{-1} and 0.18 m^{-1}, respectively.

5.4.2 RDI-TV algorithm

As previously discussed, the presence of obscuring media can lead to a high level of photon scattering. Due to low levels of photon returns, this can lead to an increase in noise in single-photon depth and intensity measurements or even pixels where no information is acquired, resulting in a degradation in image quality. This means that the cross-correlation algorithm does not perform well in these conditions. In order to process single-photon data acquired in high levels of scattering media, a more sophisticated algorithm was applied to the data obtained at these field trials. The RDI-TV algorithm has been previously shown to be a good candidate algorithm for single-photon data reconstruction where there is only one target depth but contains multiple surfaces [5.32,5.33]. This algorithm is described in detail in Chapter 4 of this Thesis and in ref. [5.33].

5.4.3 M-NR3D algorithm

A third algorithm, M-NR3D, was used to process the data presented in this Chapter. This algorithm differs from the RDI-TV algorithm in that it considers the full histogram cube as it contains more information than the preliminary estimates of depth (D_{init}) and intensity (I_{init}). M-NR3D is based on the minimisation of a cost function that accounts for the Poisson statistics of the single-photon data, and improves the methodology used in the RDI-TV algorithm. It achieves this by (i) accounting for non-local spatial correlations between target reflectivities; (ii) assuming the presence of few number of peaks in each group of pixel neighbourhoods [5.34–5.36]; (iii) accounting for the correlations between multi-temporal 3D images of the target scene acquired in succession. In this Chapter, the algorithm will be denoted as NR3D when performing an independent processing of the data and M-NR3D for a joint processing of several images. The cost function C_f used to restore multi-temporal 3D images composed of K frames is given by:

$$C_f(X) = \sum_{k=1}^{K} L_k(Y_k, X_k) + T_1\phi_1(X) + T_2\phi_2(X), \tag{5.4}$$

where $L_k(Y_k,X_k)$ is the log-likelihood of the data, X_k is the matrix representing the cloud points of the data after denoising for the kth frame, and $T\varphi_1$ and $T\varphi_2$ are two regularization terms. Note that in contrast to the RDI-TV algorithm, which processes images independently, the M-NR3D algorithm performs a joint processing in order to improve the restoration quality. Further details on the M-NR3D algorithm are given in ref. [5.37].

5.5 Experimental results and discussion

This Section presents results obtained using the pixel-wise cross-correlation, the RDI-TV, and the M-NR3D algorithms from data acquired through high levels of scattering media. For scenarios where there was a very high level of scattering and where the reconstructed depth profiles are significantly degraded, a signal-to-reconstruction error (SRE) value is provided. The SRE is given as:

$$SRE = \sum_{i=1}^{N_p} 10 \log_{10} \left(\frac{d_{ref}(i)^2}{(d_{ref}(i) - d(i))^2} \right), \tag{5.5}$$

where d_{ref} is the reference depth profile (or ground-truth image), d is the reconstructed depth profile, and N_p is the total number of pixels in the image. The ground truth image is taken from data with the highest quality depth reconstruction, no obscurant present, and with the longest acquisition time available. The SRE values are given in decibels (dB) with a higher SRE representing a better reconstruction [5.37]. This simple metric gives an indication of the reconstructed quality of an image taken in degraded conditions when compared to the reference image taken in clear conditions.

5.5.1 Black canister smoke

The first obscurant investigated was the black canister smoke at a stand-off distance of 9.5 m into the obscurant chamber (approximately 26.5 m from the system position). The canisters containing the black smoke were ignited at several points within the chamber and, once a sufficient level of obscurant was present, measurements were performed using both the $\lambda = 1550$ nm system and the visible system to acquire attenuation coefficients for both wavelengths. The dispersion rate of the black smoke from the chamber allowed for a 60 second measurement (6 ms per-pixel) duration repeated every 60 seconds for an overall measurement duration of approximately 8 minutes. A plot of the attenuation coefficient for both the visible band and $\lambda = 1550$ nm is shown in Figure 5.9.

Figure 5.9: A comparison of the attenuation coefficient as a function of time for both λ = 1550 nm and the visible band for a target position of 9.5 metres in black canister smoke.

The results show that attenuation coefficient at λ = 1550 nm is lower than in the visible band over the entire duration of the measurements. The λ = 1550 nm attenuation coefficient measured was very low meaning that a high level of propagation was achieved, even at the start of the measurement set. Reconstructed depth and intensity profiles obtained using pixel-wise cross-correlation from data obtained at the start of the measurement set are shown in Figure 5.10.

(a) **(b)**
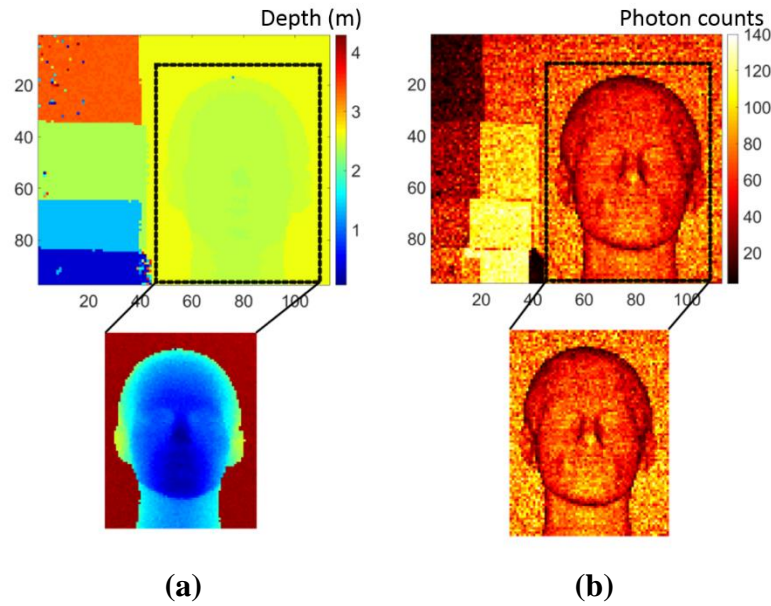
Figure 5.10: Reconstructed depth (a) and intensity (b) profiles of the target scene through 9.5 metres of black canister smoke for an attenuation coefficient of α$_{1550\ nm}$ = 0.1 m^{-1} obtained using pixel-wise cross-correlation.

127

These results were obtained at attenuation coefficients of approximately $\alpha_{1550\,nm} = 0.1$ m^{-1} and $\alpha_{visible} = 0.57$ m^{-1}, equivalent to $N_{AL(1550\,nm)} = 0.95$ and $N_{AL(visible)} = 5.4$. Figure 5.10 (a) shows that both the depth and intensity profiles were successfully reconstructed from the first measurement in the set meaning that a more challenging scenario was required to evaluate the system performance. Moreover, these results were obtained using only the simple pixel-wise cross-correlation algorithm with no need for the more sophisticated reconstruction algorithms. These results demonstrate a clear advantage of SWIR operation compared with visible detection approaches in this type of obscurant.

5.5.2 White canister smoke

Due to obtaining results from the very start of the measurement set with black smoke, the measurements were repeated with the target placed at a more challenging stand-off distance of 24 metres into the obscurant (approximately 41 metres from the system position). A white version of the canister smoke was used for these measurements. A shorter per pixel acquisition time of 3 ms was used, resulting in a measurement format of a 30 second measurement duration repeated every 60 seconds for an overall period of approximately 7 minutes. The attenuation coefficient measurements for both the visible band and $\lambda = 1550$ nm are shown in Figure 5.11.
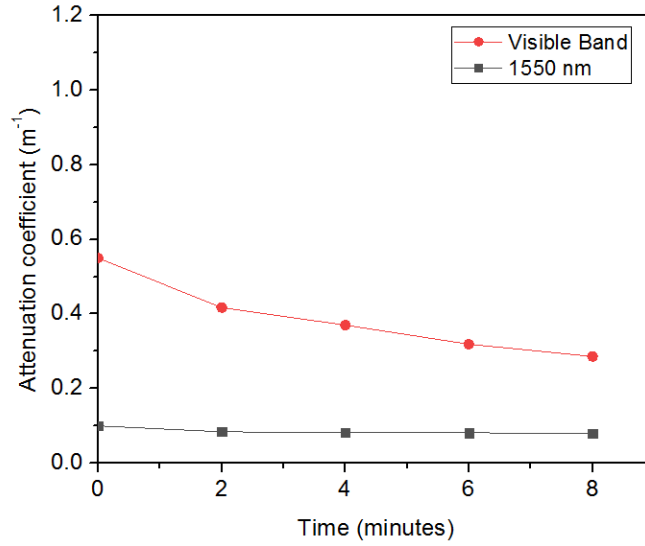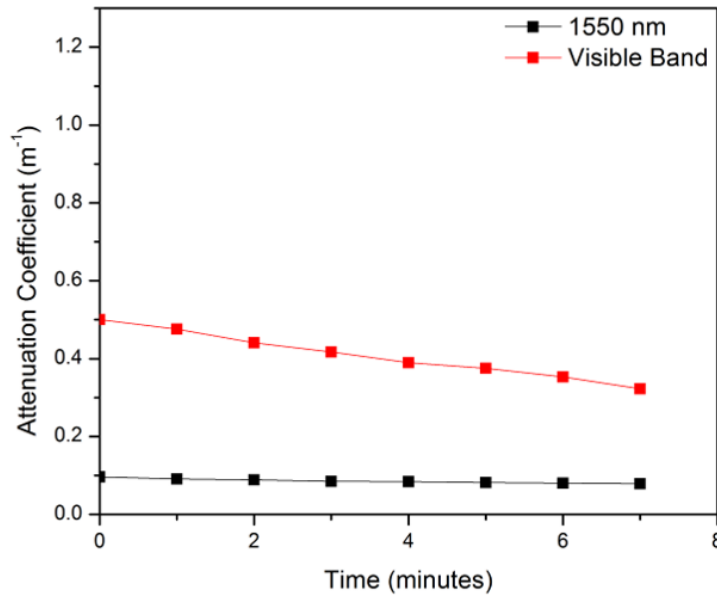

Figure 5.11: A comparison of the attenuation coefficient as a function of time
for both $\lambda = 1550$ nm and the visible band for a target position of 24 metres
in white canister smoke.

Attenuation coefficients of $\alpha_{1550nm} = 0.1$ m^{-1} and $\alpha_{visible} = 0.5$ m^{-1}, equivalent to $N_{AL(1550\,nm)} = 2.4$ and $N_{AL(visible)} = 12$ were measured at the beginning of the attenuation set.

The visible band attenuation decreases over the measurement duration while the SWIR band remains relatively constant. Figure 5.12 shows results obtained in both clear conditions and in high density white canister smoke. In order to provide a good visual representation of the polystyrene head, depth data were only selected from a range of 0.2 metres around the target and a subset of pixels containing only target information from the head is shown. Figure 5.12 (a) and 5.12 (d) show RGB photographs of the target scene at the point of measurement for both clear conditions and in white canister smoke; Figure 5.12 (b) and 5.12 (e) show the depth profiles obtained using the pixel-wise cross-correlation approach. Figure 5.12 (c) and Figure 5.12 (f) show the intensity maps obtained by summing events over a 200-bin range centred on the highest value in the cross-correlation.
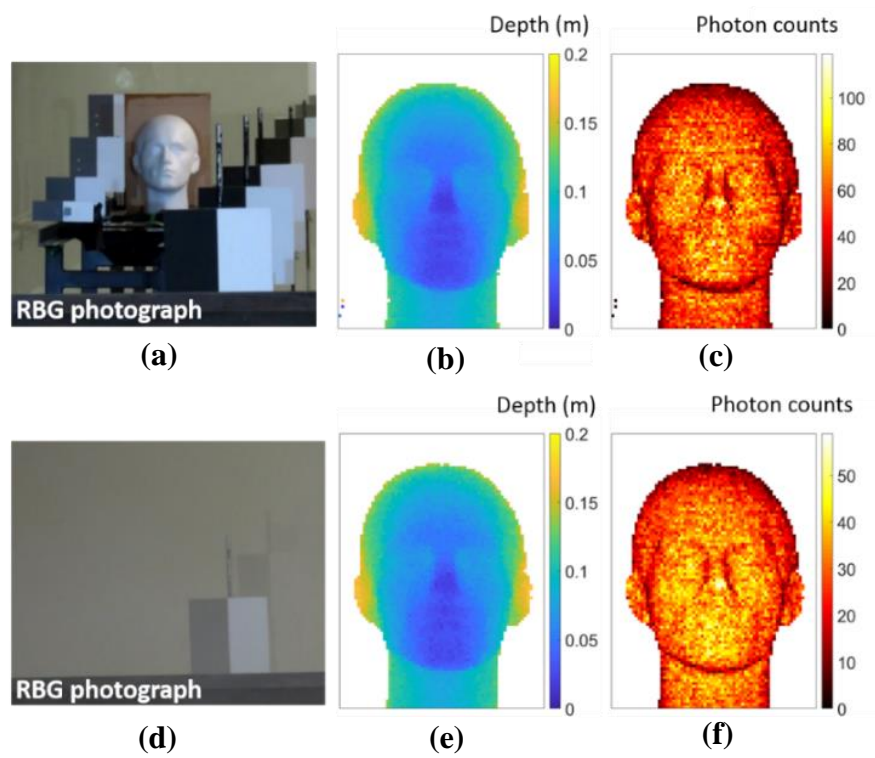
Figure 5.12: Depth and intensity profiles of the polystyrene head through 24 metres of white canister smoke obtained using pixel-wise cross-correlation. The top row shows results obtained with no obscurant present while the bottom row shows the results obtained in white smoke when the attenuation coefficient was $\alpha_{1550nm} = 0.10\ m^{-1}$ at λ = 1550 nm. This represented 2.4 attenuation lengths at λ = 1550 nm and 12.0 attenuation lengths in the visible. (a) and (d) show RGB photographs taken of the scene at the time of measurement; (b) and (e) show depth profiles of the target; and (c) and (f) show intensity profiles of the target.

The results show, that even with the very poor visibility shown in Figure 5.12 (d), the target was discernible from the first measurement in the set. In fact, the intensity profile in Figure 5.12 (f) indicates that a higher number of photons than required to obtain an accurate depth and intensity estimate were collected from the target. Therefore, shorter acquisition times were extracted from the full time-tagged single-photon data file to investigate the results obtained for a per-pixel acquisition time $\tau_{acq} = 0.01$, 0.05, and 0.1 ms. 3D point cloud representations of the target scene for the reduced acquisition times, when $\alpha_{1550nm} = 0.1 \text{m}^{-1}$, are shown in Figure 5.13.
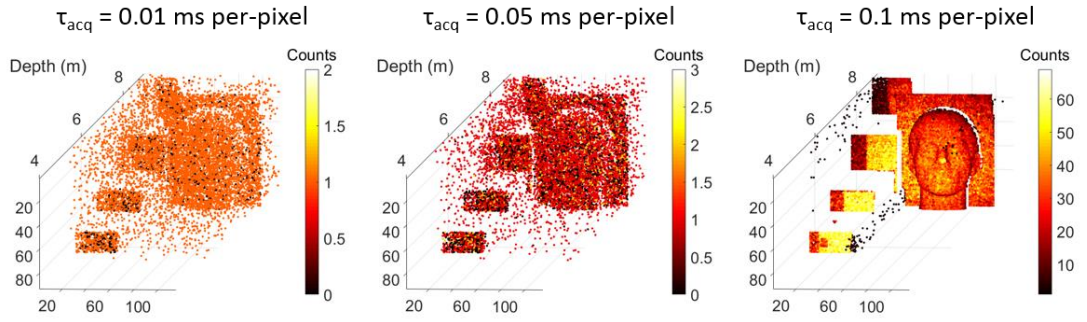
Figure 5.13: 3D point cloud representations of the target scene through 24 metres of white canister smoke at $\alpha_{1550nm} = 0.10 \text{ m}^{-1}$ for reduced acquisition times of $\tau_{acq} = 0.1$, 0.05, and 0.01 ms. The reconstructions were made using pixel-wise cross-correlation.

The results in Figure 5.13 demonstrate the decreasing quality of the image reconstruction for shorter acquisition times. However, using the cross-correlation algorithm, a partial reconstruction of the target scene was achieved with only 1 photon per pixel on average. Therefore, these results were then processed using the RDI-TV and NR3D algorithms. Figure 5.14 shows the depth profiles obtained for per-pixel acquisition times of $\tau_{acq} = 0.01$, 0.05, 0.1, and 3 ms obtained using the cross-correlation, RDI-TV, and M-NR3D algorithms. The SRE values are also given for each image with the ground truth taken from the full acquisition time data (i.e. 3 ms per-pixel) obtained using pixel-wise cross-correlation.

The results show that, at shorter acquisition times, the depth profiles obtained using pixel-wise cross-correlation exhibit high levels of noise and have many pixels where either a depth estimate could not be made or an inaccurate measurement outside the set depth threshold was obtained. However, the RDI-TV and NR3D algorithms provide much better reconstructions, even at the lowest acquisition time of $\tau_{acq} = 0.01$ ms where the head is almost fully reconstructed. However, while the RDI-TV algorithm succeeds

in reconstructing much of the data from missing pixels or bad estimates, it has a tendency to over smooth the depth profile resulting in a loss of detail in the face of the polystyrene head. The NR3D algorithm achieves good reconstruction at acquisition times as low as 0.05 ms per-pixel, but seems to struggle at 0.01 ms per-pixel. The computational time for the RDI-TV and NR3D algorithms are approximately 10s of seconds and 1000s of seconds per image, respectively. Therefore, for the shortest acquisition times, RDI-TV appears to give the best reconstruction while requiring only moderate processing times, allowing for more rapid data acquisition using a single-pixel detector.
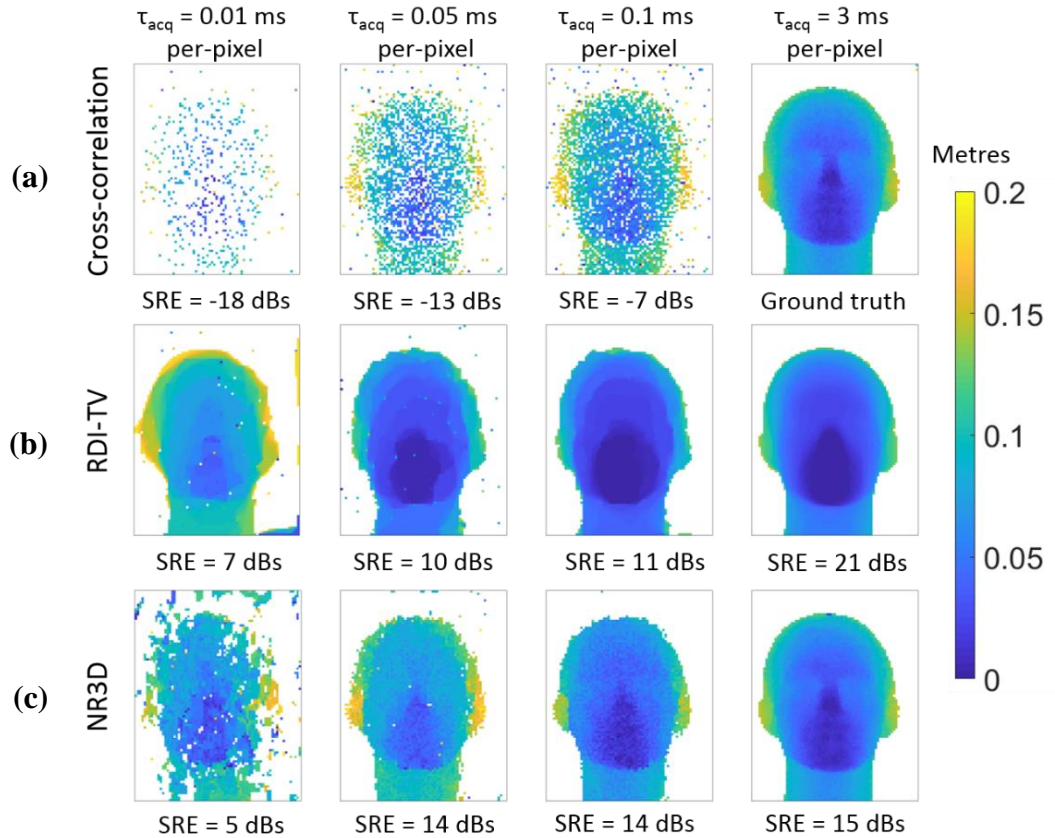
Figure 5.14: Depth profiles of the polystyrene head through 24 metres of white canister smoke for $\alpha_{1550nm} = 0.10$ m^{-1} and $\tau_{acq} = 0.01$, 0.05, 0.1, and 3 ms per-pixel obtained using (a) the pixel-wise cross-correlation, (b) RDI-TV, and (c) the NR3D algorithms.

5.5.3 Glycol vapour

In order to investigate the effects of a larger particle size on optical propagation, the next set of measurements was performed through 24 metres of glycol vapour where the particles were approximately 1.5× larger than the canister smoke particles. Due to the relatively slow dispersion of the glycol vapour out of the obscurant chamber compared to the canister smoke, a measurement format of 30 seconds scans every 60 seconds was used

resulting in a total measurement duration of 14 minutes. The attenuation coefficients for both wavelength bands over the duration of the measurement set are shown in Figure 5.15.
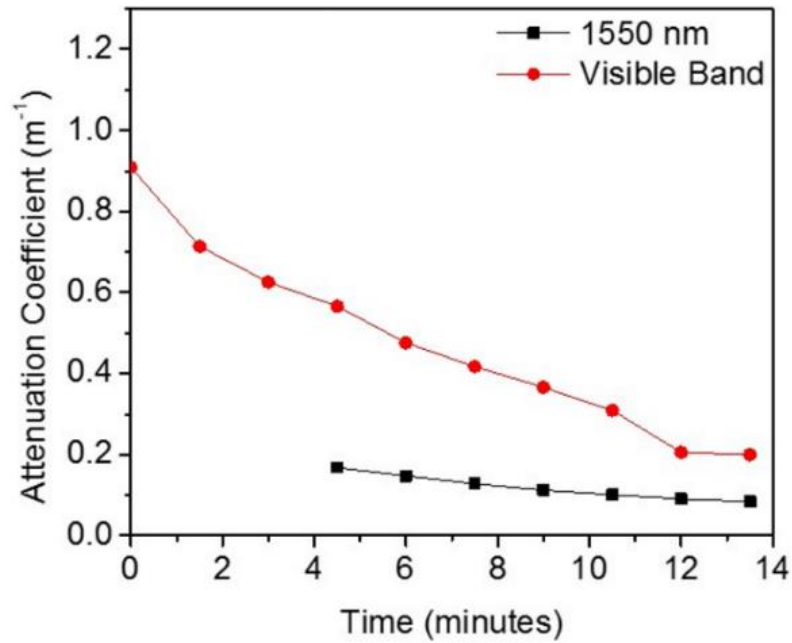
Figure 5.15: A comparison of the attenuation coefficient as a function of time for both λ = 1550 nm and the visible band for a target position of 24 metres in glycol vapour.

Due to the high level of obscurant at the beginning of the measurement set, a very low return was obtained from the target. This resulted in a large variation in the visible attenuation from the start of the measurement set to the end. The SWIR measurements also demonstrate a larger variation than in the case of the canister smoke, however, it is less significant than in the visible band. Due to the very low target returns at high obscurant densities, for the λ = 1550 nm attenuation data, only those data points where there was a sufficient signal-to-noise ratio to make a reliable attenuation coefficient measurement are shown. For these measurements, attenuation coefficient measurements could be made starting from approximately 270 seconds into the measurement set. The results show that once again there is a significant difference in the propagation for the two wavelength bands, with λ = 1550 nm demonstrating much better penetration through the glycol. Figure 5.16 shows intensity and depth profiles obtained using pixel-wise cross-correlation for $N_{AL(1550\,nm)}$ = 2.7, 3.1, 3.5, and 4.0. The corresponding visible band attenuation length measurements are also shown. 3D point cloud representations demonstrating the effects of particulate scattering on the reconstructed images are shown in Figure 5.17.
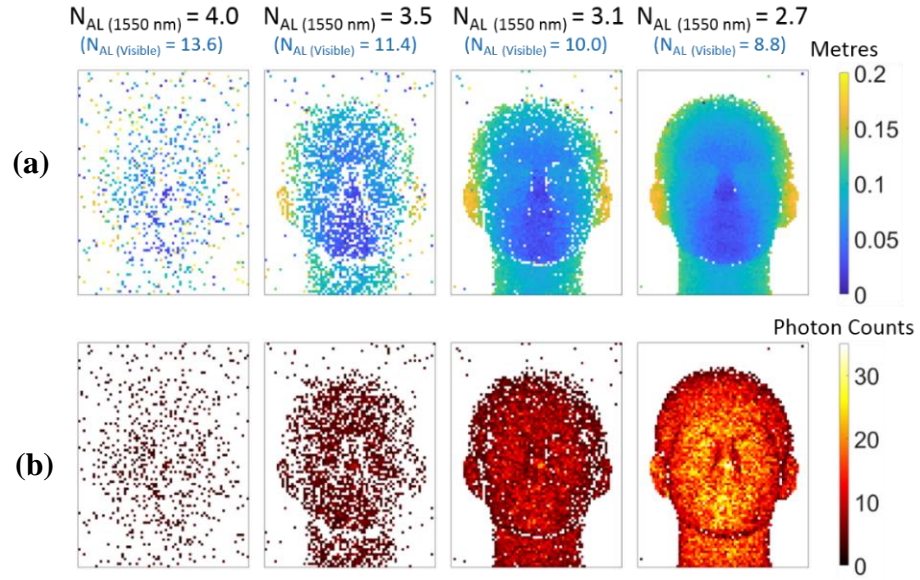
Figure 5.16: Depth and intensity profiles of the polystyrene head target through 24 metres of glycol vapour at $N_{AL\ (1550\ nm)}$ = 4.0, 3.5, 3.1, and 2.7. In the visible region, these attenuation lengths are equivalent to 13.6, 11.4, 10.0, and 8.8, respectively. (a) Depth profiles of the target obtained using pixel-wise cross-correlation where colour represents depth. (b) Presents the intensity profiles.
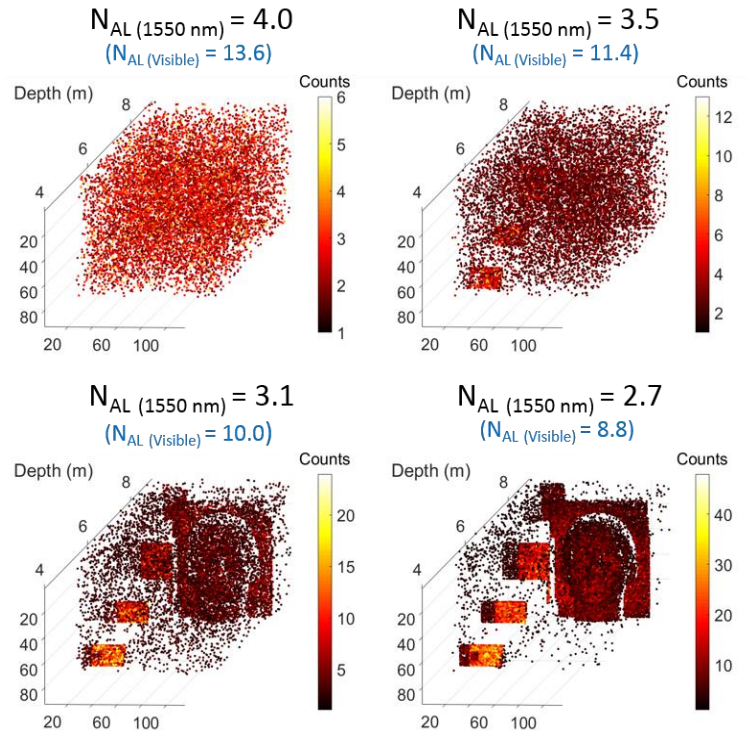
Figure 5.17: 3D point cloud representations of the target scene through 24 metres of glycol vapour at $N_{AL\ (1550\ nm)}$ = 4.0, 3.5, 3.1, and 2.7 demonstrating the effects of particulate scattering in highly attenuating media. The reconstructions were made using pixel-wise cross-correlation.

The target profiles, for both depth and intensity, begin to become discernible at approximately $N_{AL\,(1550\,nm)}$ = 4.0 and fully visible at $N_{AL\,(1550\,nm)}$ = 3.5, even with the high levels of scattering indicated in Figure 5.17. This corresponds to the equivalent of 11.4 attenuation lengths in the visible – far higher than can be seen by the human eye. However, the high level of scattering does result in many missing pixels. Therefore, the results were then processed using the RDI-TV and M-NR3D algorithms to investigate their use for single-photon data in high levels of obscurants. 3D point cloud representations and SRE values for ($N_{AL\,(1550\,nm)}$ = 3.5, 3.1, and 2.7) are shown below in Figure 5.18.
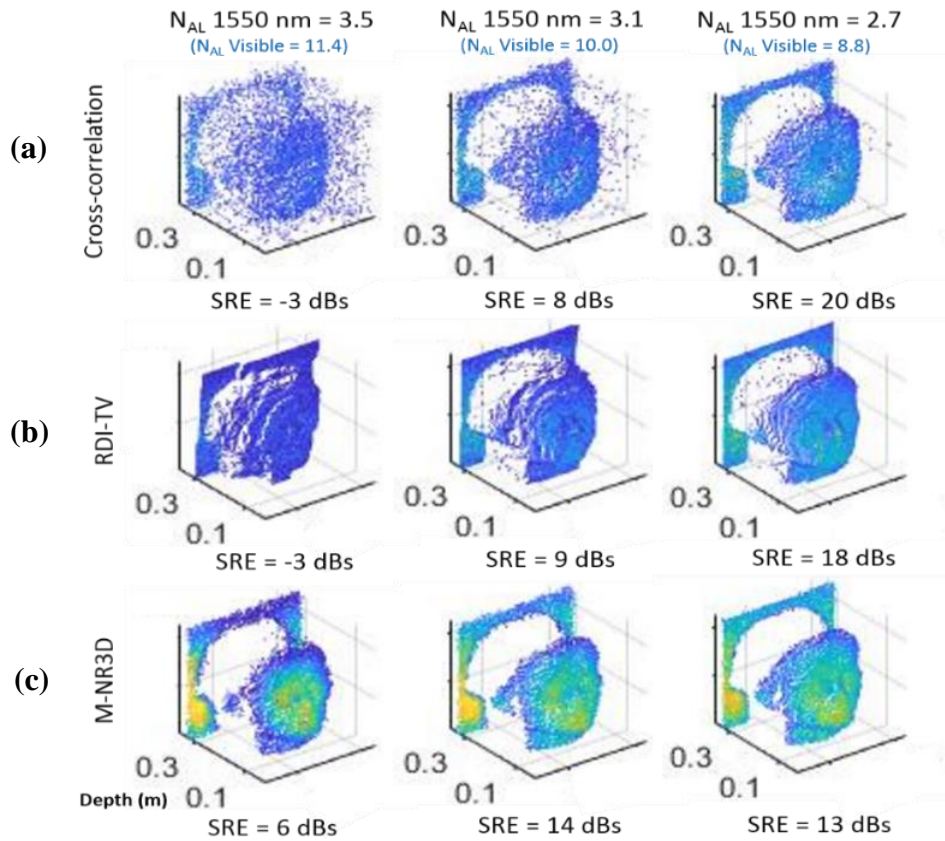
Figure 5.18: 3D point cloud representations of the polystyrene head target through 24 metres of glycol vapour at $N_{AL(1550\,nm)}$ = 3.5, 3.1, and 2.7. In the visible region, these attenuation lengths are equivalent to 11.4, 10.0, and 8.8, respectively. The data was reconstructed using: (a) cross-correlation; (b) RDI-TV; and (c) the M-NR3D algorithms.

The results indicate that both the cross-correlation and RDI-TV algorithms performed poorly on data acquired with high levels of attenuation in glycol vapour, with the finer features of the target largely unrecognisable in most cases. The advantage of the M-NR3D algorithm becomes apparent at very high levels of attenuation, with an SRE of

6 dB in comparison to -3 dB for both cross-correlation and RDI-TV. However, there is a significant trade-off with regards to the acquisition time. The M-NR3D algorithm has a much longer computational time of approximately 2500 seconds as it must jointly process the three images. The faster RDI-TV algorithm has a computational time of only approximately 100 seconds per image.

5.5.4 Water fog

The final set of measurements was performed through 5 metres of water fog. The shorter stand-off distance used during these measurements was chosen due to the high density of obscurant in the chamber at the beginning of the measurement set (i.e., $\alpha_{visible} = 1.2$ m^{-1}). However, in order to make a side-by-side comparison with glycol vapour and canister smoke, the attenuation coefficient for propagation through water fog was measured for both the 5-metre range and the 24-metre range. To account for the relatively faster dispersion of the water fog from the chamber, the scans were taken for a duration of 30 seconds, with a separation of 30 seconds between scans for a total measurement set period of 8 minutes. A plot of attenuation coefficient through 24 metres of water fog for the duration of the measurement set is shown in Figure 5.19.
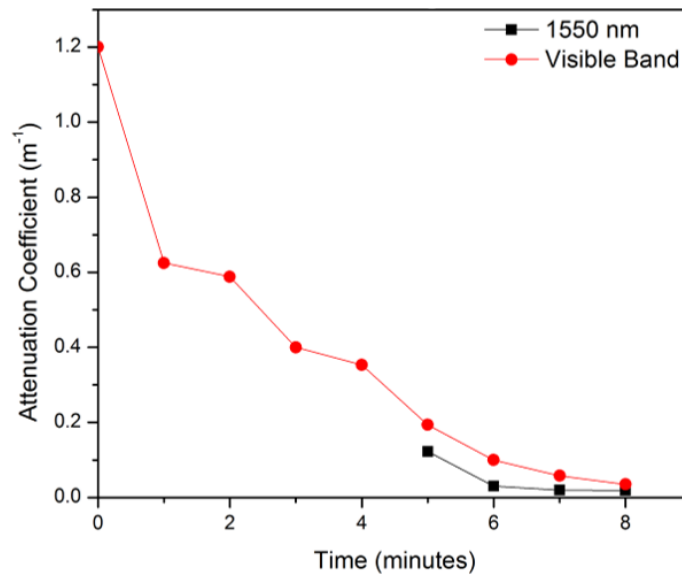
*Figure 5.19: A comparison of the attenuation coefficient as a function of time
for both λ = 1550 nm and the visible band for a target position of 24 metres
in water fog.*

For these measurements, an accurate attenuation coefficient for λ = 1550 nm could not be obtained until approximately 5 minutes into the measurement set due to a very high level of scattering in the chamber. Figure 5.19 suggests that there may be a slight advantage in working in the SWIR region for this particular particle size and density of water fog,

135

as the measurements indicate that the operating wavelength of $\lambda = 1550$ nm may have slightly lower attenuation under these conditions than the visible band. However, when the attenuation coefficient was measured over a range of 5 metres, the results indicated that there appears to be no advantage in operating at $\lambda = 1550$ nm in this particular water fog environment when compared to the visible band. This could be due to error arising from the inhomogeneity of the obscurant in the first few metres of the chamber or a consistent systematic error due to the different measurement approaches used for each wavelength band. Due to the short range and rapidly changing obscurant density during this measurement, it was difficult to make a reliable measurement of the attenuation coefficient in the visible band at the 5-metre range. However, the 24-metre data presented in Figure 5.19 suggests that the SWIR wavelength will have slightly less attenuation.

Figure 5.20 shows RGB photographs of the scene taken in synchronisation with the SWIR measurements, the number of attenuation lengths for $\lambda = 1550$ nm, and the depth and intensity profiles of the head at $N_{AL(1550\,nm)} = 2.8$, 3.1, 3.8, and 4.7 obtained with pixel-wise cross-correlation.
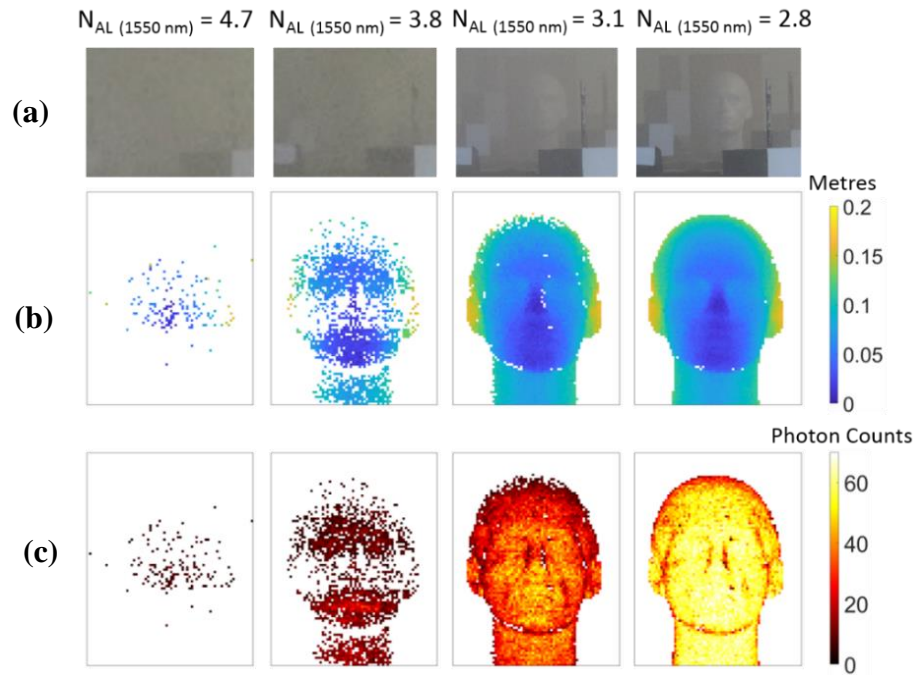
Figure 5.20: Depth and intensity profiles of the polystyrene head target through 5 metres of water fog at $N_{AL(1550\,nm)} = 4.7$, 3.8, 3.1, and 2.8 obtained using pixel-wise cross-correlation. The per-pixel acquisition time was 3 ms (approximately 30 seconds total). (a) presents RGB photographs of the scene at the point of measurement, (b) presents depth profiles of the target, and (c) presents the intensity profiles.

The results in Figure 5.20 show that at $N_{AL\,(1550\,nm)} = 3.8$ the target becomes recognisable in the depth and intensity profiles using the pixel-wise cross-correlation algorithm while at $N_{AL(1550\,nm)} = 3.1$ the target becomes fully discernible.

The results were then processed using the RDI-TV and M-NR3D algorithms. The obtained 3D point clouds and corresponding SRE values are shown in Figure 5.21 for $N_{AL\,(1550\,nm)} = 2.8$, 3.1, and 3.8.
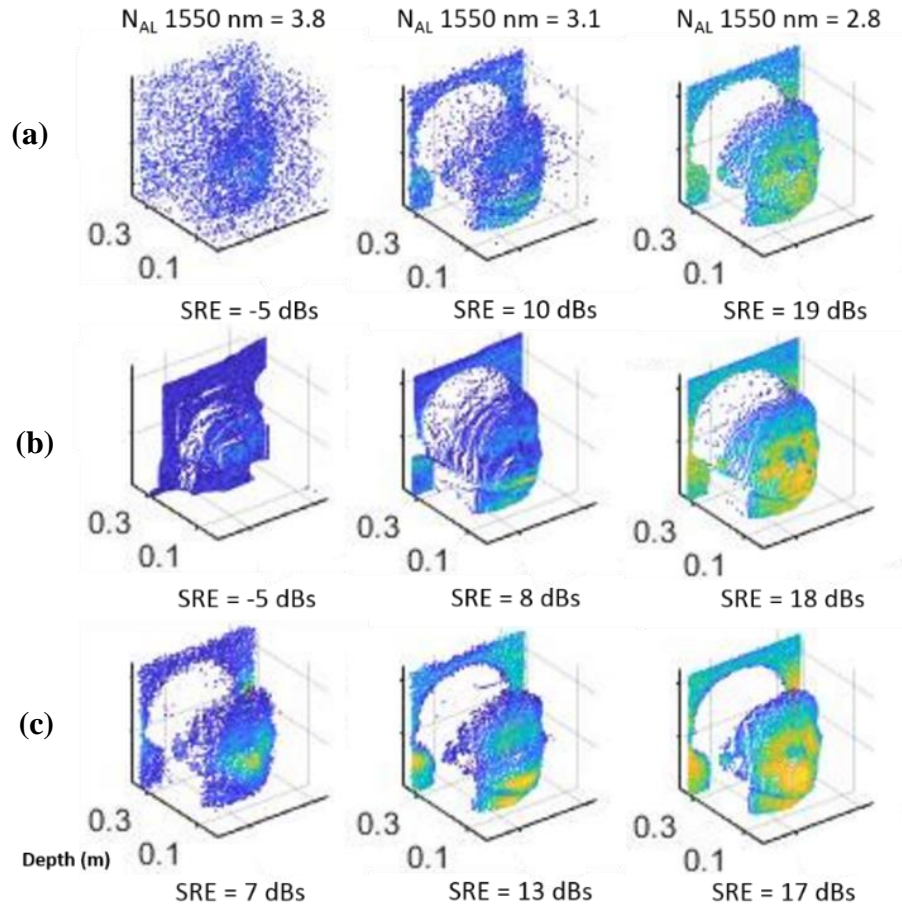
Figure 5.21: 3D point cloud representations of the polystyrene head target through 5 metres of water fog at $N_{AL(1550\,nm)} = 3.8$, 3.1, and 2.8. The data was reconstructed using: (a) cross-correlation; (b) RDI-TV; and (c) the M-NR3D algorithms.

Similar to the results obtained previously in glycol vapour, the cross-correlation and RDI-TV algorithms produce satisfactory results at lower levels of attenuation lengths but are unable to reconstruct the target at higher levels of attenuation (i.e., > 3.5 attenuation lengths at λ = 1550 nm). The M-NR3D algorithm was able to successfully reconstruct some of the finer features in the face of the target in water fog at $N_{AL(1550\,nm)} = 3.8$, however, some pixels remained empty around the edges. The RDI-TV algorithm requires a computational time of approximately 100 seconds to process each image, and the

M-NR3D algorithm takes approximately 1300 seconds for the joint processing of the three images – similar to the results in glycol vapour. These results show the potential for the M-NR3D algorithm for use in highly scattering environments such as single-photon data obtained in water fog.

5.6 Conclusions and future work

A monostatic depth imaging system based on the single-photon ToF approach was used to obtained three-dimensional depth profiles of targets through a variety of obscuring media in a 26-metre-long indoor obscurant chamber. The system was based on a single-pixel InGaAs/InP SPAD detector with a wavelength range of 900 – 1700 nm, a temporal resolution of 2 ps, and a single-photon detection efficiency of approximately 35% at λ = 1550 nm. A pulsed supercontinuum laser source alongside a series of high-performance filters were used to deliver a fibre-coupled illumination of λ = 1550 nm.

Four different obscurants were investigated in this study: black canister smoke, white canister smoke, glycol vapour, and water fog. Attenuation coefficient measurements were obtained for each obscurant for both λ = 1550 nm and the visible band. The results demonstrate that the use of 1550 nm wavelength illumination provides significant benefits over the visible band for both smoke types and glycol vapour but little or no benefit for the case of the water fog used in these measurements. As discussed in Chapter 2, at these wavelengths Mie scattering from particles suspended in the atmosphere dominate, with relatively little contribution from absorption effects [5.20]. These scattering effects are dependent on the particle size of the fog in comparison to the wavelength of the transmitted beam. Therefore, the use of SWIR wavelengths will prove highly beneficial compared to visible wavelengths for imaging applications in high densities of obscurants where the particle size is small, as in the case of smoke. The measurements presented in this Chapter had initial visibilities in the order of metres, which can be regarded as propagation in high levels of obscurants. However, further studies are necessary to examine natural fog environments with a range of droplet sizes in order to examine imaging scenarios with current interest to the scientific community. For example, target distances of 100 metres or more, which are consistent with automotive LiDAR.

Results obtained using the λ = 1550 nm imaging system were processed using three image processing algorithms; (i) pixel-wise cross-correlation, (ii) RDI-TV, and (iii) M-NR3D. The cross-correlation algorithm provides a simple, computationally

inexpensive solution while the RDI-TV and M-NR3D algorithms reconstruct depth and intensity profiles by exploiting spatial correlations in single-photon data. While the cross-correlation algorithm provided good results in both black and white canister smoke, it failed to reconstruct scenarios where much larger diameter particles were present (such as in water fog or glycol vapour). However, depth and intensity profiles were obtained at attenuation length values of up to 3.8 at λ = 1550 nm in water fog and 3.5 in glycol vapour, equivalent to > 11 attenuation lengths in the visible band using the more sophisticated RDI-TV and M-NR3D algorithms. Each algorithm's performance depends on the considered scenario, where RDI-TV appears to be more suitable for measurements containing a reduced background level. The M-NR3D algorithm is more general in the sense that it accounts for the presence of multiple peaks, it jointly processes a sequence of images (i.e., for videos of dynamic scenes) and it performs very good data restoration even in presence of high levels of scattering background. The M-NR3D algorithm, despite its computational costs, will be particularly useful in reconstructing distributed targets composed of several surfaces in the presence of obscurants and will be a feature of future work. The use of such image processing algorithms indicates significant improvements in image reconstruction in the sparse photon regime, which will assist in the move towards imaging at higher levels of atmospheric attenuation and reduced data acquisition time in future work.

This Chapter has demonstrated the use of the TCSPC technique for depth profiling through obscurants at short acquisition times (less than 1 second for the entire scan) using a single-pixel detector, making this method more suitable for a number of depth imaging applications. However, these acquisition times are still relatively slow and remain an obstacle for applications with fast dynamic scenes, such as target tracking. In recent years, large format InGaAs/InP SPAD detector arrays integrated with TCSPC electronics [5.38–5.41] have become of great interest for rapid three-dimensional imaging. The use of these detectors in SWIR 3D imaging through obscurants will be presented in the next Chapter of this Thesis.

5.7 Acknowledgements

Abderrahim Halimi specifically for use on single-photon data in challenging environments.

5.8 References

5.1. R. Tobin, A. Halimi, A. McCarthy, M. Laurenzis, F. Christnacher, and G. S. Buller, "Three-dimensional single-photon imaging through obscurants," Opt. Express 27(4), 4590–4611 (2019).

5.2. A. McCarthy, X. Ren, A. D. Frera, N. R. Gemmell, N. J. Krichel, C. Scarcella, A. Ruggeri, A. Tosi, and G. S. Buller, "Kilometer-range depth imaging at 1550 nm wavelength using an InGaAs/InP single-photon avalanche diode detector," Opt. Express 21(19), 22098–22113 (2013).

5.3. R. Tobin, A. Halimi, A. McCarthy, X. Ren, K. J. McEwan, S. McLaughlin, and G. S. Buller, "Long-range depth profiling of camouflaged targets using single-photon detection," Opt. Eng. 57(3), 031303 (2017).

5.4. A. Maccarone, A. McCarthy, X. Ren, R. E. Warburton, A. M. Wallace, J. Moffat, Y. Petillot, and G. S. Buller, "Underwater depth imaging using time-correlated single-photon counting," Opt. Express 23(26), 33911–33926 (2015).

5.5. Y. Altmann, A. Maccarone, A. McCarthy, G. Newstadt, G. S. Buller, S. McLaughlin, and A. Hero, "Robust spectral unmixing of sparse multispectral Lidar waveforms using gamma Markov random fields," IEEE Trans. Comput. Imaging 3(4), 658–670 (2017).

5.6. A. M. Wallace, A. McCarthy, C. J. Nichol, X. Ren, S. Morak, D. Martinez-Ramirez, I. H. Woodhouse, and G. S. Buller, "Design and evaluation of multispectral LiDAR for the recovery of arboreal parameters," IEEE Trans. Geosci. Remote Sens. 52(8), 4942–4954 (2014).

5.7. R. Tobin, Y. Altmann, X. Ren, A. McCarthy, R. A. Lamb, S. McLaughlin, and G. S. Buller, "Comparative study of sampling strategies for sparse photon multispectral lidar imaging: towards mosaic filter arrays," J. Opt. 19(9), 094006 (2017).

5.8. X. Ren, Y. Altmann, R. Tobin, A. Mccarthy, S. Mclaughlin, and G. S. Buller, "Wavelength-time coding for multispectral 3D imaging using single-photon LiDAR," Opt. Express 26(23), 30146–30161 (2018).

5.9. F. Nadeem, T. Javornik, E. Leitgeb, V. Kvicera, and G. Kandus, "Continental fog attenuation empirical relationship from measured visibility data," Radioeng., 19(4), 596-600 (2010).

5.10. M. Ijaz, Z. Ghassemlooy, S. Rajbhandari, H. L. Minh, J. Perez, and A. Gholami, "Comparison of 830 nm and 1550 nm based free space optical communications link under controlled fog conditions," Proc. 8th Int. Symp. Commun. Syst. Netw. Digit. Signal Process., 1-5 (2012).

5.11. I. I. Kim, B. McArthur, and E. J. Korevaar, "Comparison of laser beam propagation at 785 nm and 1550 nm in fog and haze for optical wireless communications," Proc. SPIE Opt. Wireless Commun. III, 4214, 26-37 (2001).

5.12. R. M. Pierce, J. Ramaprasad, and E. C. Eisenberg, "Optical attenuation in fog and clouds," Proc. SPIE, 4530, 58 –71 (2001).

5.13. F. Christnacher, J.-M. Poyet, E. Bacher, N. Metzger, S. Schertzer, and J.-R. Simard, "Influence of the obscurants and the illumination wavelengths on a range-gated active imaging system performance," in *Electro-Optical Remote Sensing XII* 10796, 1079603 (2018).

5.14. "SUPERK EXTREME/FIANIUM High Power Supercontinuum fibre laser series datasheet," (NKT Photonics, accessed 2019).

5.15. "MPD - InGaAs SPAD - gated datasheet," (Micro Photon Devices, accessed 2019).

5.16. "HydraHarp 400 datasheet," (PicoQuant, accessed 2019).

5.17. M. Laurenzis, F. Christnacher, D. Monnin, and T. Scholz, "Investigation of range-gated imaging in scattering environments," Opt. Eng. 51(6) 061303 (2012).

5.18. Permaflect is a trademark of LABSPHERE, INC., 231 Shaker Street, POB 70, North Sutton, NH 03260 US, www.labsphere.com

5.19. F. Christnacher, S. Schertzer, N. Metzger, E. Bacher, M. Laurenzis, and R. Habermacher, "Influence of gating and of the gate shape on the penetration capacity of range-gated active imaging in scattering environments," Opt. Express 23(26), 32897–32908 (2015).

5.20. H. G. Houghton, "The size and size distribution of fog particles," J. Appl. Phys. 2(6), 467–475 (1932).

5.21. H. Koschmieder, "Theorie der horizontalen Sichtweite," Beitr. Phys. fr. Atm. 12, 33-55 and 171-181 (1924).

5.22. International Commission on Illumination, 17-1407, http://www.cie.co.at/eilv/1407 (accessed June 2019).

5.23. O. V. Kalashnikova, H. A. Willebrand, and L. M. Mayhew, "Wavelength and altitude dependence of laser beam propagation in dense fog," Proc. SPIE 4635, 278–288 (2002).

5.24. S. G. Narasimhan and S. K. Nayar, "Vision and the atmosphere," Int J Comput Vis. 48(3), 233–254 (2002).

5.25. E. J. McCartney, *Optics of the Atmosphere (Wiley, 1976).*

5.26. C. F. Bohren and D. R. Huffman, *Absorption and scattering of light by small particles* (Wiley, 1983).

5.27. D. F. Swinehart, "The Beer-Lambert law," J. Chem. Educ. 39(7), 333 (1962).

5.28. J. Rapp and V. K. Goyal, "A few photons among many: unmixing signal and noise for photon-efficient active imaging," IEEE Trans. Comput. Imaging 3(3), 445–459 (2017).

5.29. A. Kirmani, D. Venkatraman, D. Shin, A. Colaço, F. N. C. Wong, J. H. Shapiro, and V. K. Goyal, "First-photon imaging," Science 343(6166), 58–61 (2014).

5.30. D. B. Lindell, M. O'Toole, and G. Wetzstein, "Single-photon 3D imaging with deep sensor fusion," ACM Trans. Graph. 37(4), 1–12 (2018).

5.31. J. Tachella, Y. Altmann, X. Ren, A. McCarthy, G. S. Buller, S. McLaughlin, and J.-Y. Tourneret, "Bayesian 3D reconstruction of complex scenes from single‑photon Lidar data", SIAM J. Imaging Sci. 12(1), 521‑550 (2019).

5.32. A. M. Pawlikowska, A. Halimi, R. A. Lamb, and G. S. Buller, "Single-photon three-dimensional imaging at up to 10 kilometers range," Opt. Express 25(10), 11919–11931 (2017).

5.33. A. Halimi, R. Tobin, A. McCarthy, J. Bioucas-Dias, S. McLaughlin, and G. S. Buller, "Restoration of multidimensional sparse single-photon 3D-LiDAR images," IEEE, Trans. Comput. Imaging, accepted, (2018).

5.34. P. Sprechmann, I. Ramirez, G. Sapiro, and Y. C. Eldar, "C-HiLasso: A collaborative hierarchical sparse modeling framework," IEEE Trans. Signal Process. 59, 4183-4198 (2011).

5.35. H. K. Aggarwal and A. Majumdar, "Hyperspectral unmixing in the presence of mixed noise using joint-sparsity and total variation," IEEE J. Sel. Top. Appl. Earth Obs. Remote Sens. 9, 4257-4266 (2016).

5.36. A. Halimi, J. Bioucas-Dias, N. Dobigeon, G. S. Buller, and S. McLaughlin, "Fast hyperspectral unmixing in presence of nonlinearity or mismodelling effects," IEEE Trans. Comput. Imaging 3(2), 146-159 (2017).

5.37. A. Halimi, R. Tobin, A. McCarthy, S. McLaughlin, and G. S. Buller, "Restoration of multilayered single-photon 3d lidar images," 2017 25th European Signal Processing Conference (EUSIPCO), Kos, 708-712 (2017).

5.38. M. Entwistle, M.A. Itzler, J. Chen, M. Owens, K. Patel, X. Jiang, K. Slomkowski, and S. Rangwala, "Geiger-mode APD camera system for single-photon 3D LADAR imaging," Proc. SPIE 8375, Advanced Photon Counting Techniques VI, 83750D (2012).

5.39. M.A. Itzler, M. Entwistle, M. Owens, K. Patel, X. Jiang, K. Slomkowski, S. Rangwala, P.F. Zalud, T. Senko, J. Tower, and J. Ferraro, "Comparison of 32 x 128 and 32 x 32 Geiger-mode APD FPAs for single photon 3D LADAR imaging," Proc. SPIE 8033, Advanced Photon Counting Techniques V, 80330G (2011).

5.40. M. Henriksson, and P. Jonsson, "Photon-counting panoramic three-dimensional imaging using a Geiger-mode avalanche photodiode array," Opt. Eng. 57(9) 093104 (2018).

5.41. M. Henriksson, L. Allard, and P. Jonsson, "Panoramic single‑photon counting 3D lidar," Proc. Vol. 10796, Electro-Optical Remote Sensing XII; 1079606 (2018).

Chapter 6: Imaging through obscurants at λ = 1550 nm using a 32 × 32 InGaAs/InP SPAD detector array

6.1 Introduction

This Chapter will describe a bistatic active imaging system based on the single-photon time-of-flight (ToF) approach using arrayed SPAD detectors in the SWIR region. The system incorporates a 32 × 32 InGaAs/InP single-photon avalanche diode (SPAD) detector array and is operated at a wavelength of 1550 nm. This system can be used to measure the depth profile of objects in both clear conditions and in challenging environments, such as through high levels of particulate scattering. The use of the time-correlated single-photon counting (TCSPC) technique using single-pixel InGaAs/InP detectors for target depth profiling in highly scattering environments has been detailed previously in Chapter 4 and Chapter 5 of this Thesis. While single-pixel based systems have been previously demonstrated to be highly successful in acquiring depth and intensity profiles in highly attenuating environments, such as through camouflage [6.1], in turbid water [6.2], and in smoke and fog [6.3], data acquisition times can be prohibitively long (i.e., up to tens of seconds) due to the point-and-stare method of data acquisition. The use of arrayed InGaAs/InP detectors in active light detection and ranging (LiDAR) systems can significantly reduce data acquisition times, potentially by several orders of magnitude, allowing for rapid, high-resolution, three-dimensional (3D) depth profiling in challenging outdoor scenes [6.4,6.5].

Firstly, this Chapter will present an overview of the system and key experimental parameters. In addition, a characterisation of the detector will be provided in Section 6.2, with discussion of parameters such as the dark count rate (DCR), the single-photon detection efficiency (SPDE), and the timing response of the detector. Then, an adapted LiDAR model for the bistatic active imaging system based on the photon-counting LiDAR equation is described in Section 6.3 alongside predictions on the ranging performance of the system. Finally, the performance of the system is evaluated in Section 6.4 over distances of 50 and 150 metres in the presence of obscurants, and at a longer range of 1463 metres in clear conditions. Conclusions and future work are presented in Section 6.5.

6.2 Overview of system configuration and key experimental parameters

This Section presents an overview of the system configuration and key experimental parameters used in both the characterisation of the detector and for in-situ measurements. Parameters such as the DCR, the SPDE, and the instrumental response of the detector will be discussed alongside the illumination source and data acquisition.

6.2.1 Princeton Lightwave Kestrel 32 × 32 InGaAs/InP SPAD detector array

The detector used in the experiments presented in this Chapter was the Princeton Lightwave (PLW) Kestrel 32 × 32 Geiger-Mode Flash 3-D LiDAR Camera (Princeton Lightwave, USA) [6.6,6.7]. This camera is based on InGaAs/InP SPAD detector array technology and has a 32 × 32 pixel format focal plane array (FPA) with dimensions of 3.2 mm × 3.2 mm, providing a pixel pitch of 100 µm × 100 µm. The dimensions of the camera are 10 cm × 10 cm × 9 cm and a Chassis C-mount is provided for optical component attachment. A photograph of the detector and a close-up of the FPA is shown in Figure 6.1.
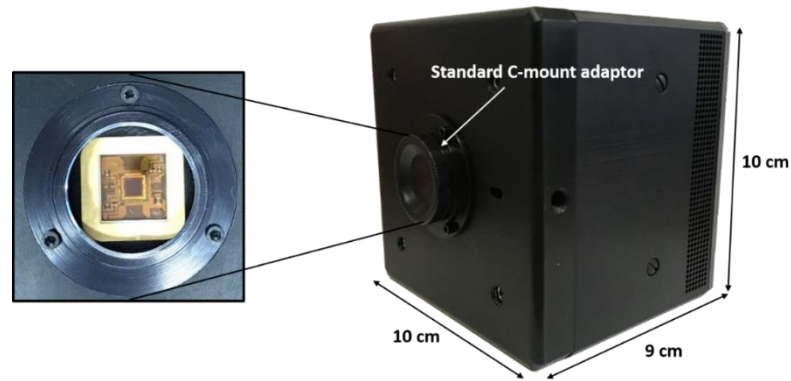
Figure 6.1: The PLW Kestrel 32 × 32 InGaAs/InP SPAD array and a close-up photograph of the FPA. The array has dimensions of 3.2 mm × 3.2 mm, providing a pixel pitch of 100 µm × 100 µm. A Chassis C-mount is provided for optical component attachment and the camera has dimensions of 10 cm × 10 cm × 9 cm.

This sensor can be used for single-photon and low-light detection in the near infrared with an operational wavelength range of 1400 – 1620 nm, as stated by the manufacturer [6.8]. The camera has the capability of 250 – 1250 ps timing bins for gated operation up to 2 µs, providing a 3.75 cm time-of-flight resolution per photon return for a maximum gating range of 300 metres. For all the results presented in this Chapter, a 250 ps timing bin size was used in order to achieve the highest level of temporal resolution. The maximum frame rate of the camera is 186,000 Hz. However, in order to assure stable operation

144

during measurements, a frame rate of 150,421 Hz (translating to a frame period of 6.648 µs) was chosen. A summary of these key parameters, as stated by the manufacturer, is presented in Table 6.1.

Table 6.1: Table of key parameters for the Princeton Lightwave Kestrel 32 × 32 InGaAs/InP SPAD detector as shown in ref. [6.8].

Parameter	Value/comment
Sensor type	InGaAs/InP SPAD
Camera dimensions	100 × 100 × 90 mm
Camera weight	1.3 kg
Array format / dimensions	32 × 32 pixels / 3.2 × 3.2 mm
Pixel pitch	100 × 100 µm
Wavelength range	1400 – 1620 nm
Time bin duration (T_{bin})	250 – 1250 ps
Gate duration	$4 - (8000 \cdot T_{bin})$ ns
Maximum frame rate	186,000 Hz
Mean photon detection efficiency at λ = 1550 nm	18%
Mean dark count rate	318 kHz
Timing jitter	500 ps (maximum)
Data output format	CameraLink

6.2.1.1 Single-photon detection efficiency

As discussed in Chapter 3, the SPDE is defined as the ratio of the number of photons incident on the active area of the detector and the number of detected photons. This is affected by two main mechanisms: absorption probability and triggering efficiency [6.9]. Both of these mechanisms are affected by the breakdown voltage of the SPAD, which is highly temperature dependent [6.10,6.11]. The PLW InGaAs/InP SPAD detector contains a temperature control system comprising a temperature sensor and a thermo-electric cooler (TEC) inside the FPA. This control system automatically monitors ambient conditions and adjusts the FPA settings accordingly; maintaining temperature stabilisation and reducing thermal noise.

The mean SPDE of the detector, as stated by the manufacturer [6.8], is approximately 18% when using an operational wavelength of 1550 nm. However, the SPDE of the detector during operation is determined by a user-selected sensitivity setting, which alters the excess bias. The sensitivity setting ranges from 1 – 100% with 100% being the most sensitive. A plot of the SPDE as a function of the sensitivity setting is shown in Figure 6.2.
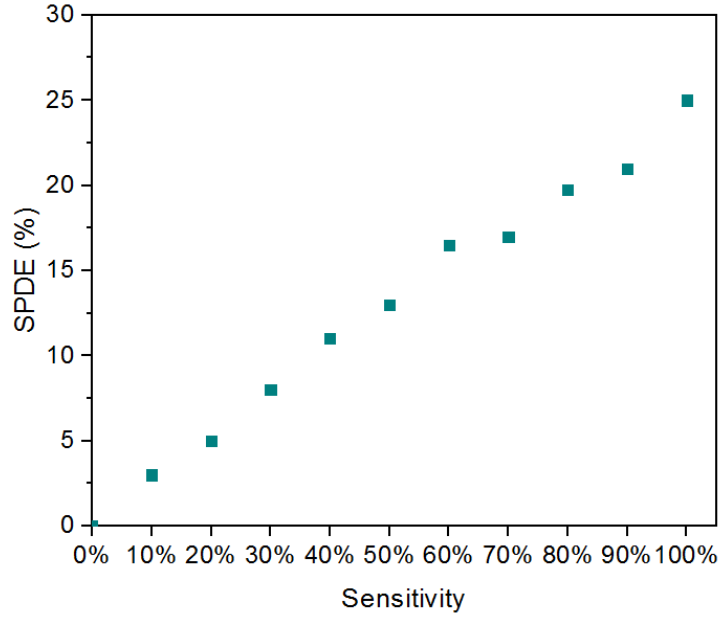
Figure 6.2: Plot of the SPDE as a function of sensitivity setting for the PLW 32 × 32 InGaAs/InP SPAD array. The maximum achievable SPDE of the detector is approximately 25% for a sensitivity setting of 100%.

The results presented in this Chapter were all obtained using a sensitivity setting of 100%, which corresponds to a SPDE of approximately 25%.

6.2.1.2 Dark count rate

The DCR of the detector was measured in a dark laboratory with the lens cap on the objective lens to avoid ambient counts. As discussed in Chapter 3, dark counts in SPAD detectors are caused by three mechanisms: thermal noise, charge carriers generated by tunnelling, and afterpulsing effects [6.12,6.13]. In InGaAs/InP SPAD detectors, dark counts generated by afterpulsing effects are comparably high compared to visible band SPAD detectors, such as Si-SPADs [6.14–6.16]. In order to reduce these effects, the DCR measurements were performed with a relatively short detector gate width of 20 ns. A repetition rate of 150,421 Hz and a sensitivity setting of 100% were selected to approximate the standard detector parameters used during field trials. The DCR is defined in units of counts per second, and therefore data were recorded for a 1 second acquisition time for simplicity. However, due to the gated configuration of the detector resulting in periods of detector inactivity, the DCR was normalised to simulate a free-running configuration. Thus, the DCR for gated-mode was calculated as follows:

$$DCR = \frac{N_{dark}}{\nu_{rep}\tau_{acq}\tau_{gate}},\qquad(6.1)$$

146

where N_{dark} is the number of recorded dark counts, ν_{rep} is the repetition rate (Hz), τ_{acq} is the acquisition time (s), and τ_{gate} is the gate width (s). A DCR map (where colour corresponds to count rate) for the entire FPA alongside the corresponding histogram detailing the DCR distribution over the FPA for a sensitivity setting of 100% (approximately 25% SPDE) are shown in Figure 6.3.
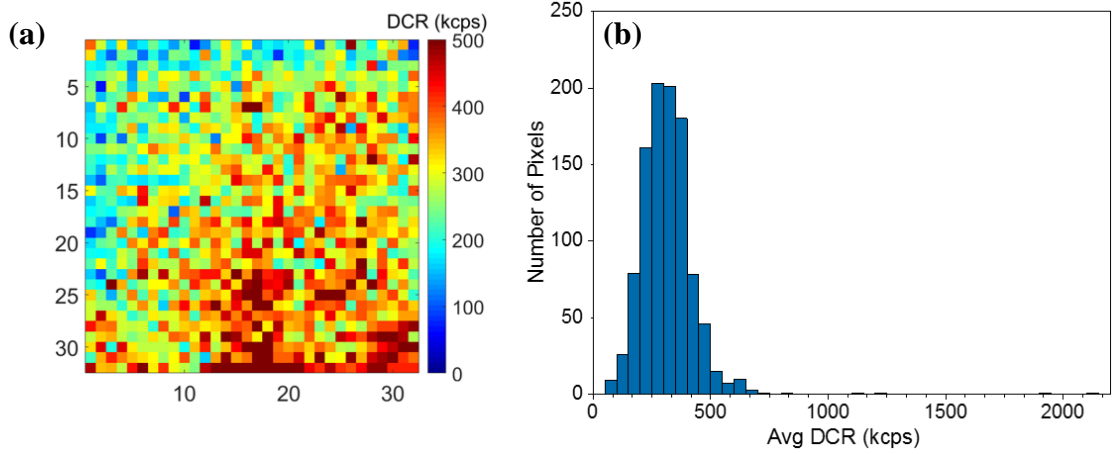
Figure 6.3: (a) A DCR map (where colour corresponds to count rate) for the entire FPA. (b) The corresponding histogram detailing the DCR distribution over the FPA at a sensitivity setting of 100% (approximately 25% SPDE) for a 1 second acquisition at a repetition rate of 150,421 Hz taken in a dark laboratory.

The results in Figure 6.3 show that the distribution of the DCR across the pixels in the FPA ranges from approximately 50 − 750 kcps with a mean value of approximately 318 kcps at these settings. In this measurement, four pixels exhibited a DCR significantly higher than the average measured value for the array. These are known as 'hot-pixels' and largely arise from mid band-gap traps in the SPAD material, which can result in a lower breakdown voltage (and consequently a higher DCR) due to a substantial reduction of the activation energy of the pixel [6.15]. While these hot-pixels are very common in sensor arrays, they can cause optical cross-talk between pixels and aberrations in images which must then be eliminated in post-processing [6.17–6.19].

An average DCR for the array was also measured for different gate widths in order to demonstrate the effects of afterpulsing in the camera. Figure 6.4 shows the average DCR over a full range of sensitivity settings for gate widths of 20, 100, and 200 ns.
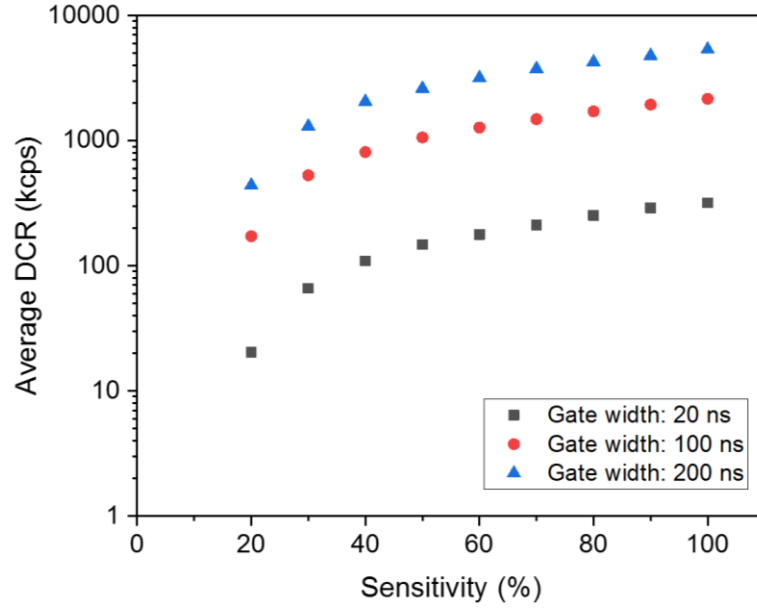
Figure 6.4: Plots of the average DCR for the InGaAs/InP SPAD array as a function of the sensitivity setting (i.e., SPDE%) for gate widths of 20, 100, and 200 ns. As the gate width is increased, the average DCR also increases due to the deleterious effects of afterpulsing.

DCRs of approximately 318 kcps, 2160 kcps, and 5370 kcps were found for gate widths of 20 ns, 100 ns, and 200 ns, respectively. The results in Figure 6.4 show that as the gate width is increased, the average DCR also increases due to the deleterious effects of afterpulsing. The longer the detector is active, the higher the likelihood of trapped carriers being subsequently released - initiating spurious avalanche events and resulting in a higher DCR. Therefore, for all measurements presented in this Chapter, the gate width was kept to the minimum size required for each target scenario.

6.2.1.3 Instrumental response of the array

As discussed in Chapter 4, in order to reconstruct a depth profile of a target using a pixel-wise cross-correlation algorithm, an accurate instrumental response of the system must be known. For a single-pixel detector a single long-acquisition measurement is adequate to obtain this information. However, in such an arrayed detector each pixel has an individual SPAD detector with its own dedicated timing electronics, often resulting in a variation in the timing response from pixel to pixel. In order to characterise the instrumental response of the PLW 32 × 32 SPAD array, a 500,000 binary frame measurement (approximately 3 seconds acquisition with a repetition rate of 150,421 Hz) was made of a uniform, cooperative surface (a Spectralon Diffuse Reflectance panel, Spectralon, Labsphere, Inc). This was obtained in dark laboratory conditions over a short

stand-off distance of 2 metres using a 100% sensitivity setting for the camera. The maximum average optical power level (220 mW) of the laser source was used in order to replicate operating conditions during long-range measurements, with neutral density filters used to reduce the power so that the detector FPA was not damaged. Timing histograms of the instrumental response of several pixels of the array are shown in Figure 6.5 (a) alongside a photon count map (Figure 6.5 (b)) showing the number of counts in the peak bin in each pixel and a peak bin location map (Figure 6.5 (c)) which shows the bin location that contains the peak in each pixel. The peak bin locations in Figure 6.5 (c) were arbitrarily numbered from 1 – 4 to demonstrate the shift across the array.
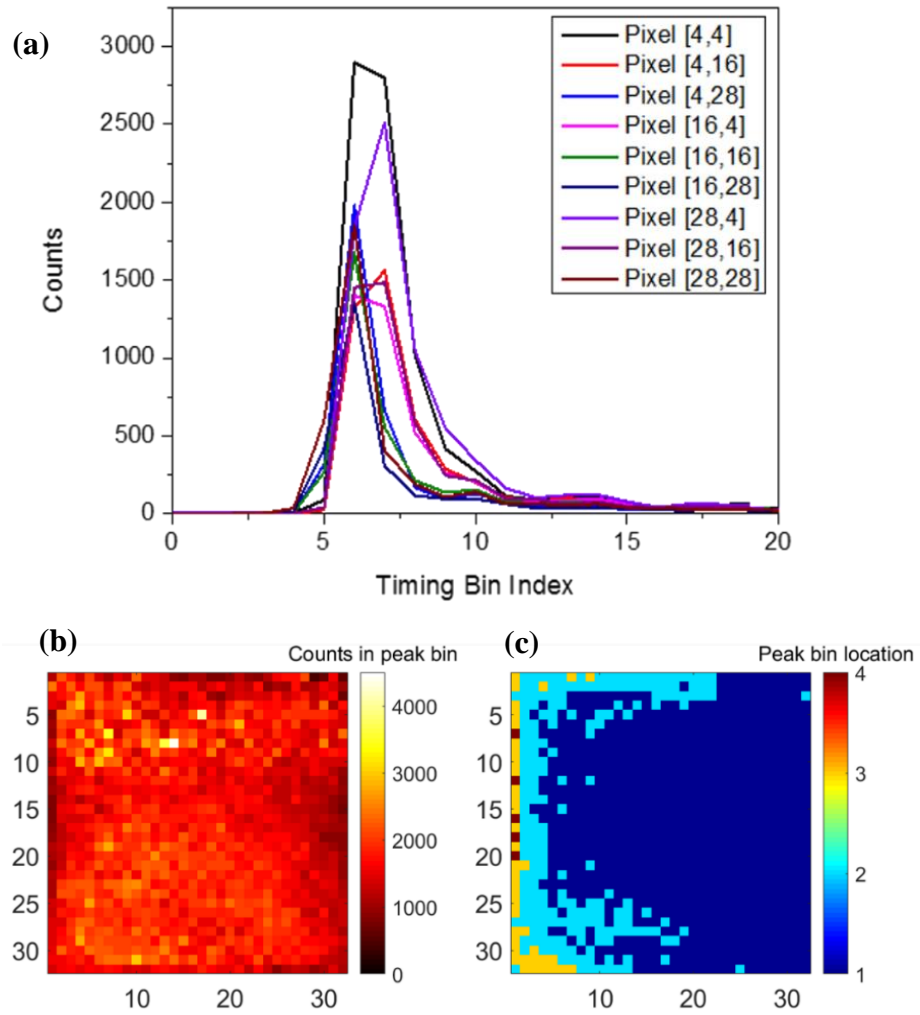
Figure 6.5: The instrumental response function of several pixels of the PLW 32 × 32 SPAD array obtained for 500,000 binary frames from a uniform, cooperative surface in a dark laboratory over a 2 m stand-off distance at a 100% sensitivity setting. (a) shows the timing histograms from several pixels; (b) shows a photon count map with the number of counts in the peak bin in each pixel of the array; and (c) shows a peak bin location map which shows the bin location that contains the peak in each pixel of the array.

As indicated in Figure 6.5 (a), each pixel of the array has a non-identical instrumental response varying in both amplitude and shape. The bin location that contains the target peak can also vary by as much as 1 ns across the array. This is due to varying latency present in the timing electronics of each individual SPAD detector. This is taken into consideration during data reconstruction by using a separate instrumental response for each pixel.

6.2.1.4 Depth resolution

The minimum timing bin size of the PLW 32 × 32 InGaAs/InP SPAD array is 250 ps, which corresponds to a ToF depth of approximately 3.75 cm. Due to Poissonian statistics, the depth resolution of a time-correlated single-photon counting (TCSPC) system is highly dependent on the number of photons detected - with a higher number of detected photons providing better depth resolution [6.20]. This is true as long as the background is relatively low in comparison to the signal. This means that there exists a trade-off between the acquisition time of a measurement and the achievable depth resolution, as the uncertainty in the depth is simply the standard deviation in the measurement, calculated as follows:

$$\bar{\sigma} = \frac{\sigma}{\sqrt{N}}, \qquad (6.2)$$

where σ is the mean timing jitter of the system in each measurement and N is the number of integrated photon counts.

In order to investigate the depth resolution of the system, a custom-made 3-D pillar depth chart was produced. The chart was manufactured using 3-D printing, cleaned to remove excess printing residue, and painted with white primer in order to create a highly reflective surface. The main section of the chart had dimensions of 90 × 90 mm and comprised multiple square pillars with equidistant spacing of 15 mm and 5 mm depth increments - ranging from 5 – 90 mm. A smaller grid with 1 mm depth increments (ranging from 1 – 4 mm) was placed above the main section. A CAD model and photograph of the 3D pillar depth chart is shown in Figure 6.6.
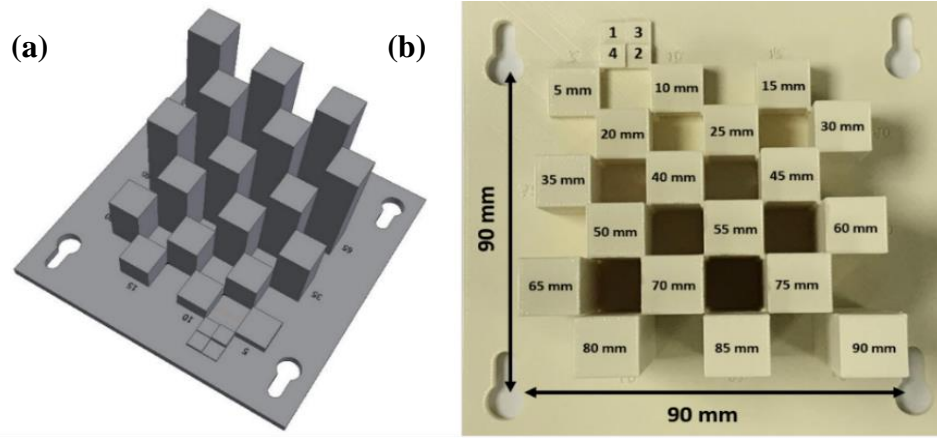
Figure 6.6: (a) A CAD model of the 3-D pillar depth chart. (b) A photograph of the 3D pillar depth chart comprised multiple square pillars with equidistant spacing of 15 mm and 5 mm depth increments.

A depth measurement (shown in Figure 6.7) of the pillar depth chart was obtained using a 20 ns gate width, a repetition rate of 150,421 Hz, an acquisition time of 1 second, and a sensitivity setting of 100%. The target was placed at a stand-off distance of approximately 2 metres in a dark laboratory. A pulsed fibre-coupled laser (operated at an illumination wavelength of λ = 1550 nm) with an average optical power level of 220 mW was used to flood illuminate the target. To avoid damage to the sensitive FPA, a neutral density (ND) filter with an optical transmission of 0.01% (ND4) was used in the transmission channel of the laser to reduce the optical power.
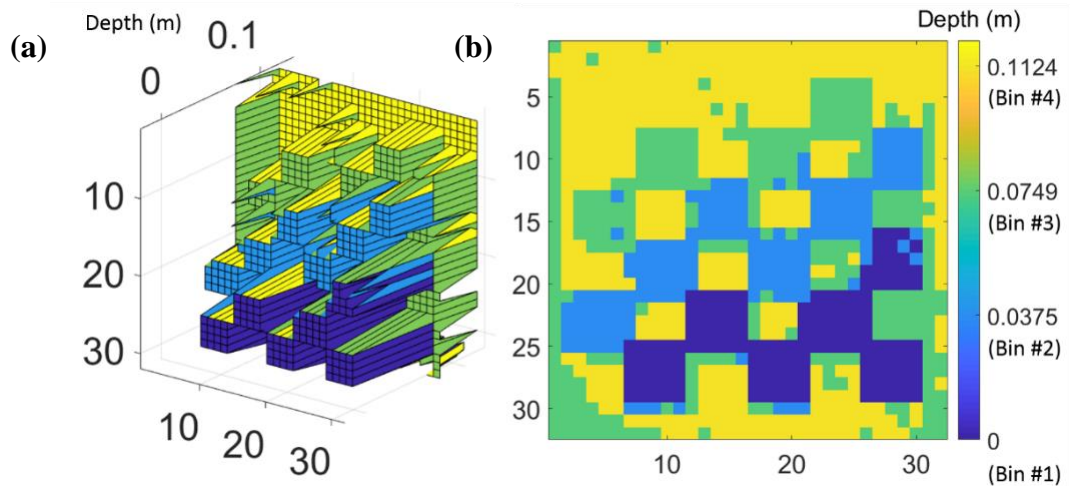
Figure 6.7: Depth profiles of the pillar depth chart obtained using the PLW 32 × 32 SPAD array using a 20 ns gate, a repetition rate of 150,421 Hz, a 1 second acquisition time, and sensitivity setting of 100%. (a) 3D representation of the pillar depth chart. (b) 2-D depth profile of the pillar depth chart. These results were acquired using pixel-wise cross-correlation.

151

The results in Figure 6.7 (a) and (b) show that four separate depth estimates, ranging from 0 – 11.24 cm, were obtained. As expected, these estimates have depth increments of 3.75 cm, corresponding to four sequential 250 ps timing bins. As discussed, this depth resolution could be further improved during data processing using methods described in [6.20].

6.2.1.5 Camera control and data acquisition

The PLW 32 × 32 SPAD array is controlled through an industry standard CameraLink interface - supporting Base, Medium and Full mode - and is connected via standard CameraLink cables to a National Instruments PCIe-1433 framegrabber card housed within the control computer. The camera field-programmable gate array (FPGA) allows a high-speed data transfer of 125 Mb/line over 32 parallel lines (one for each pixel row), which output data from the focal plane array (FPA). The control interface on the host computer allows for simple camera configuration and control by the user via a simple graphical user interface (GUI). The camera supports both external and internal triggering for image acquisition and an external or internal master clock, allowing for easy synchronisation with an illumination source in order to obtain accurate ToF measurements. The camera was powered by a TDK-Lambda 100 W embedded switch mode power supply at 28 V and 3 A.

ToF data for each frame period is stored in binary format, where either a detection event is registered (1) or it is not (0), for each of the 1024 pixels in the array. The memory is cleared after each frame to begin a new accumulation for the next frame. This binary data can then be converted to create timing histograms based on the user-selected timing bin size, frame period, and repetition rate of the camera for subsequent depth and intensity profile reconstruction.

6.2.2 Illumination source

The laser source used for all measurements in this Chapter was a pulsed fibre laser (BKtel, France) operated at an illumination wavelength of λ = 1550 nm [6.21]. An IPS 3610D direct current (DC) power supply (RS Components, UK) was used to supply a voltage of 5.2 V to the laser. While the laser source has a large operational repetition rate range (0 – 2 MHz), a rate of 150,421 Hz was selected in order that the laser was synchronised with the detector to achieve ToF measurements. The laser was mounted directly on to an aluminium breadboard (as shown in Figure 6.8 (a)) for portability, and to avoid accidental

damage to the delicate fibre output. A block diagram of the laser is shown in Figure 6.8 (b).
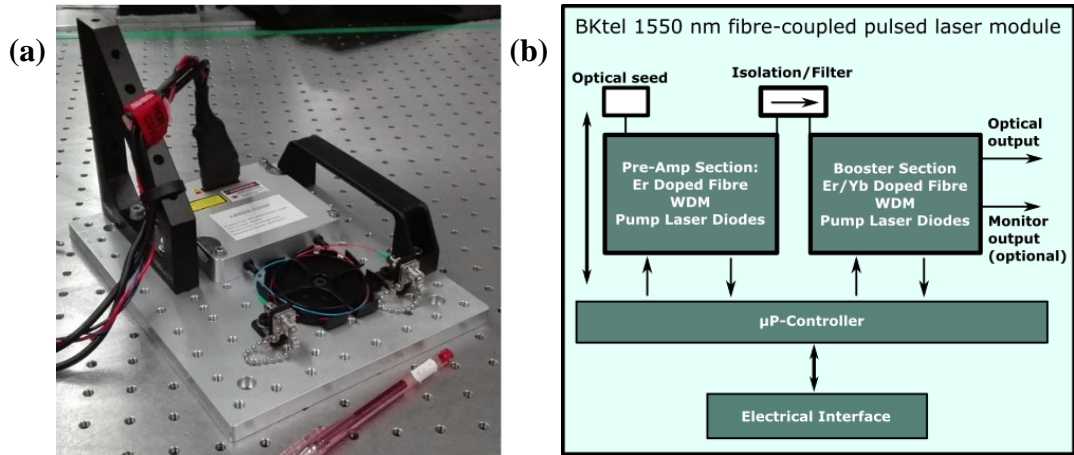
Figure 6.8: (a) The λ = 1550 nm pulsed fibre laser (BKtel, France). (b) Block diagram of the laser adapted from ref. [6.21]. The laser has a pulse width of approximately 400 ps and a maximum average optical power of approximately 220 mW at a repetition rate of 150,421 Hz.

The optical power output of the laser is fibre-coupled via a FC/APC 900 µm single-mode fibre, and is user-controlled via the software TeraTerm by selecting the current setting of the laser. The average output power as a function of current was measured using a fibre-coupled Newport 1936-R optical power meter, for a repetition rate of 150,421 Hz.

The measured output power was found to be approximately linear with respect to increasing current, with the lasing threshold occurring at a current of 1000 mA and a maximum output power of approximately 220 mW at 3000 mA. The central wavelength of the source was measured as 1549.7 nm using a Yokogawa AQ6370D optical spectrum analyser (OSA). This was measured via a fast scan (shown in Figure 6.9 (a)) of 0.2 s/100 nm over a wavelength range of 100 nm performed using an average optical power level of 0.8 mW. A 9 nm at full width half maximum (FWHM) wide band-pass (BP) filter with a central wavelength that was matched to that of the laser source, > 70% optical transmission, and an average out-of-band optical density (OD) > 4 was used to minimise the unwanted effects of any potential amplified spontaneous emission (ASE) from the laser source [6.22]. The pulse length of the laser source was investigated using a fibre-coupled, single-pixel InGaAs/InP SPAD detector with a timing resolution of 2 ps (Micro Photon Devices (MPD), Italy) [6.23]. A detector gate width of 30 ns and a hold-off time of 40 µs were selected and a 300 second integration time was used. A timing histogram of the photon returns from a uniform, cooperative surface is shown in

Figure 6.9 (b). This result was acquired in a dark laboratory at a repetition rate of 150,421 Hz using an extremely low optical power to avoid saturation of the detector. The pulse length of the laser source was measured to be 413 ps FWHM.
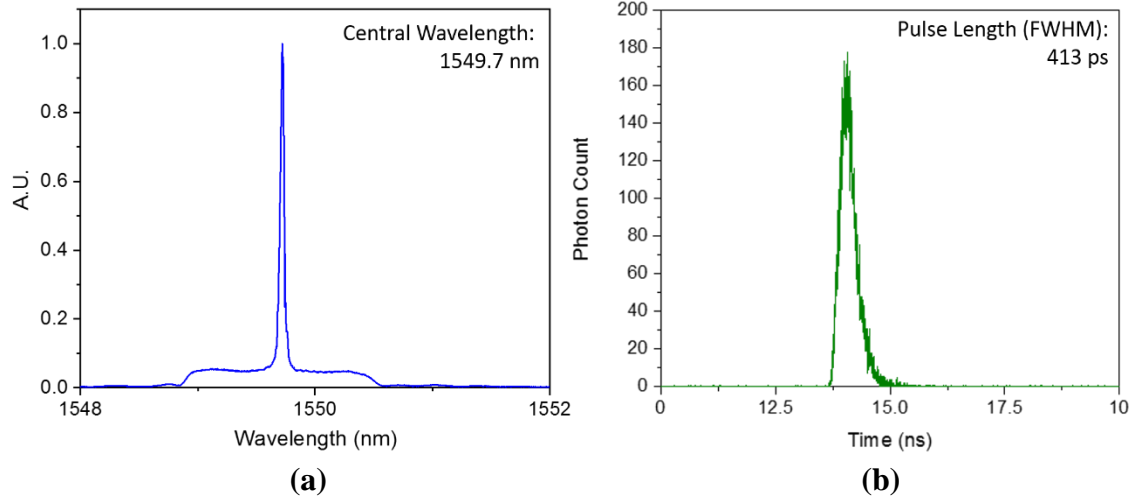
Figure 6.9: (a) The normalised spectral response of the BKtel 1550 nm pulsed fibre laser. The central wavelength was found to be 1549.7 nm. (b) A single-pixel timing histogram obtained from a uniform, cooperative surface measured with the MPD InGaAs gated detector for an integration time of 300 seconds. The pulse length was measured to be 413 ps at FWHM. The 0 ns point in time with respect to the signal was chosen arbitrarily.

6.2.3 Raptor Ninox 640 VIS-SWIR 640 × 512 InGaAs array

In the field trials presented later in this Chapter, a Raptor Ninox 640 VIS-SWIR InGaAs PIN array (Raptor Photonics, UK) was used for both alignment of the PLW field-of-view (FoV) with the illumination beam and capturing synchronised SWIR reference videos during measurements. The Raptor Ninox 640 has dimensions of approximately $123 \times 89 \times 64$ mm and has a standard C-mount connection optical interface. A photograph of the camera (taken from [6.24]) is shown in Figure 6.10 (a). The sensor has an active area of 9.6×7.68 mm with a pixel format of 640×512 and a pixel pitch of 15×15 µm. The wavelength range of the camera is $400 - 1700$ nm. The efficiency varied between 0 and ~93% across the wavelength range of the camera with a $> 80\%$ efficiency at $\lambda = 1550$ nm. The maximum frame rate is 120 Hz, and the data output format is 14-bit CameraLink.
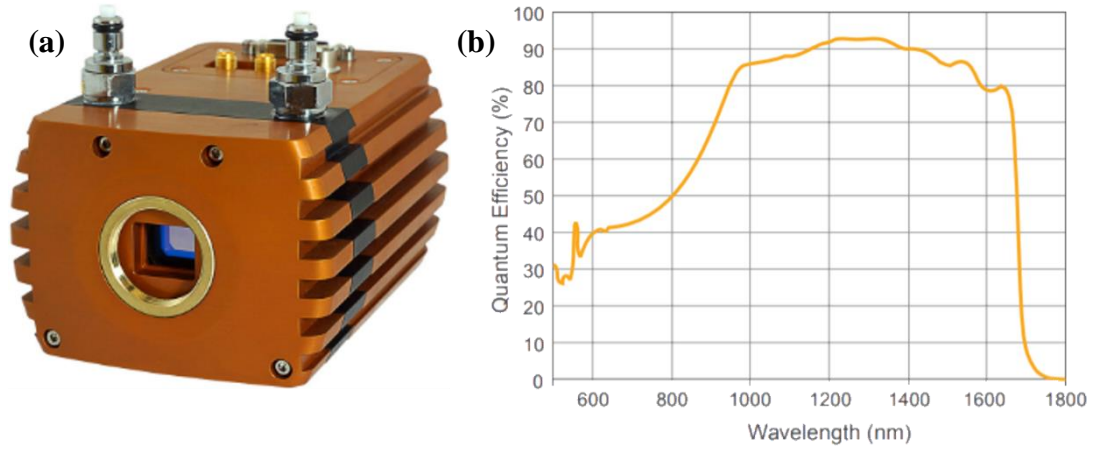
Figure 6.10: (a) A photograph of the Raptor Ninox 640 camera; (b) The quantum efficiency of the sensor over the entire wavelength range. Both images taken from ref. [6.24].

A summary of these key parameters, as stated by the manufacturer, is given in Table 6.2.

Table 6.2: Key parameters for the Raptor Ninox 640 camera listed in ref. [6.24].

Detector parameter	Value/comment
Sensor type	InGaAs PIN-Photodiode
Camera dimensions	123 × 89 × 64 mm
Camera weight	0.9 kg
Array format / dimensions	640 × 512 pixels / 9.6 × 7.68 mm
Pixel pitch	15 × 15 µm
Wavelength range	400 – 1700 nm
Photon detection efficiency at λ = 1550 nm	> 80%
Maximum frame rate	120 Hz
Data output format	CameraLink

The broad spectral response of this sensor means that, with the appropriate optical filters mounted on the optical interface, it can be used to image scenes at specific wavelength bands. For example, Figure 6.11 shows passive images of a colleague taken at a stand-off distance of 50 metres with a 300 mm effective focal length (EFL) objective lens optimised for a wavelength range of 900 – 1700 nm. Figure 6.11 (a) shows a close-up reference photo taken with a visible camera. Figure 6.11 (b) shows a passive image taken with the Raptor Ninox 640 camera operating over its full wavelength range. Figure 6.11 (c) shows a passive image taken with the Raptor Ninox 640 camera using a high performance long-pass (LP) filter with a cut-on wavelength of 1400 nm mounted on the optical interface. The low photon returns from the face and hands shown in Figure 6.11 (c) demonstrates the low reflectivity of human skin in the SWIR region [6.25].

155

(a) **(b)** **(c)**
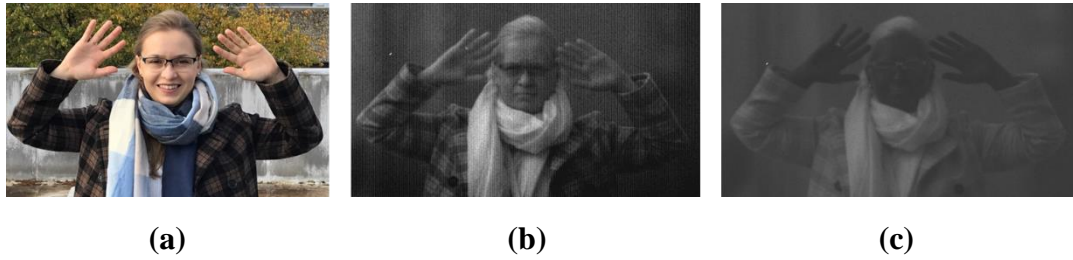
Figure 6.11: Passive images of a group member taken at a stand-off distance of 50 metres. (a) Close-up RGB photograph taken with a visible for reference; (b) Image taken with the Raptor Ninox camera over the full wavelength range (400 – 1700 nm) of the sensor; (c) Image taken with the Raptor Ninox 640 camera using a long-pass filter with a cut-on wavelength of 1400 nm.

6.2.4 SWIR Objective lenses

Two lenses were primarily used as the objective lenses for both the PLW and Raptor Ninox cameras during field trials. The first was a 300 mm EFL lens with a maximum aperture diameter of 85 mm (f/3.5) (Figure 6.12 (a)), and the second was a 500 mm EFL lens with a maximum aperture diameter of 71 mm (f/7) (Figure 6.12 (b)). Both of these lenses are optimised for a wavelength range of 900 – 1700 nm and have transmissions of > 95% at λ = 1550 nm.

Optec 300 mm EFL SWIR lens

Optec 500 mm EFL SWIR lens

99 mm   293 mm

85 mm   400 mm

(a) **(b)**
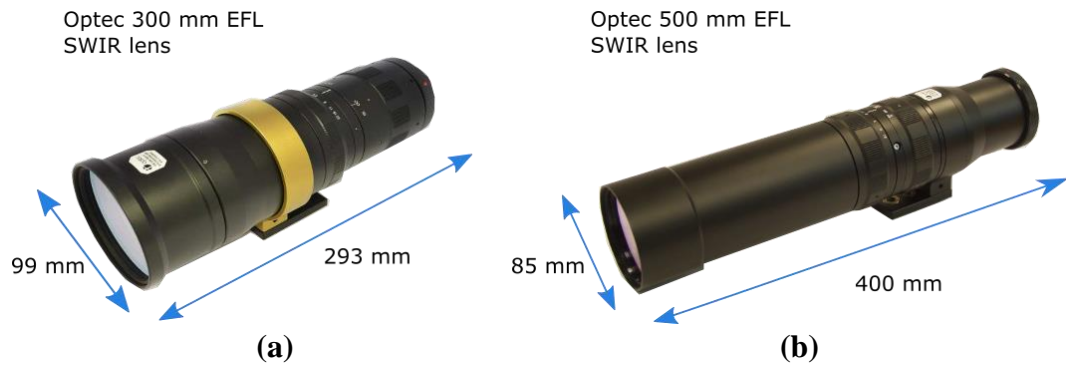
Figure 6.12: The two SWIR lenses used as objective lenses for the PLW and Raptor Ninox camera during field trials: (a) a 300 mm EFL lens with a maximum aperture of 85.7 mm (f/3.5) and (b) a 500 mm EFL lens with a maximum aperture of 71.4 mm (f/7).

These lenses have an M42 optical interface and were attached to the standard C-mount interface of the cameras using an adaptor. Both lenses were mounted to the main system breadboard for stability. A brief summary of the lens parameters is given in Table 6.3.

Table 6.3: Summary of key parameters for the 300 mm and 500 mm SWIR objective lenses used in these field trials.

Lens parameter	Value/comment	
	OB SWIR 300/3.5	**OB SWIR 500/7**
Wavelength range	SWIR 900 – 1700 nm	
Focal length	300 mm	500 mm
Maximum f-number	f/3.5	f/7
Transmission at λ = 1550 nm	> 95%	> 97%
Maximum diameter	99 mm	85 mm
Length	293 mm	400 mm
Mass	2 kg	2.4 kg
Optical interface	M42 interface	

6.2.5 System configuration and key parameters

During the field trials reported in this Chapter, measurements were made over several stand-off distances from tens of metres to kilometre ranges, and in a variety of weather conditions ranging from heavy rain to bright sunlight. This meant that the system design had to be portable and modular, while remaining robust to a wide range of conditions. Photographs of the system in-situ at the Porton Down Battery Hill Laboratory are shown in Figure 6.13 (a) and (b).
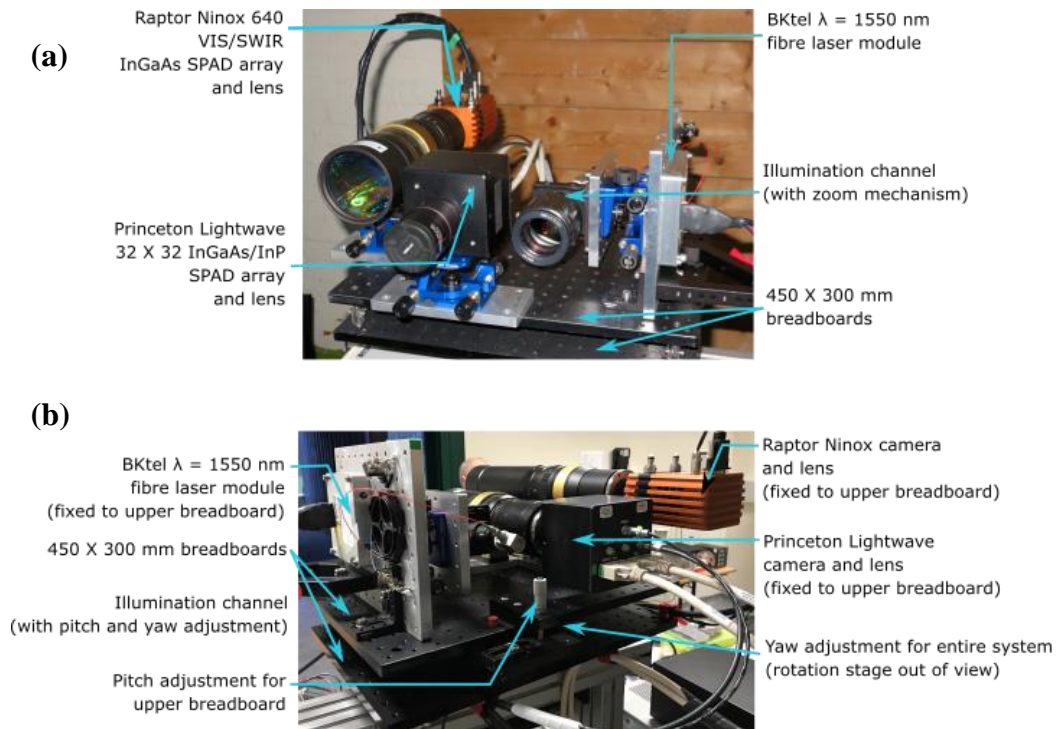
Figure 6.13: Photograph showing the key components of the bistatic system in-situ at the Porton Down Battery Hill Laboratory: (a) front view of the system and (b) rear view of the system.

The system was set up in a bistatic configuration in order to avoid potential issues with back-reflections from optical components causing damage to the sensitive FPA. The bistatic configuration was comprised of two main parts: the illumination source and the two SWIR cameras. The BKtel pulsed fibre laser source, the PLW 32 × 32 SPAD array, and the Raptor Ninox 640 camera were all mounted on the same M6-threaded 450 × 300 mm aluminium breadboard, which was attached to a custom-built basic aluminium structure to raise the imaging system off the optical bench, such that they shared the same FoV. This upper breadboard was then fixed to an identical lower breadboard so that a pitch adjustment mechanism could be attached between the two (as shown in Figure 6.13). The two breadboards were then attached to a small rotation stage allowing for yaw adjustment of the entire system. This set up allowed for fast and easy control of the imaging system for all target scenarios and distances presented in this Chapter. A full schematic of the bistatic system configuration used in these field trials is shown in Figure 6.14.
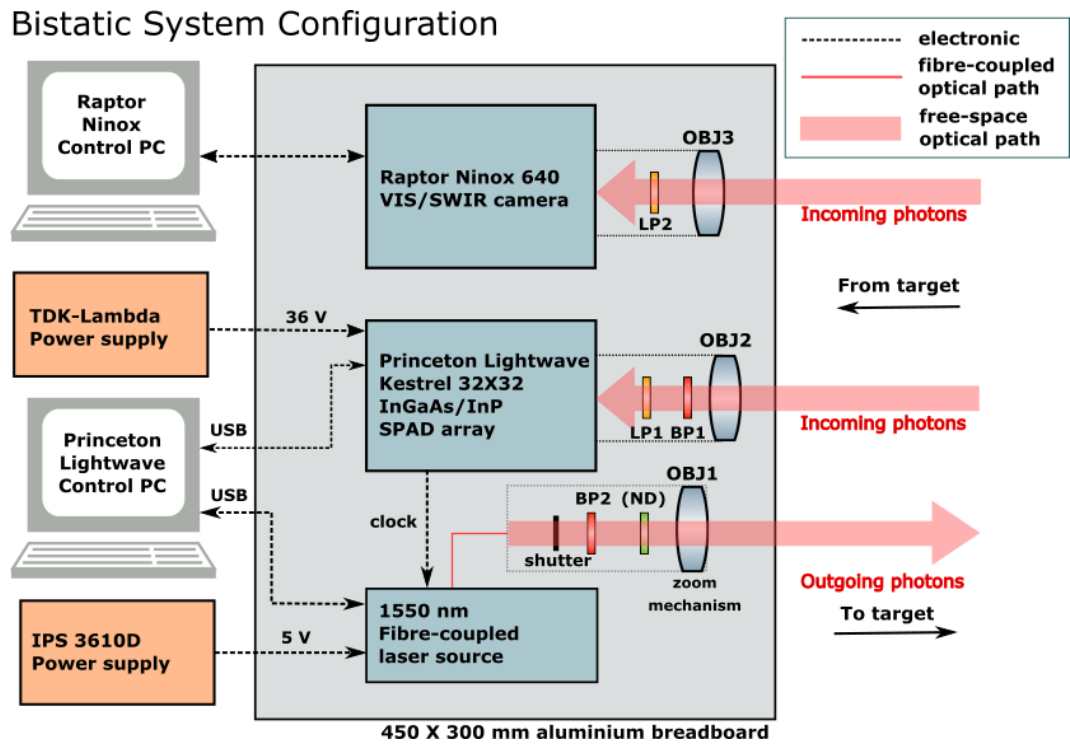
Figure 6.14: Schematic showing the key components and configuration of the bistatic imaging system comprising the Princeton Lightwave Kestrel 32 × 32 InGaAs/InP SPAD array, Raptor Ninox 640 camera, and λ = 1550 nm pulsed illumination source. Optical components include: objective lenses (OBJ1, OBJ2, OBJ3); longpass filters (LP1, LP2); bandpass filters (BP1, BP2); and an ND filter (ND) when required.

The optical layout for the illumination channel is shown in Figure 6.15. The BKtel laser module was fixed to the upper breadboard (as shown in Figure 6.13) and coupled via a 900 µm diameter single-mode optical fibre to an FC/APC reflective collimator. This collimator has a transmission of > 97.5% over a wavelength range of 450 − 2000 nm, and outputs a 4 mm (0.13 NA fibre) diameter collimated beam. This layout was chosen so that the output fibre could be quickly decoupled allowing the average optical power to be monitored using a fibre-coupled power meter throughout the course of the field trials. The light was then routed through a 9 mm FWHM bandpass filter (BP2) with a central wavelength of 1554 nm in order to suppress any potential out-of-band light or ASE produced by the laser source. A two-lens system, comprised of a 9 mm EFL lens and a 75 mm EFL lens used in a telecentric configuration to create a manual zoom mechanism, was used to flood illuminate the target scene with the output beam. These achromatic lenses were optimised for use in the SWIR region of the spectrum. In some cases, such as at shorter ranges or for calibration measurements, an ND filter was used in the transmit channel to lower the average optical power of the outgoing light to avoid potential over saturation of the detector. For safety considerations, a manual beam shutter - inserted between the filters and the reflective collimator - was used to block the beam when the system was not in use.

Figure 6.15: The illumination layout used for the bistatic depth imaging system. Optical components included a reflective collimator, a bandpass filter (BP2), and a zoom mechanism comprised of two lenses (9 mm and 75 mm) in a telecentric layout. If required, an ND filter was inserted prior to the zoom mechanism to reduce the output power. A manual shutter was used to block the beam when the system was not in use.

The PLW 32 × 32 SPAD array camera and corresponding objective lens were attached to a mount, which was subsequently fixed to the upper breadboard alongside the illumination optics. This mount has four exterior locking screws, allowing for accurate fine-tuning of the position of the camera. A C-mount lens tube with SM1 threading was used to house a high-performance bandpass and longpass filter (LP1 and BP1 in Figure 6.14) to reduce potential detection events from ambient illumination. The high-performance bandpass filter was selected to have a central wavelength that was matched to that of the laser source and has an average out-of-band optical density (OD) > 6. The transmission of this BP filter was measured over a range of 400 – 2000 nm. The central wavelength of the BP filter was measured to be 1554 nm with a peak transmission of 94.9% and a 9.3 nm FWHM while achieving excellent out-of-band rejection. However, while this does not match the measured central wavelength of the laser source, this is most likely due to an offset in the calibration measurement on the BP filter. The longpass filter had a cut-on wavelength of 1500 nm with a transmission >98% and an OD > 5 for wavelengths below this threshold. The transmission plots for BP1 and LP1 are shown in Figure 6.16 (a) and Figure 6.16 (b), respectively.

(a) **(b)**
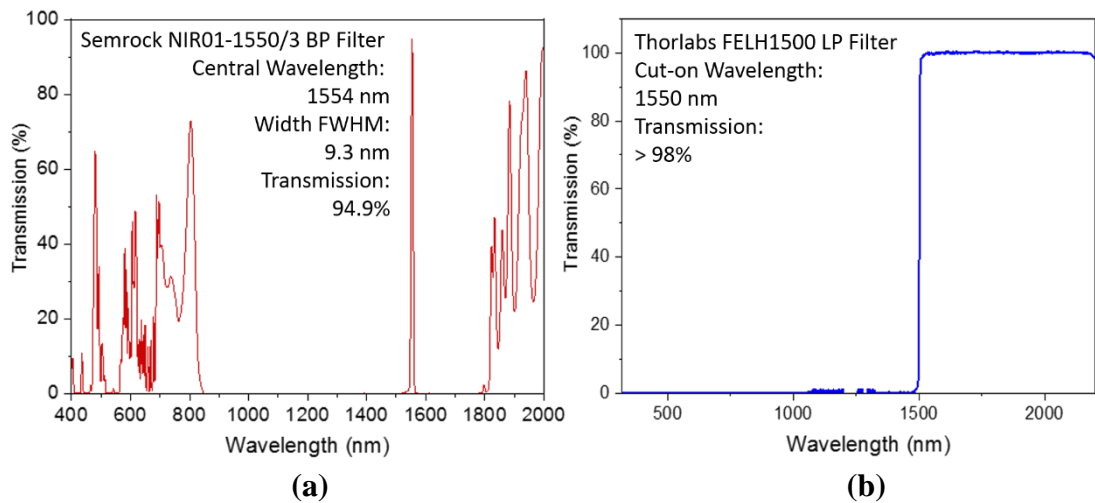
Figure 6.16: (a) Transmission of the 1550 nm BP filter over a wavelength range of 400 – 2000 nm. The central wavelength was measured to be 1554 nm, the filter width was measured to be 9.3 nm, and the peak transmission at the central wavelength was measured to be 94.9%. (b) Transmission of the LP filter over a wavelength range of 320 – 2200 nm. The cut-on wavelength was measured to be 1500 nm, and the transmission > 98%.

The Raptor Ninox 640 camera and corresponding optical components were mounted on an identical mount, to the upper breadboard next to the PLW SPAD array. A longpass

filter with a cut-on wavelength of 1400 nm, a transmission of $> 80\%$, and an OD > 5 allowed for image acquisition exclusively in the SWIR region of the spectrum. The 300 mm EFL and 500 mm EFL SWIR objective lenses (discussed previously in this Chapter) were mounted to each sensor as necessary depending on the desired FoV and stand-off distance of the target. The overall system jitter was found to be approximately 485 ps.

6.3 Adapted LiDAR model for the bistatic depth imaging system

In order to predict the potential ranging performance of the bistatic depth imaging system in the presence of obscurants such as fog and smoke, a LiDAR model based on a photon counting adaptation of the general LiDAR equation presented in [6.26] was developed.

6.3.1 General form of the photon-counting LiDAR equation.

The photon-counting LiDAR equation in its most general form can be written as:

$$P(R) = KG(R)\beta(R)T(R), \qquad (6.3)$$

where P is the signal power received by the imaging system from a stand-off distance of R [6.26]. Two of the contributing factors to the LiDAR model, K and $G(R)$, are intrinsic to the LiDAR system and are therefore determined by the configuration and performance of the system hardware and components. The first factor, K, describes the performance of the LiDAR system, including parameters such as optical component transmission efficiency, detector efficiency, and the overall temporal response of the system. The second factor, $G(R)$, describes the measurement geometry of the system, which is dependent on the range of the target. The two extrinsic factors, β and T, are environmental factors that can vary greatly depending on atmospheric conditions during measurements. The first of these extrinsic factors, $\beta(R)$, indicates the backscatter coefficient, which describes the ability of the atmosphere to scatter light back in the direction of propagation. The second extrinsic factor, the transmission term $T(R)$, describes the range-dependent reduction of light caused by forward scattering and absorption due to the atmosphere. These two factors are highly sensitive to the presence of smoke or fog, with high levels of obscurants resulting in much lower photon levels received by the LiDAR system.

The following Section of this Thesis describes a LiDAR equation based on the general photon-counting model described above and adapted for the configuration of the bistatic depth imaging system detailed in this Chapter. This equation calculates the expected number of photon returns in the timing histogram bin containing the highest peak for a

single pixel in the SPAD array. It is important to note that, due the non-uniformity of the detector response across the 32 × 32 FPA (shown in Figure 6.3 (a)), these results are estimated based on the response of a central SPAD in the array (e.g., pixel [17:17]) that gives an average response. Therefore, pixels on the outer edges of the array may produce marginally different results. However, by operating the SPAD array at a setting of 100% sensitivity (i.e., maximum bias level) the non-uniformity across the pixels array is minimised.

6.3.2 Adapted LiDAR equation for the bistatic depth imaging system

This Section describes each parameter considered in the adapted LiDAR equation. As discussed above, the resulting number of photons detected by the LiDAR system is greatly affected by the optical configuration of the system and atmospheric conditions during measurements. Therefore, these parameters will have to be considered for each measurement scenario and altered if any modifications are made to the system.

6.3.2.1 Average optical power and wavelength dependence

The number of photons collected by the LiDAR system is linearly dependent on the average optical power used. Knowing both the average optical power level, P_{out}, and the illumination wavelength, λ, the rate of photon emission per second, γ, from the illumination source can be calculated as follows:

$$\gamma = \frac{\lambda P_{out}}{hc},$$
(6.4)

where c is the speed of light in a vacuum and h is Planck's constant.

6.3.2.2 Acquisition time

The acquisition time, τ_{acq}, for the SPAD array can be defined as the amount of time the system acquires data from the target for each measurement. Since each of the 1024 arrayed pixels measure the scene simultaneously, the total acquisition time for one measurement can be taken to be the number of measured frames, N_f, divided by the fixed repetition rate, f_{rep}, of the laser source and camera:

$$\tau_{acq} = \frac{N_f}{f_{rep}},$$
(6.5)

6.3.2.3 Target reflectivity

Target reflectivity, ρ, can be defined as the percentage of incident light reflected from the target. When light is incident on a target, photons are either absorbed, transmitted, or scattered depending on the properties of the surface and material. Factors such as surface roughness, colour, and the orientation of the target all have a significant effect on the number of photons reflected by the target and thus, the number of photons received by the LiDAR system.

6.3.2.4 Geometric factor

Due to geometrical limitations, the LiDAR system is unable to collect all photons that are scattered back from the target. In practice, the number of photons collected by the system is dependent on both the area of the objective lens, A_{lens}, and the target range, R. In an ideal scenario, the target acts as a perfect Lambertian reflector such that all the light is scattered and none is transmitted meaning only half of the overall solid angle should be considered. Therefore, the ratio of the number of photons scattered by the target, P_s, and the number of photons collected by the system, P_c, at a stand-off distance, R, is as:

$$\frac{Pc}{Ps} = \frac{A_{lens}}{2\pi R^2}. \tag{6.6}$$

In a bistatic system, the separation of the detector and the source should be considered in determining the true range of the target. However, due to the minimal separation distance of these components in the bistatic set-up used in this system configuration, we can make the assumption that since $R \gg d$ (where d is the separation distance between the source and the detector) then we can approximate the target range as simply R.

Another geometrical consideration is that if the illumination spot does not match the size of the detection window at the target. For example, if the illumination over-fills the detection window (as shown in Figure 6.17) then photons from outside the detection window will not be detected by the system.
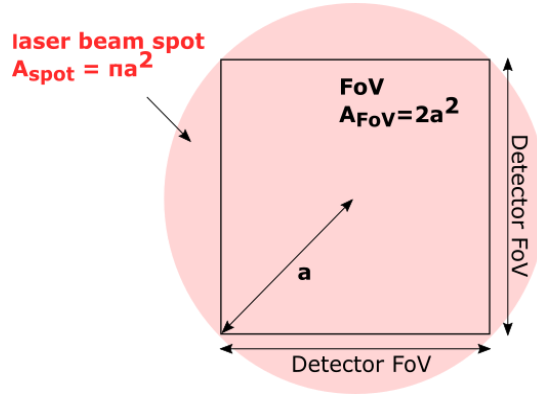
Figure 6.17: Example of the illumination over-filling the system detection window. A correction factor must be applied, as photons from outside the window will not be detected by the system.

The area of the detection window, A_{FoV}, with radius a is given as:

$$A_{FoV} = 2a^2,$$ (6.7)

and the area covered by the laser beam spot A_{spot} with radius a is given as:

$$A_{spot} = \pi a^2,$$ (6.8)

Therefore, the corrected ratio (*corr*) can be expressed as the ratio between these two areas:

$$corr = \frac{2a^2}{\pi a^2} \cong \frac{7}{11}.$$ (6.9)

Thus, with consideration of these lost photons, the range-dependent geometrical term for the adapted LiDAR equation is as follows:

$$G(R) = \frac{7A_{lens}}{22\pi R^2}.$$ (6.10)

6.3.2.5 Environmental attenuation

Atmospheric attenuation is highly dependent on weather, ambient conditions, and the wavelength of the propagating light. While in clear conditions the level of attenuation is low, in a degraded visual environment the high level of obscurants in the atmosphere can result in significant levels of atmospheric attenuation due to particulate scattering. Therefore, the transmission term of the adapted LiDAR equation, ς_{attn}, considers the fraction of light that is attenuated due to the volume of scattering media present in the round trip between the LiDAR system and the target as follows:

$$\varsigma_{attn} = e^{-2\alpha R},$$ (6.11)

164

where the attenuation coefficient, α (m^{-1}), is dependent on the relative size of the scattering particles, χ. The particle size parameter is dependent on both the propagation wavelength, λ, and the radius of the scattering particles, $r_{particle}$, as follows:

$$\chi = \frac{2\pi r_{particle}}{\lambda}. \tag{6.12}$$

6.3.2.6 Internal attenuation

The internal system coefficient, ε_{int}, considers losses within the LiDAR system due to optical components and any potential misalignments. Optical loss within the system can arise from spectral or spatial filtering, coupling losses, and transmission losses in the optical fibres. Since the internal system coefficient is dependent on the optical set-up it must be revised if modifications, such as a change in objective lens or optical filters, are made.

6.3.2.7 Temporal response coefficient

The temporal response coefficient, t_{resp}, is the instrumental response of the system. This is determined by taking a measurement from a flat, cooperative target positioned perpendicular to the laser propagation and calculating the ratio between the number of counts in the highest bin in the histogram peak and the total number of photons in the entire histogram peak.

6.3.2.8 Detector efficiency

The single-photon detector efficiency, η, is dependent on the sensitivity setting (i.e., the excess bias) of the SPAD detector and the operational wavelength of the laser source. As previously discussed, the detector efficiency for the PLW 32 × 32 InGaAs/InP SPAD array at an operational wavelength of 1550 nm and a sensitivity setting of 100% corresponds to an SPDE, η, of approximately 25%.

6.3.2.9 Background level

The background level is defined as the number of counts registered by the LiDAR system that do not originate from target returns. These can arise from dark counts of the SPAD detector, from atmospheric scattering effects, or from ambient light. This means that the level of background varies with both the ambient conditions and the system configuration. Thus, the background level must be measured for each specific optical configuration and for changes in environmental conditions during measurements. The level of background for each measurement can estimated from a flat section of the timing histogram containing

no photon returns from target surfaces. The average number of background counts per-bin per-second, n_b, can be obtained using the following equation:

$$n_b = \frac{N_{counts} f_{rep}}{N_{bins} N_f},$$

(6.13)

where N_{counts} is the number of counts in the selected region of the timing histogram, N_{bins} is the number of timing bins in this region, f_{rep} is the repetition rate of the laser source and camera, and N_f is the number of binary frames used for the measurement.

6.3.2.10 Signal-to-noise ratio

The signal-to-noise ratio, *SNR*, of the photon return peak and the average background level can be estimated from the number of photons in the bin with the highest count in the return peak, n_p, and the average number of background counts per bin per second, n_b, as follows:

$$SNR = \frac{n_p}{\sqrt{n_p + n_b}}.$$

(6.14)

In order to use the proposed adapted LiDAR equation to estimate the maximum number of attenuation lengths achievable by the system in various configurations, a minimum threshold for the *SNR* (*SNR$_{min}$*) had to be established. This threshold was empirically measured from timing histograms with very low return signal and was found to have a *SNR$_{min}$* = 1.8 for this system when processed using pixel-wise cross-correlation. In fact, this is a conservative estimate as other work on underwater imaging [6.27] placed the lower limit for single-pixel imaging at 1.4 for single-photon data. The estimate of *SNR$_{min}$* is a subjective analysis, based on the ability to register an image, and will be affected by the number of pixels recorded in the image and in this field trial, the system was limited to only a 32 × 32 pixel format. It should also be noted that the depth image analysis is pixel-wise, and that use of image processing exploiting spatial correlations would further reduce the *SNR$_{min}$* to much less than the 1.8 value quoted here.

6.3.2.11 Adapted LiDAR equation

By considering the general form of the photon-counting LiDAR equation and the parameters discussed in this Chapter, the adapted LiDAR equation for the bistatic depth imaging system can be expressed as follows:

$$\frac{n_b}{N_p} = \frac{P_{out}\lambda}{hc}\frac{N_f}{f_{rep}}\frac{7A_{lens}}{22\pi R^2}e^{-2\alpha R}\varepsilon_{int}t_{resp}\eta, \tag{6.15}$$

where n_p is the number of photons in the histogram bin with the highest count in the return peak subsequently divided by the total number of pixels in the array, N_p, to obtain the estimated number of photon returns for a single pixel.

6.3.3 Simulations

Several simulations were performed using this adapted LiDAR equation to estimate the maximum achievable performance of the bistatic depth imaging system in different environmental conditions. An example of the system parameters and values used to make these estimates is shown in Table 6.4. These parameters were chosen so that they reflected the actual parameters used in the field trials presented in this Chapter.

Table 6.4: An example of the system parameters and values used to estimate the maximum achievable performance of the bistatic depth imaging system in different environmental conditions.

System parameter	Value/comment
Wavelength λ	1550 nm (10 nm FWHM)
Camera/Laser repetition rate (f$_{rep}$)	150,421 Hz
Average optical power level P$_{out}$	220 mW
Lens diameter Φ	85 mm
Target range	150 m
Target reflectivity ρ	~ 95%
Internal attenuation τ$_{int}$	~ 70% (Estimated by taking in to account the transmission losses in the spectral filters and lenses used in the system.)
Temporal response τ$_{resp}$	0.3 (Calculated using a known instrumental response for the SPAD array)
Detector efficiency η	~ 25% at 100% sensitivity setting as specified by the manufacturer
Average number of background counts per bin per second n$_b$	~ 100
SNR$_{min}$	1.8

The adapted LiDAR equation was used to estimate the number of photons collected by the system over the full average optical power range of the illumination source $(0-220\,\text{mW})$. This analysis was performed for 1.5, 3, 4.5, 5.25, and 6 attenuation lengths, as shown in Figure 6.18 (a). The SNR as a function of the average optical power was also investigated (Figure 6.18 (b)) for several values of attenuation length (i.e., $5.25-6.3$ in 0.15 increments) in order to determine the maximum achievable number of attenuation lengths using this particular laser source.

Figure 6.18: (a) Semi-logarithmic plot of photon counts in the histogram bin versus the highest return peak as a function of average optical power level for different numbers of attenuation lengths estimated using the adapted LiDAR equation. (b) A plot of the SNR as a function of average optical power for various values of attenuation lengths at λ = 1550 nm estimated using the adapted LiDAR equation. The estimated minimum threshold SNR_{min} = 1.8 is shown by the dotted red line.

It is evident from Figure 6.18 (a) that, as expected, as the output power of the laser increases the number of photon returns from the target collected by the system increases. This means that the use of the full available average optical power of the laser would be greatly beneficial for imaging in high levels of obscurants. Figure 6.18 (b) indicates that the maximum achievable number of attenuation lengths with this system set-up is approximately 6 attenuation lengths (i.e., an attenuation coefficient of $\alpha = 0.40$ m^{-1}) at 150 m. This is dependent on the level of background, with lower background levels potentially allowing for imaging at higher atmospheric attenuation. This estimate is also based on the current system configuration which has a system efficiency (due to loss in the receive channel, but not including detector efficiency) of approximately 70%, meaning that the use of better performance optical components could potentially lead to an increase in system performance.

The distance between the target location and the LiDAR system has a significant effect on the number of return photons collected by the objective lens. The proposed adapted LiDAR equation was used to investigate the number of photon counts in the bin with the highest peak for a single-pixel over a range of 200 – 1000 metres, and at different levels

of attenuation (shown in Figure 6.19 (a)). Figure 6.19 (b) estimates the maximum achievable number of attenuation levels for stand-off distances from $150 - 500$ metres.

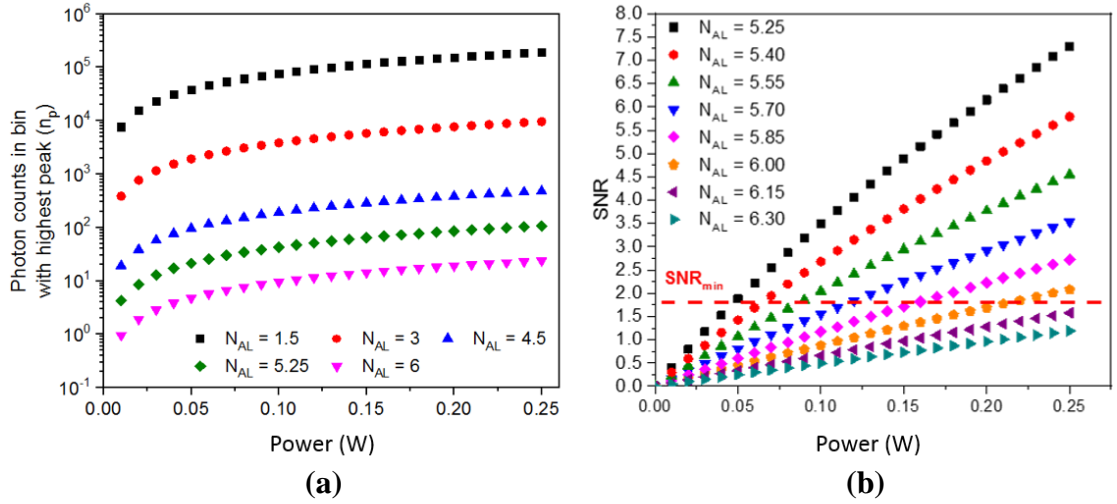*Figure 6.19: (a) Semi-logarithmic plot of photon counts in the histogram bin with the highest return peak as a function of target range for different numbers of attenuation lengths estimated using the adapted LiDAR equation. (b) Plot of maximum achievable number of attenuation lengths as a function of SNR for several target ranges. The estimated minimum threshold $SNR_{min} = 1.8$ is shown in red.*

Figure 6.19 (a) demonstrates that the number of photon returns collected by the LiDAR system decreases significantly at longer target ranges for very high levels of attenuation. For example, less than one return photon is predicted for a 200 m range for 6 attenuation lengths. Figure 6.19 (b) indicates that a maximum of 6 attenuation lengths is achievable for a range of 150 metres using the current system configuration, and up to 3 attenuation lengths at a 300 metre range. If the target range is extended to 500 metres, it may no longer be possible to make an accurate depth estimate with the current system configuration in such highly attenuating environment. However, with modifications and improvements to the transceiver, it may be possible to acquire depth images at these extended ranges.

Another parameter that has a significant effect on the number of photons detected by a LiDAR system is the diameter of the objective lens of the receiver, with a larger aperture diameter, φ, improving the return collection. A plot of the number of photon counts in the histogram bin with the highest return peak as a function of the lens diameter for varying attenuation lengths ($1 - 7$ attenuation lengths) is shown in Figure 6.20 (a). Figure

6.20 (b) shows the maximum achievable number of attenuation lengths as a function of the *SNR* for increasing lens diameters.
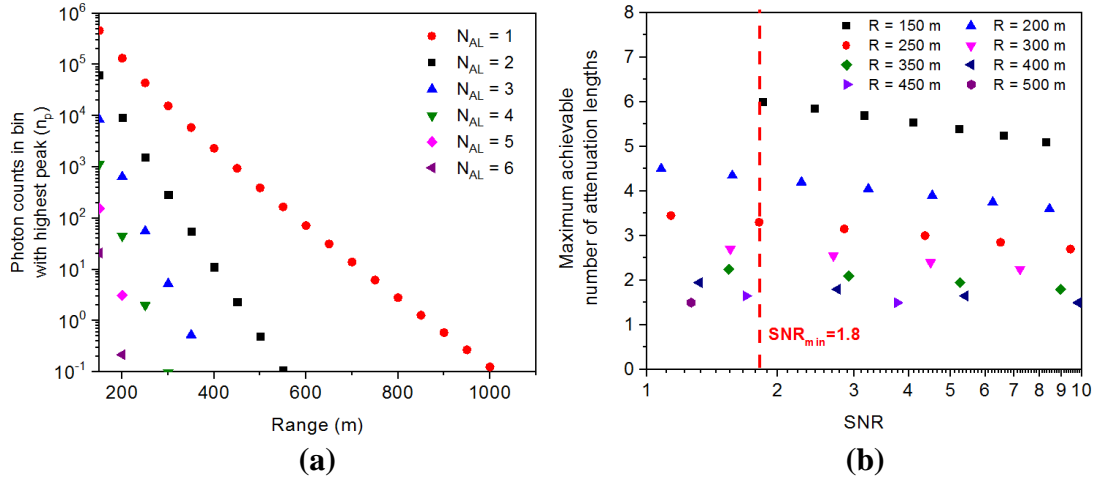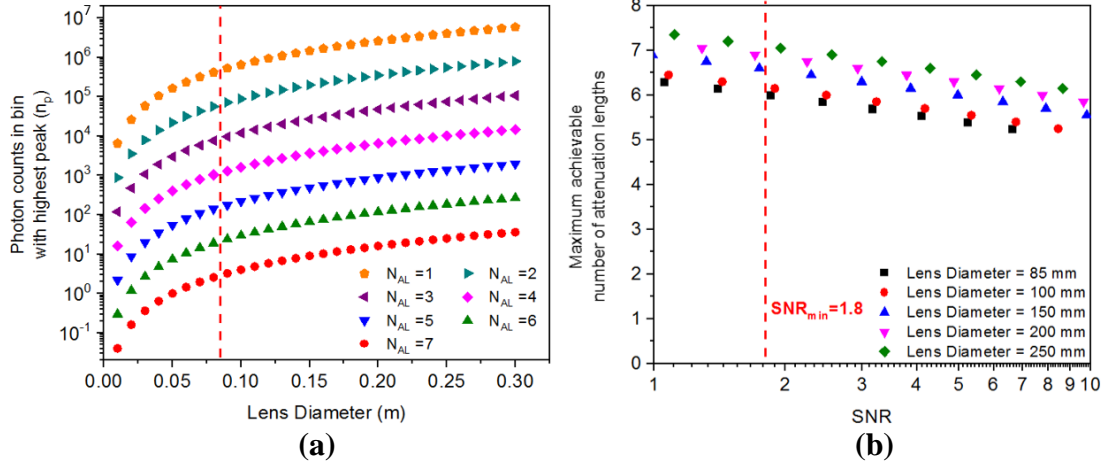

Figure 6.20: (a) Semi-logarithmic plot of the number of photon counts in the histogram bin with the highest return peak as a function of lens diameter for different numbers of attenuation lengths estimated using the adapted LiDAR equation. (b) Plot of maximum achievable number of attenuation lengths as a function of SNR for several objective lens diameters. The estimated minimum threshold SNR_min = 1.8 is shown in red.

It is evident from the simulation results in Figure 6.20 (a) that a larger aperture lens can significantly increase the number of photon returns collected by the LiDAR system. Objective lenses with aperture sizes up to 85 mm were used to obtain the results presented in this Chapter. However, for future field trials the objective lens for the receiver could be switched to a larger aperture lens to achieve imaging at a higher number of attenuation lengths (see Figure 6.20 (b)).

Weather conditions, solar background, detector dark counts, and back-scattering from obscuring media will all contribute to the average level of background counts recorded by the LiDAR system. This background level has a direct impact on the minimum *SNR* threshold (*SNR_min*) required to obtain a depth estimate, with a higher background level resulting in a lower number of achievable attenuation lengths. For example, Figure 6.21 shows a plot of the maximum achievable number of attenuation lengths as a function of the *SNR* (setting *SNR_min* = 1.8) for different levels of background counts per bin per second.
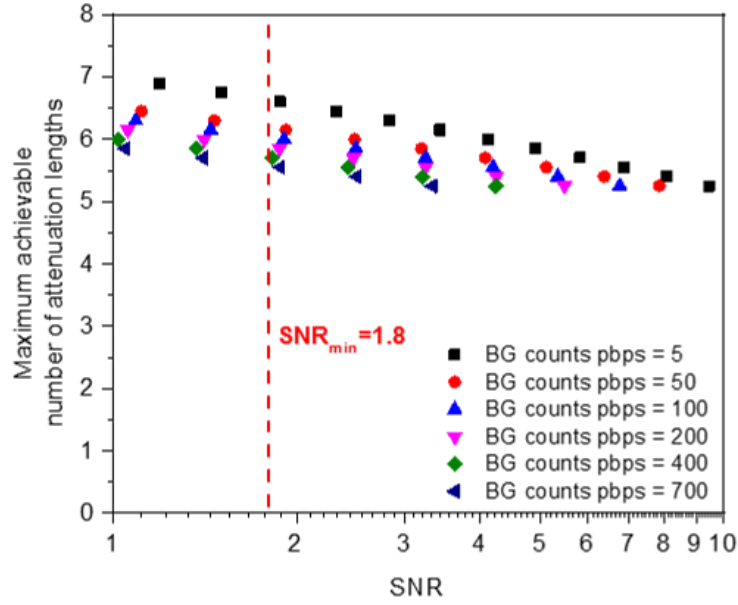
Figure 6.21: Plot of maximum achievable number of attenuation lengths as a function of SNR for different average background levels. The minimum threshold $SNR_{min} = 1.8$ is shown in red.

It is clear from the results shown in Figure 6.21 that it is desirable to maintain as low a background level as possible in order to achieve maximum penetration through obscurants. A major factor in achieving this is the use of high-performance optical filters in the receive path such as longpass and narrow width bandpass filters that are well-matched to the laser emission. The use of a restricted FoV will also reduce the background level. Another method is to perform imaging either at night or indoors with no ambient lighting although this is impractical for many applications.

In conclusion, by using the maximum available optical power of the laser source, an objective lens diameter in the order of 85 mm, and with the system configuration described in this Chapter, the proposed LiDAR model predicts that imaging through obscurants at up to 6 attenuation lengths at a range of up to 150 m should be possible (Figure 6.22). This is of course highly dependent on the level of background due to ambient illumination, the optical components used, and the target, as previously discussed. If the target is more complex or less reflective than estimated, this is likely to lower the number of attenuation lengths achievable. Therefore, further investigation of the reflectivity of targets with different materials and geometry are required to improve this model further.
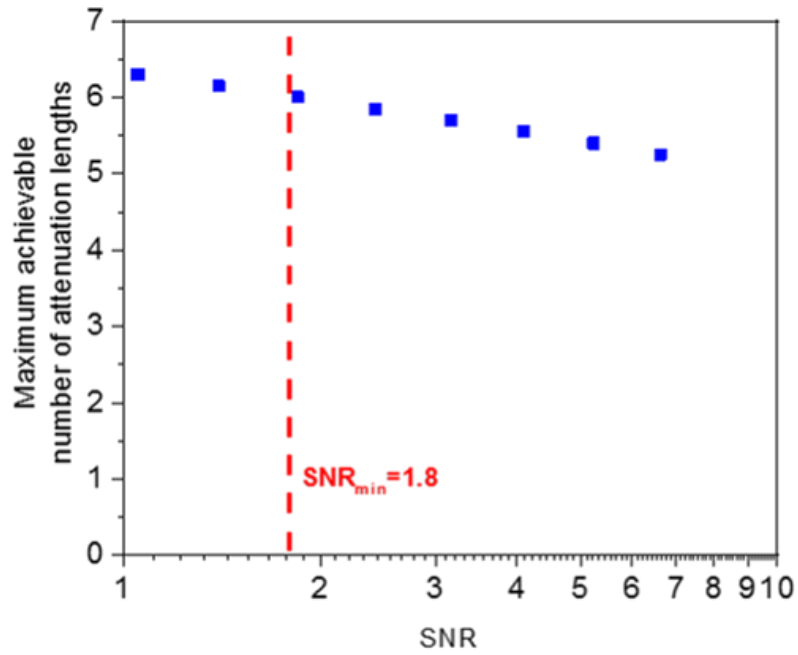
Figure 6.22: Plot of the maximum achievable number of attenuation lengths as a function of SNR for an average optical power level of 0.220 W, a lens diameter of 85 mm, and at a target range of 150 metres. The minimum threshold SNR_{min} = 1.8 is shown in red.

6.4 Experimental layout for the Porton Down field trials

This Section gives details of experiments conducted at field trials undertaken at Dstl Porton Down Battery Hill Laboratory (BHL) in Salisbury to evaluate the performance of the arrayed detector depth imaging system described in this Chapter.

6.4.1 Measurement ranges, procedures, and targets

Measurements were performed in both indoor and outdoor environments in daylight conditions for short (50 metres), mid (150 metres), and long (1463 metres) ranges to identify the conditions and parameters for optimum sensor performance at each range. The indoor range was housed in the BHL gun shed with the system located 50 metres from the target position. The 150 and 1463 metre range measurements were performed with targets placed outdoors and the system housed within the main building of the BHL.

For the short and mid-range measurements, an obscurant was introduced to the sensor line-of-sight. A smoke gun, using disposable gas canisters, was used to produce a glycol-based vapour with particle sizes ranging from $1 - 2\,\mu$m. This vapour condenses upon reaching normal atmospheric conditions and produces a dense, non-toxic, white smoke designed for use in agricultural, theatrical, or military training exercises. The variable output of the smoke gun was regulated such that anything from light mist to a

172

dense fog could be produced. To contain the obscurant, a polyethylene marquee (shown in Figure 6.23) with dimensions of 3 m (H) × 4 m (W) × 10 m (L) was erected in the system line-of-sight.

For each measurement, the marquee was filled with the glycol vapour until a sufficient density was achieved. The marquee door was then opened to allow measurements of the targets while the glycol vapour dispersed from the marquee over the duration of the measurement, as shown in Figure 6.23. For the 50 m range, two large fans were used to disperse the obscurant for improved uniformity.

Figure 6.23: Photographs showing the dispersion of the obscurant from the point where the marquee door was opened to the end of the full measurement duration.

In order to evaluate the system performance when imaging through various densities of glycol vapour, a 1 m × 1 m 3D panel chart (Figure 6.24) comprising four flat, white panels set at 10 cm depth increments was imaged. This target provided a cooperative surface allowing for both calibration and evaluative measurements and could be positioned in the target scene as required.
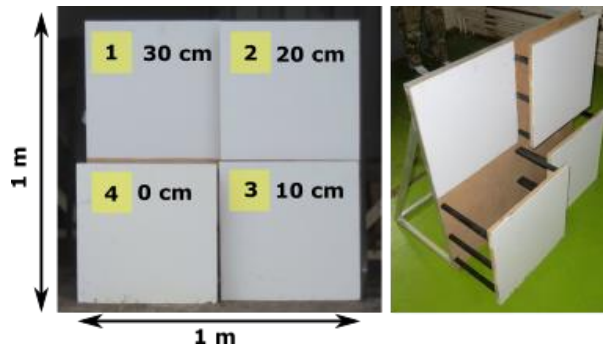

Figure 6.24: Front and side views of the 3D panel chart target with 10 cm depth increments.

For each measurement the λ = 1550 nm system was synchronised with a transmissometer (discussed later) and the Raptor camera, via a countdown, such that the measurements were matched with the data acquired from the array. Data were acquired until the point

at which either the target was visible, or the detector was saturated. At this point, the camera was shut off and the laser blocked to avoid damage to the highly sensitive SPAD detector array.

6.4.2 Quantitative measurements of the number of attenuation lengths

The number of attenuation lengths (N_{AL}) at λ = 1550 nm between the system and the target was calculated from single-photon data collected from a known area of the 3D panel chart for each measurement using the Beer-Lambert law [6.28] in a similar fashion to the results presented in Chapter 5 of this Thesis. The equation used to calculate this is as follows:

$$N_{AL} = \alpha d = \frac{1}{2} \ln \left[\frac{C_o}{C} \right], \tag{6.16}$$

where C is the number of photons in the target return peak in the presence of obscurant, C_0 is the number of photons in the target return peak in the absence of obscurant, d is the one-way distance of propagation, and α is the attenuation coefficient. Due to the longer stand-off distances and higher levels of attenuation used in these measurements than those presented in Chapter 5 of this Thesis, the target return peak in the timing histograms was sometimes of the same magnitude as the background level. Moreover, as discussed previously in Section 6.2.1.3, each pixel in the array has a non-identical response. Therefore, in this case, C and C_0 were calculated from timing histograms summed over a 9×9 pixel neighbourhood for a 1 second data acquisition to acquire an accurate measurement of the number of attenuation lengths for the entire measurement duration. A reference measurement (used to calculate C_0) on the 3D panel chart was performed using an appropriate level of ND filter in the transmission channel in order to attenuate the illumination beam when no obscurant was present. This was done to avoid damage to the detector FPA, and a suitable level of ND was chosen for each measurement scenario, target range, and system configuration. Attenuation measurements were also taken using a transmissometer for both λ = 1550 nm and λ = 637 nm for comparison between SWIR and visible wavelengths. An example of single-pixel timing histograms acquired for one second of single-photon data over a 50 metre stand-off distance using the 32 × 32 PLW SPAD array is shown in Figure 6.25. Timing histograms from both a reference measurement and a noisy measurement are shown.
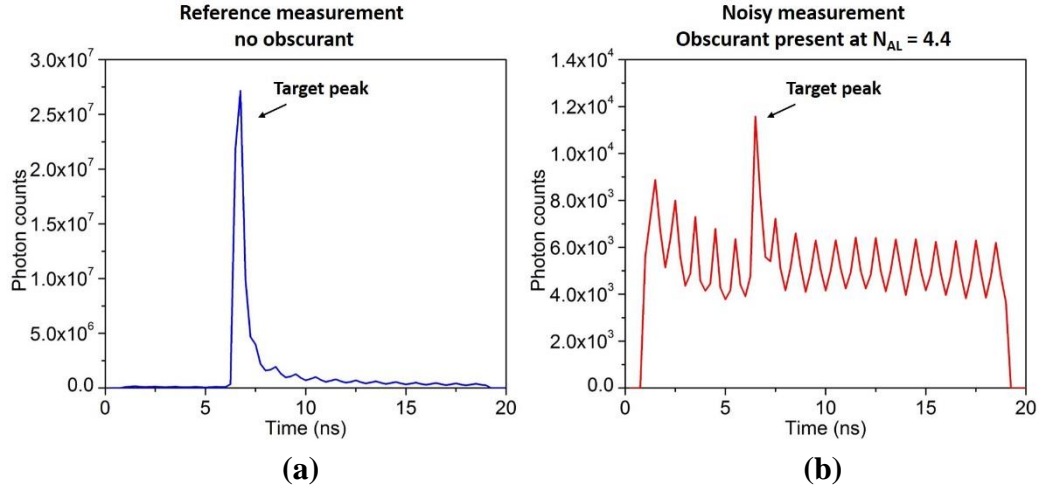
Figure 6.25: Examples of single-pixel timing histograms acquired for one second of single-photon data over a 50 metre stand-off distance using the 32 × 32 PLW SPAD array for (a) a reference measurement with no obscurant present and (b) a measurement taken when the number of attenuation lengths between the system and the target (one-way) was 4.4.

As shown in Figure 6.25, the *SNR* is significantly lower when an obscurant is present during measurements due particulate scattering resulting in a loss of light to and from the target. Thus, in order to obtain an accurate calculation of the number of attenuation lengths, a background subtraction was performed for each measurement. For the results presented in Chapter 5 of this Thesis, the background was estimated by calculating the average background per-pixel from a flat region of the timing histogram without a return peak. However, the normalised timing histogram shown in Figure 6.26 (taken from the background region in Figure 6.25 (b)) indicates that the detector exhibits a periodic pattern in the background level repeating in 4 timing bin intervals (i.e., every 1 ns) which creates 'false peaks'. This may be due to a known issue of the timing electronics in the SPAD array causing small variations in the timing bin size during operation. This periodic pattern makes it difficult to obtain a true background reading when the signal level is close to the background level. Moreover, if the return peak happens to be located in the same bin position as one of the 'false peaks', this may cause an attenuation length measurement to be inaccurate. Therefore, for the results presented in this Chapter, the background was estimated by summing the counts in ± 2 bins around the 'false peak' adjacent to the target peak and subtracting this from the same number of bins centred on the target return peak. Further characterisation of this effect would be required before future use of the system to improve the attenuation length measurements.

175
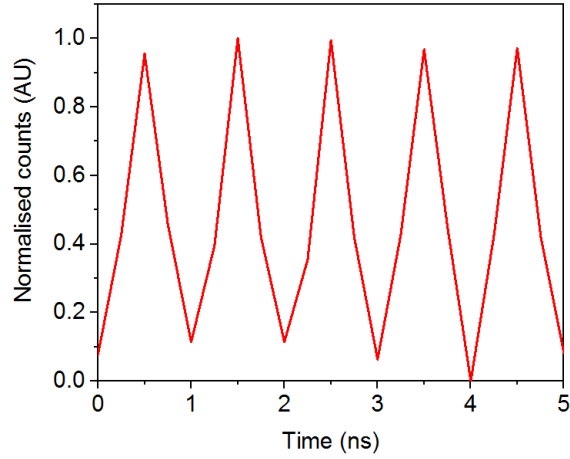
Figure 6.26: Example of a timing histogram with no target return peak demonstrating periodic 'false peaks' arising in the background of the measurement at 1 ns intervals.

6.5 Analysis and discussion of experimental results

This Section presents analysis and discussion of the experimental results for the 50 m, 150 m, and 1463 m ranges obtained in these field trials. All the results presented here were obtained using the pixel-wise cross-correlation algorithm described in Chapter 4 of this Thesis.

6.5.1 50 m indoor range

The first set of measurements were performed at a range of 50 metres (100 metres round-trip) inside the indoor gun shed at the BHL range. The depth imaging system and the Raptor Ninox SWIR passive imaging camera were housed at one end of this facility, while the target scene and marquee were set up at the far side as indicated in Figure 6.27.

(a)   **(b)**
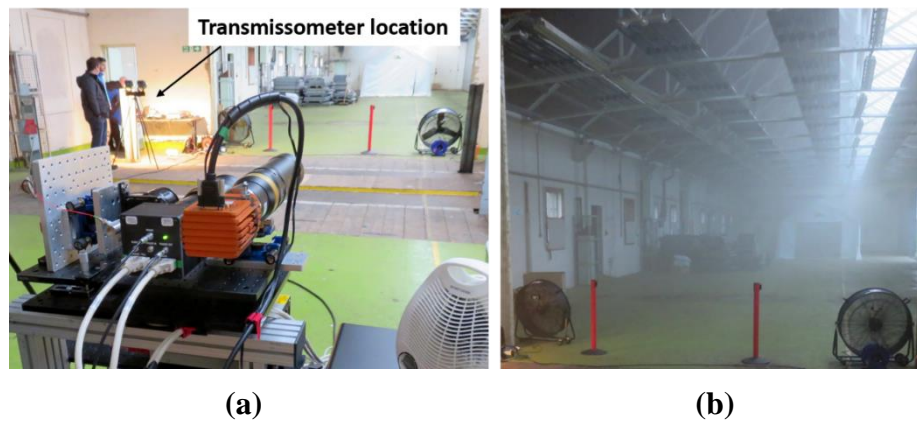
Figure 6.27: Photographs taken of the indoor range. Photograph (a) shows the λ = 1550 nm system located 50 m from the target position, and photograph (b) shows the 50 m range during a measurement with obscurant present.

A transmissometer operating at both visible (λ = 637 nm) and infrared (λ = 1550 nm) wavelengths was set up to the left of the sensor location approximately 10 m closer to the target to obtain a second measurement of the number of attenuation lengths between its position and the target. The transmissometer laser beam was directed through the marquee to a corner cube retro-reflector located behind the marquee and reflected back to a fibre-coupled InGaAs photodiode.

Firstly, a set of measurements were made on the 3D panel chart in order to evaluate the system performance. For these measurements, the 300 mm EFL lens was used as the receiver objective lens of the PLW 32 × 32 SPAD array. This resulted in a FoV of approximately 0.53 × 0.53 m at 50 m meaning that the central region of the 1 m × 1 m 3D panel target was imaged. A detector gate size of 20 ns (or 80 timing bins at 250 ps) was selected to encompass the entire target while reducing potential afterpulsing. The 3D panel chart was flood-illuminated with 220 mW optical power from the illumination source, which was subsequently aligned with the detector FoV using the Raptor Ninox camera. Attenuation results for this measurement obtained by the Dstl transmissometer (for both λ =1550 nm and λ = 637 nm) and the λ = 1550 nm depth imaging system are shown in Figure 6.28. The attenuation curves are shown from 200 seconds until the end of the measurement (590 seconds). This is due to the transmissometer being unable to obtain an accurate value prior to this point because of a high density of obscurant.
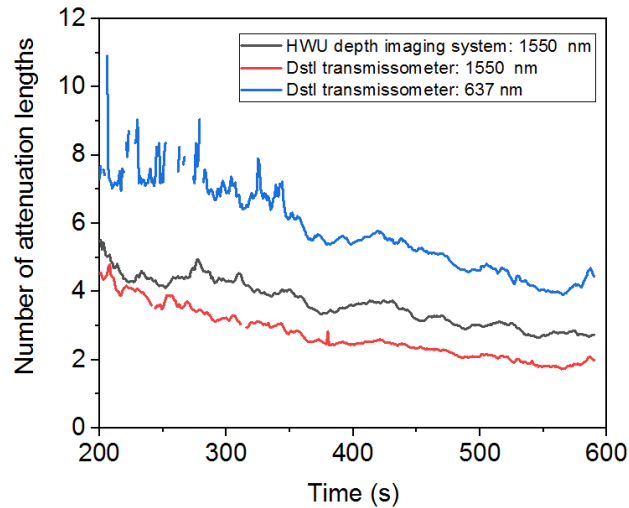
Figure 6.28: Plots of the number of attenuation lengths as a function of time for the PLW 32 × 32 SPAD detector array at λ = 1550 nm (black), the transmissometer at λ = 1550 nm (red) and λ = 637 nm (blue) obtained from the 3D panel chart at a stand-off distance of 50 metres using a 300 mm EFL objective lens and a detector gate size of 20 ns.

These results indicate that λ = 1550 nm light has lower attenuation than that at λ = 637 nm, likely due to the particle size distribution of the glycol vapour and the reduced solar background at SWIR wavelengths. These results further demonstrate the benefits of SWIR wavelengths over the visible band. A discrepancy of approximately one attenuation length was found between the λ = 1550 nm results for the Heriot-Watt imaging system and the Dstl transmissometer. However, it is important to note that the systems used for this calibration were different in some respects: (1) the stand-off distances were different, and several metres apart near the target in the region of most dense fog (the calibration target of the single-photon measurements was placed several metres further away than the retro-reflector used for the transmissometer); (2) the direction of the line of sight was significantly different; and (3) the height of transmission was different (the transmissometer optical path was slightly higher). Moreover, despite the use of large fans to enhance dispersion, the obscurant was not homogenous throughout the propagation region meaning there was potential for each system to see a different obscurant density at the same instance throughout the measurement time.

Figure 6.29 presents timing histograms acquired by the 32 × 32 InGaAs/InP SPAD array at λ = 1550 nm (summed from a 9 × 9 pixel neighbourhood). As the number of attenuation lengths between the target and the system increases the number of photons in the target return peak decreases until it is similar to the background level.
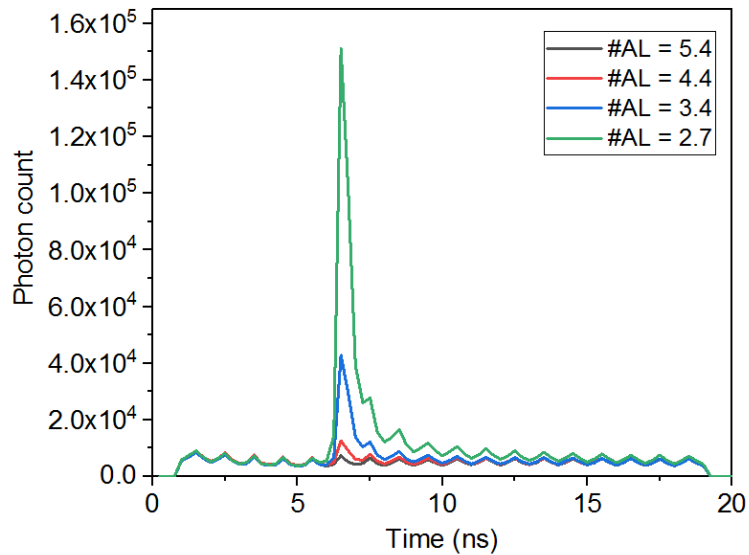
Figure 6.29: Timing histograms summed from a 9 × 9 pixel neighbourhood obtained as the obscurant dispersed during the measurement of the 3D panel chart at 50 m taken by the 32 × 32 InGaAs/InP SPAD array. The timing histograms for $N_{AL(λ = 1550 nm)}$ = 5.4, 4.4, 3.4, and 2.7 are shown as examples.

At high densities of obscurants where a return signal can be measured, the target peak can still be differentiated from the background. However, the presence of an obscurant prior to the target position can result in a peak at the start of the timing histogram that is larger than the target peak itself (as shown in Figure 6.30). This can result in issues when using the pixel-wise cross-correlation algorithm to reconstruct the target depth profile as this algorithm only operates on the largest peak in the histogram. This can result in incorrect depth estimates if the peak from the obscurant is higher than the signal return.
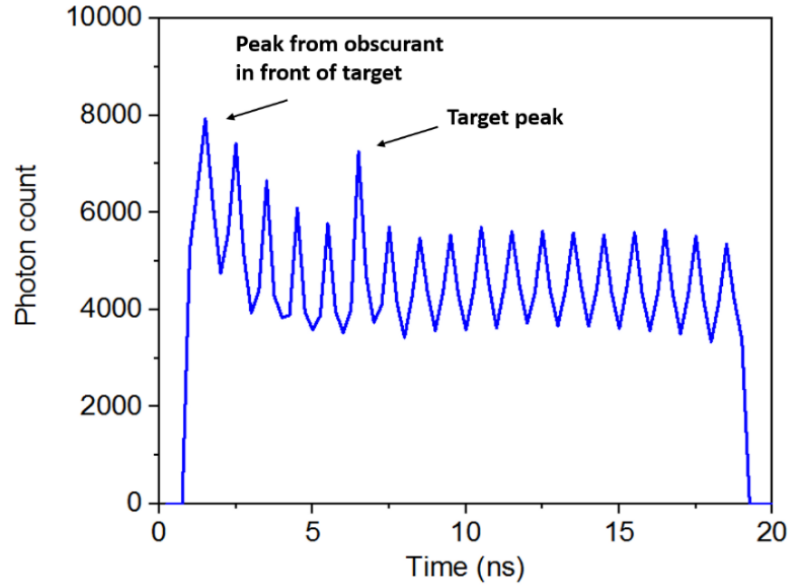
Figure 6.30: A timing histogram (aggregated for a 9 × 9 pixel neighbourhood) obtained from the 3D panel chart at a very high level of obscurant (i.e., $N_{AL(1550\,nm)} = 5$) using the 32 × 32 InGaAs/InP SPAD array at a range of 50 m. The presence of obscurant prior to the target results in a peak at the beginning of the histogram that is larger than the target peak.

For the measurements presented in this Chapter, this issue generally occurred when the number of attenuation lengths ($N_{AL(1550\,nm)}$) between the system and the target (one-way) is greater than 5. In order to investigate the consequence of this issue on image quality, the cross-correlation algorithm was used to reconstruct depth profiles using: the full detector gate width of 20 ns (80 timing bins in the histogram) and a detector gate width of 15 ns (60 timing bins in the histogram). This reduced gate removes the first twenty timing bins in the histogram, avoiding the large initial peak resulting from the obscurant. Figure 6.31 shows depth profiles of the target at the stand-off distance of 50 m obtained using an acquisition time of 1 second at an average optical power level of 220 mW for the full and reduced gate widths.
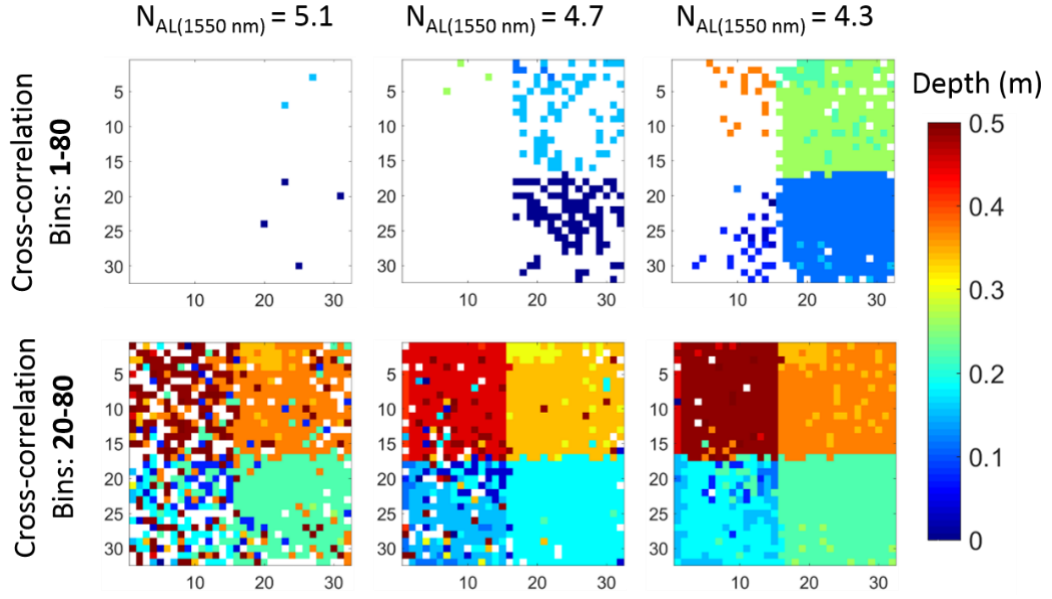
Figure 6.31: Depth profiles of the 3D panel chart at 50 metres (indoors) obtained with the PLW 32 × 32 InGaAs/InP SPAD array acquired with an acquisition time of 1 second per image at three different values of attenuation lengths. The target was reconstructed using pixel-wise cross-correlation for bin ranges of 1-80 (top row) and 20-80 (bottom row).

The results in Figure 6.31 show that a significant improvement to the reconstructed depth profiles was achieved by removing the first 20 timing bins in the histogram. In fact, it was not possible to reconstruct the depth profile using cross-correlation when all 80 bins of the timing histogram were considered for 5.1 attenuation lengths, whereas, it was possible to almost fully reconstruct the entire depth profile of the target by simply omitting the first 20 bins. Therefore, for all subsequent results presented in this Chapter, the timing bins prior to the target peak containing large peaks due to the presence of obscurant were omitted. Moreover, for all measurements, a depth threshold was set such that all depths outwith a pre-determined distance around the target were considered to be inaccurate estimates, disregarded, and presented in the depth profiles as empty pixels. Figure 6.32 shows the depth profiles of the 3D panel chart taken with the PLW 32 × 32 SPAD detector array, the corresponding RGB images taken in the visible (using a Nikon D750 camera), and SWIR images taken with the passive Raptor Ninox camera for $N_{AL(\lambda = 1550\ nm)}$ = 6.2, 5.2, 4.2, and 3.2. These depth profiles were recorded with an acquisition time of 1 second using an average optical power level of 220 mW. For the cross-correlation, a reduced number of bins (60 bins at 250 ps per bin) was considered and the number of photons in a range of 4 timing bins around the centroid location was summed to obtain an estimate of the intensity (or reflectivity) of the target.
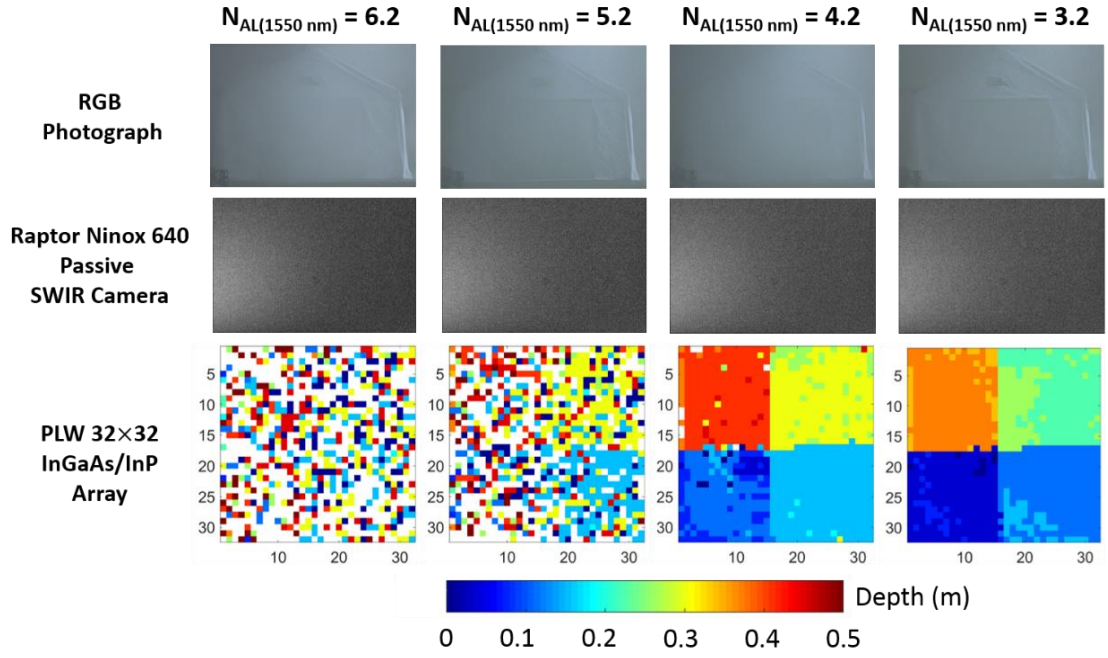
Figure 6.32: Images of the target scene at a stand-off distance of 50 metres indoors at several densities of the glycol vapour. (Top) RGB photographs for the visible region of the scene taken with a Nikon D750 camera. (Middle) Passive images of the scene obtained by the Raptor Ninox camera configured for operation in the SWIR region. (Bottom) Depth profiles of the target obtained with the PLW 32 × 32 InGaAs/InP SPAD array for a 1 second acquisition time. The target was reconstructed using pixel-wise cross-correlation.

Panels 2 and 3 of the 3D chart begin to become discernible at approximately 6.2 attenuation lengths (one-way) due to the higher sensitivity of the pixels on the right side of the array as previously discussed. The full depth chart becomes easily discernible at 4.2 attenuation lengths. The transmissometer measurements shown in Figure 6.28 estimate that the visible attenuation is approximately double the SWIR attenuation meaning that these images were acquired through approximately 12 and 8 attenuation lengths in the visible region, respectively. In both the visible RGB photographs and the passive SWIR images in Figure 6.32, the target scene was not imaged successfully even at $N_{AL(\lambda = 1550\,nm)} = 3.2$, demonstrating the potential of the PLW camera for imaging through obscurants at SWIR wavelengths. The acquisition time of one second used for cross-correlation was arbitrarily chosen to provide a good quality depth image. However, the average number of return photons from the target for a one second acquisition was far greater than required to make an accurate depth estimate. Therefore, the depth profiles were then processed using fewer frames (i.e., shorter acquisition times), which were

extracted at one second intervals of the acquired data. Figure 6.33 shows the resultant depth profiles of the 3D panel chart reconstructed via cross-correlation using 150,421 frames (1 second acquisition), 15,042 frames (0.1 second acquisition) and 1504 frames (0.01 second acquisition). A depth threshold of 0.7 metres was applied to the data.
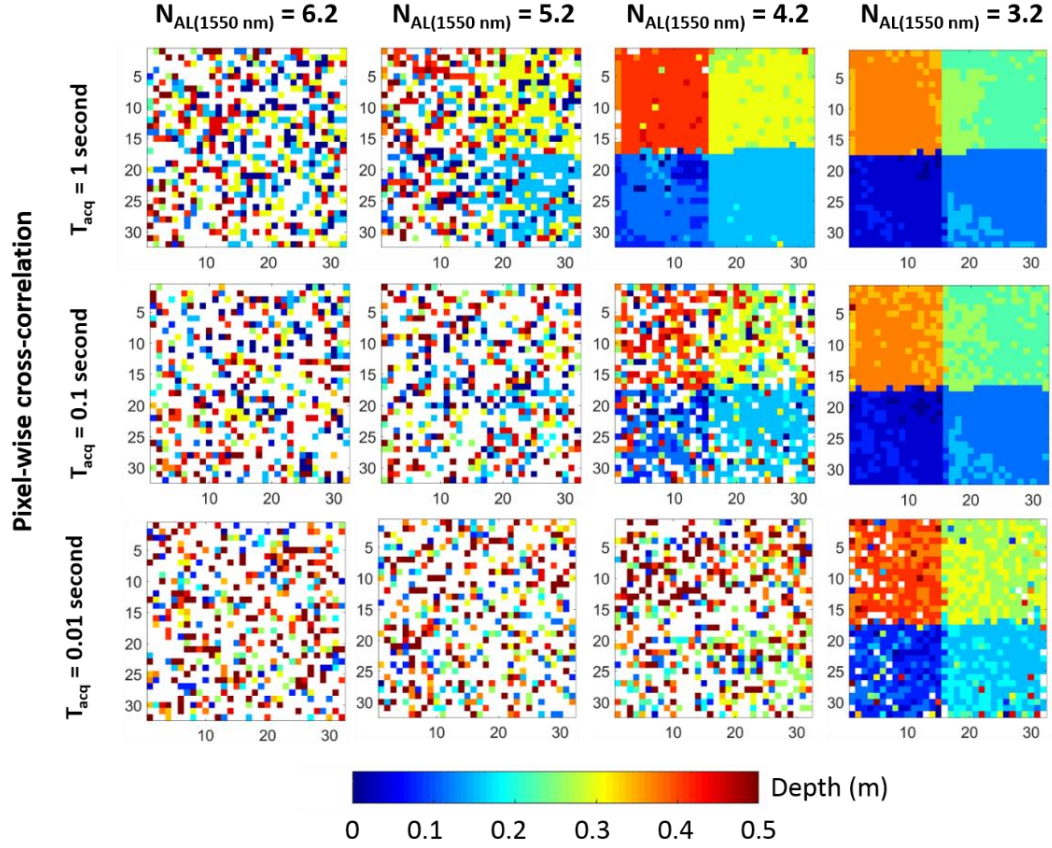
Figure 6.33: Depth profiles of the target at a stand-off distance of 50 metres indoors obtained by the PLW 32 × 32 InGaAs/InP SPAD array for various obscurant densities reconstructed using pixel-wise cross-correlation. The results for three different acquisition times of (top) 1 second, (middle) 0.1 seconds, and (bottom) 0.01 seconds are shown.

An analysis of these depth profiles indicating the average photons per pixel (PPP) (for pixels within the given threshold criteria only) and the signal-to-reconstruction error (SRE) was also calculated in order to provide a quantitative metric, as discussed in Chapter 5 of this Thesis. The results are presented in Table 6.5. This simple metric gives an indication of the reconstructed quality of an image taken in degraded conditions when compared to the reference image taken in clear conditions. The number of reconstructed pixels with relevant target data (denoted 'sampled pixels') for each image is also given.

Table 6.5: Average photons per pixel (PPP), number of sampled pixels, and signal-to-reconstruction error (SRE) values for $\tau_{acq} = 1$, 0.1, and 0.01 seconds for $N_{AL(\lambda = 1550 \, nm)} = 6.2$, 5.2, 4.2, and 3.2 obtained from measurements of the 3D panel chart at a stand-off distance of 50 m indoors. The average power level used for these measurements was 220 mW.

N_{AL} (1550 nm)	$\tau_{acq} = 1$ second			$\tau_{acq} = 0.1$ second			$\tau_{acq} = 0.01$ second		
	Avg. PPP	# of Sampled Pixels	SRE	Avg. PPP	# of Sampled Pixels	SRE	Avg. PPP	# of Sampled Pixels	SRE
3.2	1445	1024	17.6	142	1024	17.8	14	973	4.2
4.2	517	1016	15.4	43	873	0.6	4	513	-5.8
5.2	287	636	-0.1	21	444	-5.0	3	361	-7.0
6.2	184	517	-2.9	18	416	-5.7	2	343	-7.3

The results in Table 6.5 show a decreasing number of average photons per pixel, number of pixels reconstructed ('sampled pixels'), and SRE at increasing numbers of attenuation lengths, as expected due to higher levels of particulate scattering at higher numbers of attenuation resulting in lower signal. Figure 6.33 shows that panels of the 3D chart become discernible at > 4.2 attenuation lengths at $\lambda = 1550$ nm with an average photon return per-pixel of 43 and an SRE of 0.6 for an acquisition time of 0.1 seconds. At an acquisition time of 0.01 seconds, the panels are discernible at > 3.2 attenuation lengths at $\lambda = 1550$ nm with an average photon return of 14 photons per pixel and an SRE of 4.2. It is clear from these results that very rapid measurements of targets obscured by high densities of obscurants can be made using the PLW 32×32 SPAD detector array - even in the sparse photon regime.

In addition, the average depth of each panel of the 3D chart was also investigated for attenuation lengths of $N_{AL(\lambda = 1550 \, nm)} = 3.2$ and 4.2 at acquisition times of 1, 0.1, and 0.01 seconds. The panel closest to the system position (panel 4 in Figure 6.24) was used as the reference point (0 cm) and the average depth of panels 1-3 was calculated relative to this distance. Only depth estimates from pixels inside the set threshold were considered and the location of each panel was assumed to be unknown. The results are shown in Table 6.6.

Table 6.6: Average depth measurements for panels 1-4 of the 3D panel chart (10 cm depth increments between panels) obtained at τ_{acq} = 1, 0.1, and 0.01 seconds for $N_{AL(\lambda = 1550\,nm)}$ = 3.2. Panel 4 is used as a reference depth and thus is set to zero. The number of sampled pixels is also shown.

N_{AL} (1550 nm)	τ_{acq} = 1 second				τ_{acq} = 0.1 second				τ_{acq} = 0.01 second			
	Avg. panel depth (cm)				Avg. panel depth (cm)				Avg. panel depth (cm)			
	1	2	3	4 (Ref)	1	2	3	4 (Ref)	1	2	3	4 (Ref)
3.2	33 ± 1	20 ± 1	8 ± 1	0 ± 1	32 ± 2	20 ± 1	8 ± 1	0 ± 1	26 ± 6	20 ± 4	8 ± 4	0 ± 4
# of Sampled Pixels	255 (255)	272 (272)	240 (240)	225 (255)	255 (255)	272 (272)	240 (240)	225 (255)	233 (255)	266 (272)	233 (240)	213 (255)
4.2	28 ± 5	20 ± 2	6 ± 1	0 ± 1	10 ± 2	11 ± 3	6 ± 4	0 ± 4	16 ± 3	5 ± 3	0 ± 3	0 ± 4
# of Sampled Pixels	247 (255)	272 (272)	240 (240)	225 (255)	190 (255)	242 (272)	223 (240)	194 (255)	119 (255)	130 (272)	126 (240)	122 (255)

For $N_{AL(\lambda = 1550\,nm)}$ = 3.2, all the panels gave accurate depth estimates for each of the acquisition times, even when the average number of photons per pixel was as low as 14 for τ_{acq} = 0.01 seconds. For $N_{AL(\lambda = 1550\,nm)}$ = 4.2 only estimates from the 1 second acquisition obtained accurate results. Figure 6.33 indicates that in the depth profile acquired for a 0.1 second acquisition time many pixels did, in fact, obtain an accurate depth estimate. However, many noisy pixels within the original 0.7 m threshold (but not related to the actual target depth) were also present. These noisy pixels are likely due to returns from scattering within the given depth threshold resulting in an apparent inaccurate depth estimate of the panels in this case. Thus, this result could be improved by performing further thresholding in the depth range chosen from prior knowledge of the actual panel spacing and positioning.

6.5.2 150 m outdoor range

The second set of measurements were performed outdoors in daylight conditions at a range of 150 metres (300 metres round-trip). The systems were housed in the southwest facing room of the BHL. The target scene, with the 3D panel chart target, was set up approximately 10 metres behind the marquee at the far side of the target. The target was housed within an intermodal container to help shield it from adverse weather conditions.

All measurements at this range were performed with an average optical power of approximately 220 mW and a repetition rate of 150,421 Hz. The receiver objective lens (OBJ2 in Figure 6.14) selected for this range was the 300 mm EFL SWIR lens, resulting in a FoV of 1.6 × 1.6 metres at the target range of 150 m. Since the FoV was considerably larger at 150 m than at 50 m, the resultant data contained information from the entire 3D panel chart as well as superfluous information from the back wall of the intermodal container. However, this lens was chosen over the 500 mm EFL (which would give a smaller FoV) due to a larger aperture diameter. At longer distances, a larger aperture size is advantageous to collect as many return photons as possible. Thus, for all depth profiles presented in this Section, a subsampled image only containing the 3D panel chart is presented for clarity. The attenuation results for measurements performed at the 150 m range for λ =1550 nm are shown in Figure 6.34. For this measurement data, no transmissometer attenuation measurements were available for comparison.
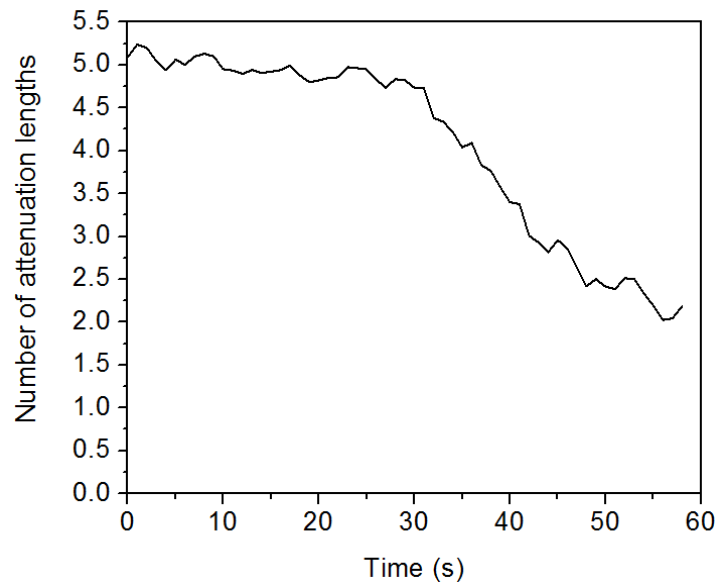
Figure 6.34: Plot of the number of attenuation lengths as a function of measurement time for λ = 1550 nm obtained by the PLW camera at a stand-off distance of 150 metres from the system position using a 300 mm EFL objective lens and a detector gate size of 20 ns.

The results indicate that the obscurant was very dense (> 5 attenuation lengths at λ =1550 nm) until approximately 30 seconds into the measurement set where it began to disperse rapidly due to windy conditions over the subsequent 30 seconds. This meant that the measurement duration was limited to approximately 60 seconds to avoid saturating the detector when the density of obscurant was very low. The reconstructed depth profiles, from 31 seconds onwards, for 1 second of data acquisition are shown in

Figure 6.35. A reference measurement of the target obtained in clear conditions is also shown, as well as the SRE and average PPP values.

Figure 6.35: Depth profiles of the 3D depth chart at 150 metres (outdoors) taken with the 32 × 32 PLW SPAD array acquired with an acquisition time of 1 second per image at different values of attenuation lengths. Also shown is the SRE for each reconstruction and the number of average photon returns per-pixel.

These results show that, despite the longer range and higher ambient background compared to the indoor 50 m measurements, it was still possible to partially reconstruct the 3D depth chart at up to approximately 4.7 attenuation lengths with an average photons per pixel of 84. In addition, it was possible to fully reconstruct the profile at approximately 3.8 attenuation lengths with an average photons per pixel of 642 using cross-correlation. These results are consistent with the results from the 50 m range in terms of image reconstruction quality as a function of the magnitude of return photons received by the system with only slight degradation in the SRE being observed. Moreover, as expected, an overall lower number of attenuation lengths were achieved by the system for the 150 m range. This is most likely due to the increased background illumination from solar background in the outdoor range and less photons returning from the target over the

longer distance. These results are slightly lower than the predictions obtained from the adapted LiDAR model. This could be attributed to the adverse weather conditions, such as rain, experienced during measurements, which will have affected the number of photons collected by the system due to particulate scattering, absorption effects, and a change in target reflectivity due to the presence of water on the panels.

For completion, the same analysis as for the 50 m range was repeated for this measurement data, and the results for 0.1 seconds and 0.01 seconds are shown in Figure 6.36 and Figure 6.37, respectively, alongside the corresponding SRE and average photon per pixel values.
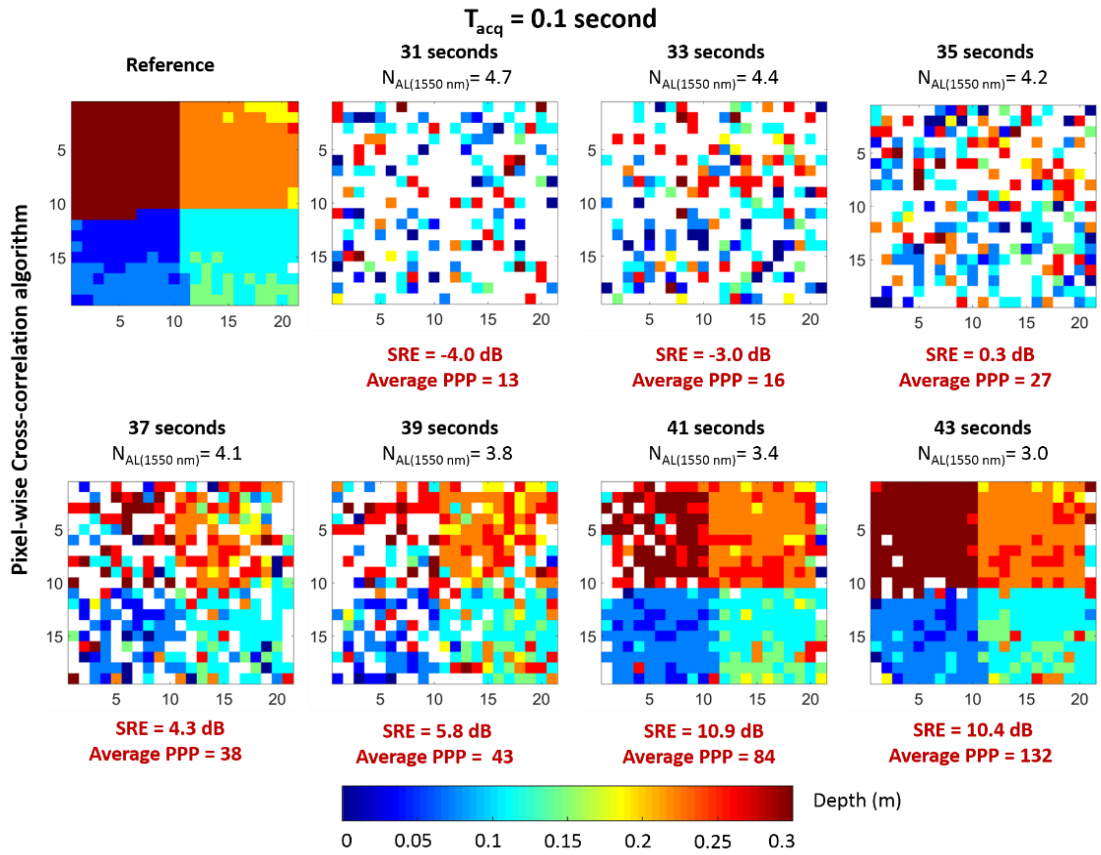
Figure 6.36: Depth profiles of the 3D depth chart at 150 metres (outdoors) taken with the 32 × 32 PLW SPAD array acquired with an acquisition time of 0.1 second per image at different numbers of attenuation lengths. Also shown is the SRE for each reconstruction and the number of average photon returns per-pixel.
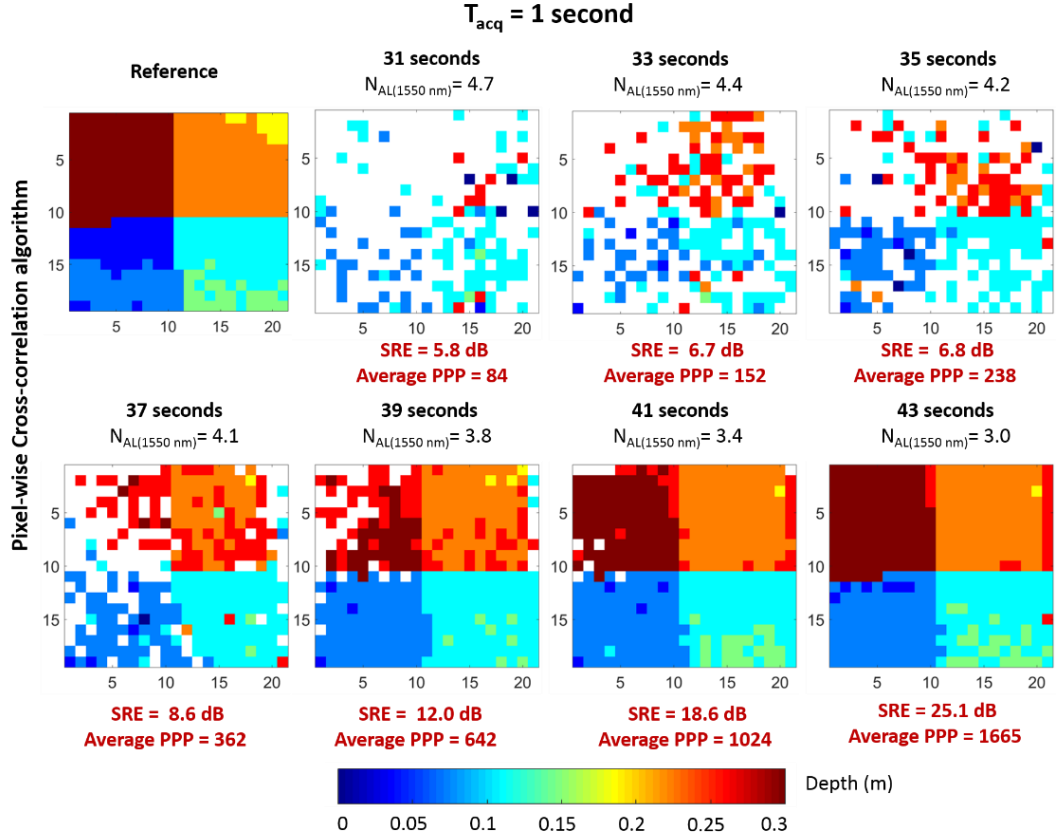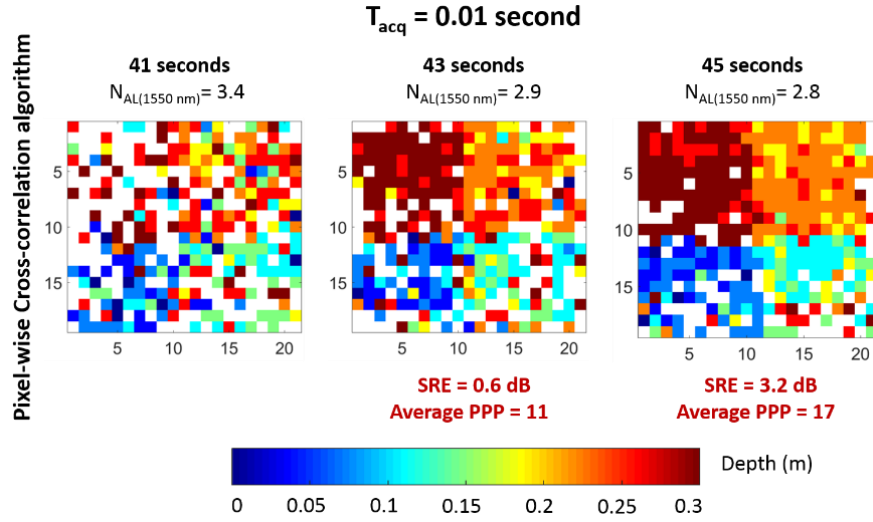
Figure 6.37: Depth profiles of the 3D depth chart at 150 metres (outdoors) taken with the 32 × 32 PLW SPAD array acquired with an acquisition time of 0.01 second per image at different values of attenuation lengths between transceiver and target. Also shown is the SRE for each reconstruction and the number of average photon returns per-pixel.

The results shown in Figure 6.36 show that the 3D panel chart is successfully reconstructed with cross-correlation using a 0.1 second acquisition time at approximately 3.4 attenuation lengths with an average photons per pixel of 84 and an SRE of 10.9. For an acquisition time of 0.01 seconds, the target does not become discernible until approximately 2.8 attenuation lengths (17 photons per pixel on average and an SRE of 3.2) while - in the case of the 50 m range - the system could achieve successful depth estimates at > 3.2 attenuation lengths. This is once again most likely due to the more challenging scenario (long-range and outdoor conditions). These results demonstrate that the system is capable of rapid three-dimensional imaging outdoors in high levels of solar background and adverse weather conditions.

6.5.3 1463 m outdoor range

The final set of measurements were performed at a range of 1463 metres (2926 metres round-trip) with no obscurant present at the target scene to better understand the sensor performance at more challenging distances. The system was housed indoors in the BHL facility as shown in Figure 6.38 (a). The target scene consisted of a stationary vehicle, a tree, and a wooden building positioned at unknown distances relative to one another as shown in Figure 6.38 (b).

(a)   (b)
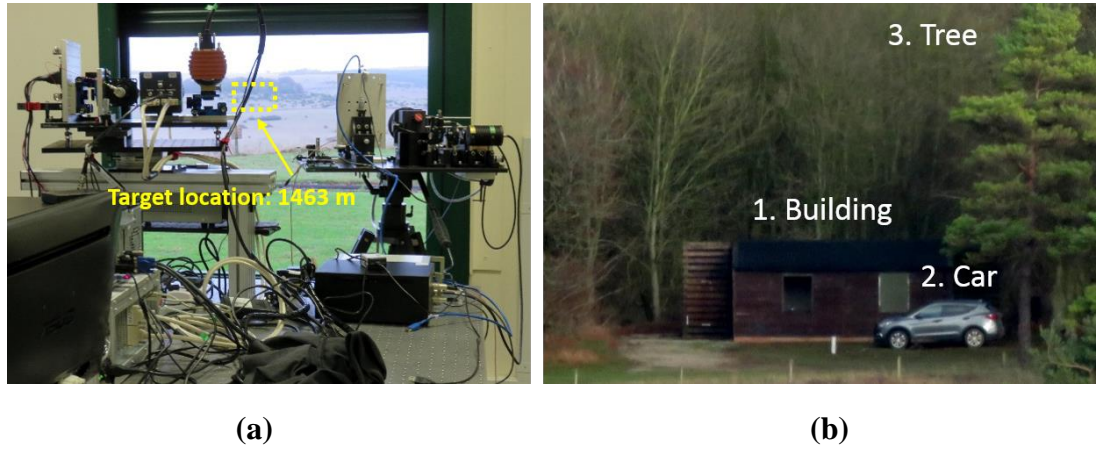
Figure 6.38: (a) A photograph of the target scene location at 1.463 km taken from the viewpoint of the imaging systems housed in the Battery Hill Laboratory. (b) A close-up photograph of the target scene comprising a stationary vehicle, a tree, and a wooden building.

For these measurements, the ambient background level varied greatly over the course of a single measurement - with conditions at the target scene ranging from very dull and overcast to direct sunshine. The conditions at the target scene was monitored by the Raptor Ninox 640 camera, and passive images showing the variation in the ambient background light experienced over the course of one measurement set is shown in Figure 6.39.

Figure 6.39: Passive SWIR images of the 1.463 km target scene taken by the Raptor Ninox 640 camera showing the large variation of the ambient background level over the course of a measurement.

The average number of background counts per pixel was investigated for data taken from the start of the measurement when conditions at the target were dull and then at the end when the ambient light levels was high. Figure 6.40 shows the passive SWIR image of the target scene at 1463 km acquired by the Raptor Ninox 640 camera, an intensity profile that shows the number of background counts collected in each pixel, and the average number of background counts per pixel.

189
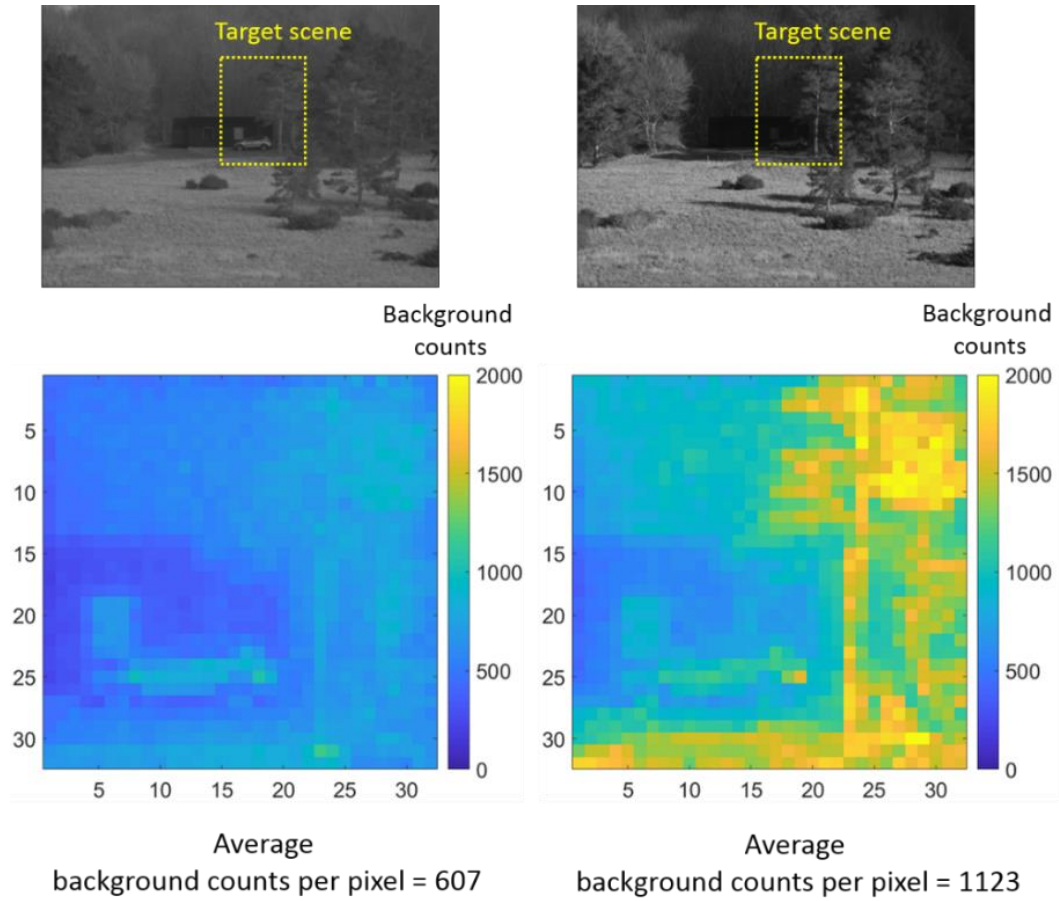
Figure 6.40: (Top) Passive SWIR images of the target scene acquired by the Raptor Ninox 640 camera demonstrating the changing ambient conditions during a measurement. (Bottom) Intensity profiles that show the background counts in each pixel along with the average background counts per pixel.

It was found that, depending on the conditions, the average background counts per pixel could be up to double (607 average background counts per pixel when dull and 1123 in direct sunlight) when the ambient light level is high, reiterating the importance of background subtraction and mitigation in single-photon measurements.

A stationary scene was used to assess the depth imaging system's long-range capabilities - with different levels of ND used in the transmission channel to simulate the presence of an obscuring media. The maximum available average optical power level of 220 mW and a repetition rate of 150,421 Hz was used for all measurements performed at the 1463 km range. The 500 mm EFL Optec SWIR lens (maximum aperture diameter of 85 mm) was used to collect the return photons, resulting in a FoV of approximately 9.4 × 9.4 m at the target. A detector gate of 200 ns, equivalent to a range of 30 metres around the target, was selected.

Figure 6.41 shows a point cloud representation of the depth profile acquired of the target scene with a one second data acquisition time and no ND filter present in the transmission channel. A depth threshold of 30 metres was applied to the depth profile. The result indicates a distance of approximately 14.5 metres between the car and the tree, and approximately 5.2 metres between the car and the building. The shadow of the car can be observed on the wall of the building by way of missing data points and individual branches on the tree are discernible at this distance.
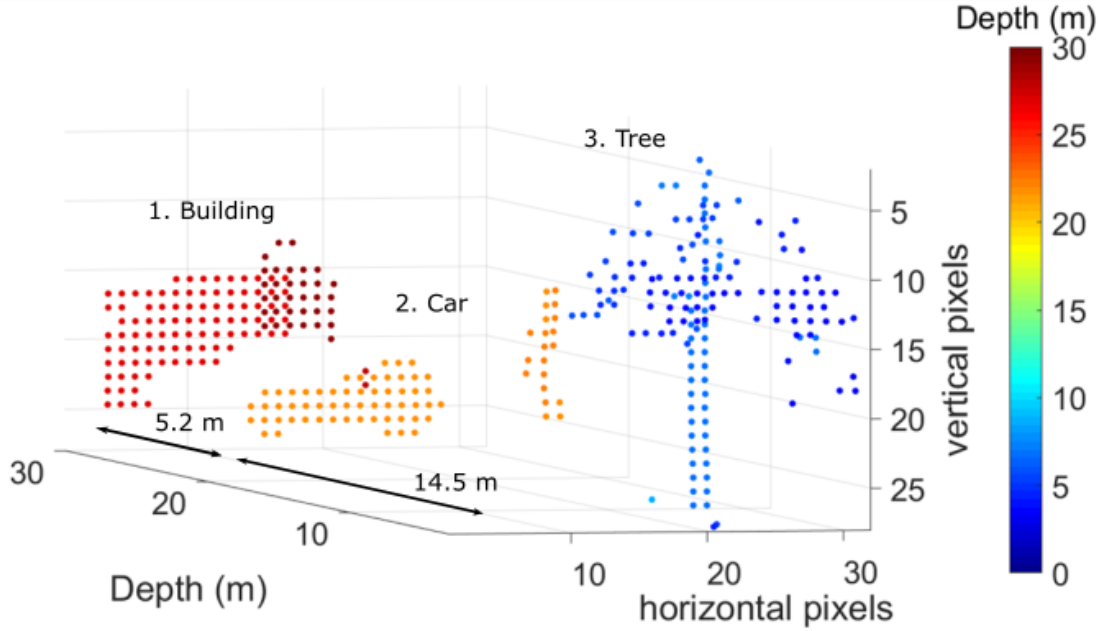
Figure 6.41: Point cloud illustrating the depth profiles of the three targets, a building, a car, and a tree, at the 1463 km scene.

Figure 6.42 shows the resultant depth profiles taken at acquisition times of τ_{acq} = 1, 0.1, and 0.01 seconds for no ND filter, ND1 (10% of the original light transmitted), and ND2 (1% of the original light transmitted) in the transmission channel, respectively. This is the equivalent to 1.2 attenuations lengths between the system and the target location (2.4 round-trip) at λ =1550 nm for the ND1 filter and 2.3 (4.6 round-trip) attenuation lengths for the ND2 filter.
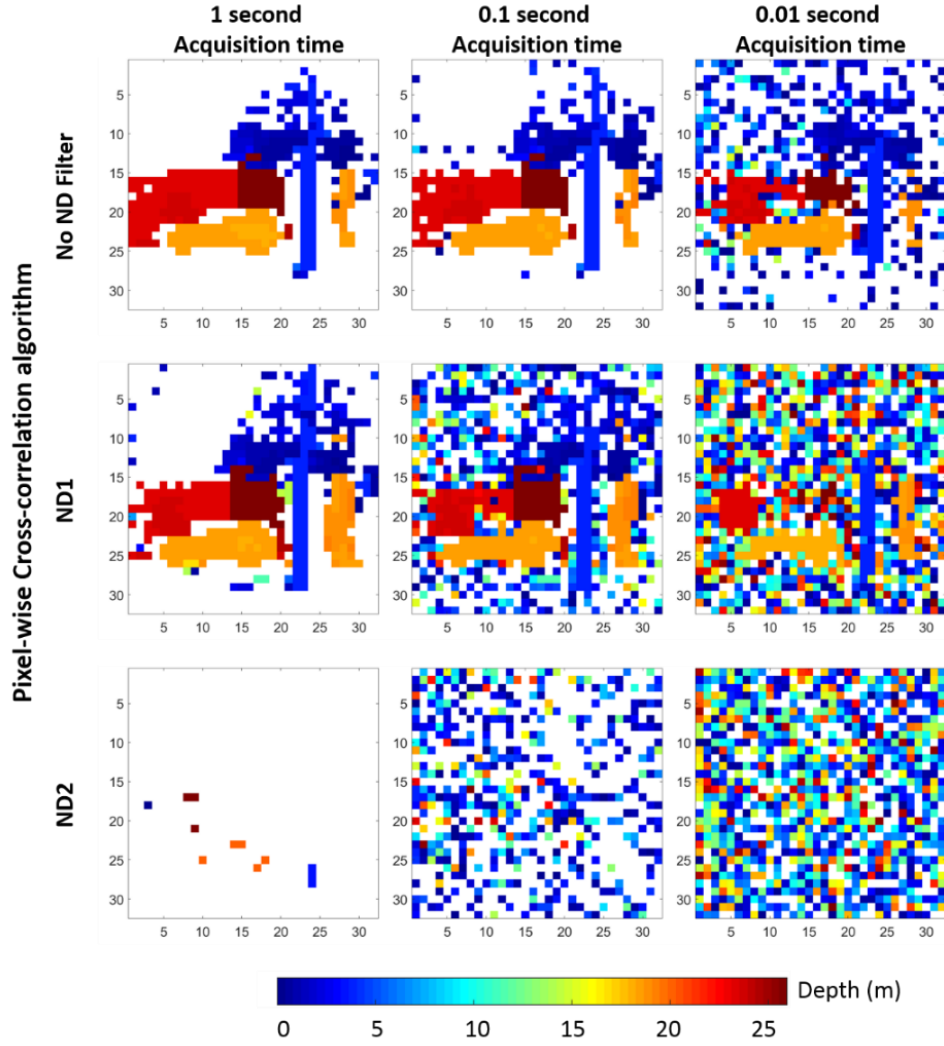
Figure 6.42: Depth profiles obtained using pixel-wise cross-correlation of the target scene comprising a stationary vehicle, a tree, and a building at 1463 metres taken with the PLW 32 × 32 SPAD array acquired with acquisition times of 1, 0.1, and 0.01 seconds per image at different levels of ND filters in the transmission channel to simulate the presence of obscurants.

The results show that depth estimates of all three target objects can be made even at an acquisition time of 0.01 seconds using an ND1 filter in the transmission channel (equivalent to 20 mW average optical power). For the ND2 filter (equivalent to 2 mW average optical power), only a few pixels from each target gave accurate depth estimates when using pixel-wise cross-correlation – even for a 1 second data acquisition. However, these results show the potential for the use of the system for kilometre range depth imaging in the sparse photon regime both with and without the presence of obscurants.

6.6 Conclusions and future work

A bistatic depth imaging system based on the single-photon ToF approach was used to obtain three-dimensional depth profiles of targets through varying densities of glycol-based vapour composed of particle radii in the range of $1 - 2$ µm. The system was based on a Princeton Lightwave Kestrel 32×32 SPAD detector array with a wavelength range of $1400 - 1600$ nm, a temporal resolution of 250 ps, and an SPDE of approximately 25% at the operating wavelength of $\lambda = 1550$ nm. The DCR of the SPAD detector array was characterised for several gate widths at a repetition rate of 150,421 Hz. The DCR was found to be approximately 318 kcps at a gate width of 20 ns and 5370 kcps at a gate width of 200 ns. A pulsed fibre laser was used to provide an illumination wavelength of $\lambda = 1550$ nm with an average optical output power of approximately 220 mW at a repetition rate of 150,421 Hz.

In addition, a LiDAR model was presented to evaluate the potential ranging performance of the system. This model was based on the photon-counting LiDAR equation and adapted for this specific system configuration. Several parameters, both intrinsic and extrinsic, were used to evaluate the system performance in a range of conditions including different target ranges and different levels of obscuring media. The results suggested that successful depth imaging should be achievable in highly scattering environments at up to 6 attenuation lengths in the SWIR region at target distances up to 150 metres. However, this estimation is highly dependent on the level of background due to ambient illumination during measurements, the optical components used, and the target reflectivity and geometry. Further improvements could be made with larger aperture lenses and improved control of the background level.

Depth profiles of targets were successfully acquired at stand-off distances of 50 and 150 metres (indoors and outdoors respectively) through 10 metres of obscurant contained within a marquee at field trials hosted at Porton Down Battery Hill Laboratory. At 50 metres, the system obtained images of the full target scene at approximately 5.0 attenuation lengths using pixel-wise cross-correlation and partial reconstructions at up to 6.0 attenuation lengths for a one second data acquisition. At acquisition times of 0.1 and 0.01 seconds, successful depth reconstruction was achieved at approximately 4.0 and 3.0 attenuation lengths, respectively. At 150 m, partial target reconstruction was achieved at 4.7 attenuation lengths and full reconstruction at 3.4 attenuation lengths for a one second data acquisition. Successful reconstructions were achieved at 3.2 and 2.8 attenuation lengths for acquisition times of 0.1 and 0.01 seconds, respectively. The benefits of SWIR

wavelengths over the visible region for imaging through obscurants were demonstrated with λ = 1550 nm being almost twice as penetrative as λ = 637 nm. These results are mostly consistent with the simulations performed with the adapted LiDAR equation, albeit slightly lower than predicted. This is most likely due to a lower target reflectivity than expected, adverse weather conditions such as precipitation, and a higher background level during actual measurements than the parameters used in the model prior to the field trials.

Depth estimates were also obtained at a range of 1463 metres to better understand the sensor performance at more challenging distances using various levels of neutral density filters to simulate high levels of obscurants. Target depth estimates were successfully made at 0.01 seconds acquisition time using an ND1 filter in the transmission channel to simulate imaging at kilometre range in obscurants, and to explore the possibilities of examining identifying and tracking moving targets.

A simple pixel-wise cross-correlation algorithm performed all processing of the results presented in this Chapter. While this algorithm is simple and computationally inexpensive, more advanced image processing algorithms, which exploit spatial correlations in sparse single-photon data [6.29,6.30], could be used to improve upon the results presented here. Moreover, the use of the bistatic depth imaging system for successful video imaging and target identification in highly scattering media was investigated during these field trials to demonstrate the use of the system for rapid acquisition of dynamic scenes. Thus future work will focus on the development of more advanced image processing algorithms to process single-photon data at real-time frame rates. This will be discussed in further detail in the next Chapter of this Thesis.

In conclusion, the λ = 1550 nm arrayed single-photon detector system exhibited highly effective depth imaging at up to 6.2 attenuation lengths between transceiver and target in daylight conditions with a low power, eye-safe (220 mW average) source, at much shorter acquisition times than the single-pixel imaging system presented in Chapters 4 and 5. Future experiments will utilise this system to achieve successful real time depth imaging and target identification at kilometre ranges.

6.7 Acknowledgements

transmissometer measurements. Thanks go to the team at Dstl at the Porton Down field trials for their help for set up and organisation.

6.8 References

6.1. R. Tobin, A. Halimi, A. McCarthy, X. Ren, K. J. McEwan, S. McLaughlin, and G. S. Buller, "Long-range depth profiling of camouflaged targets using single-photon detection," Opt. Eng. 57(3), 031303 (2017).

6.2. A. Maccarone, A. McCarthy, X. Ren, R. E. Warburton, A. M. Wallace, J. Moffat, Y. Petillot, and G. S. Buller, "Underwater depth imaging using time-correlated single-photon counting," Opt. Express 23(26), 33911–33926 (2015).

6.3. R. Tobin, A. Halimi, A. McCarthy, M. Laurenzis, F. Christnacher, and G. S. Buller, "Three-dimensional single-photon imaging through obscurants," Opt. Express 27(4), 4590 (2019).

6.4. M. Henriksson and P. Jonsson, "Photon-counting panoramic three-dimensional imaging using a Geiger-mode avalanche photodiode array," Opt. Eng. 57(9), 093104 (2018).

6.5. M. Henriksson, L. Allard, and P. Jonsson, "Photon Counting Panoramic 3D imaging," Imaging and Applied Optics, SM3H.4 (2018).

6.6. M. Entwistle, M.A. Itzler, J. Chen, M. Owens, K. Patel, X. Jiang, K. Slomkowski, and S. Rangwala, "Geiger-mode APD camera system for single-photon 3D LADAR imaging," Proc. SPIE 8375, Advanced Photon Counting Techniques VI, 83750D (2012).

6.7. M.A. Itzler, M. Entwistle, M. Owens, K. Patel, X. Jiang, K. Slomkowski, S. Rangwala, P.F. Zalud, T. Senko, J. Tower, and J. Ferraro, "Comparison of 32 x 128 and 32 x 32 Geiger-mode APD FPAs for single photon 3D LADAR imaging," Proc. SPIE 8033, Advanced Photon Counting Techniques V, 80330G (2011).

6.8. "Kestrel 32 x 32 Geiger-Mode Flash 3-D LiDAR Camera data sheet," (Princeton Lightwave, accessed 2019).

6.9. D. Bronzi, F. Villa, S. Tisa, A. Tosi, and F. Zappa, "SPAD Figures of Merit for Photon-Counting, Photon-Timing, and Imaging Applications: A Review," IEEE Sens. J. 16(1), 3–12 (2016).

6.10. M. Hofbauer, B. Steindl, and H. Zimmermann, "Temperature dependence of dark count rate and after pulsing of a single-photon avalanche diode with an integrated active quenching circuit in 0.35 μm CMOS," J. Sens., 9585931 (2018).

6.11. C. Niclass, M. Gersbach, R. Henderson, L. Grant, and E. Charbon, "A single photon avalanche diode implemented in 130-nm CMOS technology," IEEE J. Sel. Top. Quantum Electron. 13(4), 863-869 (2007).

6.12. E. A. G. Webster, and R. K. Henderson, "A TCAD and Spectroscopy Study of Dark Count Mechanisms in Single-Photon Avalanche Diodes," in IEEE Trans. Electron Devices 60(12), 4014-4019 (2013).

6.13. D. P. Palubiak and M. J. Deen, "CMOS SPADs: Design Issues and Research Challenges for Detectors, Circuits, and Arrays," IEEE J. Sel. Top. Quantum Electron. 20(6), 409–426 (2014).

6.14. P. A. Hiskett, G. S. Buller, A. Y. Loudon, J. M. Smith, I. Gontijo, A. C. Walker, P. D. Townsend, and M. J. Robertson, "Performance and design of InGaAs/InP photodiodes for single-photon counting at 1.55 µm," Appl. Opt. 39(36), 6818–6829 (2000).

6.15. A. Lacaita, F. Zappa, S. Cova, and P. Lovati, "Single-photon detection beyond 1 µm: performance of commercially available InGaAs/InP detectors," Appl. Opt. 35(16), 2986–2996 (1996).

6.16. G. Ribordy, J.-D. Gautier, H. Zbinden, and N. Gisin, "Performance of InGaAs/InP avalanche photodiodes as gated-mode photon counters," Appl. Opt. 37(12), 2272–2277 (1998).

6.17. R. Lussana, F. Villa, A. Dalla Mora, D. Contini, A. Tosi, and F. Zappa, "Enhanced single-photon time-of-flight 3D ranging," Opt. Express 23, 24962-24973 (2015).

6.18. F. Villa, D. Bronzi, Y. Zou, C. Scarcella, G. Boso, S. Tisa, A. Tosi, F. Zappa, D. Durini, S. Weyers, U. Paschen, and W. Brockherde, "CMOS SPADs with up to 500 µm diameter and 55% detection efficiency at 420 nm," J. Mod. Opt. 61(2), 102-115 (2014).

6.19. Y. Maruyama, J. Blacksberg, and E. Charbon. "A 1024x8, 700-ps time-gated SPAD line sensor for planetary surface exploration with laser Raman spectroscopy and LIBS", IEEE J. Solid-State Circuits 49(1), 179-189 (2014).

6.20. S. Pellegrini, G. S. Buller, J. M. Smith, A. M. Wallace, and S. Cova, "Laser-based distance measurements using picosecond resolution time-correlated single-photon counting," Meas. Sci. Technol. 11, 712-716 (2000).

6.21. "GFL and HFL series user's manual," (Laser 2000, accessed 2019).

6.22. K. Barat, "Laser Safety: Tools and Training," (CRC Press, 2008).

6.23. "MPD - InGaAs SPAD - gated datasheet," (Micro Photon Devices, accessed 2019).

6.24. "Raptor Ninox 640 VIS-SWIR datasheet," (Raptor Photonics, accessed 2019).

6.25. C. C. Cooksey, B. K. Tsai, and D. W. Allen, "A collection and statistical analysis of skin reflectance signatures for inherent variability over the 250 nm to 2500 nm spectral range," Proc. SPIE 9082, 908206–11 (2014).

6.26. R. D. Richmond and S. C. Cain, *Direct-Detection LADAR Systems,* (SPIE, 2010).

6.27. A. Maccarone, A. McCarthy, X. Ren, R. E. Warburton, A. M. Wallace, J. Moffat, Y. Petillot, and G. S. Buller, "Underwater depth imaging using time-correlated single-photon counting," Opt. Express 23, 33911 (2015).

6.28. D. F. Swinehart, "The Beer-Lambert Law," J. Chem. Educ. 39(7), 333 (1962).

6.29. A. Halimi, R. Tobin, A. McCarthy, J. Bioucas-Dias, S. McLaughlin, and G. S. Buller, "Restoration of multidimensional sparse single-photon 3D-LiDAR images," IEEE, Trans. Comput. Imaging, accepted, (2018).

6.30. Y. Altmann, X. Ren, A. McCarthy, G. S. Buller, and S. McLaughlin, "Lidar Waveform-Based Analysis of Depth Images Constructed Using Sparse Single-Photon Data," IEEE Trans. Image Process. 25(5), 1935–1946 (2016).

Chapter 7: Imaging dynamic complex scenes using a 32 × 32 TCSPC SPAD array

7.1 Introduction

This Chapter will demonstrate the potential of the single-photon avalanche diode (SPAD) detector array system described in Chapter 6 of this Thesis for the acquisition of full-field, video-rate, three-dimensional (3D) data. This arrayed single-photon detector has been previously demonstrated to be successful for the rapid acquisition of single-photon data obtained in challenging environments, such as long-range aerial imaging [7.1], in outdoor scenes with high ambient background [7.2], or in high levels of atmospheric scattering [7.3] as shown in Chapter 6. The recent interest in the integration of the light detection and ranging (LiDAR) approach in advanced driver assistance systems (ADAS) and fully autonomous vehicles has highlighted the need for real-time depth profiling at distances up to hundreds of metres [7.1,7.4–7.8]. LiDAR systems incorporating the time-correlated single-photon counting (TCSPC) approach offer the high timing resolution required for object recognition at ranges relevant to vehicles travelling at high velocities (i.e., > 200 metres). The implementation of InGaAs/InP single-photon detectors in LiDAR systems allows for operation at short-wave infrared (SWIR) wavelengths. As discussed in Chapter 2 of this Thesis, the use of SWIR wavelengths in LiDAR systems has several advantages over visible band wavelengths, such as compatibility with the loss less telecommunications window, decreased solar background [7.9], and high atmospheric transmission [7.10,7.11]. In addition, the eye-safety threshold is increased by a factor of 20 or more compared to visible wavelengths, permitting the use of higher optical power levels. Thus, InGaAs/InP SPAD detectors with TCSPC capability [7.1,7.12] are a good candidate technology for integration in ADAS systems. However, a major bottleneck in the use of single-photon LiDAR systems is that current state-of-the-art algorithms designed to reconstruct depth profiles using single-photon data suffer from long execution times (10s to 100s of seconds) [7.13–7.21], limiting their use in many applications which rely on near instantaneous target analysis.

This Chapter presents the results obtained using a state-of-the-art algorithm designed for the 'real-time' image reconstruction of complex scenes at 320 metres [7.22]. A brief overview of the system and key parameters are provided in Section 7.2, and a description of the experimental layout is given in Section 7.3. The algorithm framework is described

in Section 7.4. Results obtained from a variety of scenes with increasing complexity are shown in Section 7.5. Finally, conclusions and future work are given in Section 7.6.

7.2 System configuration and key parameters

The system used for the measurements presented in this Chapter was based on the 32 × 32 single-photon array Kestrel camera manufactured by Princeton Lightwave (PLW) [7.23,7.24]. A full description of the system is given in Chapter 6 of this Thesis and a schematic is shown in Figure 7.1.
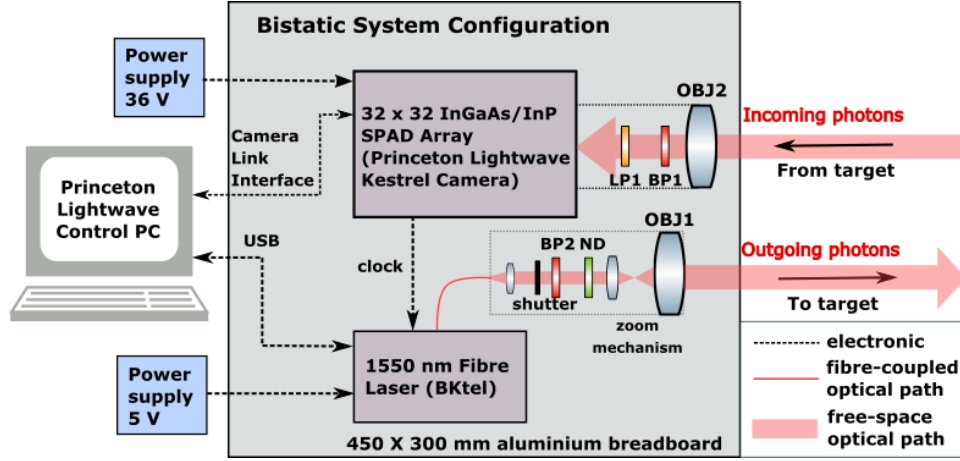
Figure 7.1: Schematic showing the key components and configuration of the bistatic imaging system comprising the Princeton Lightwave Kestrel 32 × 32 InGaAs/InP SPAD array and the λ = 1550 nm pulsed illumination source. Optical components include: objective lenses (OBJ1, OBJ2); a longpass filter (LP1); bandpass filters (BP1, BP2); and an ND filter (ND).

The InGaAs/InP SPAD detector array had a single-photon detection efficiency (SPDE) of approximately 25% (as stated by the manufacturer) and a measured average dark count rate of approximately 320 kcps at the operating wavelength of 1550 nm. The camera was operated with a timing bin resolution of 250 ps and a gate duration of 40 ns, corresponding to a measurement depth range of 6 metres. A fibre laser source (BKtel, France [7.25]) with an operating wavelength of 1550 nm and a pulse duration of approximately 400 ps was used to provide flood-illumination at the target scene. It was operated at a repetition rate of 150,421 Hz (clock signal provided by the PLW camera), and the resulting average optical power level was approximately 220 mW. The output fibre from the laser module was connected to a reflective collimation package and the exiting beam was then passed through a 12 nm full-width at half-maximum (FWHM) bandpass filter (BP2 in Figure 7.1). This filter was matched to the operating wavelength of the laser source in order to remove any amplified spontaneous emission (ASE) that

was present. A neutral density (ND) filter with an optical density of 0.5 and transmission of approximately 32% at $\lambda = 1550$ nm was used to reduce the average optical power level to approximately 70 mW to avoid saturating the sensitive detector. The zoom mechanism (described in Chapter 6) enabled the diameter of the illuminating beam at the scene of interest to be adjusted to match the field-of-view (FoV) of the camera. The Raptor Ninox 640 camera (Raptor Photonics, UK [7.26]) described in Chapter 6 was used to align the system to the target scene.

The system was implemented as a bistatic arrangement with the apertures of OBJ1 and OBJ2 separated by approximately 125 mm. This configuration was used to avoid potential issues with back-reflections from optical components. The detector objective lens (OBJ2 in Figure 7.1) was used to collect scattered photon returns from the target scene. The lens was designed for use in the wavelength range of $900 - 1700$ nm and had a 500 mm effective focal length (EFL) with a fixed f-number of f/7. This resulted in a FoV of approximately 2×2 metres at the target stand-off distance of 320 metres, i.e., each individual pixel covered an area of approximately 65×65 mm. The receive channel was spectrally filtered in order to reduce the detection of ambient illumination. A pair of high performance passive spectral filters (LP1 and BP1 in Figure 7.1) was mounted between the rear element of the lens and the sensor of the camera. The longpass (LP) filter had a cut-on wavelength of 1500 nm (LP1) and the BP filter (BP1) had a 9 nm FWHM with a central wavelength of 1550 nm. A summary of the key system parameters is given in Table 7.1.

Table 7.1: Summary of key system parameters

Parameter	Value/comment
Target stand-off distance	~320 m
Illumination source	1550 nm fibre laser
Average optical power level	70 mW
Laser and detector repetition rate	150,421 Hz
Time between binary frames	6.648 µs
Detector	32 × 32 InGaAs/InP SPAD array
Detector single-photon detection efficiency	25% at detector sensitivity setting of 100%
Detector gate width	40 ns
Histogram timing bin size	250 ps
System timing jitter	~ 485 ps
Objective lenses	Laser zoom mechanism (OBJ1) 9 mm +75 mm EFL lens, Detector (OBJ2): 500 mm EFL, 85 mm diameter aperture
Spectral filters in transmit channel	Bandpass (BP2): 1550 nm – 12 nm at FWHM Neutral density filter (ND): OD 0.5
Spectral filters in receive channel	Longpass (LP1): Cut on 1500 nm Bandpass (BP1): ~1550 nm – 9 nm FWHM

7.3 Experimental layout

The system was located in the rooftop laboratory of the David Brewster building at Heriot-Watt University to shield sensitive components from adverse weather – such as wind and rain. The target scene was erected at ground level at a stand-off distance of 320 metres from the system location. Three different target scenarios were used to evaluate both the imaging performance of the system in cluttered scenes and the real-time capabilities of the reconstruction algorithm. The first target scenario comprised of a single actor moving erratically, the second of two actors walking in parallel through the scene, and the third of the two actors walking in parallel but obscured by a layer of camouflage netting. The commercially available camouflage had dimensions of 3 × 2 metres and was positioned approximately 3 metres in front of a wooden backboard, perpendicular to the laser beam propagation.

A CCD camera was placed next to the target scene at ground level to provide an RGB reference video for each measurement. A diagram of the imaging set-up is shown in Figure 7.2.
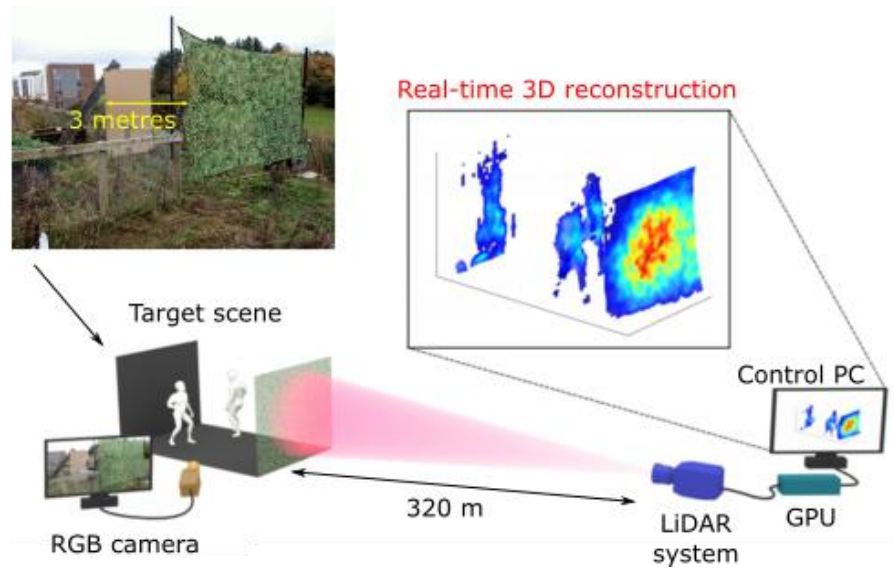

Figure 7.2: The LiDAR system was positioned on the rooftop laboratory at a stand-off distance of approximately 320 metres from the target scene. An RGB camera filmed during measurements to obtain reference videos. A graphics-processing unit (GPU) was used to obtain real-time 3D reconstructions of each scenario.

7.4 Computational methods

In recent years, the image processing community has proposed several algorithms designed to reconstruct images obtained in challenging environments, such as objects hidden in clutter or obscured by fog or smoke. These algorithms generally fall into two distinct categories. The first category contains algorithms that work on a single surface per pixel by using classical image processing tools to construct depth and intensity profiles [7.13–7.17]. The RDI-TV algorithm described in Chapters 4 and 5 of this Thesis belongs in this category. While these algorithms have proven to be successful in the reconstruction of single-photon data, they generally require a relatively high amount of supervised parameter tuning. In addition, the single-surface framework of these algorithms means that they are not robust to complex scenes with multiple depth surfaces, or scenes with regions that do not present any surface (target detection). The second category of algorithms improves upon this framework and the methods are much more robust to multi-surface scenes. These algorithms are primarily based on Bayesian models and Markov chain Monte Carlo (MCMC) methods and have demonstrated accurate image reconstruction of an arbitrary number of surfaces per pixel [7.20–7.21]. However, execution times remain prohibitively long for real-time processing of LiDAR data. Therefore, this Section describes a novel algorithm [7.22] designed to reconstruct 3D images of complex (multi-layered) scenes from LiDAR data at video framerates. This algorithm was designed by Julián Tachella and Dr Yoann Altman of Heriot-Watt University with input from myself based on LiDAR data obtained with the system described in Section 7.2 of this Chapter.

7.4.1 Real-time 3D reconstruction algorithm

While current state-of-the-art algorithms require processing times on the order of seconds or minutes, the real-time 3D reconstruction algorithm is capable of reconstructing 3D profiles of complex multi-surface scenes at video framerates (i.e., dozens of frames per second). A diagram of the algorithm framework is shown in Figure 7.3.
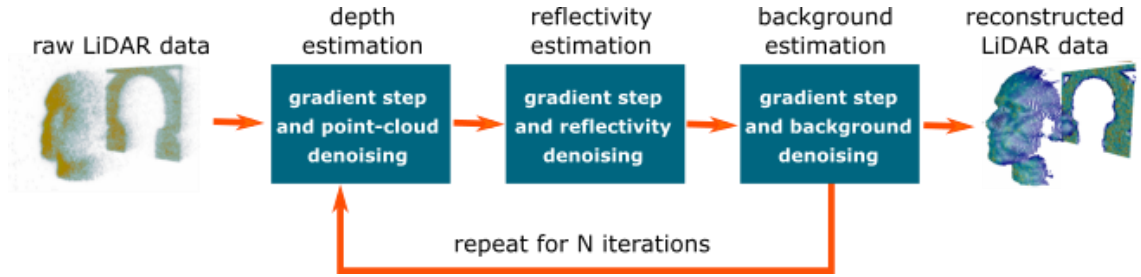
Figure 7.3: Diagram of the real-time algorithm framework. Depth, reflectivity, and background estimations are obtained from the raw LiDAR data by applying an iterative gradient step and point-cloud denoiser. These estimates are then used to reconstruct the 3D target profile.

The raw LiDAR data was processed using the algorithm, which was implemented on the graphics-processing unit (GPU) of the control computer. The algorithm obtains depth, intensity, and background estimates through optimisation of the initial LiDAR point cloud alternating between gradient steps and denoising steps [7.27]. Although this is performed over many iterations, both the gradient and denoising steps can process each pixel in parallel resulting in very low processing times. The algorithm applies a point cloud denoising method based on the algebraic point set surfaces (APSS) algorithm, which is an off-the-shelf computer graphics point cloud denoiser for distributed surfaces [7.28,7.29]. The APSS approach fits a smooth continuous surface to the depth points taken from the raw LiDAR data over many iterations to obtain an accurate 3D reconstruction. Unlike conventional (image) depth denoisers, the APSS approach can handle an arbitrary number of surfaces per pixel, making it ideal for the measurements presented in this Chapter. This approach is repeated for the reflectivity estimation step. In this case, the denoising step consists of low-pass filtering of the reflectivity points, only considering correlations between neighbouring pixels in the same surface. A minimum admissible reflectivity threshold was set so that any outliers were excluded from the final reconstruction. The level of background was estimated using the same approach, but no spatial correlations were considered, as the background in a bistatic system is not necessarily spatially correlated.

As discussed in Chapter 6, one of the limitations of the PLW SPAD array detector is that the 32 × 32 pixel format of the arrayed detector results in a relatively low image resolution. However, the real-time 3D reconstruction algorithm allows the use of a super-resolution scheme [7.30] where each coarse LiDAR pixel is divided into a 3 × 3 neighbourhood of finer pixels, as shown in Figure 7.4. This means that the point cloud

can be converted from a 32 × 32 pixel format to a 96 × 96 pixel format, significantly improving the potential image resolution of the PLW array camera.
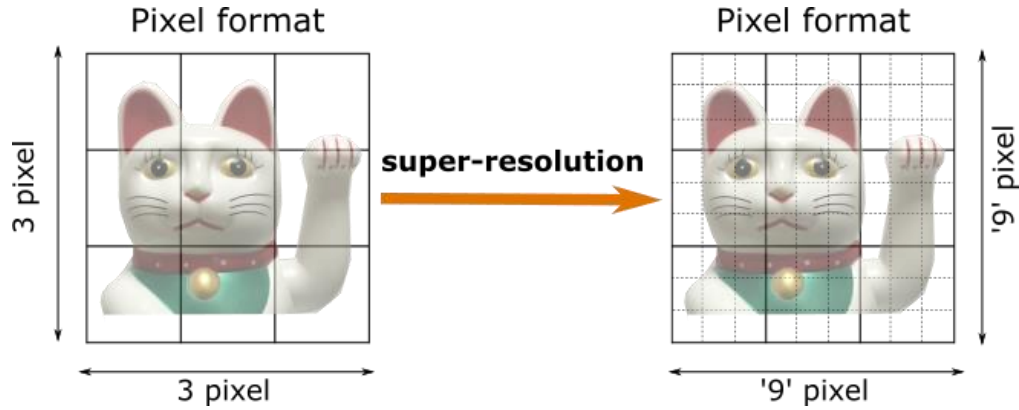
Figure 7.4: An example of a super-resolution scheme, which divides one coarse LiDAR pixel into a neighbourhood of 3 × 3 smaller pixels. This creates a large pixel format image and improves the resolution of the imaging system.

7.5 Experimental results and discussion

This Section presents results from preliminary tests obtained outdoors at a stand-off distance of 320 metres using the real-time reconstruction algorithm. An average optical power level of approximately 70 mW was used and data were acquired for approximately 6 seconds for all measurements. The ambient conditions were overcast but with relatively high ambient background levels.

The first scenario was comprised of an actor moving quickly and erratically through a distance of approximately 3 metres. This scene contained a single depth-surface per pixel. For each measurement, the algorithm aggregated 20 ms worth of raw data (corresponding to approximately 3000 binary frames) to create a single grayscale frame. The analysis of the grayscale frames was then displayed at a rate of 50 frames per second, providing video frame-rates. RGB reference photos, a 2D rendered representation of the raw LiDAR data point cloud, and the reconstructed 3D profile of the target obtained using the proposed algorithm are shown in Figure 7.5.

RGB Reference   Raw LiDAR data   Reconstructed LiDAR data

(a)   (b)   (c)
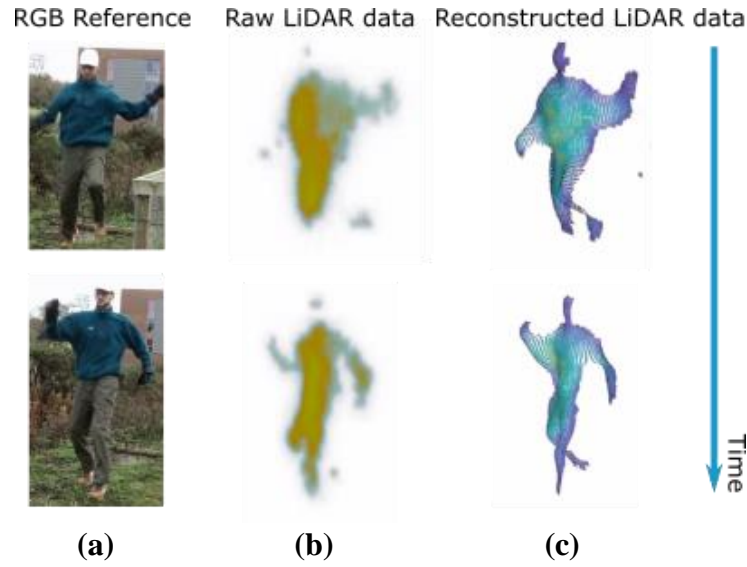
Figure 7.5: Measurements of an unobstructed actor at a stand-off distance of 320 metres. The time between images was two seconds. (a) shows the RGB reference photograph, (b) shows a 2D rendered representation of the raw LiDAR data point cloud, and (c) shows the reconstructed 3D profiles of the scene obtained using the real-time 3D reconstruction algorithm for a grayscale frame acquisition time of 20 ms, displayed at 50 frames per second.

The results show that the proposed algorithm is capable of real-time reconstruction of a fast moving, erratic target at hundreds of metres range. In these results, each pixel observed only a single depth-surface. Each frame had approximately 520 photons per pixel, where 210 photons were due to target returns and 310 photons were related to dark counts of the detector or ambient illumination from solar background. Due to the use of the super-resolution scheme, the target reconstruction also provides a much better depth resolution than what was obtained with the raw LiDAR data.

The second scenario comprised of two actors passing one another while walking briskly through a distance of 3 metres. A wooden backboard was place directly behind the two actors to create a second depth surface. This scenario was designed to investigate the robustness of the algorithm to scenes with multiple targets, and to evaluate whether the real-time reconstruction could differentiate the targets as they passed one another. Figure 7.6 shows the RGB reference images (Figure 7.6 (a)), a 2D rendered representation of the raw LiDAR data point cloud (Figure 7.6 (b)), and the reconstructed 3D data obtained using the proposed algorithm (Figure 7.6 (c)).

204
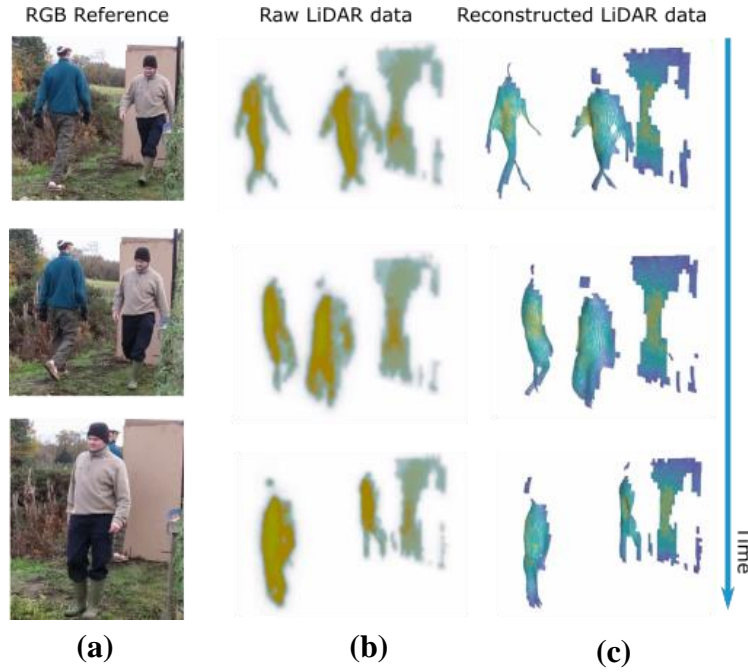
Figure 7.6: Measurements of two unobstructed actors walking in front of a wooden backboard at a stand-off distance of 320 metres. The time between images was one second. These results were obtained using the real-time 3D reconstruction algorithm. (a) shows the RGB reference photograph, (b) shows a 2D rendered representation of the raw LiDAR data point cloud, and (c) shows the reconstructed 3D profiles of the scene for a grayscale frame acquisition time of 20 ms, displayed at 50 frames per second.

The results show that the proposed algorithm is successful in reconstructing scenes containing multiple targets at real-time frame rates. In addition, the algorithm was capable of differentiating the two moving targets as they passed each other. In this case, each frame had approximately 900 photons per pixel, where 543 photons were due to target returns.

The final scenario was used to evaluate the robustness of the proposed algorithm to complex scenes with hidden objects and multiple depth-surfaces per pixel. In this measurement, a camouflage net was erected in front of the actors and backboard, directly in the system's line-of-sight. The two actors then walked briskly through a distance of 3 metres between the backboard and camouflage netting. RGB reference photos, a 2D rendered representation of the raw LiDAR data point cloud, and the reconstructed 3D profile of the target obtained using the proposed algorithm are shown in Figure 7.7.
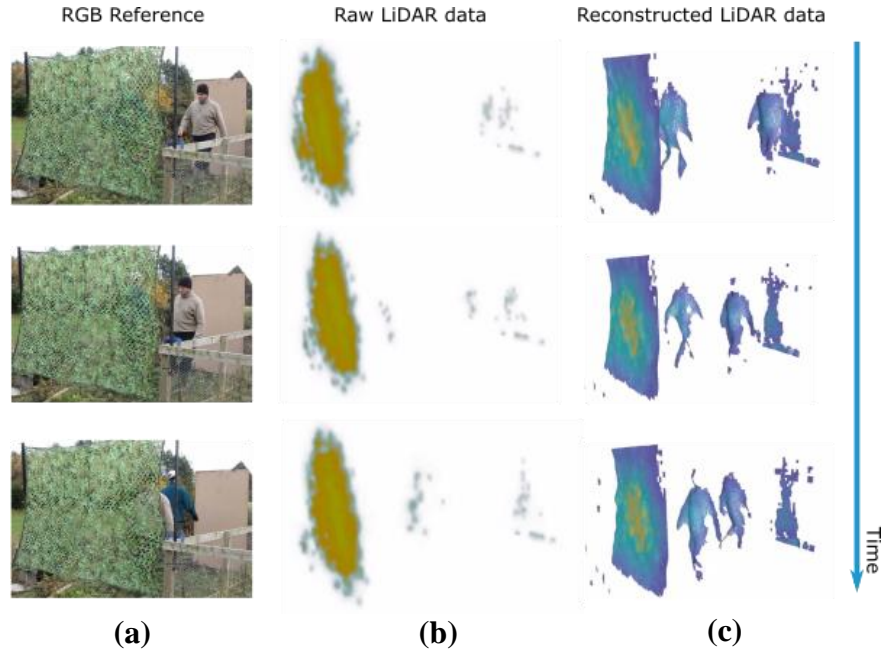
Figure 7.7: Measurements of the two actors obscured by camouflage netting at a stand-off distance of 320 metres. The time between images was one second. These results were obtained using the real-time reconstruction algorithm. (a) shows the RGB reference photograph, (b) shows a 2D rendered representation of the raw LiDAR data point cloud, and (c) shows the reconstructed 3D profiles of the scene for a grayscale frame acquisition time of 20 ms, displayed at 50 frames per second.

The results shown in Figure 7.7 demonstrate the potential of the algorithm for the successful real-time 3D reconstruction of complex scenes. In the raw LiDAR data (Figure 7.7 (b)) the depth profiles of the actors cannot be identified as most of the photon returns were reflected by the camouflage netting, resulting in no depth information in most of the target pixels associated with the human targets. However, using the proposed algorithm, both targets were imaged in real-time (50 grayscale frames per second). Each frame had approximately 900 photons per pixel, where 450 photons are due to target returns. Most pixels have two surfaces present, except for those in the left and right borders of the camouflage netting, where there is only one return per pixel. A maximum number of three surfaces per pixel were found in some parts of the reconstructed image due to the contour of the human targets.

While these results were performed using a relatively low pixel format array (32 × 32 coarse LiDAR pixels or 96 × 96 pixels after the use of a super-resolutions scheme), the proposed algorithm is capable of handling data from larger pixel format arrays while maintaining video-rate processing times. Figure 7.8 (a) shows that the processing time

remains constant at approximately 10 ms per frame up to a 150 × 150 pixel format, due to the parallel structure afforded by the GPU. At larger pixel formats the processing time increases to approximately 30 ms per frame for a 400 × 400 pixel format. This is due to hardware limitations, as the single GPU used in this work (an NVIDIA Xp) does not have enough processors to handle so many pixels at the same time. Thus, future advances in GPU technology would alleviate this issue, bringing down processing times for larger format arrays. Another factor that increases the processing time is the number of active bins in the raw LiDAR data. Figure 7.8 (b) shows a plot of the processing time as a function of the number of active bins. The results show that there is an almost linear dependency, as in this case the per-pixel computations are not parallelised meaning that there is a trade-off between the number of active bins selected for the measurement (i.e., the measurement depth range) and the processing time. Therefore, the number of active bins in the timing histogram must be carefully considered for each scene when obtaining the original LiDAR data.
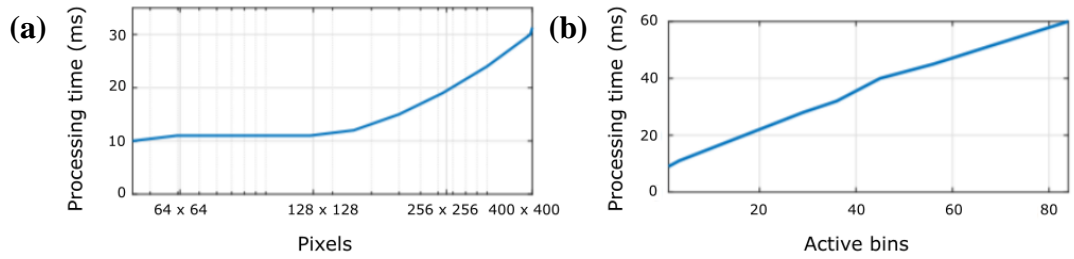
Figure 7.8: Processing times of the real-time 3D reconstruction algorithm as a function of the number of (a) pixels in the detector array and (b) number of active histogram bins.

7.6 Conclusions and future work

A bistatic depth imaging system based on the single-photon ToF approach was used to obtain long-range data of moving targets in complex scenes, such as behind camouflage netting. The system was based on a 32 × 32 InGaAs/InP SPAD detector array with a wavelength range of 1400 – 1600 nm, a temporal resolution of 250 ps, an SPDE of approximately 25% at the operating wavelength of 1550 nm. The array was operated at a repetition rate of 150,421 Hz. A pulsed fibre laser was used to provide a flood-illumination of the target scene with an average optical power level of approximately 70 mW, resulting in eye-safe imaging in the SWIR band.

This Chapter presented a novel algorithm capable of 3D reconstruction of LiDAR data with multiple depth surfaces at video-frame rates. A range of measurements involving

fast moving targets, both unobstructed and hidden from view, were performed at a stand-off distance of 320 metres. The results show that the algorithm is successful in providing real-time 3D reconstructions of LiDAR data of complex scenes in outdoor environments with processing times as low as 10 ms per grayscale frame. This is a significant improvement on current state-of-the-art algorithms, which generally have processing times in the region of 10s to 100s of seconds [7.13–7.21]. The results show that the processing time of this algorithm is mainly dependent on two factors: (i) the size of the pixel format of the detector array and (ii) the number of active bins used to acquire the LiDAR data. The former is limited only by the GPU implemented in the system, and future advances in GPU technology will allow for faster data reconstruction of larger scale arrays. The latter is a limitation inherent to the TCSPC LiDAR approach. Thus, the selected measurement depth range of the LiDAR system should be carefully chosen in each imaging scenario based on the requirements of the scene.

The results presented in this Chapter demonstrate the potential for the implementation of single-photon counting approaches using InGaAs/InP SPAD arrays in modern embedded systems, such as driverless cars. The high timing resolution, long-range capabilities, and low optical power levels inherent to the TCSPC approach fulfils many of the requirements of current systems [7.1,7.4]. However, further investigation is necessary to evaluate the system and proposed algorithm in more challenging scenarios. This will include the investigation of targets travelling at higher velocities, over larger distances, and in adverse conditions – such as in heavy precipitation, fog, and smoke.

7.7 Acknowledgements

Dr Aongus McCarthy and Professor Gerald S. Buller provided advice and input on the system configuration, experimental parameters, and the measurement scenarios. Dr Robert J. Collins captured the RGB reference videos. The proposed real-time 3D reconstruction algorithm was designed and coded by Julián Tachella and Dr Yoann Altmann with input from myself based on LiDAR data obtained with the system described in Section 7.2 of this Chapter. Nicolas Mellado provided the raw LiDAR data images.

7.8 References

7.1.   M. Entwistle, M.A. Itzler, J. Chen, M. Owens, K. Patel, X. Jiang, K. Slomkowski, and S. Rangwala, "Geiger-mode APD camera system for single-photon 3D LADAR imaging," Proc. SPIE 8375, Advanced Photon Counting Techniques VI, 83750D (2012).

7.2.   M. Henriksson and P. Jonsson, "Photon-counting panoramic three-dimensional imaging using a Geiger-mode avalanche photodiode array," Opt. Eng. 57(9), 093104 (2018).

7.3.   P. Soan, M. Silver, J. Parsons, P. Feneyrou, A. Martin, R. Tobin, A. McCarthy, A. Halimi, S. Chan, K. McEwan, J. Miah, B. Stewart, J. Leach, and G. Buller, "Comparative assessment of different active imaging technologies for imaging through obscurants," Proc. SPIE. 10796, in Electro-Optical Remote Sensing XII, 107960C (2018).

7.4.   J. Hecht, "Lidar for self-driving cars," Opt. Photonics News 29(1), 26–33 (2018).

7.5.   A. Azim and O. Aycard, "Detection, classification and tracking of moving objects in a 3D environment," IEEE Intelligent Vehicles Symposium, 802–807 (2012).

7.6.   A. Petrovskaya and S. Thrun, "Model based vehicle detection and tracking for autonomous urban driving," Auton. Robots 26(2), 123–139 (2009).

7.7.   C. Guo, W. Sato, L. Han, S. Mita, and D. McAllester, "Graph-based 2D road representation of 3D point clouds for intelligent vehicles," 2011 IEEE Intelligent Vehicles Symposium, 715–721 (2011).

7.8.   D. Steinhauser, O. Ruepp, and D. Burschka, "Motion segmentation and scene classification from 3D LIDAR data," IEEE Intelligent Vehicles Symposium, 398–403 (2008).

7.9   R. E. Bird, R. L. Hulstrom, and L. J. Lewis, "Terrestrial solar spectral data sets," Sol. Energy 30(6), 563–573 (1983).

7.10   I. I. Kim, M. Mitchell, and E. J. Korevaar, "Measurement of scintillation for free-space laser communication at 785 nm and 1550 nm," Optical Wireless Communications II, 3850, 49–63 (1993).

7.11   F. Nadeem, T. Javornik, E. Leitgeb, V. Kvicera, and G. Kandus, "Continental Fog Attenuation Empirical Relationship from Measured Visibility Data," Radioengineering 19(4), 596–600 (2010).

7.12. M. A. Itzler, r. Ben-Michael, C.-F. Hsu, K. Slomkowski, A. Tosi, S. Cova, F. Zappa, and R. Ispasoiu, "Single photon avalanche diodes (SPADs) for 1.5 µm photon counting applications," J. Mod. Opt. 54(2–3), 283–304 (2007).

7.13. Y. Altmann, X. Ren, A. McCarthy, G. S. Buller, and S. McLaughlin, "Lidar waveform-based analysis of depth images constructed using sparse single-photon data," IEEE Trans. Image Process. 25(5), 1935–1946 (2016).

7.14. Y. Altmann, X. Ren, A. McCarthy, G. S. Buller, and S. McLaughlin, "Robust Bayesian target detection algorithm for depth imaging from sparse single-photon Data," IEEE Trans. Comput. Imaging 2(4), 456–467 (2016).

7.15. D. Shin, A. Kirmani, V. K. Goyal, and J. H. Shapiro, "Photon-efficient computational 3-D and reflectivity imaging with single-photon detectors," IEEE Trans. Comput. Imaging 1(2), 112–125 (2015).

7.16. J. Rapp and V. K. Goyal, "A few photons among many: unmixing signal and noise for photon-efficient active imaging," IEEE Trans. Comput. Imaging 3(3), 445–459 (2017).

7.17. D. B. Lindell, M. O'Toole, and G. Wetzstein, "Single-photon 3D imaging with deep sensor fusion," ACM Trans Graph 37(4), 1–12 (2018).

7.18. A. Halimi, Y. Altmann, A. McCarthy, X. Ren, R. Tobin, G. S. Buller, and S. McLaughlin, "Restoration of intensity and depth images constructed using sparse single-photon data," 24th European Signal Processing Conference (EUSIPCO), 86–90 (2016).

7.19. D. Shin, F. Xu, F. N. C. Wong, J. H. Shapiro, and V. K. Goyal, "Computational multi-depth single-photon imaging," Opt. Express 24(3), 1873–1888 (2016).

7.20. J. Tachella, Y. Altmann, X. Ren, A. McCarthy, G. Buller, S. McLaughlin, and J. Tourneret, "Bayesian 3D reconstruction of complex scenes from single-photon lidar data," SIAM J. Imaging Sci. 12(1), 521–550 (2019).

7.21. S. Hernandez-Marin, A. M. Wallace, and G. J. Gibson, "Bayesian analysis of lidar signals with multiple returns," IEEE Trans. Pattern Anal. Mach. Intell. 29(12), 2170–2180 (2007).

7.22. J. Tachella, Y. Altmann, N. Mellado, A. McCarthy, R. Tobin, G. S. Buller, J.-Y. Tourneret, and S. McLaughlin, "Real-time 3D reconstruction of complex scenes using single-photon lidar: when image processing meets computer graphics," ArXiv190506700 Phys. (2019).

7.23. M. Entwistle, M.A. Itzler, J. Chen, M. Owens, K. Patel, X. Jiang, K. Slomkowski, and S. Rangwala, "Geiger-mode APD camera system for single-photon 3D LADAR imaging," Proc. SPIE 8375, Advanced Photon Counting Techniques VI, 83750D (2012).

7.24 M.A. Itzler, M. Entwistle, M. Owens, K. Patel, X. Jiang, K. Slomkowski, S. Rangwala, P.F. Zalud, T. Senko, J. Tower, and J. Ferraro, "Comparison of 32 x 128 and 32 x 32 Geiger-mode APD FPAs for single photon 3D LADAR imaging," Proc. SPIE 8033, Advanced Photon Counting Techniques V, 80330G (2011).

7.25. "GFL and HFL series user's manual," (Laser 2000, accessed 2019).

7.26. "Raptor Ninox 640 VIS-SWIR datasheet," (Raptor Photonics, accessed 2019).

7.27. J. Bolte, S. Sabach, and M. Teboulle, "Proximal alternating linearized minimization for nonconvex and nonsmooth problems," Math. Program. 146(1), 459–494 (2014).

7.28. G. Guennebaud and M. Gross, "Algebraic point set surfaces," ACM SIGGRAPH 2007 Papers, (2007).

7.29. G. Guennebaud, M. Germann, and M. Gross, "Dynamic sampling and rendering of algebraic point set surfaces," Comput. Graph. Forum 27(2), 653–662 (2008).

7.30. X. Niu, "An overview of image super-resolution reconstruction algorithm," 11th International Symposium on Computational Intelligence and Design (ISCID), 02, 16–18 (2018).

Chapter 8: Conclusions and outlook

This final Chapter will summarise and conclude the work presented throughout this Thesis.

8.1 Summary of conclusions

In recent years there has been increasing interest in the use of Light Detection and Ranging (LiDAR) systems for the high-resolution imaging of targets in visually degraded environments [8.1–8.5]. This Thesis presented work on the characterisation of two single-photon depth profiling systems for free-space imaging through scattering media such as camouflage, smoke, and fog. Both systems used the time-of-flight (ToF) approach alongside the time-correlated single-photon counting (TCSPC) technique, which offers high temporal resolution and excellent surface-to-surface resolution. The measurements presented in this Thesis were all performed using an operating wavelength of 1550 nm using indium gallium arsenide/indium phosphide (InGaAs/InP) single-photon avalanche diode (SPAD) detectors. The use of short-wave infrared (SWIR) wavelengths in LiDAR systems has several advantages over visible wavelength systems, such as high atmospheric transmission [8.6,8.7], low solar background [8.8], and compatibility with the fibre optics low-loss telecommunications window. In addition, it allows the use of higher optical power levels due to an increased threshold in eye-safety for compared to wavelengths in the retinal hazard region (i.e., $400 - 1400$ nm) [8.9,8.10]. To the best of the author's knowledge, the work described in this Thesis represents the first application of the TCSPC technique using InGaAs/InP SPAD detectors for free-space imaging in obscurants at SWIR wavelengths.

Chapters $1 - 3$ presented an introduction to LiDAR imaging, the TCSPC technique, and single-photon detection.

Chapter 4 presented work performed as part of the NATO SET 205 field trials in Virginia, USA, which included several LiDAR systems from different NATO countries. The aim of this field trial was to evaluate the long-range imaging performance of the $\lambda = 1550$ nm depth imaging system for both unobstructed and obstructed targets [8.2]. In this work, a monostatic depth imaging system based on the TCSPC approach was used to obtain three-dimensional depth profiles of targets at a stand-off distance of 230 metres. The system comprised of a pulsed supercontinuum laser source operated at an average optical power level of < 1 mW at a repetition rate of 19.5 MHz for all measurements. A series of high-performance filters was used to deliver a fibre-coupled illumination of

$\lambda = 1550$ nm. The detection system comprised of a single-pixel InGaAs/InP single-photon avalanche diode (SPAD) with a wavelength range of $900 - 1700$ nm, a temporal resolution of 2 ps, and a single-photon detection efficiency of approximately 35% at $\lambda = 1550$ nm. This investigation was successful in both the imaging and identification of a range of hazardous and non-hazardous targets in challenging outdoor scenarios with a high level of ambient background. The results showed that depth and intensity profiles of the targets could be reconstructed for unobstructed targets using a simple cross-correlation algorithm from data with acquisition times as low as 1 second. The target objects of interest were easily identifiable in the depth profiles with sub-centimetre depth resolution. The second set of measurements were performed using the same target set behind a double layer of camouflage netting. By gating the timing histogram, the target profile could be successfully reconstructed with the target items easily identifiable. However, in this case, many missing pixels where no data was acquired were present in both the depth and intensity estimates, due to the optical signal being blocked by the camouflage netting. Therefore, the data were processed using the more sophisticated Restoration of Depth and Intensity using the Total Variation (RDI-TV) algorithm, which was designed to exploit spatial correlations in single-photon data. This algorithm provided good reconstruction results, with accurate depth and intensity estimates obtained at well below one photon per pixel, on average.

In Chapter 5, the same monostatic depth imaging system was used to obtained three-dimensional depth profiles of targets through a variety of obscuring media in a 26-metre-long indoor obscurant chamber, at an illumination wavelength of 1550 nm [8.3]. The average optical power level for all measurements presented in this Chapter was less than 1.5 mW at a repetition rate of 15.6 MHz. These measurements were performed in collaboration with the French-German Research Institute of Saint-Louis (ISL), who provided visible band measurements that served as a comparison for the 1550 nm depth imaging system. The obscurant chamber was housed in an indoor tunnel on-site at ISL in France. Four different obscurants were investigated in this study: black canister smoke, white canister smoke, glycol vapour, and water fog. Attenuation coefficient measurements were obtained for each obscurant for both $\lambda = 1550$ nm and the visible band. The results demonstrate that the use of 1550 nm wavelength illumination provides significant benefits over the visible band for both smoke types and glycol vapour but little or no benefit for the case of the water fog used in these measurements. The data were processed using three image processing algorithms of varying complexity; (i)

pixel-wise cross-correlation, (ii) RDI-TV, and (iii) the Multidimensional Nonlocal Reconstruction of 3D (M-NR3D) images algorithm. While the cross-correlation algorithm provided good results in both black and white canister smoke, it failed to reconstruct scenarios where much larger diameter particles were present (such as in water fog or glycol vapour). Depth and intensity profiles were obtained at attenuation length values of up to 3.8 at $\lambda = 1550$ nm in water fog and 3.5 in glycol vapour, equivalent to > 11 attenuation lengths in the visible band using the more sophisticated RDI-TV and M-NR3D algorithms. Each algorithm's performance was dependent on the considered scenario. The RDI-TV algorithm appeared to be more suitable for measurements containing a reduced background level, while the M-NR3D algorithm performed very good data restoration even in presence of high levels of scattering background. Moreover, the M-NR3D algorithm is more general in the sense that it accounts for the presence of multiple peaks.

Chapter 6 presented a bistatic depth imaging system based on the single-photon ToF approach, which was used to rapidly obtain three-dimensional depth profiles of targets through varying densities of glycol-based vapour at an illumination wavelength of 1550 nm [8.11]. The detection system was comprised of a 32×32 InGaAs/InP SPAD detector with a wavelength range of $1400 - 1600$ nm, a temporal resolution of 250 ps, and a single-photon detection efficiency (SPDE) of approximately 25% at the operating wavelength of $\lambda = 1550$ nm. The illumination source was a pulsed fibre laser with an average optical output power of approximately 220 mW at a repetition rate of 150,421 Hz. The average DCR of the detector was measured be approximately 318 kcps at a gate width of 20 ns and 5370 kcps at an increased gate width of 200 ns. A LiDAR model, which was based on the photon-counting LiDAR equation and adapted for this specific system configuration, was presented in this Chapter to evaluate the potential ranging performance of the system. The results suggested that successful depth imaging should be achievable using this system in its current configuration in highly scattering environments at up to 6 attenuation lengths at target distances up to 150 metres using SWIR illumination. However, this estimation was highly dependent on the level of background due to ambient illumination during measurements, the optical components used, and the target reflectivity and geometry. The performance was the system was evaluated over several target ranges (50, 150, and 1463 m) as part of a Dstl field trial at Porton Down in the U.K. At a 50 m stand-off distance, the system obtained images of the full target scene at approximately 5.0 attenuation lengths using pixel-wise

cross-correlation and partial reconstructions of the scene were obtained at up to 6.0 attenuation lengths for a one-second data acquisition. A partial target reconstruction was achieved at 4.7 attenuation lengths and full reconstruction at 3.4 attenuation lengths for a one second data acquisition at a stand-off distance of 150 m. A transmissometer with an illumination wavelength of 637 nm was used to obtain transmission measurements in the visible wavelength band. This comparison highlighted the benefits of SWIR wavelengths over the visible region for imaging through obscurants, as the 1550 nm illumination was indicated to be almost twice as penetrative as the 637 nm wavelength. Depth estimates were also obtained at a range of 1463 metres with no obscurant present. This was performed to better understand the sensor performance at more challenging distances using various levels of neutral density filters to simulate high levels of obscurants. Target depth estimates were successfully made at 0.01 seconds acquisition time using an ND1 filter (10% optical transmission) to simulate imaging at kilometre range in obscurants, and to explore the possibilities of examining, identifying, and tracking moving targets.

In Chapter 7, the same bistatic depth imaging system was used to obtain data of moving targets at stand-off distances of 325 m in complex scenes, such as behind camouflage netting [8.12]. A pulsed fibre laser was used to provide a flood-illumination of the target scene with an average optical power level of approximately 70 mW, resulting in eye-safe imaging in the SWIR band. A novel algorithm capable of 3D reconstruction of LiDAR data with multiple depth surfaces at video-frame rates was used to reconstruct depth profiles of the target scene. The results show that the algorithm is successful in providing real-time 3D reconstructions of LiDAR data of complex scenes in outdoor environments with processing times as low as 10 ms per grayscale frame. These results indicate a significant improvement on current state-of-the-art algorithms, which generally have processing times in the region of 10s to 100s of seconds for similar data.

8.2 Outlook

This Thesis has demonstrated that depth imaging using illumination wavelengths of 1550 nm in combination with highly sensitive single-photon counting techniques is a powerful approach for the identification of a target in extreme conditions, such as targets obscured by camouflage or in high levels of scattering media. For example, depth profiles of targets were obtain at up to 6 attenuation lengths through glycol-based vapour using a bistatic arrayed detector imaging system. This is estimated to be equivalent to approximately 12 attenuation lengths for visible band systems - a significant improvement on existing depth imaging systems for imaging in high levels of particulate

scattering [8.11,8.13]. However, several modifications could be made to further extend the capability of the two systems described in this Thesis. In Chapter 6, a photon-counting LiDAR model was presented that indicated that the maximum achievable number of attenuation lengths by a system is dependent on several factors, such as the optical power level and the aperture size of the receiver objective lens. Thus, the use of an illumination source with a higher maximum power level may allow for the imaging of targets over a greater number of attenuation lengths, whilst remaining eye-safe at SWIR wavelengths. However, the use of higher optical power levels requires careful consideration and care to avoid damaging the use of the highly sensitive single-photon detectors. The use of a larger aperture diameter objective lens could also potentially increase the number of achievable attenuation lengths, as more photons could be collected by the system. However, this would also increase the number of background counts collected by the system due to ambient light, so improved spectral filtering may be required in this case.

All of the results presented in this Thesis were acquired using artificially generated obscurants, such as canister smoke, glycol-based vapour, and water-based fog produced by a sprinkler system [8.3,8.11]. Therefore, future work will include depth profiling of targets in a wider range of environments, such as in natural fog or haze. This will also involve a comparison between the visible spectrum and SWIR wavelengths through high levels of obscurants in outdoor scenarios with high ambient background levels.

This work performed in this Thesis has revealed several limitations of current single-photon counting LiDAR systems. For example, data acquisition using scanning systems that use a point-and-stare approach can take a relatively long duration, as the scan speed has a lower limitation placed on it due to the movement of the scanning mirrors. This means that target identification in scenarios that require near-instantaneous feedback, such as in situations with fast moving targets, may prove challenging. In addition, the ability to make a successful measurement using single-photon counting systems is largely based on the signal-to-noise ratio (SNR) of the data, as discussed in Chapter 3. The work presented in Chapter 6 of this Thesis and in ref. [8.4] shows that there is a minimum SNR required to make a successful depth measurement, which is based on both the system configuration and the environmental conditions during measurements. The system configuration can always be optimised using improved components and hardware. However, if the environmental conditions during measurements are so extreme that this minimum SNR is not achieved, obtaining accurate measurements may prove difficult. This means that certain countermeasures against

single-photon LiDAR systems could be employed. For example, Chapter 5 demonstrated that the presence of obscurants with large particle size distributions can hinder successful data acquisition. Large densities of such obscurants could be deployed to hide targets from view of the system. Moreover, the number of photon returns collected by the system is dependent on the scattered reflectivity of the target, as well as the operating wavelength of the system as shown in ref. [8.14] and in Chapter 4 of this Thesis. This means that the material used in the composition of targets can be carefully selected to avoid detection from single-photon counting LiDAR systems.

A further limitation of the approach used in this Thesis is the use of periodic laser sources which can result in range ambiguity, as well as being more readily detected by laser warning devices. As shown in other single-photon depth imaging work [8.15], the use of pseudo-random pulse sequences can be used to avoid both potential system limitations. Development of ideal laser sources in terms of their potential for randomising their repetition rate and their compatibility with improved spectral filtering to help reduce the effects of the solar background, will remain a key aspect of future single-photon LiDAR research.

Both systems described in this Thesis were based on InGaAs/InP SPAD detector technology. As mentioned previously, InGaAs/InP SPADs are currently the best candidate technology for single-photon counting applications in the SWIR due to their compatibility with compact Peltier cooling systems. These detectors are commercially available in both single-pixel formats [8.16] and as SPAD arrays [8.17,8.18], and offer relatively low DCRs, low timing jitters and SPDEs of up to a maximum of 45% at a detection wavelength of 1550 nm at near-room temperatures. However, germanium-on-silicon (Ge-on-Si) SPAD detectors have become potential candidates for SWIR single-photon detection due to the good absorption properties exhibited by germanium at room temperatures for wavelengths up to 1600 nm and the excellent multiplication properties of Si [8.19]. Recently, custom-made Ge-on-Si SPADs operated at a wavelength of 1310 nm have been reported [8.20] that demonstrate record low NEPs compared to those reported in literature [8.21–8.23]. These detectors have SPDE values that are comparable to commercially available InGaAs/InP SPAD detectors, and demonstrate considerably reduced afterpulsing effects, which is a drawback of InGaAs/InP detectors. Currently, these devices require further optimisation to reduce the dark count rate at increased operating temperatures to enable efficient single-photon imaging at a wavelength of 1550 nm. Recently, detectors that incorporate tin (Sn) into

Ge have been demonstrated, which expand the spectral detection range to 2 µm and beyond [8.24–8.26]. However, these Ge:Sn detectors have never been shown in terms of SPAD operation. Regardless, future work will incorporate these alternative detectors for imaging in highly scattering media and in outdoor environments.

As discussed in Chapter 3, superconducting nanowire single-photon detectors (SNSPDS) provide improved timing resolution, high single-photon detection efficiencies, and very wide spectral range [8.27]. As discussed in this Thesis, SWIR wavelengths have higher atmospheric transmission and have a reduced solar background compared to visible wavelengths, and this becomes even more apparent at longer wavelengths above 1550 nm. Thus, the implementation of SNSPDs that extend wavelength detection sensitivity to 2.3 µm [8.28] in single-photon LiDAR systems is the aim of future work as these detectors have the potential to enhance depth resolution and extend imaging ranges in outdoor environments.

As discussed in Chapter 2, the LiDAR technique can be used to make multispectral measurements in order to obtain the spectral response information of a target object [8.29–8.31]. Preliminary investigations of the recovery of range and spectral profiles associated with remote three-dimensional scenes sensed via single-photon multi-spectral LiDAR has been performed [8.32,8.33]. In this work, two different spatial/spectral sampling strategies were considered and their performance for a similar overall number of detected photons was compared [8.32]. The results suggest a way forward for the integration of single-photon detector arrays with mosaic filters for use in a range of emerging photon-starved two-dimensional and three-dimensional imaging applications. Simultaneous multi-spectral measurements using only one single-photon detector were also performed [8.33]. By observing multiple wavelengths at each spatial location, a single waveform with wavelength-to-time mapped peaks could be obtained. These preliminary results suggest that single-photon multi-spectral LiDAR using mosaic filters could be used for a number of applications, such as vegetation analysis [8.31] and the discrimination of man-made objects in natural environments [8.34]. For example, water is strongly absorbing at a wavelength of 1550 nm relative to nearby wavelengths such as 1310 nm [8.35]. Thus, the water content in foliage could be investigated by using a single-photon multi-spectral LiDAR system with an illumination wavelength of 1550 nm and a reference wavelength of 1310 nm, for example.

Another potential use for SWIR single-photon counting LiDAR systems is the remote sensing of greenhouse gases and pollutants, as carbon dioxide, carbon monoxide,

methane, and nitrous oxide have their fundamental absorption bands located in the mid-infrared [8.36,8.37]. In particular, the fundamental absorption band of carbon dioxide is centred on 1573 nm [8.38] and a secondary absorption line is located at approximately 2100 nm [8.39]. Detection of these greenhouse gases is critical to the investigation of the Earth's atmosphere, atmospheric chemistry, and for monitoring climatic change.

Finally, this Thesis has demonstrated that single-photon depth profiling of targets in extreme environments can be greatly improved through the use of sophisticated image processing algorithms that exploit spatial correlations in single-photon data [8.2,8.3,8.12]. This is particularly important for the free space depth profiling of targets at long-ranges and in high levels of scattering media, where the return signal can be much less than one photon on average. Chapter 7 presented an algorithm that was used for the real-time reconstruction of single-photon data of a moving target with processing times as low as 10 ms per grayscale frame. This preliminary investigation was performed with a complex scene typically containing more than one surface per pixel. Future work will investigate the use of the arrayed detector imaging system for the real-time reconstruction of ultra-fast movement (i.e., 1000s of frames per second), for target tracking, for much longer target ranges, and in more complex scenes containing many different surfaces.

8.3 References

8.1.   M. Henriksson, H. Larsson, C. Grönwall, and G. Tolt, "Continuously scanning time-correlated single-photon-counting single-pixel 3-D lidar," Opt. Eng. 56(3), 031204 (2016).

8.2.   R. Tobin, A. Halimi, A. McCarthy, X. Ren, K. J. McEwan, S. McLaughlin, and G. S. Buller, "Long-range depth profiling of camouflaged targets using single-photon detection," Opt. Eng. 57(3), 031303 (2017).

8.3.   R. Tobin, A. Halimi, A. McCarthy, M. Laurenzis, F. Christnacher, and G. S. Buller, "Three-dimensional single-photon imaging through obscurants," Opt. Express 27(4), 4590 (2019).

8.4.   A. Maccarone, A. McCarthy, X. Ren, R. E. Warburton, A. M. Wallace, J. Moffat, Y. Petillot, and G. S. Buller, "Underwater depth imaging using time-correlated single-photon counting," Opt. Express 23(26), 33911–33926 (2015).

8.5.   A. M. Pawlikowska, A. Halimi, R. A. Lamb, and G. S. Buller, "Single-photon three-dimensional imaging at up to 10 kilometers range," Opt. Express 25(10), 11919–11931 (2017).

8.6.   I. I. Kim, M. Mitchell, and E. J. Korevaar, "Measurement of scintillation for free-space laser communication at 785 nm and 1550 nm," in *Optical Wireless Communications II* 3850, 49–63 (1999).

8.7. F. Nadeem, T. Javornik, E. Leitgeb, V. Kvicera, and G. Kandus, "Continental fog attenuation empirical relationship from measured visibility data," Radioengineering 19(4), 596–600 (2010).

8.8. R. E. Bird, R. L. Hulstrom, and L. J. Lewis, "Terrestrial solar spectral data sets," Sol. Energy 30(6), 563–573 (1983).

8.9. "Safety of laser products – Part 1: Equipment classification, requirements and user's guide" (IEC 60825-1, 1993).

8.10. International Commission on Illumination, 17-1407, http://www.cie.co.at/eilv/1407

8.11. P. Soan, M. Silver, J. Parsons, P. Feneyrou, A. Martin, R. Tobin, A. McCarthy, A. Halimi, S. Chan, K. McEwan, J. Miah, B. Stewart, J. Leach, and G. Buller, "Comparative assessment of different active imaging technologies for imaging through obscurants," in *Electro-Optical Remote Sensing XII* 10796, 107960C (2018).

8.12. J. Tachella, Y. Altmann, N. Mellado, A. McCarthy, R. Tobin, G. S. Buller, J.-Y. Tourneret, and S. McLaughlin, "Real-time 3D reconstruction of complex scenes using single-photon lidar: when image processing meets computer graphics," ArXiv190506700 Phys. (2019).

8.13. G. Satat, M. Tancik, and R. Raskar, "Towards photography through realistic fog," in *2018 IEEE International Conference on Computational Photography (ICCP)*, 1–10 (2018).

8.14. A. McCarthy, R. J. Collins, N. J. Krichel, V. Fernández, A. M. Wallace, and G. S. Buller, "Long-range time-of-flight scanning sensor based on high-speed time-correlated single-photon counting," Appl. Opt. 48(32), 6241–6251 (2009).

8.15. N. J. Krichel, A. McCarthy, and G. S. Buller, "Resolving range ambiguity in a photon counting depth imager operating at kilometer distances," Opt. Express 18(9), 9192–9206 (2010).

8.16. A. Tosi, A. Della Frera, A. Bahgat Shehata, and C. Scarcella, "Fully programmable single-photon detection module for InGaAs/InP single-photon avalanche diodes with clean and sub-nanosecond gating transitions," Rev. Sci. Instrum. 83(1), 013104 (2012).

8.17. M. Entwistle, M.A. Itzler, J. Chen, M. Owens, K. Patel, X. Jiang, K. Slomkowski, and S. Rangwala, "Geiger-mode APD camera system for single-photon 3D LADAR imaging," Proc. SPIE 8375, Advanced Photon Counting Techniques VI, 83750D (2012).

8.18. P. Yuan, R. Sudharsanan, X. Bai, J. Boisvert, P. McDonald, E. Labios, M. S. Salisbury, G. M. Stuart, H. Danny, A. A. Portillo, A. B. Roybal, S. Van Duyne, G. Pauls, S. Gaalema, "32 x 32 Geiger-mode ladar camera," Proc. SPIE 7684, Laser Radar Technology and Applications XV, 76840C (2010).

8.19. W. C. Dash and R. Newman, "Intrinsic Optical Absorption in Single-Crystal Germanium and Silicon at 77°K and 300°K," Phys. Rev. 99(4), 1151–1155 (1955).

8.20. P. Vines, K. Kuzmenko, J. Kirdoda, D. C. S. Dumas, M. M. Mirza, R. W. Millar, D. J. Paul, and G. S. Buller, "High performance planar germanium-on-silicon single-photon avalanche diode detectors," Nat. Commun. 10(1), (2019).

8.21. R. E. Warburton, G. Intermite, M. Myronov, P. Allred, D. R. Leadley, K. Gallacher, D. J. Paul, N. J. Pilgrim, L. J. M. Lever, Z. Ikonic, R. W. Kelsall, E. Huante-Cerón, A. P. Knights, and G. S. Buller, "Ge-on-Si single-photon avalanche diode detectors: design, modeling, fabrication, and characterization at wavelengths 1310 and 1550 nm," IEEE Trans. Electron Devices 60(11), 3807–3813 (2013).

8.22. N. J. D. Martinez, M. Gehl, C. T. Derose, A. L. Starbuck, A. T. Pomerene, A. L. Lentine, D. C. Trotter, and P. S. Davids, "Single photon detection in a waveguide-coupled Ge-on-Si lateral avalanche photodiode," Opt. Express 25(14), 16130–16139 (2017).

8.23. Z. Lu, Y. Kang, C. Hu, Q. Zhou, H. Liu, and J. C. Campbell, "Geiger-Mode Operation of Ge-on-Si Avalanche Photodiodes," IEEE J. Quantum Electron. 47(5), 731–735 (2011).

8.24. A. Gassenq, F. Gencarelli, J. Van Campenhout, Y. Shimura, R. Loo, G. Narcy, B. Vincent, and G. Roelkens, "GeSn/Ge heterostructure short-wave infrared photodetectors on silicon," Opt. Express 20(25), 27297 (2012).

8.25. H. Cong, C. Xue, J. Zheng, F. Yang, K. Yu, Z. Liu, X. Zhang, B. Cheng, and Q. Wang, "Silicon Based GeSn p-i-n Photodetector for SWIR Detection," IEEE Photonics J. 8(5), 1–6 (2016).

8.26. M. Oehme, M. Schmid, M. Kaschel, M. Gollhofer, D. Widmann, E. Kasper, and J. Schulze, "GeSn p-i-n detectors integrated on Si with up to 4% Sn," Appl. Phys. Lett. 101(14), 141110 (2012).

8.27. R. H. Hadfield, "Single-photon detectors for optical quantum information applications," Nat. Photonics 3(12), 696–705 (2009).

8.28. G. G. Taylor, D. Morozov, N. R. Gemmell, K. Erotokritou, and R. H. Hadfield, "2.3μm wavelength single photon LIDAR with superconducting nanowire detectors," in Conference on Lasers and Electro-Optics, JTh2A.93 (2019).

8.29. Y. Altmann, A. Maccarone, A. McCarthy, G. Newstadt, G. S. Buller, S. McLaughlin, and A. Hero, "Robust spectral unmixing of sparse multispectral Lidar waveforms using Gamma Markov random fields," IEEE Trans. Comput. Imaging 3(4), 658–670 (2017).

8.30. G. S. Buller, R. D. Harkins, A. McCarthy, P. A. Hiskett, G. R. MacKinnon, G. R. Smith, R. Sung, A. M. Wallace, R. A. Lamb, K. D. Ridley, and J. G. Rarity, "Multiple wavelength time-of-flight sensor based on time-correlated single-photon counting," Rev. Sci. Instrum. 76(8), 083112 (2005).

8.31. A. M. Wallace, A. McCarthy, C. J. Nichol, X. Ren, S. Morak, D. Martinez-Ramirez, I. H. Woodhouse, and G. S. Buller, "Design and Evaluation of Multispectral LiDAR for the Recovery of Arboreal Parameters," IEEE Trans. Geosci. Remote Sens. 52(8), 4942–4954 (2014).

8.32. R. Tobin, Y. Altmann, X. Ren, A. McCarthy, R. A. Lamb, S. McLaughlin, and G. S. Buller, "Comparative study of sampling strategies for sparse photon multispectral lidar imaging: towards mosaic filter arrays," J. Opt. 19(9), 094006 (2017).

8.33. X. Ren, Y. Altmann, R. Tobin, A. Mccarthy, S. Mclaughlin, and G. S. Buller, "Wavelength-time coding for multispectral 3D imaging using single-photon LiDAR," Opt. Express 26(23), 30146–30161 (2018).

8.34. Y. Li, A. Majumder, H. Zhang, and M. Gopi, "Optimized multi-spectral filter array based imaging of natural scenes," Sensors 18(4), (2018).

8.35. L. S. Rothman, D. Jacquemart, A. Barbe, D. Chris Benner, M. Birk, L. R. Brown, M. R. Carleer, C. Chackerian, K. Chance, L. H. Coudert, V. Dana, V. M. Devi, J.-M. Flaud, R. R. Gamache, A. Goldman, J.-M. Hartmann, K. W. Jucks, A. G. Maki, J.-Y. Mandin, S. T. Massie, J. Orphal, A. Perrin, C. P. Rinsland, M. A. H. Smith, J. Tennyson, R. N. Tolchenov, R. A. Toth, J. Vander Auwera, P. Varanasi, and G. Wagner, "The HITRAN 2004 molecular spectroscopic database," J. Quant. Spectrosc. Radiat. Transf. 96(2), 139–204 (2005).

8.36. J. S. Dam, P. Tidemand-Lichtenberg, and C. Pedersen, "Room temperature mid-IR single photon spectral imaging," Nat. Photonics 6, 788–793 (2012).

8.37. M. N. Abedin, M. G. Mlynczak, and T. F. Refaat, "Infrared detectors overview in the short-wave infrared to far-infrared for CLARREO mission," in *Infrared Remote Sensing and Instrumentation XVIII*), 7808 (2010).

8.38. I. Robinson, J. W. Jack, C. F. Rae, and J. B. Moncrieff, "Development of a laser for differential absorption lidar measurement of atmospheric carbon dioxide," in U. N. Singh and G. Pappalardo, 92460U (2014).

8.39. T. Somekawa, N. Manago, H. Kuze, and M. Fujita, "Differential optical absorption spectroscopy measurement of CO2 using a nanosecond white light continuum.," Opt. Lett. 36(24), 4782–4784 (2011).